University of Southampton

Faculty of Engineering and the Environment

Engineering Materials

Damage Assessment of Particle-Toughened Carbon Fibre Composites Subjected to Impact and Compression-After-Impact using 3D X-ray Tomography

by

Daniel John Bull

Thesis for the degree of Doctor of Philosophy

April 2014

Supervisors:

Professor S. Mark Spearing

Professor Ian Sinclair

Engineering Materials

Faculty of Engineering and the Environment

UNIVERSITY OF SOUTHAMPTON

ABSTRACT

FACULTY OF ENGINEERING AND THE ENVIRONMENT

Doctor of Philosophy

DAMAGE ASSESSMENT OF PARTICLE-TOUGHENED CARBON FIBRE COMPOSITES SUBJECTED TO IMPACT AND COMPRESSION-AFTER-IMPACT USING 3D X-RAY IMAGING TECHNIQUES

by Daniel John Bull

In this thesis, particle-toughened and untoughened, carbon fibre composite material systems with quasi-isotropic layups were investigated. This was to understand better the toughening behaviour leading to increased impact damage resistance and post-impact compression damage tolerance performance. To achieve this, mechanical testing and conventional ultrasonic C-scan methods were combined with damage assessments using several 3D X-ray computed tomography techniques. These consisted of lab based micro-focus computed tomography (µCT), synchrotron radiation computed tomography (SRCT) and synchrotron radiation computed laminography (SRCL). Mechanical impact and compression-after-impact experiments were undertaken to establish the ranking of damage resistant and damage tolerant properties between material systems. This was followed up by damage assessments from CT scans and laminography to characterise the damage macroscopically and microscopically, linking these observations and quantifications back to the overall damage resistance and damage tolerance of the material systems.

Through qualitative and quantitative assessment of the damage mechanisms it is revealed that particle-toughened systems strongly suppressed the extent of delaminations but had little effect on matrix cracks. The suppression of delaminations was achieved through energy absorption and crack-shielding mechanisms consisting of; particle-matrix debonding, crack deflection and bridging effects, which were observed in the resin-rich regions between the plies. Based on quantification of SRCT data in this study, it is suggested that bridging micromechanisms contributed most significantly to increases in damage resistance over the untoughened material.

Ex situ time-series experiments were also employed in this work. µCT scans of fully intact test coupons under incremental loads enabled internal damage initiation and propagation to be monitored. This was done for quasi-static indentation (QSI) and compression-after-impact (CAI) experiments.

For QSI work, comparisons between impact and QSI experiments showed both similarities and differences between the two loading conditions. The most significant differences were observed in two material systems which resulted in a lower damage area under QSI loading than low velocity impact at applied energies above 30 J. This behaviour correlated to a larger extent of bridging ligament formation. It is suggested that the extent of bridging micromechanisms are linked to the improved damage resistance under QSI and that this toughening mechanism is potentially sensitive to strain-rate, hence a loss of damage resistance under impact.

For CAI experiments, the sequence of events leading to failure was established. Based on *ex situ* µCT scans of material systems subjected to post-impact near-failure compressive loads, it was observed that delaminations propagating into the undamaged cone contributed to failure of the coupon by linking surrounding delaminations. This effect more than doubled the unsupported length of the sublaminates, significantly reducing buckling stability and in-plane load carrying capability. Particle-toughened systems maintained a higher residual compressive strength for a given damage area compared to the untoughened systems. It is suggested that particles suppressed delamination growth into the undamaged cone, increasing stability and enabling more load to be carried prior to failure.

Overall, the experimental findings in this thesis will improve the understanding of the mechanisms contributing to failure and the particle-toughening processes which will support the development of superior carbon fibre-reinforced composite systems. The results also support the development of finite element models to ensure the most important mechanisms are included and captured.

List of acronyms

µCT	Microfocus computed tomography
BVID	Barely visible impact damage
CAI	Compression-after-impact
CFRP	Carbon fibre reinforced polymer
COD	Crack-opening displacement
QSI	Quasi-static indentation
ROI	Region of interest
SRCL	Synchrotron radiation computed laminography
SRCT	Synchrotron radiation computed tomography

Nomenclature

ε_B	Buckling strain of sublaminate
δ	Impactor displacement
$\bar{\delta}$	Mean crack-opening displacement
δ_{ij}	Adjusted length at voxel ij
ϕ	Correction factor accounting for crack bowing
λ	Centre-to-centre particle spacing
σ_{br}	Bridging stresses
σ^{CAI}	Ultimate compressive residual strength
Γ_t	Tearing energy of the rubber particles
a	Acceleration of the impactor
	Dimensions of half the elliptical axis parallel to the loading direction
	Half length of the delamination in the loading direction
A	Cross-sectional area of composite
A_{11}, A_{12}, A_{22}	Terms from ABD matrix with coordinate 1 in the loading direction
b	Length of remaining uncracked region
	Dimensions of half the elliptical axis perpendicular to the loading direction
B_y	Percent bending of plate during compression-after-impact
$D_{11}, D_{12}, D_{22}, D_{66}$	Terms from ABD matrix with coordinate 1 in the loading direction
E	Young's modulus
	Equivalent Young's modulus of the quasi-isotropic laminate
E^*	Young's modulus of the rubber particles
E_c	Young's modulus of the modified epoxy
E_m	Young's modulus of the matrix
E_o	Young's modulus of the unmodified epoxy
E_p	Young's modulus of the particle
f	Volume fraction of rubber particles
F_1	Interpolating function
f_{ul}	Area fraction of bridging ligaments
$F(t)$	Force measured from the dynamic load cell as a function of time
F_B	Buckling load of sublaminate
F_C	Critical threshold force for the onset of delamination
F_{max}	Maximum force at the point of failure
g	Acceleration due to gravity
g_{ij}	Grey scale value at voxel ij
g_{air}	Greyscale value of air
g_{mat}	Greyscale value of material away from a crack
G_{IIC}	Mode II critical strain energy release rate
h	Drop height
	Laminate thickness
K_I	Mode I stress intensity factor
K_2	Mode II stress intensity factor
K_3	Mode III stress intensity factor
K_o	Unmodified epoxy stress intensity factor
K_b	Shielding stress intensity factor

K_c	Modified epoxy stress intensity factor
K_{Ic}	Fracture toughness of rubber-modified epoxy
K_I	Applied far-field stress intensity
K_L	Limiting stress intensity factor that specifies the failure of the trailing end of the reinforced zone
l_{ul}	Bridging-zone size
L	Delamination length across the sublaminate
m	Mass of the impactor
n	Points along the trace of a fracture profile
Q^F	Flexural membrane modulus
Q^M	Flexural membrane modulus
r	Rotational factor
$2r$	Diameter of particles
$2s$	Surface-to-surface particle spacing
t	Laminate thickness Time during impact test
t_1	Time the first (lower) flag prong passes the lightgate detector
t_2	Time the second (upper) flag prong passes the lightgate detector
t_2	Time of initial contact obtained from the force-time curve
u^*	Critical crack-opening
v	Poisson's ratio
v_i	initial velocity of the impactor at the point of first contact with the test coupon
v_{lam}	Poisson's ratio of the base laminate
v_m	Poisson's ratio of the matrix
v_p	Poisson's ratio of the particle
W_{12}	Distance between leading edges of the first (lower) and second (upper) flag prongs
y_i	Vertical distance from the mean line to the i^{th} data point

Contents

List of Tables

List of Figures

Declaration of Authorship

I, Daniel John Bull, declare that the thesis entitled ‘Damage Assessment of Particle-Toughened Carbon Fibre Composites Subjected to Impact and Compression-After-Impact using 3D X-ray Imaging Techniques’ and the work presented in the thesis are both my own, and have been generated by me as the result of my own research. I confirm that:

- This work was done wholly or mainly while in candidature for a research degree at this University;
- Where any part of this thesis has previously been submitted for a degree or any other qualification at this University of any other institution, this has been clearly stated;
- Where I have consulted the published work of others, this is always clearly attributed;
- Where I have quoted from the work of others, the source is always given. With the exception of such quotations, this thesis is entirely my own work;
- I have acknowledged all main sources of help;
- Where the thesis is based on work done by myself jointly with others, I have made clear exactly what was done by others and what I have contributed myself;
- Parts of this work have been published as indicated in the list of publications provided with this manuscript.

Signed:

Date:

Acknowledgments

I wish to thank particular individuals and groups for which this work would otherwise not be possible.

Firstly thanks to my two supervisors; Professor Mark Spearing and Professor Ian Sinclair for their knowledge, support and encouragement throughout the project.

Thanks to Dr Richard Boardman, Dr Mark Mavrogordato, Dr Anna Scott and Dr Dmitry Grinev at mu-VIS, for their very much appreciated help and support.

The work in this thesis benefited considerably through the use of synchrotron facilities at the Swiss Light Source (SLS) and the European Synchrotron Radiation Facility (ESRF). My particular thanks to assistance provided by Bernd Pinzer and others on the TOMCAT beamline at the SLS, and Lucas Helfan for his expert knowledge and help on laminography on Beamline ID19 at the ESRF.

My appreciation and thanks goes out to the staff at Cytec Engineered Materials Ltd, for the sponsorship and supply of materials used in this project. Particular thanks to Sam Hill and Dr Kingsley Ho for their invaluable roles as my technical points of contact. Additional funding was provided by the EPSRC, grant number EP/H01506X/1.

Thanks to the staff within the Faculty of Engineering and the Environment, graduate school office and finance office for their tireless efforts behind the scenes.

The mechanical experimental work has been made possible with the assistance of staff and students working in the labs. Particular thanks to Rob Barnes, Dr Andy Robinson and the team at the EDMC.

I would like to thank my friends and colleagues at the University of Southampton, which made the PhD enjoyable to work on by providing invaluable advice for academic discussion and many distractions. Whilst it is not possible to name everyone, I would especially like to thank Richard Critchley, Jenny Crump, Faye Gillard, Nick Alderman, Liam Goodes, Maria Leyva, and Matt Worsdale.

For those who contributed directly and indirectly towards my PhD, your help has been much appreciated.

Chapter 1

Introduction

1.1 Background and motivation

Carbon fibre reinforced polymer (CFRP) materials are increasingly being used in aircraft structures due to their superior stiffness to weight and strength to weight properties compared to conventional materials; these allow weight savings in current and future aircraft [1]. The new Airbus A350-XWB and Boeing 787 Dreamliner are the latest commercial aircraft which demonstrate a significant increase in the use of composite materials. The Boeing 787 has been designed and manufactured with CFRP dominating the primary structures, including the main fuselage skin, wings and vertical and horizontal stabilisers. Comparison with the Boeing 777 launched in June 1994 and the Boeing 787 shows an increase from 12 % composites to 50 %, respectively by weight, reflecting an increased premium on weight saving, due to significantly higher fuel cost and also a greater confidence in designing and manufacturing with this material [2].

A significant disadvantage associated with carbon fibre composites is their poor impact damage resistance, which directly adversely affects the residual compressive strength of the material [1, 3, 4]. Most composite materials are essentially brittle and absorb impact energy through fracture mechanisms, unlike metals that absorb energy through plastic deformation [5] . Barely visible impact damage (BVID) produced by low velocity impact is of general concern, due to the creation of internal damage with a lack of visible surface damage other than a shallow dent, or back-face damage which is often not easily accessible for inspection [6]. This poses a problem as the extent of damage is usually internal and significant in size. It is this damage, in particular delaminations, which have a strong effect on the residual compressive strength [3, 7]. This is usually mitigated by a design approach in which aircraft structures are required to incorporate the anticipated maximum local loss in strength into the design, increasing the structural weight, possibly unnecessarily [8]. In order to minimise these issues,

tougher composite materials are desired, with better damage resistant and damage tolerant properties [1].

Delaminations are of significant concern in composite laminate materials. Delaminations form sublaminates with lower flexural stiffness characteristics, and lower in-plane load carrying capability due to the onset of local failure by buckling [4, 9, 10]. It is reported that the mode II driven delamination has a direct bearing on the damage resistance. By increasing the mode II toughness at the interply regions, the damage resistance and subsequent damage tolerance can be increased [11, 12]. To achieve this, thermoplastic toughening particles can be included at the interlaminar resin-rich regions [13, 14]. This thesis aims to gain a better understanding of particle toughening mechanisms comparing particle-toughened systems to an untoughened counterpart without particles.

The anisotropic and heterogeneous nature of carbon fibre laminates means the damage mechanisms and interactions between different modes of damage are distinctly dependent on the three-dimensional (3D) spatial relationships and interactions. Established damage assessment techniques such as C-scan [15, 16] and optical microscopy [17], that are commonly used to investigate post-impact and compression-after-impact damage behaviour have significant limitations for 3D analysis. In terms of microstructural and micromechanical analysis, the latter is typically undertaken after cross-sectional cutting or thermal deplying [18, 19]. This is a destructive technique that may artificially affect the results via sectioning damage and/or the release of internal stress states. Extended 3D imaging is possible via serial sectioning [20], however even with automation, this remains a time-consuming method of preparing significant depths of material, notwithstanding the destructive nature and underlying potential to introduce sectioning artefacts. In the case of ultrasonic C-scans, time-of-flight methods allow some depth measurement, but it is not strictly possible to distinguish different damage modes, spatial resolutions are low, and overlapping damage cannot be distinguished [21-24].

3D techniques such as X-ray computed tomography and laminography may allow internal composite damage features to be detected non-invasively, at high resolutions, and in 3D. The use of these techniques is relatively new in the

application of composite damage assessment, with few published studies using these methods to study composite material systems [21, 25-37].

Industrial microfocus CT (µCT) scanners have successfully been used to study impact damage at spatial resolutions down to ~4 µm [21, 35, 38, 39]. To gain higher resolutions, use of synchrotron radiation computed tomography (SRCT) can routinely enable rapid sub-micron scanning, revealing features down to the size of individual fibres in standard/commercial aerospace composite systems [32, 34, 36, 37]. However, due to the frequent use of aerospace composites in highly laterally extended (*i.e.* planar) forms, high resolution imaging frequently requires local regions of interest to be cut out in order to achieve voxel sizes on the order of 1 µm and below. To avoid these issues, synchrotron laminography has also been used to study carbon fibre damage enabling relatively large planar coupons to be scanned at such high resolutions [31].

Since both laboratory- and synchrotron-based imaging techniques routinely offer resolutions in the micrometer and sub-micrometer range for samples in cm to mm lengthscales, the combination of using both techniques can offer a comprehensive view of the macroscopic and microscopic damage behaviour. In addition to this, the relatively non-destructive nature of this technique can allow for time series studies to be achieved, contingent on resolution and sample size requirements [26, 31, 34].

Many studies have investigated the susceptibility of composite damage by out-of-plane deflection through quasi-static indentation and impact events [40, 41]. The former loading condition is desirable due to eliminating oscillations in force-time data [42] and the ability to interrupt the experiment for non-destructive testing [43]. Whilst most studies report similarities between the two loading conditions based on conventional measurements, they do acknowledge that the dynamic nature of impact should be taken into account [40, 44]. The limited understanding of the similarities and differences between the two loading conditions provides a motivation for comparing the internal damage mechanisms. Computed tomography can achieve this non-destructively with the added benefit of being able to monitor damage initiation and growth [43]. Such information is important to the understanding of how and where various damage modes are occurring.

Internal comparison between loading conditions offers a better understanding of the mechanisms that may be sensitive to strain-rate behaviour. Additionally, this will help to ensure finite element models are capturing the correct mechanisms.

A similar lack of understanding is currently seen in post-impacted compression failure in composites. Since compressive failure is usually instantaneous and catastrophic, identification of critical failure modes is not easily accomplished. The opaque nature of carbon fibre, coupled with the complexity in assessing the various internal damage modes, has resulted in a lack of studies which systematically monitor damage initiation and growth, prior to catastrophic failure [45]. Such understanding of the damage characteristics at the point prior to failure and post-failure is necessary to ensure damage features are correctly included in finite element models used to predict failure load and for the development of better damage tolerant material systems.

1.2 Project aims

There are two overarching aims in this project. The first aim is to gain a better understanding of how particle-containing fibre-reinforced composite systems lead to improvements in damage resistance and damage tolerance. The second aim is to bring the application of multi-scale 3D X-ray imaging to the field of impact damage in composite materials; understanding the limitations and benefits of these techniques, and developing image-processing tools to quantify data.

The following specific objectives of this thesis are to:

- Investigate the feasibility of multi-scale 3D tomography for studying impact damage and compression-after-impact. This will form a methodology for the rest of the work in the thesis.
- Develop a partial volume correction technique that increases the accuracy of crack-opening measurements from µCT data.
- Create techniques to measure the extent of damage and the effectiveness of toughening micromechanisms.
- Understand the 3D impact damage behaviour, the modes of damage and their interactions from impact events on both 1 mm and 4.5 mm thick composite materials with a quasi-isotropic layup and on toughened and untoughened systems.

- Investigate how particles play a role in toughening, the micro-mechanisms that lead to increased fracture toughness.
- Identify the similarities and differences between quasi-static indentation and impact-induced damage.
- Investigate the post-impact compression mechanisms leading up to final failure.

1.3 Contributions to the analysis and understanding of composite damage

To satisfy the aims of this thesis, this work contributes to the field of composite materials and structures in several key areas:

- It is the first study to use extensively a range of laboratory and synchrotron based X-ray computed tomography techniques to understand better the damage mechanisms in particle-toughened and untoughened composite materials.
- It is the first study to use computed tomography to study initiation and propagation of damage mechanisms at incremental load steps in *ex situ* quasi-static indentation and compression-after-impact experiments.
- Image-processing techniques have been developed to obtain measurements of damage and microstructures from 3D imaging. This includes a partial volume correction algorithm to measure more accurately crack-openings from microfocus computed tomography, and tools to quantify the extent of bridging, crack deflection and increases in crack path length based on 3D synchrotron CT images.
- The use of multi-scale computed tomography has resulted in a better understanding of the role that particles play in determining the damage resistance and damage tolerance though qualitative and quantitative damage assessments.
- The observations have resulted in better-informed comparisons of damage evolution between low velocity impact and quasi-static indentation loading conditions.
- The observations have resulted in a better understanding of damage initiation and growth under quasi-static indentation loading conditions.
- The observations have resulted in a better informed understanding of the damage processes leading to compression-after-impact failure and the role particles play in maintaining a higher residual compressive strength.

1.4 Thesis structure

The content of this thesis is based on six journal papers, which have been written during the course of this research, four of these have been accepted for publication, and the other two are in preparation or are under review. These papers constitute chapters 4-9, overall the structure of the thesis is set out as follows:

Chapter 2 presents a literature review that describes the background, theory and fundamentals based on previous studies. This chapter covers several key areas consisting of; low velocity impact damage, compression-after-impact, quasi-static indentation, toughening techniques, damage micro-mechanisms, previous CT work on composite damage and finite element modelling. Chapter 3 describes the experimental methods and materials used in this thesis. Chapter 4 shows the benefits and limitations of using different 3D imaging techniques consisting of; µCT, SRCT and SRCL, for studying impact damage in composites. The understanding of these techniques resulted in refinements to the approach to the experimental work in the remaining chapters. Chapter 5 demonstrates a partial volume correction technique for improved measurement of crack-opening displacements obtained through lab-based micro-focus CT and compares these to SRCT measurements. Chapter 6 discusses the toughening mechanisms involved in suppressing delaminations in 1 mm thick particle-toughened and untoughened carbon fibre/epoxy coupons. Chapter 7 makes comparisons between four particle-toughened and one untoughened system subjected to low velocity impact and includes quantification of the extent of key toughening processes identified earlier in Chapter 6. Chapter 8 uses micro-focus CT to track damage initiation and growth in composite materials subjected to quasi-static indentation loads. The observations were also compared to composites subjected to low velocity impact to make a better informed analysis of the similarities and differences between the two loading conditions. Chapter 9 studies the development of damage leading to compression-after-impact failure and explains how particle-toughening allows the laminates to sustain higher residual loads. The sequence of events leading to failure are also assessed and are related to suggestions for how to predict better the compression-after-impact strength using finite element modelling. Finally, Chapter 10 presents the conclusions of this work and suggests possible routes for

future work. Due to the nature of chapters 4-9 as published articles that are necessarily self-contained, there is some common information between chapters resulting in repetition. Where this occurs it will be highlighted so as to help guide the reader.

1.5 List of publications

The following journal papers and conference proceedings have been produced as a direct output from this work:

1.5.1 Journal papers

Bull, D. J., Helfen, L., Sinclair, I., Spearing, S. M., and Baumbach, T*., A Comparison of Multi-Scale 3D X-ray Tomographic Inspection Techniques for Assessing Carbon Fibre Composite Impact Damage.* Composites Science and Technology, 2013. Vol **75**. pp. 55-61. DOI:10.1016/j.compscitech.2012.12.006.

Bull, D. J., Sinclair, I., and Spearing, S. M., *Partial volume correction for approximating crack opening displacements in CFRP material obtained from micro-focus X-ray CT scans.* Composites Science and Technology, 2013. Vol **81**, pp. 9-16. DOI:10.1016/j.compscitech.2013.03.017.

Bull, D. J., Sinclair, I., Spearing, S. M., and Helfen, L., *Three-dimensional assessment of low velocity impact damage in particle-toughened composite laminates using micro-focus X-ray computed tomography and synchrotron radiation laminography*. Composites Part A, 2013. Vol **52**, pp. 62-69. DOI:10.1016/j.compositesa.2013.05.003.

Bull, D. J., Scott A.E., Spearing, S. M., and Sinclair, I., *The influence of toughening-particles in CFRPs on low velocity impact damage resistance performance.* Composites Part A, 2014. Vol **69**, pp. 47-55. DOI:10.1016/j.compositesa.2013.11.014.

Bull, D. J., Sinclair, I., and Spearing, S. M., *Importance of damage details in the response to low velocity impact and quasi-static indentation loading on particle-toughened carbon-fibre composite materials.* In preparation.

Bull, D. J., Sinclair, I., and Spearing, S. M., *Observations of damage development from compression-after-impact experiments using ex situ microfocus computed tomography*. Composites Science and Technology, 2014. Accepted in press. 10.1016/j.compscitech.2014.04.008

1.5.2 Conference papers

Bull, D. J., Helfen, L., Sinclair, I., and Spearing, S. M., *Composite laminate impact damage assessment by high resolution 3D X-ray tomography and laminography*. Proceedings of the 18th International Conference on Composite Materials, Jeju, S. Korea, 2011.

Bull, D. J., Helfen, L., Sinclair, I., and Spearing, S. M., *Multi-scale 3D imaging of carbon fibre laminate impact and compression-after-impact damage using computed tomography and laminography*. Proceedings of the 15th European Conference on Composite Materials, Venice, Italy, 2012.

Bull, D. J., Sinclair, I., and Spearing, S. M., *Quasi-static indentation and compression-after-impact damage growth monitoring using microfocus X-ray computed tomography.* Proceedings of the 19th International Conference on Composite Materials, Montreal, Canada, 2013.

Bull, D. J., Sinclair, I., and Spearing, S. M., *The role of particle-toughening to improve post-impact compressive strength*. Proceedings of the 16th European Conference on Composite Materials, Seville, Spain, 2014.

1.6 References

[1] Soutis, C., *Carbon fiber reinforced plastics in aircraft construction.* Materials Science and Engineering a-Structural Materials Properties Microstructure and Processing, 2005. **412**(1-2): pp. 171-176.

[2] Smock, S.D., *The Dreamliner: a materials revolution aerospace industry*, in *Design News*. 2007. pp. 73-76.

[3] Richardson, M.O.W. and Wisheart, M.J., *Review of low-velocity impact properties of composite materials.* Composites Part a-Applied Science and Manufacturing, 1996. **27**(12): pp. 1123-1131.
[4] de Freitas, M. and Reis, L., *Failure mechanisms on composite specimens subjected to compression after impact.* Composite Structures, 1998. **42**(4): pp. 365-373.
[5] Mahzan, S., Staszewski, W.J., and Worden, K., *Experimental studies on impact damage location in composite aerospace structures using genetic algorithms and neural networks.* Smart Structures and Systems, 2010. **6**(2): pp. 147-165.
[6] Polimeno, U. and Meo, M., *Detecting barely visible impact damage detection on aircraft composites structures.* Composite Structures, 2009. **91**(4): pp. 398-402.
[7] Chen, H.R. and Sun, X.N., *Residual compressive strength of laminated plates with delamination.* Composite Structures, 1999. **47**(1-4): pp. 711-717.
[8] Morgeneyer, T.F., Helfen, L., Sinclair, I., Proudhon, H., Xu, F., and Baumbach, T., *Ductile crack initiation and propagation assessed via in situ synchrotron radiation-computed laminography.* Scripta Materialia, 2011. **65**(11): pp. 1010-1013.
[9] Sanchu-Saez, S., Barbero, E., Zaera, R., and Navarro, C., *Compression after impact of thin composite laminates.* Composites Science and Technology, 2005. **65**(13): pp. 1911-1919.
[10] Hawyes, V.J., Curtis, P.T., and Soutis, C., *Effect of impact damage on the compressive response of composite laminates.* Composites Part a-Applied Science and Manufacturing, 2001. **32**(9): pp. 1263-1270.
[11] Cartie, D.D.R. and Irving, P.E., *Effect of resin and fibre properties on impact and compression after impact performance of CFRP.* Composites Part a-Applied Science and Manufacturing, 2002. **33**(4): pp. 483-493.
[12] Tang, Y.Y., Sun, B.Z., and Gu, B.H., *Impact Damage of 3D Cellular Woven Composite from Unit-cell Level Analysis.* International Journal of Damage Mechanics, 2011. **20**(3): pp. 323-346.
[13] Groleau, M.R., Shi, Y.B., Yee, A.F., Bertram, J.L., Sue, H.J., and Yang, P.C., *Mode II fracture of composites interlayered with nylon particles.* Composites Science and Technology, 1996. **56**(11): pp. 1223-1240.
[14] Gao, F., Jiao, G.Q., Lu, Z.X., and Ning, R.C., *Mode II delamination and damage resistance of carbon/epoxy composite laminates interleaved with thermoplastic particles.* Journal of Composite Materials, 2007. **41**(1): pp. 111-123.
[15] Aymerich, F. and Meili, S., *Ultrasonic evaluation of matrix damage in impacted composite laminates.* Composites Part B-Engineering, 2000. **31**(1): pp. 1-6.
[16] Bland, P.W. and Dear, J.P., *Observations on the impact behaviour of carbon-fibre reinforced polymers for the qualitative validation of models.* Composites Part a-Applied Science and Manufacturing, 2001. **32**(9): pp. 1217-1227.
[17] Davies, G.A.O. and Zhang, X., *Impact Damage Prediction in Carbon Composite Structures.* International Journal of Impact Engineering, 1995. **16**(1): pp. 149-170.

[18] Garg, A.C. and Mai, Y.W., *Failure Mechanisms in Toughened Epoxy-Resins - a Review.* Composites Science and Technology, 1988. **31**(3): pp. 179-223.
[19] Hull, D. and Shi, Y.B., *Damage Mechanism Characterization in Composite Damage Tolerance Investigations.* Composite Structures, 1993. **23**(2): pp. 99-120.
[20] Spowart, J., Mullens, H., and Puchala, B., *Collecting and analyzing microstructures in three dimensions: A fully automated approach.* JOM, 2003. **55**(10): pp. 35-37.
[21] McCombe, G.P., Rouse, J., Trask, R.S., Withers, P.J., and Bond, I.P., *X-ray damage characterisation in self-healing fibre reinforced polymers.* Composites Part a-Applied Science and Manufacturing, 2012. **43**(4): pp. 613-620.
[22] de Freitas, M., Silva, A., and Reis, L., *Numerical evaluation of failure mechanisms on composite specimens subjected to impact loading.* Composites Part B-Engineering, 2000. **31**(3): pp. 199-207.
[23] Aymerich, F., Pani, C., and Priolo, P., *Damage response of stitched cross-ply laminates under impact loadings.* Engineering Fracture Mechanics, 2007. **74**(4): pp. 500-514.
[24] Preuss, T.E. and Clark, G., *Use of Time-of-Flight C-Scanning for Assessment of Impact Damage in Composites.* Composites, 1988. **19**(2): pp. 145-148.
[25] Archer, E., King, S, Quinn, JP, Buchanan, S and McIlhagger. *Impact damage analysis of 3D woven carbon fibre composites using computed tomography*. in *18th international conference on composite materials*. 2011. South Korea: The Korean society for composite materials.
[26] Buffiere, J.Y., Maire, E., Adrien, J., Masse, J.P., and Boller, E., *In Situ Experiments with X ray Tomography: an Attractive Tool for Experimental Mechanics.* Experimental Mechanics, 2010. **50**(3): pp. 289-305.
[27] Bull, D.J., Helfen, L., Sinclair, I., Spearing, S.M., and Baumbach, T., *A comparison of multi-scale 3D X-ray tomographic inspection techniques for assessing carbon fibre composite impact damage.* Composites Science and Technology, 2013. **75**: pp. 55-61.
[28] Crupi, V., Epasto, G., and Guglielmino, E., *Computed Tomography analysis of damage in composites subjected to impact loading.* V. Crupi et alii, Frattura ed Integrità Strutturale, 2011. **17**: pp. 32-41.
[29] Helfen, L., Myagotin, A., Rack, A., Pernot, P., Mikulik, P., Di Michiel, M., and Baumbach, T., *Synchrotron-radiation computed laminography for high-resolution three-dimensional imaging of flat devices.* Physica Status Solidi a-Applications and Materials Science, 2007. **204**(8): pp. 2760-2765.
[30] Hufenbach, W., Böhm, R., Gude, M., Berthel, M., Hornig, A., Ručevskis, S., and Andrich, M., *A test device for damage characterisation of composites based on in situ computed tomography.* Composites Science and Technology, 2012. **72**(12): pp. 1361-1367.
[31] Moffat, A.J., Wright, P., Helfen, L., Baumbach, T., Johnson, G., Spearing, S.M., and Sinclair, I., *In situ synchrotron computed laminography of damage in carbon fibre-epoxy [90/0](s) laminates.* Scripta Materialia, 2010. **62**(2): pp. 97-100.
[32] Moffat, A.J., Wright, P., Buffiere, J.Y., Sinclair, I., and Spearing, S.M., *Micromechanisms of damage in 0 degrees splits in a [90/0](s) composite*

material using synchrotron radiation computed tomography. Scripta Materialia, 2008. **59**(10): pp. 1043-1046.
[33] Schilling, P.J., Karedla, B.P.R., Tatiparthi, A.K., Verges, M.A., and Herrington, P.D., *X-ray computed microtomography of internal damage in fiber reinforced polymer matrix composites.* Composites Science and Technology, 2005. **65**(14): pp. 2071-2078.
[34] Scott, A.E., Mavrogordato, M., Wright, P., Sinclair, I., and Spearing, S.M., *In situ fibre fracture measurement in carbon-epoxy laminates using high resolution computed tomography.* Composites Science and Technology, 2011. **71**(12): pp. 1471-1477.
[35] Tan, K.T., Watanabe, N., and Iwahori, Y., *X-ray radiography and micro-computed tomography examination of damage characteristics in stitched composites subjected to impact loading.* Composites Part B-Engineering, 2011. **42**(4): pp. 874-884.
[36] Wright, P., Fu, X., Sinclair, I., and Spearing, S.M., *Ultra high resolution computed tomography of damage in notched carbon fiber-epoxy composites.* Journal of Composite Materials, 2008. **42**(19): pp. 1993-2002.
[37] Wright, P., Moffat, A., Sinclair, I., and Spearing, S.M., *High resolution tomographic imaging and modelling of notch tip damage in a laminated composite.* Composites Science and Technology, 2010. **70**(10): pp. 1444-1452.
[38] Sutcliffe, M.P.F., Aceves, C.M., Stronge, W.J., Choudhry, R.S., and Scott, A.E., *Moderate speed impact damage to 2D-braided glass-carbon composites.* Composite Structures, 2012. **94**(5): pp. 1781-1792.
[39] Trask, R.S. and Bond, I.P., *Bioinspired engineering study of Plantae vascules for self-healing composite structures.* Journal of the Royal Society Interface, 2010. **7**(47): pp. 921-931.
[40] Lagace, P.A., Williamson, J.E., Wilson Tsang, P.H., Wolf, E., and Thomas, S., *A Preliminary Proposition for a Test Method to Measure (Impact) Damage Resistance.* Journal of Reinforced Plastics and Composites, 1993. **12**(5): pp. 584-601.
[41] Wardle, B.L. and Lagace, P.A., *On the use of quasi-static testing to assess impact damage resistance of composite shell structures.* Mechanics of Composite Materials and Structures, 1998. **5**(1): pp. 103-119.
[42] Delfosse, D. and Poursartip, A., *Energy-based approach to impact damage in CFRP laminates.* Composites Part A: Applied Science and Manufacturing, 1997. **28**(7): pp. 647-655.
[43] Tan, K.T., Yoshimura, A., Watanabe, N., Iwahori, Y., and Ishikawa, T., *Effect of stitch density and stitch thread thickness on damage progression and failure characteristics of stitched composites under out-of-plane loading.* Composites Science and Technology, 2013. **74**: pp. 194-204.
[44] Swanson, S.R., *Limits of quasi-static solutions in impact of composite structures.* Composites Engineering, 1992. **2**(4): pp. 261-267.
[45] Hahn, H.T. and Williams, J.G. *Compression failure mechanisms in unidirectional composites*. in *Composite Materials: Testing and Design (Seventh Conference), ASTM STP*. 1986.

Chapter 2

Literature review

2.1 Low velocity impact threats on aircraft

Low velocity impacts pose a threat to composite structures, particularly in the barely visible impact damage (BVID) regime. In these cases, significant internal damage can occur with little more than a small (< 0.3 mm) dent on the surface. This poses a problem if the damage is undetected, resulting in structures having to be designed to accommodate this level of damage. Impact damage has a direct effect on the residual compressive strength, therefore requiring an allowable in the design to accommodate this anticipated loss of strength [1].

In service, low velocity impact damage can occur from hailstones and foreign object damage (FOD), such as debris on the runway hitting the aircraft skin [2]. Other risks of low velocity impact damage include mishandling and maintenance of the aircraft. Transportation, handling and storage could put the aircraft at risk, for example if the wing or fuselage was to clip an object, or if an inspection or repair engineer dropped a tool on the wing. Better care in this area would reduce the risk of low velocity impact damage, however it is inevitable that mistakes will happen which demands tougher and more impact resistant and tolerant materials [3-5].

2.2 Definition of low velocity impact

Although the difference between low and high velocity impact seems obvious, many authors have introduced their own definitions of what constitutes a low velocity impact, and there can be some overlap between the two.

Some authors [6-8] consider that low velocity impact events can be treated as quasi-static wherein the onset of damage is force-dependent and dynamic effects are negligible. Depending on the target stiffness, material properties and the mass of the impactor, the impact velocity threshold to cause this behaviour is variable,

within the 1-10 ms^{-1} range [9, 10]. The transition to high velocity impact is dominated by stress wave propagation causing much more localised damage. Boundary effects become less important as the impact event is shorter than the time for the stress waves to reach the boundary edges of the structure. This differs from low velocity impact in which the structural response plays an important role in responding to the impact, resulting in more elastic energy being absorbed.

Lui and Malvem [11], and Joshi and Sun [12] suggest low or high velocity impact can be defined by the type of damage incurred within the composite laminate. Low velocity impact is characterised where there is significant matrix cracking and delaminations occur, and high velocity impact is classified by the presence of penetration-induced fibre fracture.

The most common experiments involving low velocity impacts use a relatively large mass of approximately 5 kg in accordance to ASTM D7136 standards [13-15]. Such tests lead to strain-rates in the order of 10 s^{-1} for low velocity impacts [16]. It is reported that this test can be replicated by quasi-static indentation (QSI) tests, with many studies reporting similarities between the two loading conditions [17-19]. This similarity requires that the impact velocity is sufficiently low for the contact time between the impactor and coupon to allow the material and boundary conditions to respond [20, 21]. The comparison between QSI and impact is explained in more detail in section 2.5.4.

2.3 Failure modes from low velocity impact

There are four major damage modes that are commonly identified with the heterogeneous and anisotropic behaviour of CFRP laminates absorbing low velocity impact energy [22]. These are: matrix cracks, delamination and fibre breakage. Matrix cracks can be caused by shear and tensile stresses. Matrix cracks predominantly caused by tensile stresses dominate towards the non-impacted side of the coupon beneath the impact site due to bending. Matrix cracks mainly caused by shear stresses form a “cone” surrounding the impact location. Within the cone, little damage is observed in non-penetrating cases, whereas outside the cone, delaminations are seen to be initiated by matrix cracks and propagate away from the impact site. The last damage mode to occur after matrix

cracks and delamination formation is fibre fracture, this mode of damage occurs predominantly bellow the mid-plane under the impact region. Observations of these damage modes have been documented in previous studies through sectioning of post-impacted specimens [22-25]. Figure 2.1 shows a schematic of a cross-section of an impacted specimen, illustrating the various damage modes [22].

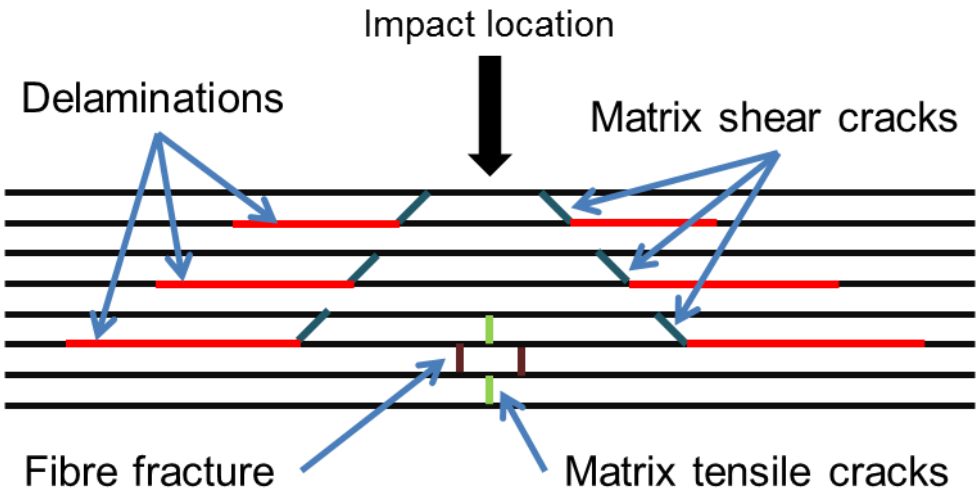

Figure 2.1: Cross-sectional view showing typical damage modes caused by an impact event [22].

2.3.1 Matrix damage

It is considered that matrix cracks are the first modes of damage to occur during an impact event [26-28]. Whilst matrix cracks do not dramatically affect the overall laminate bending stiffness during an impact event, they initiate delamination when they reach adjacent plies of a different fibre orientation [9]. It is these delaminations that dramatically change the local and global bending stiffness of the material, and have implications for reducing the residual in-plane compressive strength [3, 25, 29, 30]. Matrix cracks can be caused by tension and shear, and are oriented in the intralaminar regions running parallel to the fibre directions. Matrix damage can occur by cracking within the matrix itself, or by debonding between the fibre and polymer matrix [31].

Figure 2.1 shows matrix cracks forming a typical “pine tree” pattern associated with Hertzian contact stresses between the impactor and composite surface resulting in very high transverse shear stresses through the material which are inclined at approximately 45 degrees to the plane of the laminate [26, 27, 32-34]. Matrix cracks originating on the back-face, are associated with large local tensile bending stresses and are typically vertical within the ply [27].

2.3.2 Delamination

As noted above, it is generally agreed that matrix cracks initiate delaminations. When a matrix crack interacts with a ply of a different fibre orientation it is unable to continue in a co-planar manner as a matrix crack; this leads to crack deviation into the interface layer, creating a delamination [30, 35].

The initiation of delaminations by matrix cracks is thought to be dominated by local mode I opening in the transverse direction as intralaminar matrix cracks intersect the ply interfaces [36, 37]. Delaminations then propagate in mode II, driven by interlaminar shear stresses resulting from the overall bending of the laminate [3, 25, 29, 37, 38]. The mode I-, and mode II-dominated regions are shown in Figure 2.2. Delamination growth has been reported to be exacerbated by the bending stiffness mismatch between adjacent plies of different orientations. It is reported that the extent of delamination increases with increasing angular mismatch in adjacent ply orientations [39].

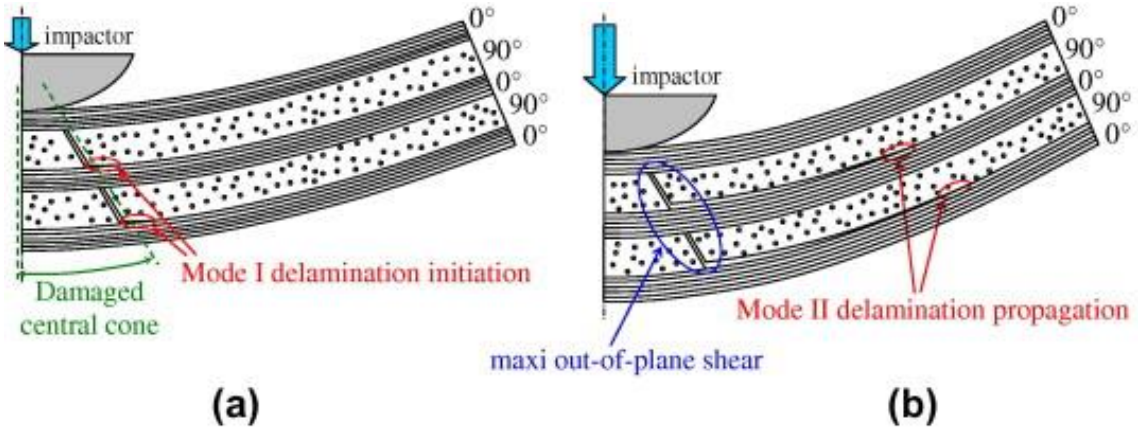

Figure 2.2: Impact damage with creation of highly damaged central conical shape: (a) delamination initiation in mode I and (b) propagation in mode II [37].

There are two characteristic shapes of delamination areas reported in the literature for impact sites in classical quasi-isotropic layups; these consist of 'peanut-shaped', and 45° segments. A significant proportion of studies report a 'peanut' shape as shown in Figure 2.3, based on ultrasonic C-scan data [40-43]. The cause of this shape is due to the delamination growth which occurs more extensively along the fibre direction than in the transverse direction of the bottom layer at the interface [44]. In work by Hull *et al.* [35] the impact damage area was reported to form 45° delaminated segments; this is shown in Figure 2.4 forming a 'spiral staircase' pattern of damage, *i.e.* a stepwise set of delaminations through the thickness of the composite. In this previous work, the de-ply technique was employed on impacted $[-45/0/45/90]_{2S}$ carbon fibre material, revealing the network of delaminations. Delaminations formed 45° segments due to interactions with matrix cracks which form parallel to the ply orientations and surround the impact site. Since ply orientations are spaced at 45° angles, delaminations were formed in 45° segments. Since there is some discrepancy over the exact shape of delaminations, potentially due to the range of damage assessment techniques employed, these may have some implications for finite element modelling work, for example using realistic delaminations to estimate residual compressive strength [45]. A clear understanding of the exact shape of delaminations is, therefore, required.

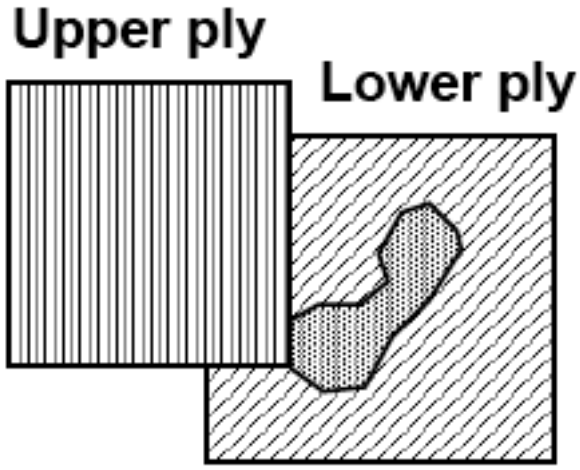

Figure 2.3: The delamination region between an upper and lower ply resembles a ‘peanut’ shape [46].

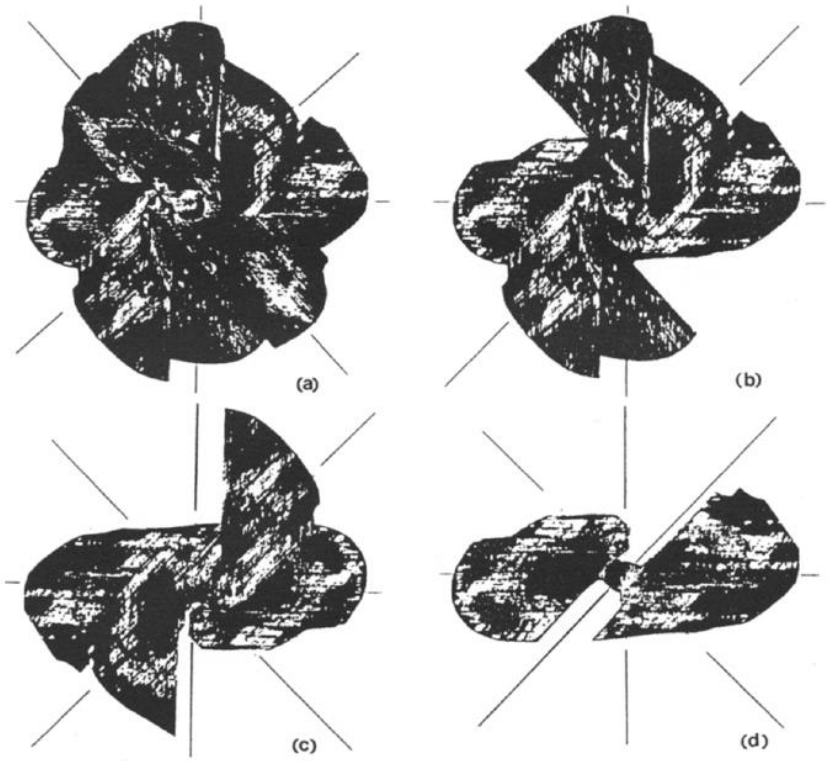

Figure 2.4: Superposition of delaminations obtained through the de-ply method showing (a) interfaces 4/5/6/7; (b) interfaces 5/6/7; (c) interfaces 6/7; (d) interface 7 [35].

In the development of tougher material systems, suppression of delaminations is desired for increasing the materials' damage-resistant properties. This potentially improves damage tolerance and residual bending stiffness properties since the extent of delamination scales with a reduction in residual compressive strength [5, 30, 47-49] and a reduction in bending stiffness [48].

2.3.3 Fibre fracture

Fibre fracture occurs at higher impact energies; and occurs much later in the fracture process than matrix cracking and delamination [27]. Should the impact force be sufficiently high to cause a large indentation, then significant fibre failure can occur directly under the impactor, due to the local high stress and indentation effects causing local shear [22]. On the non-impacted side, fibre failure can occur from bending stresses [42], see Figure 2.1. In addition to delaminations, fibre fracture is also responsible for influencing residual compressive strength [50, 51], and may be responsible for affecting the residual tensile strength [27, 52, 53].

2.4 Strategies to increase damage resistance and damage tolerance in laminates

There are several methods that have been described for creating more damage resistant and damage tolerant materials, this includes: surface protection, self-healing mechanisms, Z-pinning, stitching and particle toughening. These are explained briefly in this section; however the focus of this project is on particle-toughened systems.

2.4.1 Protective surface layers

One of the simplest solutions to improve impact resistance is to use protective layers on the surface of laminates. Layers of glass fibre, polyethylene [54], cork [55] or Kevlar plies have been used to create energy absorbing outer layers to protect carbon fibre composite material systems. An alternative method is to use

softened or toughened outer layers such as adhesives or resins filled with toughening particles [56]. Both approaches offer additional energy absorption mechanisms at the surface, reducing the energy absorbed in the structural laminates it protects. Whilst these methods offer better impact resistance, they add additional unwanted weight and thickness to the structure in addition to extra cost [38]. This is not an advantageous route for the design of lighter aircraft structures.

2.4.2 Z-pinning and stitching

The intrinsic weak point in laminate composites is at the interlaminar regions where there is no reinforcement between plies in the through-thickness "Z direction". Z-pinning provides this reinforcement by using composite pins approximately 0.5 mm in diameter or less, that are typically inserted by an ultrasonic gun through the thickness of uncured plies [57]. Large improvements to the mode I and mode II toughness have been reported in carbon fibre material systems; an increase of an order of magnitude [58]. In experiments comparing unpinned T300/914C carbon fibre epoxy systems to Z-pinned, a reduction of up to 64 % to the impact damage area was reported in the Z-pinned system. This translated to a 45 % larger compression-after-impact strength [59]. Improvements in suppressing delaminations on carbon/epoxy laminates using Z-pinning are also reported in many studies *e.g.* [58-61].

One of the key toughening mechanisms introduced by Z-pinning is bridging in the wake of the delamination front which delocalises the stresses at the crack tips by transferring forces to adjacent plies as shown in Figure 2.5. In addition to this, fracture of pins and pin pull-out add additional energy absorbing mechanisms, reducing the energy available for delaminations to propagate. Despite these toughening effects, there is some evidence that suggests that they do not increase the threshold force to cause damage, and in some cases actually reduce it [57, 59]. This threshold force is the force required to initiate delaminations, and is usually detectable as a load drop on a force-time plot (see section 2.5.2). In quasi-isotropic carbon fibre layups, a reduction of up to 14 % in threshold force is observed in z-pinned systems compared to unpinned systems [59]. There are two

possible explanations to why Z-pinning does not improve delamination initiation. Firstly, Z-pins create pockets of resin between the pin and base laminate with a relatively weak bond between them. Secondly, Z-pins are placed vertically to a mode II crack plane, and therefore are not effective in resisting shear-induced damage initiation. After delamination initiation however, the pins rotate towards the direction of the crack plane and become more effective at bridging the crack as the angle of rotation increases, and hence reduce the stresses acting at the crack tip [59].

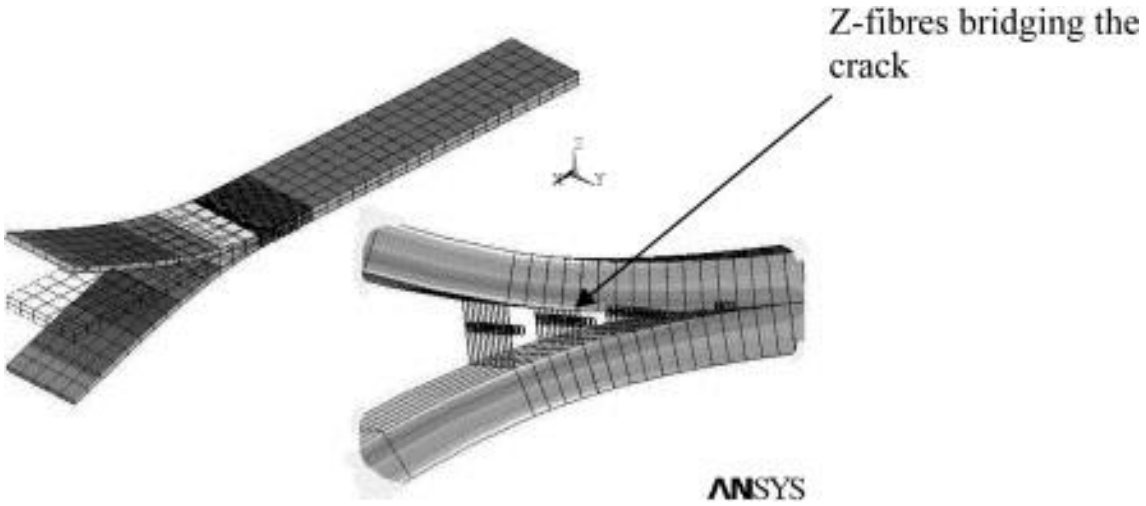

Figure 2.5: Z-fibres bridging crack from propagating [59].

Whilst many studies as discussed earlier suggest improvements to damage resistance from Z-pinning, there are still a few issues to consider; the effect on the performance properties of the material, and additional manufacturing steps required. Research has found that Z-pinning can reduce the tensile strength of plain laminates due to both fibre fracture caused by pin insertion, and formation of stress concentrations around the pins [62]. This reduction in tensile strength correlates both with Z-pin volume content, and Z-pin diameter, and has been reported to be up to approximately 25 % [63]. Z-pinning can also affect the in-plane ultimate compressive strength of the material [64] and also the compression modulus which correlates with increases in Z-pin volume content and Z-pin diameter. A 12 % and 11 % reduction to the compression modulus and ultimate compression strength respectively has been reported in quasi-isotropic carbon

fibre layups for Z-pinned laminates compared to unpinned [65]. Regarding manufacturing processes, cost and time issues can also become a problem, as Z-pinning requires an additional step in the fabrication processes [38].

2.4.3 Self-healing CFRP

Self-healing resin systems were initially created by White *et al.* [66] using microcapsules filled with uncured dicyclopentadiene (DPCD) distributed in the system. These microcapsules are designed to break when a crack reaches the capsule, allowing the uncured DPCD to be drawn into the crack through capillary action enabling the crack to be repaired.

Various alternative technologies are now being considered to produce self-healing CFRPs for engineering applications. In one approach, tubes of hollow glass fibre are filled with uncured resin distributed at specific interfaces within the laminate and are designed to break on impact and fill cracks and delaminations by capillary action [67]. Whilst self-healing CFRPs do not increase damage resistance, they do increase the damage tolerance after impact once the resin cures *i.e.* self-heals. Whilst there are reports of compressive strength recovery after impact of 90 % [68], the feasibility of this technology for commercial aircraft structures is questionable. Damage from manufacture, viscosity of the resin, shelf life, post-impact cure time to retain compressive strength, and limitations to single impact events are problems that need to be overcome [69, 70].

2.4.4 Particle toughening to increase interlaminar fracture toughness

Due to cost and processing considerations, composite materials commonly use thermoset resins that have relatively poor intrinsic impact toughness compared to thermoplastics [71]. The toughness of these resins can be improved by introducing second phase particles [72]. Considering that impact damage resistance is controlled by delaminations that normally propagate within the interlaminar

regions; the associated increase in toughness provided by second phase particles should be directed to these regions [73]. This toughening technique is the main focus in this PhD thesis.

It has been reported that thermoplastic particles are preferential to rubber toughening. This is due to the concern that the very-low stiffness rubber particles would reduce the overall stiffness of the material [74-76], whereas thermoplastic particles are relatively hard/stiff systems and offer better retention of stiffness [77, 78]. It is also shown in studies that higher modulus particles as opposed to relatively compliant rubber particles improve G_{IC} [79] and G_{IIC} [80-82] values. This has been attributed to an increase in stiffness and strength which affects the bridging toughening behaviour as discussed later.

The inclusion of particles in a matrix is reported to develop a variety of micromechanisms that may contribute to energy absorption and crack-tip shielding processes [83] including: crack deflection, crack bridging, crack-tip blunting, particle-matrix interface debonding, and particle-induced localised yielding [72, 83-88]. Whilst these micromechanisms are reported, there is debate regarding which of these micromechanisms significantly contribute to toughness. There are many factors that may be anticipated to contribute towards toughness; these include particle size, particle geometry, volume fraction, particle/matrix interfacial adhesion and particle mechanical properties [72, 83, 89, 90].

2.4.4.1 Particle-resin interfacial adhesion

It is seen that particle-resin interfacial adhesion is important for effective transfer of load across the particle [91]. Typically, adhesive strength can be improved through coatings or surface treatment applied to the particles [92].

The improvements to fracture toughness through increasing particle-resin interfacial strength was observed in one study comparing unmodified and modified silica nanoparticles introduced to a Nylon resin subjected to a notched Izod impact test. This is observed in Figure 2.6. Treatment of the modified particle was by amino-butyric acid to improve particle-resin adhesion [93]. Such improvements to impact toughness through increase particle-resin adhesion were also observed in

PP/$CaCO_3$ composites where particles were modified with a lanthanum compound [83, 94].

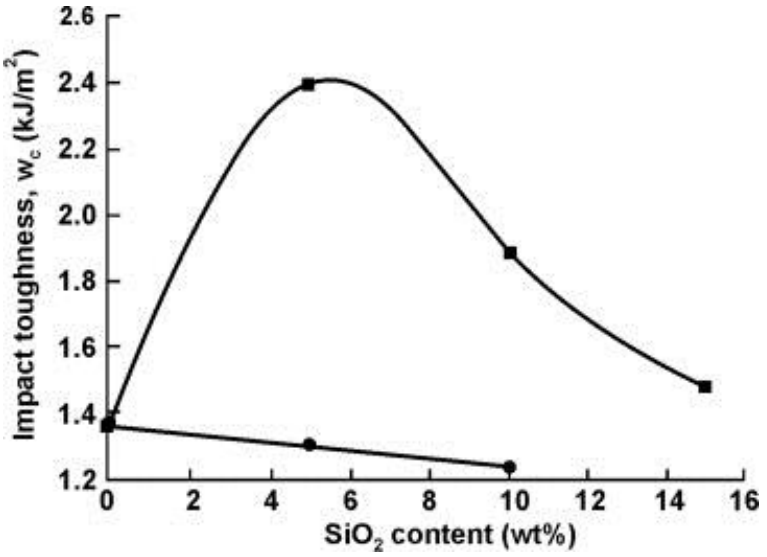

Figure 2.6: Impact toughness of nylon 6 nanocomposites filled with modified (■) and unmodified (●) silica (SiO_2) particles, respectively [93].

Whilst significant improvements to fracture toughness were observed in these studies which used thermoplastics as the base resin, systems using thermosetting resins report little enhanced toughness through improving particle-resin interfacial strength [83, 95, 96]. It is cited that on these systems, crack growth is dominated by matrix failure and particle breakage, hence interface debonding is less relevant and therefore improvements to interfacial strength are not effective at increasing toughness on these systems [83]. It is questioned however that should the particle strength be substantial enough, then it is possible particle-resin interfacial strength would be relevant in these cases. Such adhesion would enable a load transfer across the particle and toughening through bridging ligament formation discussed later in section 2.4.4.5.

2.4.4.2 Plastic deformation and crack blunting

Blunting of the crack tip can take place by local yielding in the vicinity of the crack tip, lowering near-tip stress levels for a nominal stress intensity under small scale yielding conditions [97-99]. In rubber particle-toughened epoxy systems, crack

blunting is reported to be produced by cavitation of rubber particles under the triaxial stresses at the crack tip which lowers the effective local yield stress and provokes extensive shear yielding [100].

In polymer matrices, crack blunting is reported to promote a transition in crack growth regime from a steady crack propagation, to a stick/slip state in which a saw-tooth appearance is observed in load-displacement curves due to crack initiation followed by crack arrest, see Figure 2.7 [97]. This stick/slip propagation has been attributed to localized plastic deformation and fracturing representing plastic blunting and sharpening processes. The ratios of K_{IB}, the stress intensity for the onset of crack growth representing the initiation value, and K_{IC}, the stress intensity factor for crack propagation representing the arrest value can be used to determine stable or unstable growth; *i.e.* $\frac{K_{IB}}{K_{IC}} \approx 1$ would show stable growth where as $\frac{K_{IB}}{K_{IC}} > 1$ would represent unstable growth.

The magnitude of $K_{IB}$is reported to be dependent on the radius of the blunted crack where a higher applied stress is required to re-initiate the sharp crack. It is shown in Figure 2.8 that an intermediate yield stress of the matrix phase is required to promote unsteady propagation. The effect of this behaviour is that a lower local stress concentration is present at a blunted crack tip requiring a higher applied stress to initiate the crack; from an energy point of view more energy is consumed in advancing the crack between the arrest and initiation stages as work is done deforming the crack tip at these stages [97, 101].

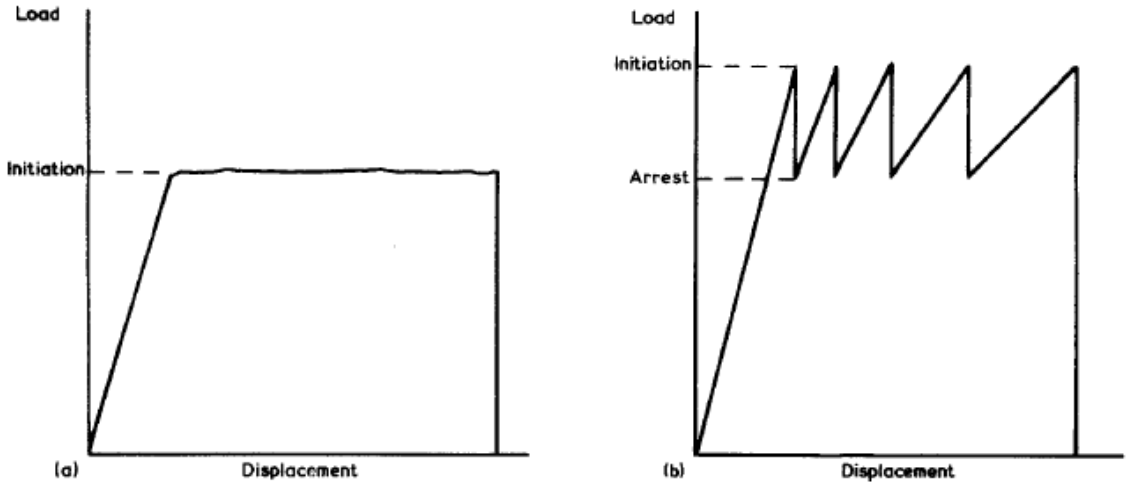

Figure 2.7: Typical load displacement curves for (a) stable continuous crack propagation and (b) unstable stick-slip crack propagation [97].

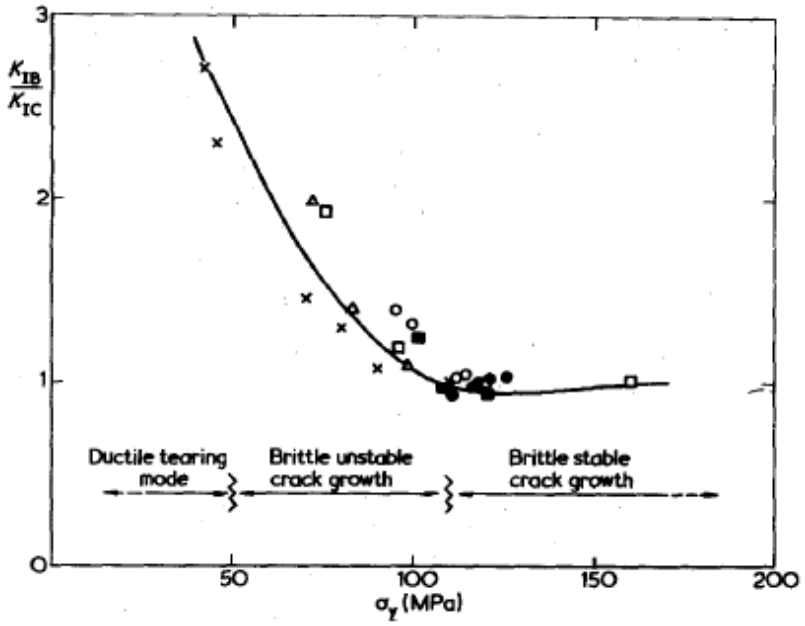

Figure 2.8: Relationship between K_{IB}/K_{IC} ratio, crack growth mode, and yield stress [97].

2.4.4.3 Increased crack path / surface area

The use of particles in thermoplastic-modified epoxies can cause deflection of the crack and a meandering crack path. This results in an increased fracture surface area and, therefore, higher energy absorption during crack propagation [102].

Expressions to calculate the increase in fracture toughness through increased crack path length based on the volume fraction of spherical particles, V_f, have been proposed [89, 103-105]:

$$\frac{K_c}{K_o} = \left(\frac{E_o}{E_c}(1 + 0.87V_f)\right)^{0.5} \quad (2\text{-}1)$$

$$\Delta G_{IC} = \frac{3\gamma_m V_f}{2} \quad (2\text{-}2)$$

where K_c is the fracture toughness of the modified epoxy, K_o is the fracture toughness of the unmodified epoxy, E_c is the Young's modulus of the modified epoxy and E_o is the Young's modulus of the unmodified epoxy, $\Delta G_{IC}$is the increase in mode I toughness, and $\gamma_m$is the specific fracture energy of the matrix. In equation (2-1) the constant 0.87 is related to toughening by pure tilt-induced crack deflections. Given a close ratio of Young's moduli between thermoplastic-modified epoxies, a volume fraction of thermoplastic modifiers of 30 % would yield only a modest increase: $\frac{K_c}{K_o} \approx 1.12$ [102]. The limitation of these 2D models is the assumption that the crack path fully deflects around one half of the particle surface area. Since the actual deviation of the crack may be less, the equation may overestimate the fracture toughness increase [89].

2.4.4.4 Crack deflection

In a mode I loaded situation, crack deflection locally reduces the crack tip driving force by deviating the crack path from the surface of maximum tensile stress, see Figure 2.9 [106]. A solution by Cotterell and Rice [107] shows that a kinked crack under purely elastic conditions when subjected to a far-field applied mode I stress intensity factor k_I can be expressed in terms of the kink angle θ and corresponding local mode I and mode II stress intensities $K_I$and K_{II} in equation (2-3):

$$K_I = cos^3\left(\frac{\theta}{2}\right) k_I$$

$$K_{II} = sin\left(\frac{\theta}{2}\right) cos^2\left(\frac{\theta}{2}\right) k_I \qquad (2\text{-}3)$$

The solution is applicable provided that the length of the deflected portion is relatively small in comparison to the overall crack length. The local crack tip driving force, K_{tip}, for coplanar growth along the deflected portion of the crack can be estimated in terms of the maximum strain energy release rate G in equation (2-4):

$$K_{tip} = (EG)^{0.5} = \left\{{K_I}^2(1-v^2) + {K_{II}}^2(1-v^2) + {K_{III}}^2(1-v^2)\right\}^{0.5} \qquad (2\text{-}4)$$

Where, K_{III}, is the local mode III stress intensity factor, E is Young's modulus and v is the Poisson's ratio. For a simple deflected crack, in-plane deflections of 30° and 90° can reduce crack-driving force on the order of 10 % and 50 % respectively [106]. The promotion of crack deflection through inclusion of particles in brittle ceramic materials has been shown to increase fracture toughness by up to a factor of 3 demonstrating the effectiveness of this toughening micro mechanism [108].

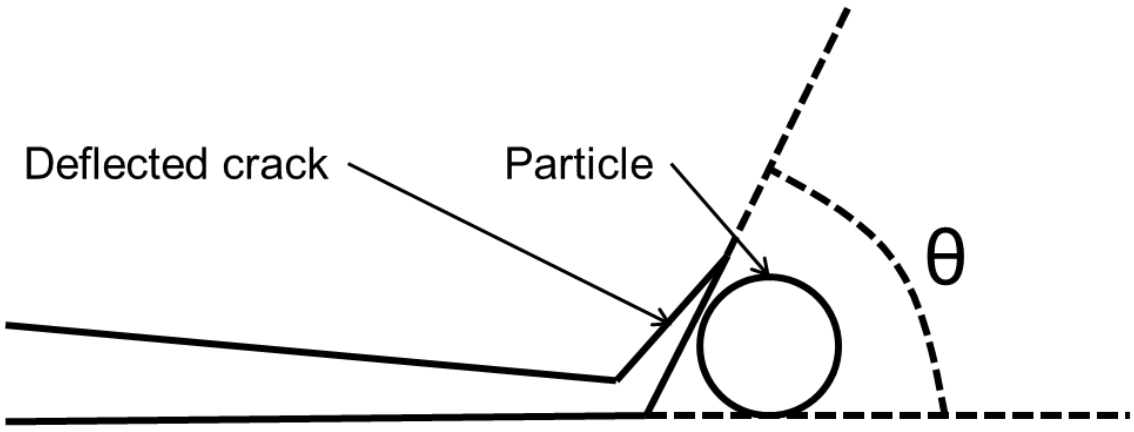

Figure 2.9: Crack tip deflection around a particle and kink angle θ [106].

2.4.4.5 Crack bridging

The use of relatively stiff polymer particles in modified epoxies has been reported to invoke crack bridging [86]. In this mechanism, the stiff particles span the two crack surfaces and apply surface tractions that effectively reduce the stress intensity applied at the crack tip. From an energy absorption consideration, the opening of the crack can cause well-adhered particles to fracture or debond at the interface, as well as deformation of the resulting ligaments, thereby contributing to the overall energy required for crack propagation [102].

The development of intact ligaments along the wake of the crack leads to a reduction in the stresses acting on the crack tip by providing traction sites; this process is illustrated in Figure 2.10. The bridging stresses, σ_{br}, acting across the crack wake change with position, falling to zero in the region beyond the critical crack-opening u^*. The crack illustrated here represents a steady-state crack, in which bridges are being both created at the crack tip and equally destroyed in the crack wake beyond the critical crack-opening displacement [97].

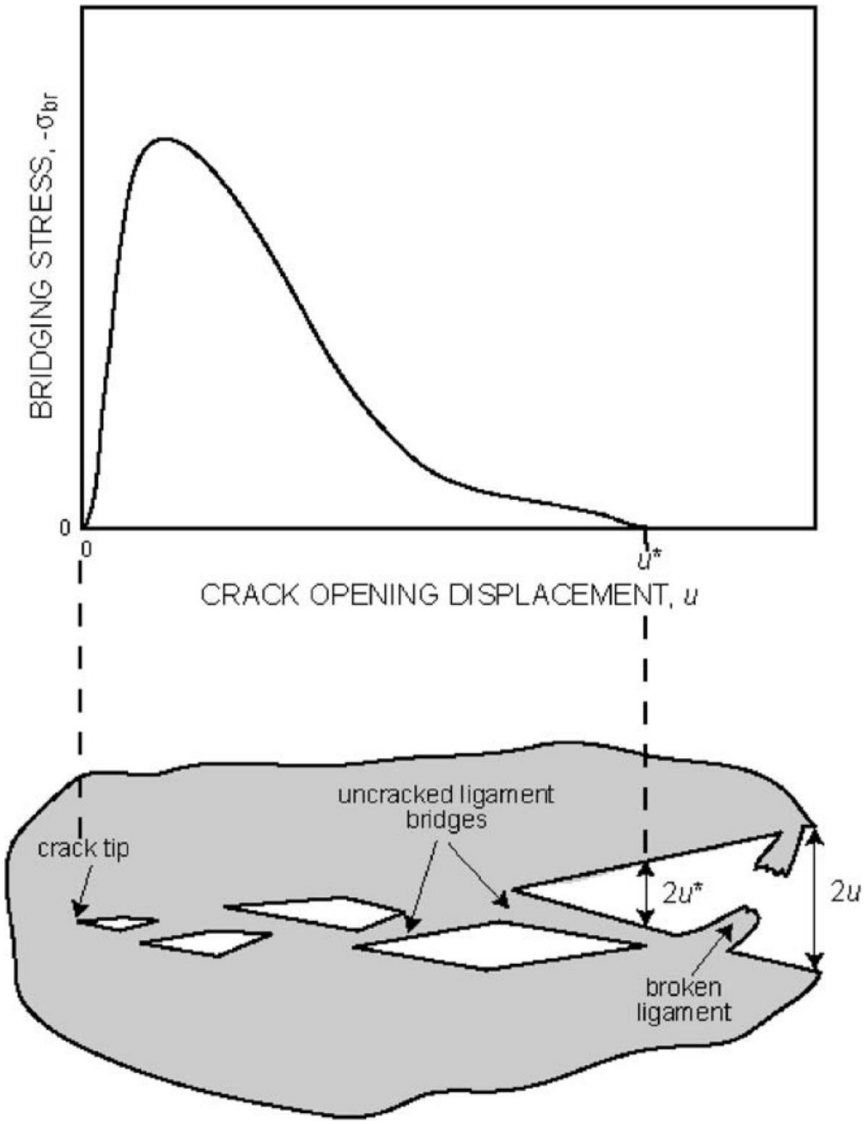

Figure 2.10: Schematic illustrating bridging stresses [97].

The degree of crack-tip shielding due to uncracked-ligament bridging in terms of the area fraction of the ligaments and applied stress intensity has been expressed in a 2D model using equation (2-5) [106] for co-planar bridging sites to calculate the shielding stress intensity, K_b:

$$K_b = -f_{ul}K_I\left[\left(1+\frac{l_{ul}}{rb}\right)^{0.5}-1\right]/\left[1-f_{ul}+\left(1+\frac{l_{ul}}{rb}\right)^{0.5}\right] \qquad (2\text{-}5)$$

Where $f_{ul}$is the area fraction of bridging ligaments on the crack plane, $K_I$is the applied (far-field) stress intensity, l_{ul} is the bridging-zone size, r is a rotational factor, and b is the length of the remaining uncracked region ahead of the crack, see Figure 2.11 for geometry. This model was tested on Al/SiC_P composites to predict the magnitude of crack-tip shielding under fatigue crack growth. An area fraction of bridges was reported between 27-31 percent, and was determined through serial sectioning, l_{ul} was approximately 400 µm behind the crack tip, and r_b was 1 mm which led to ~6 % shielding by bridging in this instance. One of the limitations in this model is that bridging ligaments are simplified as an area fraction along the length of the bridging zone l_{ul} where the traction provided by the bridging sites is likely to diminish along the length.

As crack bridging acts within the crack wake, the effect on crack propagation is crack-size-dependent. As the crack length increases, the driving force to sustain cracking will increase until a steady state is reached [106].

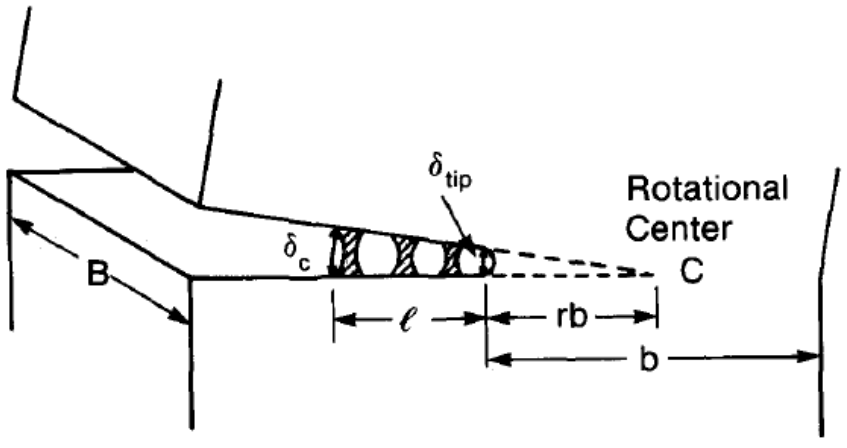

Figure 2.11: Schematic illustration of idealized fatigue crack with bridging zone, showing definitions of the rotational centre and crack-opening displacements [109].

A crack bridging model by Ahmad, Ashby and Beaumont [110] for rubber-modified epoxies is based on the idea that toughness can be improved through stretching and tearing of the rubber particles in the wake of the crack. The improvements to toughness are considered in equation (2-6) by a reduction of stress intensity at the

crack tip where these particles provide compressive tractions in the wake of the crack:

$$\frac{K_{Ic}}{Ko} = \phi(1-f) + \frac{fE^*\Gamma_t}{2\phi(1-f)K_o^2} \quad (2\text{-}6)$$

where $K_{Ic}$is the fracture toughness of the rubber-modified epoxy, $K_o$is the fracture toughness of unmodified epoxy, ϕ is a correction factor that accounts for crack bowing, f is the volume fraction of rubber particles, E^* is the Young's modulus of the rubber particles and $\Gamma_t$is the tearing energy of the rubber particles. It is reported that the improvement to toughness attributed to crack bridging is negligible in rubber-modified epoxies. This mechanism is reported to be more dominant for rigid thermoplastic particles since these are much stiffer with higher tensile strength than rubber particles [106].

A model by Rose [111] for glass-filled epoxies, equation (2-7), shows the ability of these 'impenetrable' particles to act as springs to support the wake of the crack:

$$\frac{K_c}{K_o} = \frac{[(2s/\lambda) + (2r/\lambda)(K_L/K_o)^2]^{0.5}}{F_1} \quad (2\text{-}7)$$

where $K_c$is the fracture toughness of the modified epoxy, $K_o$is the fracture toughness of the unmodified epoxy, $2s$ is the surface-to-surface particle spacing, $2r$ is the diameter of the particles, λ is the centre-to-centre particle spacing, K_L is a limiting stress intensity factor that specifies the failure of the trailing end of the reinforced zone, and F_1 is an interpolating function constructed to reproduce the correct asymptotic expansions for soft springs and for hard springs. From this equation, two key features arise. Firstly the toughness increases rapidly with volume fraction of particles, $2r/\lambda \leq 0.15$, secondly for a given K_L/K_ovalue, the toughness reaches a maximum at an intermediate volume fraction corresponding to $\frac{2r}{\lambda} = 0.5$.

This model was experimentally validated with an epoxy matrix containing a dispersion of quasi-spherical alumina trihydrate particles and presented a reasonable fit across diluted concentrations and intermediate particle volume fractions. The K_C/K_o reached ~ 2.1 for 12 µm diameter particles at an inclusion diameter / spacing ($2r/\lambda$) of ~0.4. It should be noted that comparison with experimental data was achieved through treating K_L/K_o as an adjustable parameter where the value was adjusted so to make the theoretical curve pass through one data point for each set of results on a normalised toughness vs. inclusion diameter / spacing plot. This should be seen as a curve fitting parameter which may introduce doubt as to the reliability of the model.

2.4.4.6 Influence of particles on delamination toughness

The presence of particles in the interlaminar regions enables the formation of a thick resin-rich region which has been reported to allow complete formation of plastic deformation around the crack tip [82, 86, 88, 112, 113]. Experimental work by Groleau [86] for example, shows that the untoughened interply thickness correlates with mode II critical strain energy release rate as shown in Figure 2.12. It has been widely reported that toughness improvements seen in neat resins (*i.e.* fibre-free monolithic samples) do not usually translate to equivalent improvements in composite intralaminar toughness. This has been linked to the effective scale of the crack-tip process zone; in composite materials the interply region is constrained by the fibres, and the thickness of this region is usually much less than that of the crack-tip process zone seen in the bulk material [86, 112]. An ancillary benefit of the widely used particle toughening approach is the creation of thickened resin-rich regions at ply interfaces, with corresponding contributions to toughness [114].

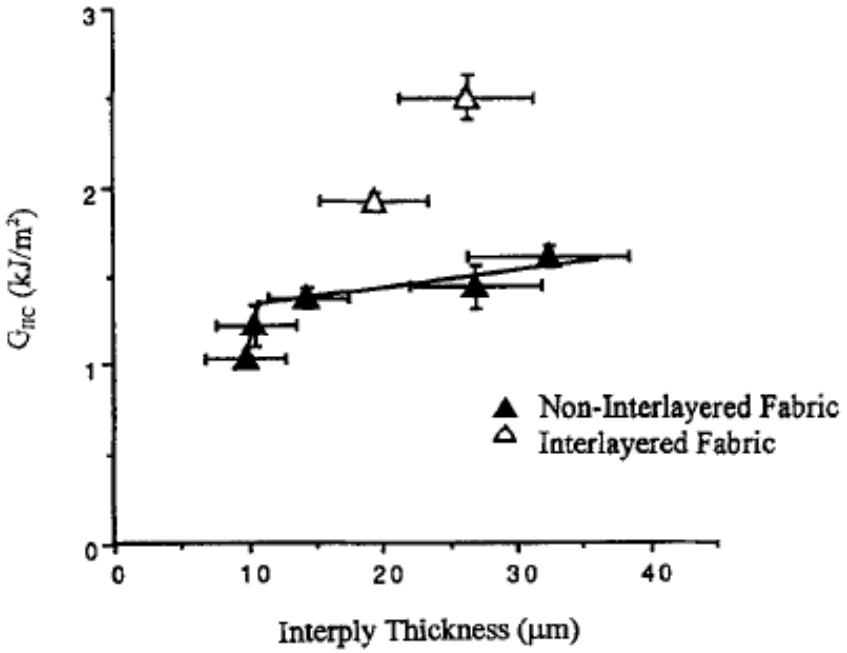

Figure 2.12: Mode II fracture toughness as a function of average interply thickness for interlayered and non-interlayered DER 331/DDS matrix specimens [86].

Particle size, particle volume fraction and the thickness of the interply region all have an effect on the fracture toughness of the resin [43, 86, 115]. Achieving the correct balance of these three variables is critical in maintaining higher fracture toughness. This is highlighted in work by Singh [116] which shows optimal particle volume fractions for different sized particles, see Figure 2.13. Whilst experimental work shows these trends clearly, a better understanding of the toughening micromechanisms and how these can be exploited to achieve greater toughness will considerably help in the development of tougher systems.

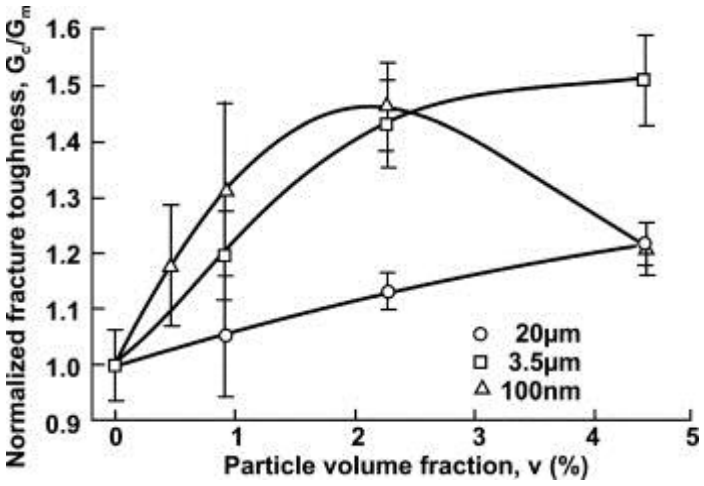

Figure 2.13: Normalised fracture toughness of aluminium-polyester composites plotted against particle volume fraction for various particle sizes [116].

2.5 Mechanical testing

To measure impact damage resistance and damage tolerance, compression-after-impact (CAI) tests are carried out as a standard element of material qualification across the aerospace industry. This test is designed to replicate an out-of-plane impact event followed by an in-plane compression test to measure the residual compressive strength. The test methods are detailed in ASTM D7136M for low velocity impact and ASTM D7137M for compression-after-impact. Prior to introduction of these ASTM standards, tests were carried out using either proprietary Airbus or Boeing impact or compression-after-impact standards, or other setups [117, 118]. This has led to some variation in test apparatus and in earlier publications. Therefore, direct comparisons between experiments using different setups cannot be made in all cases on a like-for-like basis.

2.5.1 Variations of experimental setup

There are numerous experimental setups to test different geometries, layups, environmental and loading conditions, all developed with the aim of recreating in-service conditions. These include testing the influence of environmental conditions such as temperature [119], the influence of pre-loaded test coupons under impact [120], through to how the span-to-thickness ratios affect the impact response [120]. This demonstrates the complexity inherent in evaluating the performance of

composites across the full range of potential in-service conditions. Whilst taking into account all of these factors would be out of the scope of this project, previous studies are acknowledged below and may be of interest for future work.

2.5.1.1 Temperature

Given the variability in environmental conditions that aircraft are subjected to, temperature is an important parameter to consider. A study by Río *et al*. [119] considered low velocity impact at low temperatures ranging from -150 °C to 25 °C. In this study quasi-isotropic and cross-ply carbon fibre composite systems were studied and subjected to low velocity impact. The materials were manufactured using AS4 carbon fibres and Hexcel 3501-6 resin forming coupons measuring 80 x 80 mm. Their study concluded that low temperatures caused embrittlement of the polymer matrix and a build-up of interlaminar thermal stresses, which contributed to the generation and propagation of damage when subjected to impact loads.

2.5.1.2 Preloaded structures

It is quite likely that structures in aircraft will be under a certain amount of load when impacted. Heimbs *et al*. [120] have conducted experiments to evaluate the effect of compressive preload on low velocity impact behaviour. The preload was applied in-plane along two edges under displacement-controlled conditions. It was concluded that preloaded plates led to a larger damage area for a given impact energy compared with unloaded conditions. The compressive preload caused a larger out-of-plane deflection during the impact event. This enabled greater energy absorption and subsequently led to larger delamination formation.

2.5.1.3 Span-to-thickness ratios

For large mass, low velocity impacts that are considered to be effectively quasi-static, the structural geometry plays an important role in determining the impact response [121]**.** Experiments have shown that the span-to-thickness ratio has a large influence on the stiffness of the plate. Typically, a system with a high span-to-thickness will globally have a lower bending stiffness and result in longer impact

event durations. While it has been reported that the critical impact load is more or less constant for a given thickness, widening the span between the supports will increase the energy required to initiate damage [40, 46]. In terms of damage characteristics, a larger span has been reported to change the initial damage modes from top surface delaminations to lower surface matrix cracking [121]. This is due to increased tensile bending forces at the back-face, and a reduction in local contact forces between the impactor and coupon governed by the longer time, enabling a slower deceleration.

2.5.2 Threshold impact force

Based on drop tower experiments it is largely agreed that during a low velocity impact event, a critical threshold force is reached at the impactor prior to the formation of significant delaminations [5, 6, 22, 59, 119]. This is illustrated in Figure 2.14 which shows a typical instrumented low velocity impact event, *e.g.* see [5, 6, 22, 59, 119] where a sudden load drop at point A corresponds to the critical force for the onset of delamination. Point B represents a residual force value due to the reduction in transverse stiffness of the laminate. Should there be enough residual potential energy stored in the impactor, a reloading phase may occur, point C.

As noted above, the load drop between points A and B is attributed to delaminations reducing the flexural stiffness of the test coupon. Impact events yielding forces below this value are believed to be accommodated by the elastic response of the laminate [122]. It is however unreported whether or not the presence of other modes of damage, such as matrix cracks, occurred prior to reaching this critical threshold load. Whilst the process of instrumentation can determine the onset of damage above a threshold load, the dynamic load cells used in these experiments are generally not sensitive enough to detect load changes caused by localised matrix microcracking in the early stages of the impact event [3].

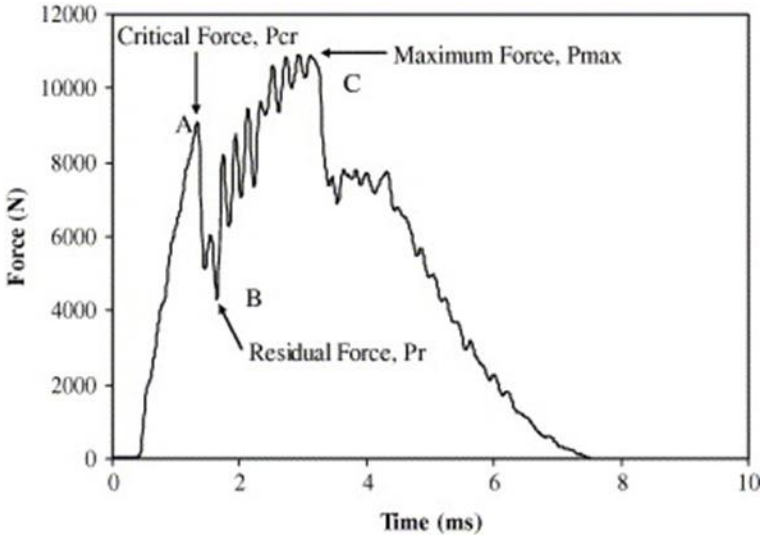

Figure 2.14: Instrumented impact showing crucial, residual and maximum forces [59].

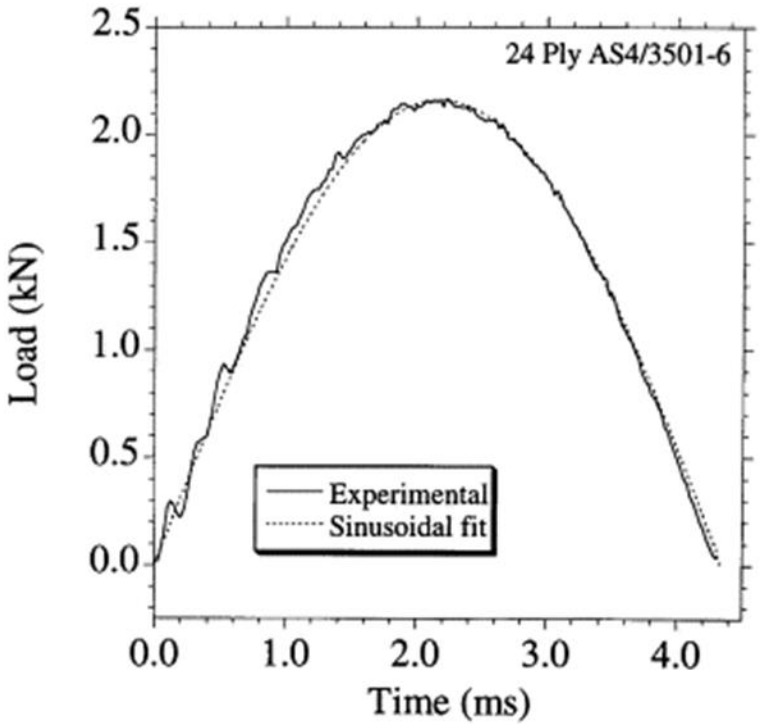

Figure 2.15: Instrumented impact at low impact energy below critical threshold energy value [3].

For impact energies that are less than the critical threshold force, a typical response curve can be seen in Figure 2.15 [3]. The graph represents a half sine fit with the experimental response correlating well to it. The low level impact causes

the plate to respond in a quasi-static, linear way showing no indication of any damage being introduced during the test. Small oscillations do exist, however, which are attributed to vibration from impact and the sensor [26].

There is a relationship between the mode II interlaminar critical energy release rate and the critical threshold force for the onset of delaminations [5, 8, 32, 41]. The predicted threshold force can be calculated using the model proposed by Davies and Zhang [41] in equation (2-8):

$$F_C^2 = \frac{8\pi^2 E t^3 G_{IIC}}{9(1-v^2)} \tag{2-8}$$

Where:

F_C	Critical threshold force for the onset of delamination on a quasi-isotropic laminate (N)
E	Equivalent Young's modulus of the quasi-isotropic laminate (N-m^{-2})
v	Poisson's ratio of the quasi-isotropic laminate
t	Laminate thickness (m)
G_{IIC}	Mode II critical inter-laminar energy release rate (J-m^{-2})

This relationship was tested by Davies *et al*. [8], who used it to calculate critical impact energies on various coupon geometries that were simply supported, see Figure 2.16. The impact velocities were low (< 3m/s) using 1 kg and 2 kg masses. They concluded that the critical mode II interlaminar energy release rate was in good agreement with experimental data for CFRP materials given the inherent scatter of critical failure loads. There are some limitations of this technique however, firstly the impact velocity needs to be low (<10 ms^{-1}), and secondly the application of this technique to strain-sensitive systems *e.g.* glass-polyester laminates was shown not to work well in one study [123].

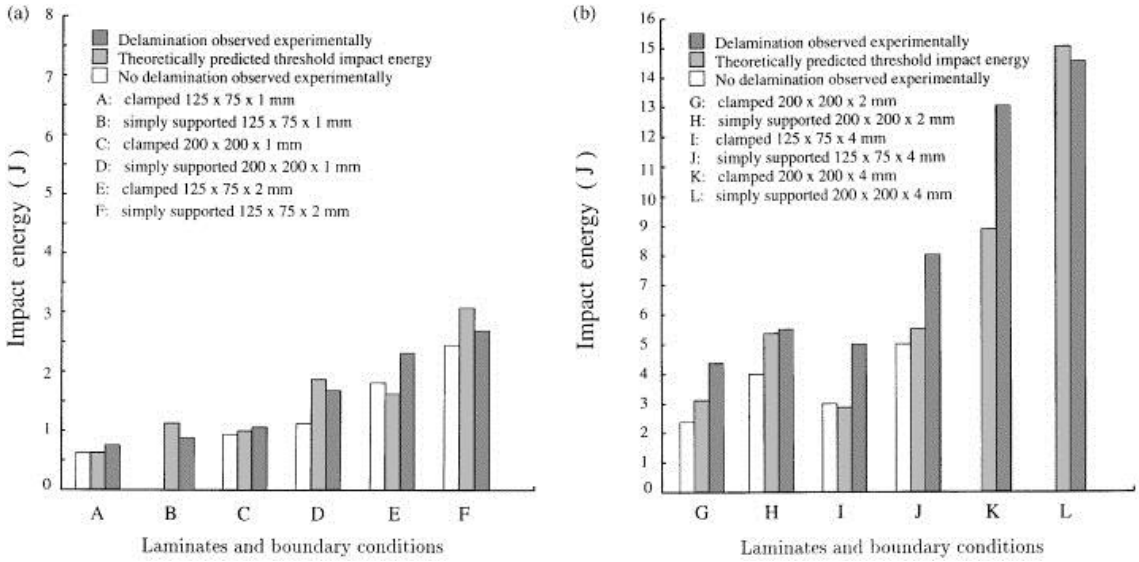

Figure 2.16: (a) Comparison of threshold impact energy for the smaller plates as predicted by the quasi-static model and the pre- and post-delamination energy levels measured experimentally; (b) comparison of threshold impact energy for the larger plates predicted by the quasi-static model and the pre- and post-delamination energy levels measured experimentally [41].

Cartié *et al*. [5] has showed that equation (2-8) can be rewritten to predict the mode II energy release rate from measurements of the critical threshold force obtained from instrumented impact tests; this showed good agreement with actual G_{IIC} measurements. Its application to toughened systems may be of limited use however as the critical threshold force may be difficult to measure from instrumented impact tests. This is due to the absence of a distinct load drop in toughened systems, attributable to a more gradual progressive failure than in untoughened systems [88].

2.5.3 Projected impact damage area by ultrasonic C-scan

Many papers report using ultrasonic C-scan methods to provide information on the projected damage area after impact [5, 6, 119, 124, 125]. Unfortunately, routine scans typically only capture the extent of delaminations, neglecting other damage modes *i.e*. matrix cracks and fibre fracture. Despite this limitation C-scan is a quick method to understand the damage resistant performance in a material system.

There are some developments and advanced procedures using the ultrasonic C-scan technique. One study has shown some success in detecting matrix cracks using oblique incidence ultrasonic techniques [126]. In addition to this, there are successful studies using time-of-flight C-scans that can give the through-thickness location of delaminations [7, 127, 128]. However, one of the major limitations with time-of-flight is that overlapping delaminations can be obscured.

Figure 2.17 shows a linear relationship between the projected delamination area and impact energy above the critical threshold level represented by the vertical lines [5]. This linear relationship between delamination area and impact energy has been commonly reported in other studies [129-131]. In the example shown in Figure 2.17, four carbon fibre systems with different resin systems of varying toughness were used and consisted of laminates 32 plies thick with a consistent quasi-isotropic layup. From delamination area vs. impact energy data, it is clear which material systems have the greatest damage resistant properties. The most damage resistant systems are shown to have a higher critical threshold value, shallower gradient and low delamination area values. It should be noted that in the example shown, impacts were considered low velocity with a relatively long contact time (approximately 10 ms) and the damage area was confined within the boundary regions of the supporting rig.

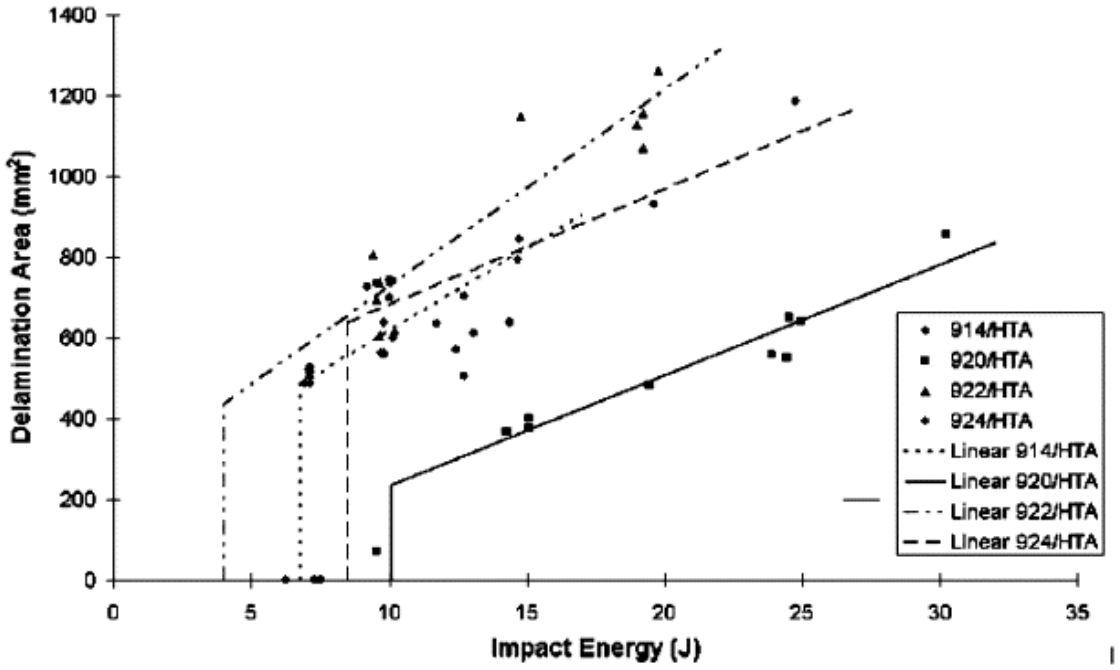

Figure 2.17: Delamination area against impact energy from different resin matrix systems [5].

2.5.4 Quasi-static indentation

Quasi-static indentation (QSI) experiments test material damage resistance from a concentrated out-of-plane load. It also serves to simulate the force-displacement relationship of large-mass, low-velocity impact damage on test coupons with relatively small unsupported regions [132]. The ASTM standard for this test is D6264M, and base plates matching that used in D7136M drop weight impact tests can also be used in combination with the test procedure. It is generally agreed in the literature that low velocity and quasi-static indentation leads to similar damage behaviours [9, 20, 133-137]. This enables damage monitoring through interrupted tests when performed with non-destructive evaluation [138, 139], and destructively after application of certain deflections on separate test coupons [140]. This allows identification of the sequence of damage events, whereas only the final damage state is identifiable after a drop weight impact test.

The slow out-of-plane movement of the crosshead allows specific damage events associated with load drops to be detected more easily compared to impact tests, where oscillations in the force history make it difficult to detect. Whilst quasi-static

tests yield more control compared to drop weight impact tests, some authors disagree about the similarities in damage between the two experiments, citing the importance of including the dynamic nature of the experiment [20, 21], others agree that if the impact contact time is sufficiently long, the event can be considered quasi-static provided the response is not governed by stress wave propagation [141]. Work by Sun *et al.* [142] verified that delamination crack propagation in graphite/epoxy laminates caused by low-velocity impacts with a heavy mass can be treated as quasi-isotropic. Their work used parallel conductive lines 2mm apart, when these lines were broken, the speed of delaminations could be measured allowing a crack-length vs. time history to be obtained.

Figure 2.18 shows a comparison between a drop weight and static indentation deflection test. The goal here is to carry out the static test to the same maximum force as the impact test and monitor displacement. In doing so, the presence of hysteresis can be seen in the area between the loading and unloading curves. Both tests show a close overlap in the loading and unloading curves suggesting that both events can be considered quasi-static events [6].

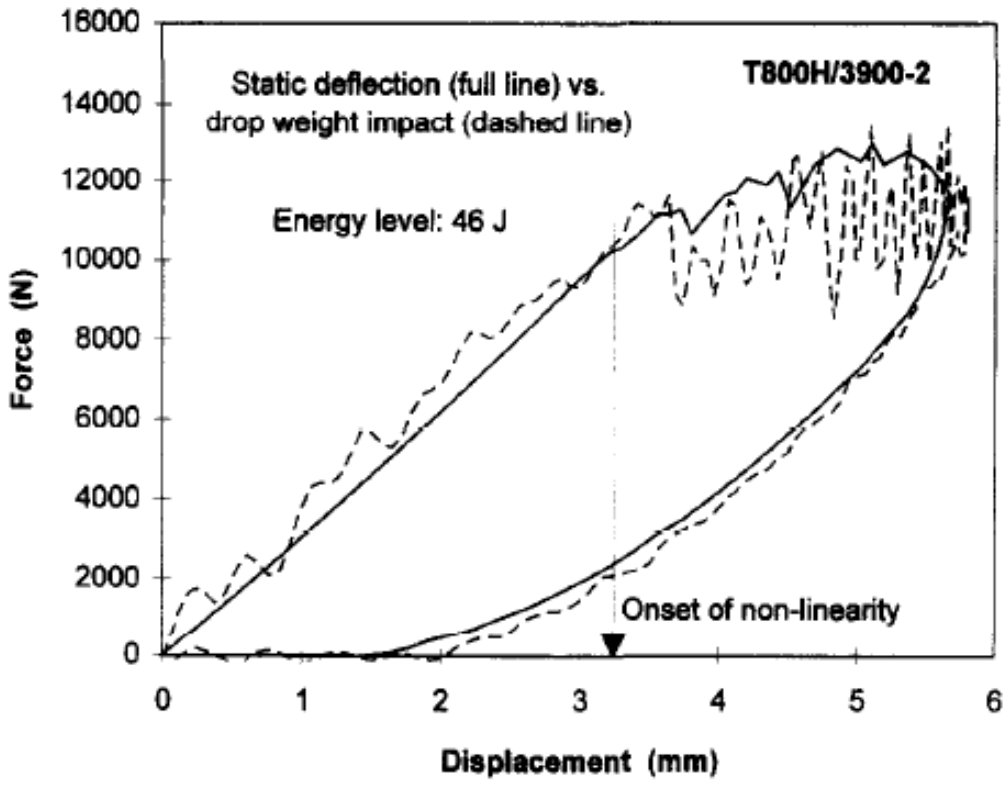

Figure 2.18: Comparisons of static deflection and drop weight impact tests for tough laminates. [6].

Gao *et al*. [88] have investigated the effects of interleaving carbon fibre prepreg with thermoplastic toughening particles which are subjected to out-of-plane quasi-static indentation. Comparison between a toughened (interleaved) and untoughened (non-interleaved) material system are shown in Figure 2.19. In this work, there was a significant load drop observed on the load-displacement curves in the brittle systems at intermediate load levels, whereas toughened systems exhibited non-linearity but no load drop. The absence of oscillations from the load-deflection curves helps in the identification of damage formation, particularly with the toughened system which does not exhibit a load drop at the delamination onset.

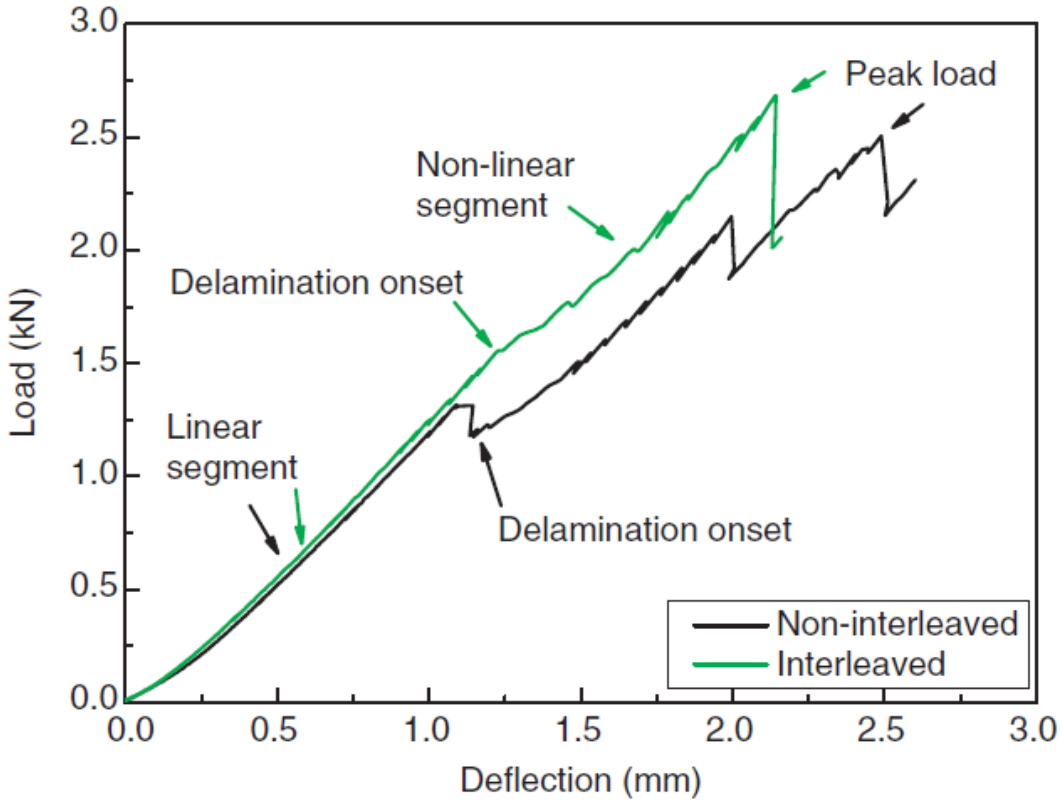

Figure 2.19 – Load-deflection curves on the non-interleaved and interleaved quasi-static indentation specimens [88].

Despite the similarities between QSI and impact, it has been noted above that QSI does not introduce the dynamic and time-dependent components of impact events; with the corresponding potential to cause differences in load and damage

response. One of the key issues surrounding the similarities between QSI and impact is whether or not an impact is considered low velocity and therefore low enough to be considered quasi-static. At higher impact velocities, stress wave propagation and dynamic effects play a significant role; typically resulting in damage that is more localised [141]. This transition between low to high velocity is difficult to define and will be specific to material type, layup, geometry, span-to-thickness ratio, boundary conditions, *etc*. that will have an effect on the equivalence of the two loading conditions [133]. In either case, the question remains as to whether QSI can replicate certain aspects of impact. These aspects include but are not limited to: permanent indentation, force-displacement characteristics and the extent and type of damage formed [18]. These parameters must be compared against an independent variable common to both QSI and impact loading conditions, typically maximum transverse load, or maximum deflection [18].

In studies that compare QSI to impact loads, similarities were observed in C-scan damage area and load deflection curves [9, 19, 135-137, 143, 144]. In these studies, carbon fibre composites were subjected to low velocity impact energies, typically less than 30 J and 10 m/s. Comparisons between the two loading conditions in these studies were achieved using identical coupon and base-plate geometry. Whilst similarities in projected damage area between loading conditions provides an understanding of the general damage resistance response of such systems to loading, micromechanical aspects have not been reported.

2.6 Compression-after-impact testing – damage tolerance

The purpose of compression-after-impact (CAI) testing is to measure the residual compressive strength and subsequently the material's damage tolerance in coupon level tests. Experiments involve application of an in-plane compressive load to an impacted test coupon positioned in an anti-buckling guide. The coupon is loaded until failure and the maximum force is recorded.

2.6.1 Applicability of laboratory test coupons to aircraft structures

In a paper by Davies *et al*. [41], the applicability of laboratory-based test coupons to larger-scale structures has been questioned. In an aircraft structure, the dynamic response can be different depending on its location; for example the structure may be locally very stiff and large, or flexible and light. Features such as curvature and how it is loaded and supported may change the dynamic response of an impact and ability to handle residual compressive loads. This will make the response different to that of a laboratory coupon under test standard conditions. On the other hand, the costs to conduct hundreds of impact tests over complete aircraft would be prohibitive. Whilst it is difficult for test coupons to replicate the exact conditions within a structure, they do enable damage resistance and damage tolerance properties in material systems to be developed and compared using standardised experiments. Such improvements to these properties can then be translated to enhancements on material toughness within structural designs; however, it is still questionable whether or not they translate well and are really truly representative at the structural level.

For the purpose of work conducted in this thesis, test coupons allow particle toughening micromechanisms to be studied across different material systems. This allows an understanding of how these micromechanisms translate to improvements in damage resistance and damage tolerance when compared against a standardised method.

2.6.2 Residual compressive strength after impact

Numerous experiments have reported losses to the residual in-plane compressive strength of composite materials after an impact event [4, 5, 59, 113, 124, 145, 146]. It is generally reported that delaminations are primarily responsible for affecting the residual compressive strength by creating sub-laminates with lower bending stiffness and load carrying capability [27, 30, 50, 147, 148]. Buckled sub-laminates cannot sustain any additional load and result in the stress having to be

redistributed to other regions [4, 27, 50]. Estimations of sublaminate buckling strains have been undertaken using Rayleigh-Ritz solutions of a circular or elliptical delaminated region, creating a sublaminate of thickness h (equation (2-9)), or Euler wide strip buckling solutions (equation (2-10)) [45, 149-153]:

$$\varepsilon_B = -\frac{315}{17b^2} \times \frac{[(b/a)^2 D_{11} + (a/b)^2 D_{22} + (58/45)^2 D_{12} + (16/9)^2 D_{66}]}{[A_{11} + ((a/b)^2 - v_{lam})A_{12} - v_{lam}(a/b)^2 A_{22}]} \quad (2\text{-}9)$$

$$\varepsilon_B = \left(\frac{\pi}{a}\right)^2 \left(\frac{D_{11}}{A_{11}}\right) = \left(\frac{\pi^2}{12}\right)\left(\frac{h}{a}\right)^2 \left(\frac{Q_{11}^F}{Q_{11}^M}\right) \quad (2\text{-}10)$$

where $Q_{11}^F = 12D_{11}/h^3$ and $Q_{11}^M = A_{11}/h$

Where ε_B is the buckling strain, A_{11}, A_{12}, A_{22}, D_{11}, D_{12},D_{22} and D_{66} are terms from the "ABD" laminate stiffness matrix (coordinate 1 in the loading direction), $v_{lam}$is the Poisson's ratio of the base laminate, a and b are the dimensions of half the elliptical axis parallel and perpendicular to the loading for the Rayleigh-Ritz case, a is the half length of the delamination in the loading direction in the Euler case, and h is the sublaminate thickness. Q^F and Q^M are equivalent flexural and membrane moduli of the buckling sublaminate respectively.

These solutions have been tested by Craven *et al.* [45] against finite element models. The model highlights that the Releyigh-Ritz methods conforms well to the buckling predictions made by the finite element models, overestimating between 10-20 % for circular delaminations and 20-30 % for elliptical solutions. The Euler strip buckling model on the other hand severely underestimated buckling strain for circular delaminations and overestimated for elliptical. This is unsurprising given the one-dimensionality of the Euler approach in contrast to the two-dimensional Rayleigh-Ritz model.

What is clear from these two equations is that the buckling strain is related to the inverse square of the sublaminate free length. This correlates with studies which report that the residual CAI strength scales inversely with low velocity impact energy, in cases for which there is a linear relationship between impact energy and the size of the projected damage area [5, 23, 35, 146]. The size of the damage area roughly correlates with the square of the length across the damage

area (area of a circle calculation). This suggests from experimental studies that the length squared across the projected damage area scales linearly with CAI strength.

An example of the relationship between impact energy and residual compressive strength is shown in a report by D.D.R. Cartié *et al.* which studied the effect of different resin systems on quasi-isotropic CFRP laminates, see Figure 2.20 [5]. In this plot, the vertical line at the lower load levels represents an immediate drop in strength after the impact energy reaches a critical threshold to create delaminations. The corresponding residual strength is shown to decrease linearly with an increase in impact energy. This work also shows a link between G_{IIC}, projected delamination area and residual CAI strength as it is reported that the resin toughness, not the fibres, controlled the extent of delamination. The tougher HTA920 system suppressed the extent of delaminations compared to the HTA922 system with mode II critical energy release rates of 729 Jm^{-2} and 298 Jm^{-2} respectively.

Since the projected size of delamination after impact is reported to affect strongly residual CAI strength by increasing instability in the region, there should be concern about subcritical delamination growth prior to failure. Growth in delaminations during in-plane compressive loading could further reduce the critical compressive strength in systems and may be an issue that needs to be included in finite element models of the CAI experiment. It is unclear in the literature whether or not there is significant delamination growth prior to critical failure in CAI tests; this highlights a need for further investigation.

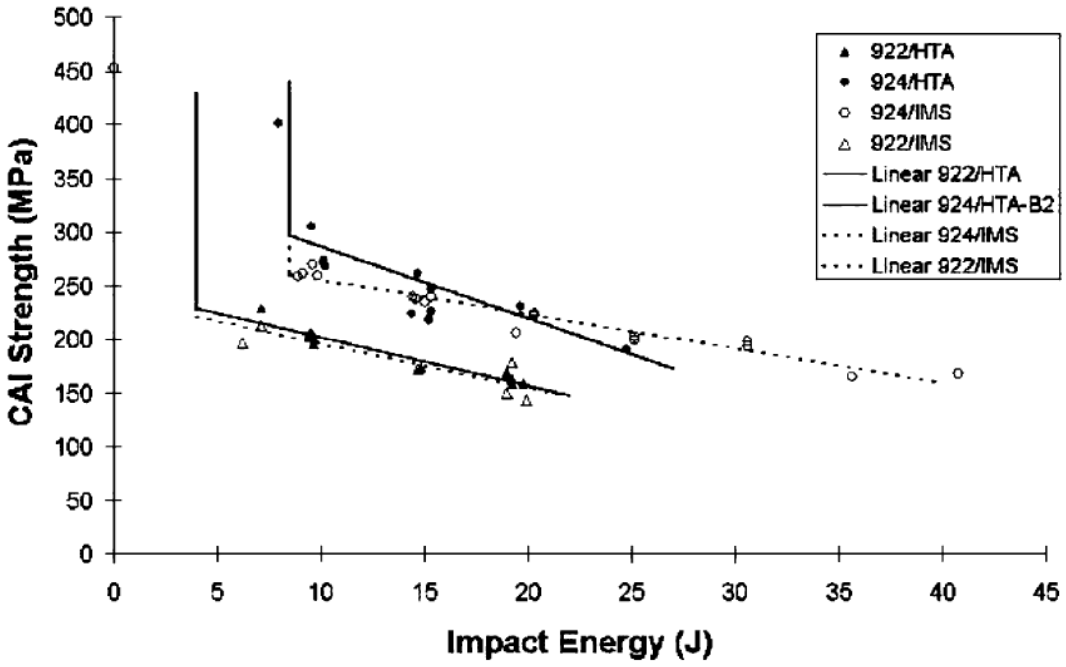

Figure 2.20 – Effects of resin matrix on CAI strength [5]

2.6.3 Failure modes from in-plane compression-after-impact

In the previous section, it was presented that the loss of compressive strength after an impact event is attributed to local instability resulting from delamination. Delaminations caused the laminate to be divided into sub-laminates with lower buckling load-carrying capabilities. In a study by Reis *et al*. [30] observing buckling behaviour, three types of buckling were detected as shown in Figure 2.21. This was studied on 977-2 Cycom prepreg systems stacked to 24 plies and measuring 150 x 100 mm with four varying quasi-isotropic stacking sequences leading to varied in-plane laminate stiffness. Coupons were subjected to low velocity impact and loaded in compression using an anti-buckling rig. Out-of-plane movement was monitored using two LVDTs positioned on opposite faces at the centre of the coupon. In (a), the most common type of buckling is shown, with over 50 % of all coupons tested reported to buckle in the direction away from the impact site, attributed to the permanent indentation depth, which leads to misalignment of the specimen [146]. The second common failure is shown in (b) where 35 % of results failed in which delamination buckling occurred by outward bulging of laminate surfaces at both sides. The remaining 15 % failed in (c) towards the impact site.

Whilst it is unreported how these different failure modes influenced the residual compression strength, it may be an issue worth considering should there be experimentally-observed variations in failure load. After failure, inspection of specimens confirmed that local delaminations extended completely across the specimen's width, but propagated only a short distance in the axial direction as shown by the C-scans in Figure 2.22 where (a) shows damage after impact and (b) shows progression of damage after compression. This is in agreement with other studies [4, 154]. It was also reported in this study that the size of the delaminated area controlled the residual strength and was independent of the stacking sequence used.

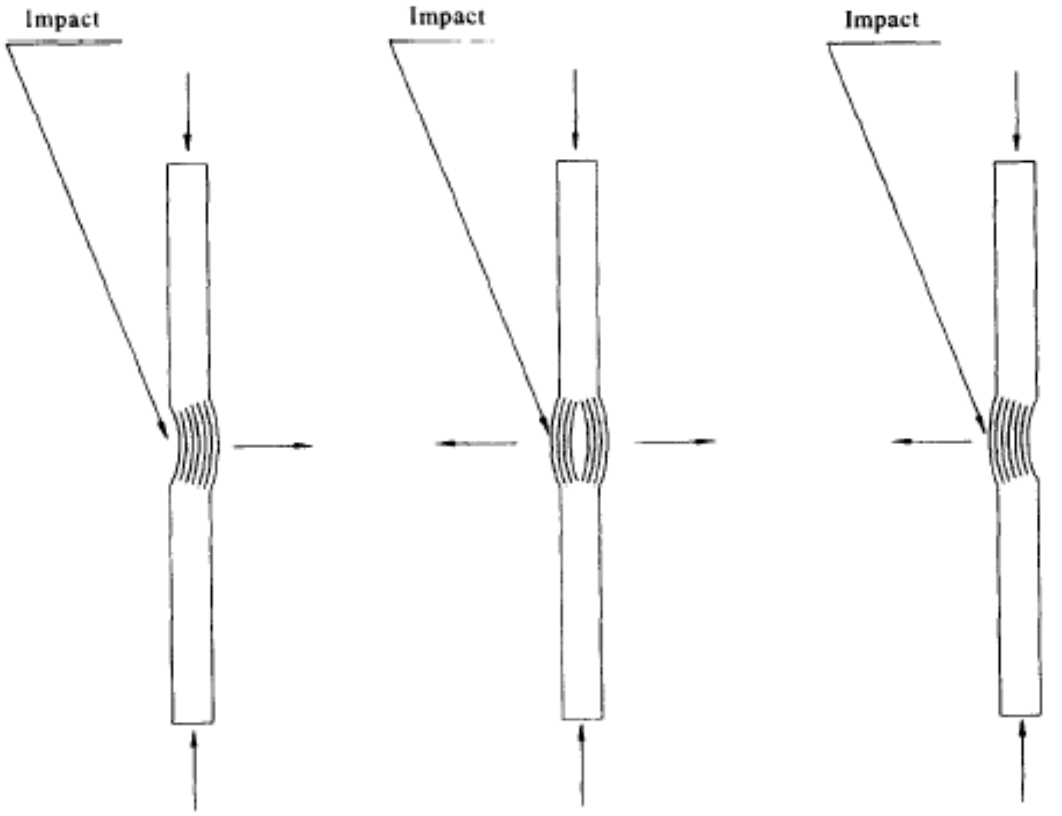

Figure 2.21: Difference delamination buckling modes, (a), (b), (c) [30].

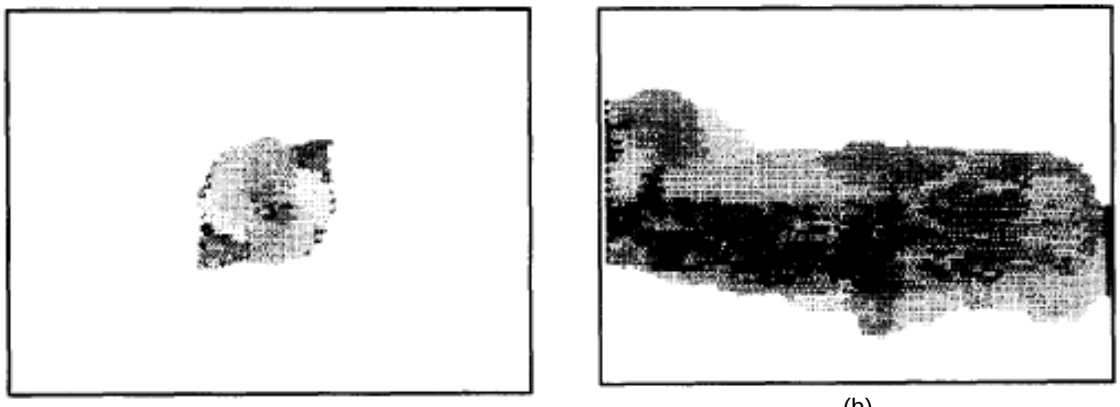

Figure 2.22(a) (b)

Figure 2.22: C-scan of (a) after impact and (b) after compression-after-impact [30].

There are several reported explanations regarding the mechanisms leading to post-impact compressive failure [155]. Whilst it is generally agreed that delaminations are predominantly responsible, due to the formation of sublaminates with a reduced flexural stiffness, and therefore lower load carrying capability, as discussed earlier, the sequences of events that lead to compressive failure are debated in the literature. Some studies report that sublaminate buckling leads to a sudden growth of damage extending laterally leading to a sudden failure of the coupon [30, 156, 157]. Another reported mechanism is that the buckled sublaminates lead to a load redistribution resulting in compressive fibre fracture [48, 158]. One study, using X-ray radiography to monitor damage growth at incremental compressive loads, suggests that sublaminate buckling at the damaged regions leads to a combination of bending and compressive loads in the remaining undelaminated part of the laminate leading to final failure [159]. At the fibre-level, microbuckling can occur on the 0° load-bearing fibres aligned with the loading direction. In comparison to fibres, the matrix resin stiffness is significantly lower. This typically leads to a kink-band formation in which deformation of the matrix can lead to rotation of the fibres and consequently fracture in two places leading to a loss in load carrying capability. Under compression loading, microbuckling can be initiated at material free edges, resin-rich regions, voids and fibre waviness [50, 160, 161].

It has been reported that the use of stitching and Z-pinning can increase CAI strength in two ways: by reducing the extent of the delamination area for a given impact energy and by improving the out-of-plane stability of sublaminates by

bridging together these regions [23, 59, 60]. With this information, it may be possible that particle-toughening micro-mechanisms such as bridging ligaments may create similar constraining behaviour.

Whilst it is believed that delaminations are the dominant damage mode in determining CAI strength, it has been reported that other impact-induced damage mechanisms may also affect the residual strength. These include matrix cracks, fibre microcracking and weakening of the interlaminar cohesive strength beyond the delamination zone [157].

The wide range of reported mechanisms that contribute to CAI failure highlights a need to clarify and identify key contributing factors. There is a current absence of systematic studies in the literature to understand the interaction of these damage processes [157]. This is made problematic due to the rapid, catastrophic failure of composites, which makes identification of critical failure modes difficult to achieve [162]. In order to develop material systems to prevent strength degradation, a detailed analysis of failure in the pre- and post-buckling loading region is required, taking into account the dominant failure mechanisms and their interactions [137].

2.7 Finite element modelling of compression-after-impact

2.7.1 Finite element failure criteria and fracture mechanics

Finite element (FE) models to predict residual compressive failure have been produced in previous studies discussed in section 2.7.2. These models can typically include failure criteria and fracture mechanics to predict structural failure, or simply perform purely elastic models to predict local buckling behaviour [45, 163]. Whilst it is beyond the scope of this thesis to review all modelling approaches in depth, excellent reviews of failure theories can be found in works by Hinton *et al*. [164], Orifici *et al.*[165], and Mishnaevsky and Brøndsted [166].

Failure criteria typically include values such as maximum stress, strain, force, displacement and rotation for example, where damage occurs when the parameters reach a critical level. Such examples of failure criteria include

stress/strain based failure, Tsai-Wu [167], and maximum stress/strain theories, Tsai [168]. Other failure criteria can provide indications of fibre/matrix failure, such as Hashin [169-171] and Puck [172]. These failure criteria can be used to generate failure envelopes, *e.g.* a biaxial stress envelope as shown in Figure 2.23 [173]. The accuracy of such failure criteria and many others has been tested in a series of world-wide failure exercises led by Hinton and Kaddour [164, 174-177]. Predictions for test cases consisting of different loading configurations, layups and material properties have been compared between failure criteria and to experimental data. One of the key findings from this work is that no failure criteria work for all conditions with the best only providing predictions which lie within 10 % accuracy for 40 % of cases [174-178] and is further highlighted by the differing failure envelopes between failure criteria solutions shown in Figure 2.23. The complex nature of composites and the vast array of material parameters and loading conditions means at present no single modelling approach can accurately account for damage and failure of laminates under all possible conditions.

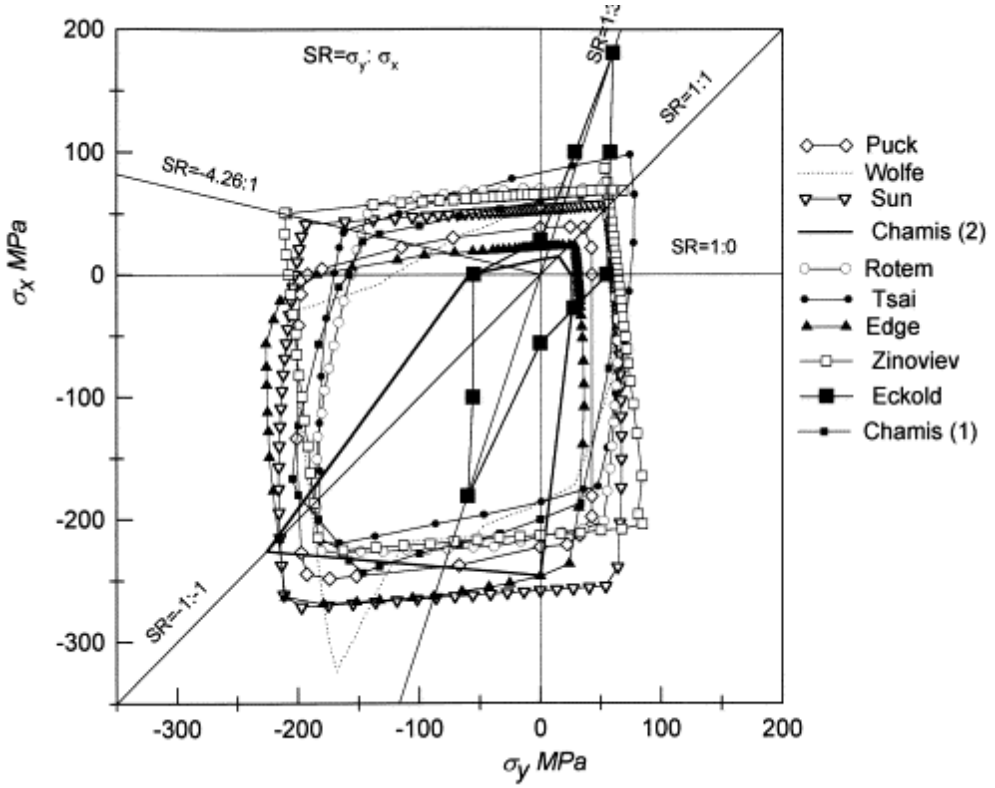

Figure 2.23: Example of biaxial failure envelopes for (90/±30/90) laminate made of E-glass [173].

Fracture mechanics approaches consider the growth of existing defects. In the case of compression-after-impact, delamination propagation is of particular interest due to its effects on structural integrity. Two widely used methods of modelling delamination propagation include the virtual crack closure technique (VCCT) [179] and cohesive zone modelling (CZM) [180]. The former technique has the limitation that a precrack is required, whereas cohesive zones can model crack initiation and propagation.

CZM models are based on traction-separation laws. For a single failure mode, the traction (t) represents the stress in the direction of failure and the separation (δ) represents change in displacement between the upper and lower cohesive element. The shape of the traction-separation curve can range from a trapezoid, polynomial, exponential and bilinear. New crack surfaces are formed when the fracture toughness is equal to the area surface under a traction-separation curve [181].

In cases where there is a mixed mode failure, a BK mixed-mode traction-separation model can be used to compute the critical energy (G_C) based on mixing mode I and mode II fracture energies. The BK material parameter, η, is determined through curve fitting experimental data [182, 183].

2.7.2 Compression-after-impact models

Compression-after-impact models typically utilise idealisations of the delaminations resulting from the impact event. To keep the models simple, a significant number of studies have focused on consolidating the complex network of delaminations into simplified circular or elliptical delaminations [184-186]. To construct these finite element models, delaminations are represented by creating untied regions within a stack of sublaminate plies, with the remaining undamaged surfaces tied together. To prevent the buckled delaminated sublaminates from penetrating the neighbouring sublaminates, surface contact behaviour is included. To enable local buckling of the model, instability has to be included, either through applying a negligibly small pressure or point load to the delaminated region, applying an initial out-of-plane deflection, or inclusion of the mode 1 and mode 2

buckling shape as imperfections. Models can be purely elastic or include delamination growth by including cohesive zones for example [45, 163]. One of the most common measures in these models is the local out-of-plane deflection response against the load applied which produces a representative graph shown in Figure 2.24 demonstrating elastic instability [163, 187].

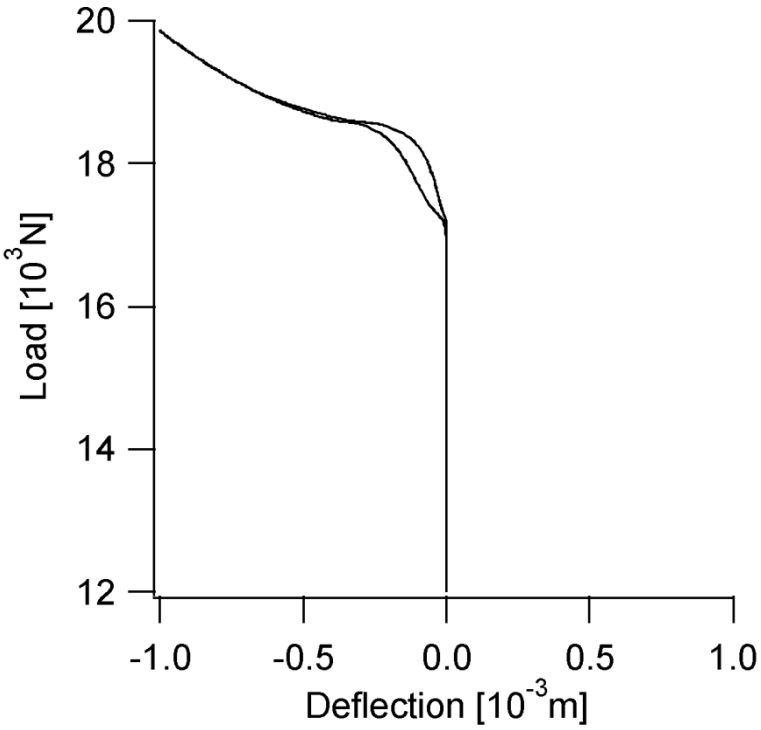

Figure 2.24: Plot representing load vs. out-of-plane deflection highlighting instability above a critical load [163].

In order to represent better the actual geometry of delaminations caused by impact, some models include more complex idealisations. Craven *et al.* [45] used models containing idealised “peanut” shaped impact damage obtained from time of flight C-scans, and varying delamination location and size. It was concluded that delamination size and shape are important factors to consider together with distribution of the shapes and delamination sizes through the thickness. This work showed that these factors led to significant differences in buckling strain, upwards of a factor of two for a given damage length in one damage model which included an undamaged region at the centre. Limitations of this work, however, include an absence of comparisons between experimental and predicted results and a lack of consideration of damage growth during loading.

Suemasu *et al.* [188] also studied two idealisations of delamination systems; a more complex delamination mode consisting of 45° “spiral” damage interlinked with matrix cracks and for comparison a simplified circular delamination model. Some damage growth prior to failure was captured in the “spiral” system at the lower interfaces towards the bottom surface, which was not captured in the simplified circular model prior to buckling failure. To model this damage growth, cohesive elements were used. This growth however was reported as not significant. Growth at the edges of delaminations were modelled in later work by Suemasu *et al*. [184] using circular delaminations; again, cohesive elements were used. His work showed early buckling of the surface sub-laminates, followed by buckling of all the sub-laminates due to the load redistribution. At loads approaching failure, delaminations started to propagate, this propagation was found to be governed by the delamination fracture toughness and this growth contributes to reducing the failure load.

Rhead *et al.* [185] simplified delaminations to circles at ply interfaces within the bottom 20 % of the material system. These are reported to be the critical locations in the laminate as described by Melin and Schon [189]. The model took into account delamination growth on these plies when they exceeded a critical mode I strain value. Comparisons between numerical and experimental data were made across eight carbon fibre material systems and the overall the accuracy of these models was within 16 % of the compression-after-impact experimental values.

To model buckling failure, some examples that have been used include non-linear buckling calculations by finite element analysis [190] and thin film sub-laminate modelling [191, 192].

The simplest FE model for impact damage was undertaken by Chen *et al*. [147] which simplified the damage area to an elliptical hole with the lateral length equivalent to the damage width and height equal to the dent diameter. Overall, the predicted failure loads were up to 36 % lower than the actual failure loads and in most cases the predicted loads were lower than the experimental data. The applicability of this technique is questionable, as the failure mechanisms in compression may be different to that of impact-induced delaminations. Typically

an open hole will initiate and grow a micro-buckle from the edge of the hole [158] unlike buckling of delaminated sub-laminates.

Overall, accurately predicting the mechanisms that lead to ultimate compressive failure is important. There are models available at present that require input of impact damage at predetermined layers using cohesive zones to model propagation, however, these are computationally expensive [193], alternatively there are very simple models that are efficient but are relatively inaccurate [194, 195]. The combination of better representation of delaminated sub-laminates and delamination growth prior to failure are commonly ignored in order to simplify models. Whilst models that better represent impact-induced delaminations and damage growth during post-impact compression may better estimate the failure load, they require added complexity and longer times to solve. Whilst it is generally understood that delaminations lead to sub-laminates with lower stiffness and buckling loads, little is known experimentally about delamination growth under in-plane compressive load prior to buckling failure. These mechanisms may be important issues to consider; delamination growth for example will further reduce the ultimate buckling load [184], but its contribution may be small in cases with little growth or where growth is only significant at certain ply interfaces. Better understanding of these issues is needed to ensure models are accurate, by including the major mechanisms leading to failure, or to provide justification for simplification of these models.

2.8 3D X-ray tomography

Tomography is commonly known as the medical technique of computed axial tomography (CAT) since its invention by G.N. Hounsfield, and the introduction of this technique into the medical practice on the 1st October 1971 [196]. The key feature of tomography is the ability to obtain information regarding a slice of matter within a bulk object [196]. Beyond its use in the medical field, it has applications in material science for studying the material's response to a range of conditions, such as fracture, response to mechanical loading, and non-destructive inspection techniques to identify defects and voids for example [197, 198]. There are several physical imaging principles that can be used in conjunction with tomographic reconstruction, including: ultrasonic, magnetic fields, electric fields and X-rays

[199]. The latter source is the most widely-used and is the method used in this thesis. Since the first application of CT in the early 1970's, this technique has advanced significantly with the capacity of today's industrial CT scanners being able to resolve structural detail to sub-micron resolutions in 3D [200]. To highlight the importance of CT, to acquire the same data, serial sectioning would be required through successive sectioning of a material. This has negative implications which include introducing damage to the sectioned region, and ultimately destroying the sample.

2.8.1 Principles of CT imaging

The key operating principles of CT are to record a series of 2D radiograph projections taken at controlled rotational increments of an object. These projections result from attenuated X-rays measured by a radiosensitive detector. The sequence of X-ray projections is reconstructed most commonly using filtered back-projection to produce a 3D volume representative of the sample [198, 201]. Once reconstructed, the 3D volume is represented by greyscale values corresponding to the X-ray attenuation through the sample [202].

In engineering considerations, two classifications of CT techniques are described, consisting of lab-based microfocus computed tomography (µCT) and synchrotron radiation computed tomography (SRCT). Whilst both work using similar principles, the key difference is the X-ray source used. This affects the routinely achievable resolutions of samples, down to 3 µm in µCT and sub-micron in SRCT [203]. Whilst the latter can offer better routinely achievable resolutions, in comparison to the relatively wide availability of commercial µCT facilities, synchrotron radiation facilities are few with limited access to beamtime.

In addition to computed tomography, synchrotron radiation computed laminography (SRCL) is an alternative technique better suited to the laterally extended geometry of composite plates. It works on the same principles as CT, *i.e.* many radiographs (> 1000 projections) are collected as a sample is rotated about an axis. The key difference is that the axis of rotation is tilted whereas in CT the axis is perpendicular to the X-ray path. This minimises the X-ray path length

variation as the sample is rotated enabling local non-destructive assessment of plate-like structures at sub-micron resolutions. Further details of the operation and capabilities of SRCL can be found in papers by L. Helfen *et al.* [204, 205].

As with all computed tomography techniques, there are some physical effects that can degrade the quality of the CT scan. These include beam-hardening, partial volume, photon starvation, motion blur, ring artefacts, and cone beam effects. Further details of these artefacts, their implications and how they can be reduced or mitigated described in an article by J.F. Barret *et al*. [206].

Beam-hardening artefacts can lead to cupping artefacts (appearance of darker regions in the centre of an object, and brighter at the edges), and the formation of dark bands or streaks between dense objects. The cause of these artefacts is largely due to the use of polychromatic X-ray sources that enable lower energies to be more easily absorbed leaving behind only high energy photons. The cause of cupping artefacts is associated with more absorption of lower energy photons where there is variations in through-thickness, *e.g.* in the centre of a cylindrical object. As there is more material to pass through at the centre of a cylinder, there is more low energy absorption in this region than at the edges. The cause of streaks and dark bands can appear between two neighbouring dense objects, this occurs due to variations in X-ray path length during rotation. At certain positions the X-ray passes through one object, however in other orientations where both objects are in line, the X-ray passes through both objects and therefore more lower-energy photons are absorbed [206, 207].

Ring artefacts are one of the most common artefacts in CT scans and appear as concentric rings in the reconstructed slices. The cause of ring artefacts is defective pixels across the detectors, which results in a slight deviation from the true grey-scale value. As the sample is rotated, the defective pixels stay at particular points in the 2D projections; when reconstructed these defective pixels trace a concentric ring [206].

2.8.1.1 Applications of µCT, SRCT and SRCL to composites

3D X-ray computed tomography has been shown to be a valuable tool for studying the anisotropic nature of composites and complex damage modes associated with the material. These include recent use of µCT for impact damage studies [208-210], and other damage assessments on carbon fibre composite materials [211, 212] and glass fibre [213, 214] with the capability of detecting matrix cracks, delaminations and voids. In these studies, the voxel sizes used ranged between 5 µm to 30 µm; at these voxel sizes, individual fibres could not be resolved.

In carbon fibre composites, it has been reported that µCT can detect crack-openings down to 20 % of the voxel size and even down to 5 % where contrast agents are used [211]. One limitation is that contrast agents require crack interconnectivity to penetrate through the whole damage network [211]. The detectability of cracks smaller than the voxel size is associated with partial volume averaging, in which two features are averaged and represented within a single voxel [206].

High resolution SRCT has been used to study composite damage at the micrometer-levels with the ability to detect individual fibres and fibre breaks, as well as micro-damage mechanisms [114, 210, 215-219]. An extensive search of the literature revealed no current published work applying SRCT to study impact damage on carbon fibre systems.

Synchrotron radiation computed laminography has been successfully used in previous studies to study damage in composite plates; this has been achieved on composites with a thickness no greater than 1 mm [204, 205, 215, 220]. As ASTM standard impact and compression-after-impact coupons are significantly thicker (~5 mm) the ability to locally scan this thickness of material at such high resolution, non-destructively, would be desirable for capturing damage micromechanisms without risk of introducing cutting artefacts, releasing residual stresses, *etc*. This requires a feasibility study to test its capabilities to this application.

To better understand the development of damage, time-series experiments have been performed using computed tomography and laminography. Previous work has studied the initiation and growth of micro-damage in composite systems by

carrying out *in situ* experiments, *i.e.* applying a load to the specimen whilst it is scanned [212, 216, 217, 220, 221]. The key benefit of this technique is to understand how damage evolves, and offers a better understanding of critical failure mechanisms, which would otherwise not be captured by studying failed specimens.

One of the key areas of development for industrial CT is on the transformation from a qualitative inspection tool to one that includes quantitative assessments. An excellent review paper by Maire, *et al.* [222] covers this area in particular with quantifying damage accumulation and crack growth. This paper highlights developing quantification strategies which could be brought to composite materials to enable numerical characterisation and comparison of damage mechanisms between material systems. Such quantification strategies are necessary to offer fairer comparisons without the bias associated with qualitative analysis.

2.9 Conclusions

Out-of-plane low velocity impact can cause subsurface internal damage in CFRPs, consisting of matrix cracks, delamination and tensile failure. Typically matrix cracks induce delaminations when they interact with plies of different orientations. These delaminations may directly affect residual in-plane compressive strength by dividing the laminate into sub-laminates with lower load carrying capabilities. To reduce delamination initiation and growth and to increase damage resistance, toughening of the interlaminar regions may be employed. There is general agreement that the mode II fracture toughness, $G_{IIC,}$ controls impact damage resistance, as delamination propagation in low velocity impact is dominated by shear stresses introduced by the transverse loading.

Particles introduced to the matrix can create toughening mechanisms that increase damage resistance and subsequently increase the residual compressive strength of the material for a given impact. Investigations that directly compare particle-toughened systems to systems without particles, under impact and compression-after-impact conditions, could not be found in the literature.

Particle size, stiffness, interfacial strength and concentration have been shown to influence the mode II fracture toughness; optimisations of these parameters and

better understanding of the toughening mechanisms are seen to be required to maximise fracture toughness. Particle-toughening mechanisms include particle-matrix debonding, micro-crack growth through plastic deformation, crack deflection and crack bridging. Further work is required to understand the relative contributions of the different micromechanisms towards higher damage resistance.

Quasi-static indentation experiments have been performed in studies and show similarities regarding the extent of damage and load-displacement curves when subjected to low velocity impact. The main benefit of this experiment is that it allows interruptions during the loading, allowing damage initiation and growth to be studied progressively, analogous to the sequence that occurs during an impact event. There are limitations however whereby dynamic effects may influence the outcome between the two loading conditions. To the author's knowledge, no work has been conducted using µCT to track the initiation and propagation of the various damage modes under incremental loads. This would enable a better understanding of the way that damage forms, and allow comparisons of damage between quasi-static indentation and impact damage loading conditions.

Whilst it is generally understood that post-impact compression failure occurs through local buckling events, the understanding of failure mechanisms leading up to failure are still relatively unclear. At present an extensive search of the literature has found no work involving 3D CT damage assessment during compression-after-impact; this is important, as a better understanding of damage mechanisms leading up to final compressive failure will aid in the development of more suitable finite element models. A better understanding of the failure mechanisms during in-plane compression will ensure finite element models are capturing the correct mechanisms. This will also aid in eliminating unnecessary complexity of future modelling work.

The use of 3D X-ray tomography has enabled damage assessment studies in composite materials. These range from macro-level studies utilising micro-focus CT scanners to detect the presence of damage mechanisms, through to high resolution micrometer-level studies using synchrotron radiation. These techniques can be used to study damage in material non-invasively and enable time-series experiments to be performed.

2.10 References

[1] Soutis, C., *Carbon fiber reinforced plastics in aircraft construction.* Materials Science and Engineering: A, 2005. **412**(1–2): pp. 171-176.

[2] Agrawal, S., Singh, K.K., and Sarkar, P., *Impact damage on fibre-reinforced polymer matrix composite – A review.* Journal of Composite Materials, 2013.

[3] Tang, Y.Y., Sun, B.Z., and Gu, B.H., *Impact Damage of 3D Cellular Woven Composite from Unit-cell Level Analysis.* International Journal of Damage Mechanics, 2011. **20**(3): pp. 323-346.

[4] Sanchez-Saez, S., Barbero, E., Zaera, R., and Navarro, C., *Compression after impact of thin composite laminates.* Composites Science and Technology, 2005. **65**(13): pp. 1911-1919.

[5] Cartie, D.D.R. and Irving, P.E., *Effect of resin and fibre properties on impact and compression after impact performance of CFRP.* Composites Part a-Applied Science and Manufacturing, 2002. **33**(4): pp. 483-493.

[6] Delfosse, D. and Poursartip, A., *Energy-based approach to impact damage in CFRP laminates.* Composites Part A: Applied Science and Manufacturing, 1997. **28**(7): pp. 647-655.

[7] McCombe, G.P., Rouse, J., Trask, R.S., Withers, P.J., and Bond, I.P., *X-ray damage characterisation in self-healing fibre reinforced polymers.* Composites Part a-Applied Science and Manufacturing, 2012. **43**(4): pp. 613-620.

[8] Davies, G.A.O., Hitchings, D., and Wang, J., *Prediction of threshold impact energy for onset of delamination in quasi-isotropic carbon/epoxy composite laminates under low-velocity impact.* Composites Science and Technology, 2000. **60**(1): pp. 1-7.

[9] Sjoblom, P.O., Hartness, J.T., and Cordell, T.M., *On Low-Velocity Impact Testing of Composite-Materials.* Journal of Composite Materials, 1988. **22**(1): pp. 30-52.

[10] Shivakumar, K.N., Elber, W., and Illg, W., *Prediction of Low-Velocity Impact Damage in Thin Circular Laminates.* Aiaa Journal, 1985. **23**(3): pp. 442-449.

[11] Liu, D. and Malvern, L.E., *Matrix Cracking in Impacted Glass Epoxy Plates.* Journal of Composite Materials, 1987. **21**(7): pp. 594-&.

[12] Joshi, S.P.a.S., C.T, *Impact-induced fracture initiation and detailed dynamic stress field in the vicinity of impact.* Proc. American Society of Composites 2nd Tech. Conf, 1987: pp. 177-185.

[13] Dale, M., Acha, B.A., and Carlsson, L.A., *Low velocity impact and compression after impact characterization of woven carbon/vinylester at dry and water saturated conditions.* Composite Structures, 2012. **94**(5): pp. 1582-1589.

[14] Dehkordi, M.T., Nosraty, H., Shokrieh, M.M., Minak, G., and Ghelli, D., *The influence of hybridization on impact damage behavior and residual compression strength of intraply basalt/nylon hybrid composites.* Materials & Design, 2013. **43**: pp. 283-290.

[15] Lopes, C.S., Seresta, O., Coquet, Y., Gurdal, Z., Camanho, P.P., and Thuis, B., *Low-velocity impact damage on dispersed stacking sequence laminates. Part I: Experiments.* Composites Science and Technology, 2009. **69**(7-8): pp. 926-936.

[16] Hsiao, H.M. and Daniel, I.M., *Strain rate behavior of composite materials.* Composites Part B-Engineering, 1998. **29**(5): pp. 521-533.
[17] Sutherland, L.S. and Soares, C.G., *The use of quasi-static testing to obtain the low-velocity impact damage resistance of marine GRP laminates.* Composites Part B-Engineering, 2012. **43**(3): pp. 1459-1467.
[18] Nettles, A.T. and Douglas, M.J., *A comparison of quasi-static indentation testing to low velocity impact testing.* Composite Materials: Testing, Design, and Acceptance Criteria, 2002. **1416**: pp. 116-130.
[19] Aoki, Y., Suemasu, H., and Ishikawa, T., *Damage propagation in CFRP laminates subjected to low velocity impact and static indentation.* Advanced Composite Materials, 2007. **16**(1): pp. 45-61.
[20] Lagace, P.A., Williamson, J.E., Tsang, P.H.W., Wolf, E., and Thomas, S., *A Preliminary Proposition for a Test Method to Measure (Impact) Damage Resistance.* Journal of Reinforced Plastics and Composites, 1993. **12**(5): pp. 584-601.
[21] Swanson, S.R., *Limits of quasi-static solutions in impact of composite structures.* Composites Engineering, 1992. **2**(4): pp. 261-267.
[22] Shyr, T.W. and Pan, Y.H., *Impact resistance and damage characteristics of composite laminates.* Composite Structures, 2003. **62**(2): pp. 193-203.
[23] Aymerich, F. and Priolo, P., *Characterization of fracture modes in stitched and unstitched cross-ply laminates subjected to low-velocity impact and compression after impact loading.* International Journal of Impact Engineering, 2008. **35**(7): pp. 591-608.
[24] Takeda, S., Minakuchi, S., Okabe, Y., and Takeda, N., *Delamination monitoring of laminated composites subjected to low-velocity impact using small-diameter FBG sensors.* Composites Part a-Applied Science and Manufacturing, 2005. **36**(7): pp. 903-908.
[25] Davies, G.A.O. and Olsson, R., *Impact on composite structures.* Aeronautical Journal, 2004. **108**(1089): pp. 541-563.
[26] Abrate, S., *Impact on composite structures*. 1998, Cambridge: Cambridge University Press. x, 289p.
[27] Richardson, M.O.W. and Wisheart, M.J., *Review of low-velocity impact properties of composite materials.* Composites Part a-Applied Science and Manufacturing, 1996. **27**(12): pp. 1123-1131.
[28] Schoeppner, G.A. and Abrate, S., *Delamination threshold loads for low velocity impact on composite laminates.* Composites Part a-Applied Science and Manufacturing, 2000. **31**(9): pp. 903-915.
[29] Lammerant, L. and Verpoest, I., *Modelling of the interaction between matrix cracks and delaminations during impact of composite plates.* Composites Science and Technology, 1996. **56**(10): pp. 1171-1178.
[30] Reis, L. and de Freitas, M., *Damage growth analysis of low velocity impacted composite panels.* Composite Structures, 1997. **38**(1-4): pp. 509-515.
[31] Zhou, G., *The use of experimentally-determined impact force as a damage measure in impact damage resistance and tolerance of composite structures.* Composite Structures, 1998. **42**(4): pp. 375-382.
[32] Zhang, X., *Impact damage in composite aircraft structures - experimental testing and numerical simulation.* Proceedings of the Institution of Mechanical Engineers Part G-Journal of Aerospace Engineering, 1998. **212**(G4): pp. 245-259.

[33] Maio, L., Monaco, E., Ricci, F., and Lecce, L., *Simulation of low velocity impact on composite laminates with progressive failure analysis.* Composite Structures, 2013. **103**(0): pp. 75-85.
[34] Choi, H.Y., Wu, H.Y.T., and Chang, F.K., *A New Approach toward Understanding Damage Mechanisms and Mechanics of Laminated Composites Due to Low-Velocity Impact .2. Analysis.* Journal of Composite Materials, 1991. **25**(8): pp. 1012-1038.
[35] Hull, D. and Shi, Y.B., *Damage Mechanism Characterization in Composite Damage Tolerance Investigations.* Composite Structures, 1993. **23**(2): pp. 99-120.
[36] Chang, F.K., Choi, H.Y., and Jeng, S.T., *Study on Impact Damage in Laminated Composites.* Mechanics of Materials, 1990. **10**(1-2): pp. 83-95.
[37] Bouvet, C., Rivallant, S., and Barrau, J.J., *Low velocity impact modeling in composite laminates capturing permanent indentation.* Composites Science and Technology, 2012. **72**(16): pp. 1977-1988.
[38] Greenhalgh, E. and Hiley, M., *The assessment of novel materials and processes for the impact tolerant design of stiffened composite aerospace structures.* Composites Part a-Applied Science and Manufacturing, 2003. **34**(2): pp. 151-161.
[39] Hong, S. and Liu, D., *On the Relationship between Impact Energy and Delamination Area.* Experimental Mechanics, 1989. **29**(2): pp. 115-120.
[40] Daniele Giugno, R.O., *Effect of geometry and boundary conditions on impact response and damage in composite plates*, in *The Aeronautical Research Institute of Sweden (FFA)*. 1998.
[41] Davies, G.A.O. and Zhang, X., *Impact Damage Prediction in Carbon Composite Structures.* International Journal of Impact Engineering, 1995. **16**(1): pp. 149-170.
[42] Sjogren, A., *Fractographic characterization of impact damage in carbon fiber/epoxy laminates.* The Aeronautical Research Institute of Sweden, 1999.
[43] Kostopoulos, V., Baltopoulos, A., Karapappas, P., Vavouliotis, A., and Paipetis, A., *Impact and after-impact properties of carbon fibre reinforced composites enhanced with multi-wall carbon nanotubes.* Composites Science and Technology, 2010. **70**(4): pp. 553-563.
[44] Choi, H.Y. and Chang, F.K., *A Model for Predicting Damage in Graphite Epoxy Laminated Composites Resulting from Low-Velocity Point Impact.* Journal of Composite Materials, 1992. **26**(14): pp. 2134-2169.
[45] Craven, R., Iannucci, L., and Olsson, R., *Delamination buckling: A finite element study with realistic delamination shapes, multiple delaminations and fibre fracture cracks.* Composites Part a-Applied Science and Manufacturing, 2010. **41**(5): pp. 684-692.
[46] Olsson, R., *A review of impact experiments at FFA during 1986 to 1998.* The Aeronautical Research Institute of Sweden, 1999.
[47] Garg, A.C., *Delamination - a Damage Mode in Composite Structures.* Engineering Fracture Mechanics, 1988. **29**(5): pp. 557-584.
[48] Wisnom, M.R., *The role of delamination in failure of fibre-reinforced composites.* Philosophical Transactions of the Royal Society a-Mathematical Physical and Engineering Sciences, 2012. **370**(1965): pp. 1850-1870.

[49] Davies, G.A.O., Hitchings, D., and Zhou, G., *Impact damage and residual strengths of woven fabric glass/polyester laminates.* Composites Part a-Applied Science and Manufacturing, 1996. **27**(12): pp. 1147-1156.
[50] Hawyes, V.J., Curtis, P.T., and Soutis, C., *Effect of impact damage on the compressive response of composite laminates.* Composites Part a-Applied Science and Manufacturing, 2001. **32**(9): pp. 1263-1270.
[51] Bibo, G.A. and Hogg, P.J., *The role of reinforcement architecture on impact damage mechanisms and post-impact compression behaviour.* Journal of Materials Science, 1996. **31**(5): pp. 1115-1137.
[52] Cantwell, W.J., Curtis, P.T., and Morton, J., *An Assessment of the Impact Performance of Cfrp Reinforced with High-Strain Carbon-Fibers.* Composites Science and Technology, 1986. **25**(2): pp. 133-148.
[53] Wang, S.X., Wu, L.Z., and Ma, L., *Low-velocity impact and residual tensile strength analysis to carbon fiber composite laminates.* Materials & Design, 2010. **31**(1): pp. 118-125.
[54] Nettles, A.T. and Lance, D.G., *On the Enhancement of Impact Damage Tolerance of Composite Laminates.* Composites Engineering, 1993. **3**(5): pp. 383-&.
[55] Petit, S., Bouvet, C., Bergerot, A., and Barrau, J.J., *Impact and compression after impact experimental study of a composite laminate with a cork thermal shield.* Composites Science and Technology, 2007. **67**(15-16): pp. 3286-3299.
[56] Hart, W.G.J. and Ubels, L.C., *Impact Energy Absorbing Surface Layers for Protection of Composite Aircraft Structures*. 1998: National Aerospace Laboratory, NLR.
[57] Partridge, I.K. and Cartie, D.D.R., *Delamination resistant laminates by Z-Fiber (R) pinning: Part I - manufacture and fracture performance.* Composites Part a-Applied Science and Manufacturing, 2005. **36**(1): pp. 55-64.
[58] Cartie, D.D.R., Troulis, M., and Partridge, I.K., *Delamination of Z-pinned carbon fibre reinforced laminates.* Composites Science and Technology, 2006. **66**(6): pp. 855-861.
[59] Zhang, X., Hounslow, L., and Grassi, M., *Improvement of low-velocity impact and compression-after-impact performance by z-fibre pinning.* Composites Science and Technology, 2006. **66**(15): pp. 2785-2794.
[60] Mouritz, A.P., *Review of z-pinned composite laminates.* Composites Part a-Applied Science and Manufacturing, 2007. **38**(12): pp. 2383-2397.
[61] Walker, L., Sohn, M.-S., and Hu, X.-Z., *Improving impact resistance of carbon-fibre composites through interlaminar reinforcement.* Composites Part A: Applied Science and Manufacturing, 2002. **33**(6): pp. 893-902.
[62] Greenhalgh, E., Lewis, A., Bowen, R., and Grassi, M., *Evaluation of toughening concepts at structual features in CFRP - Part 1: Stiffener pull-off.* Composites Part a-Applied Science and Manufacturing, 2006. **37**(10): pp. 1521-1535.
[63] Chang, P., Mouritz, A.P., and Cox, B.N., *Properties and failure mechanisms of z-pinned laminates in monotonic and cyclic tension.* Composites Part a-Applied Science and Manufacturing, 2006. **37**(10): pp. 1501-1513.
[64] Xie, S.L., Zhang, J.Q., Guo, Z.S., and Hu, H.J., *Prediction of compressive strength of z-pinned unidirectional composite laminates.* Journal of Composite Materials, 2012. **46**(4): pp. 383-390.

[65] Mouritz, A.P., *Compression properties of z-pinned composite laminates.* Composites Science and Technology, 2007. **67**(15-16): pp. 3110-3120.
[66] White, S.R., Sottos, N.R., Geubelle, P.H., Moore, J.S., Kessler, M.R., Sriram, S.R., Brown, E.N., and Viswanathan, S., *Autonomic healing of polymer composites.* Nature, 2001. **409**(6822): pp. 794-797.
[67] Williams, G., Trask, R., and Bond, I., *A self-healing carbon fibre reinforced polymer for aerospace applications.* Composites Part a-Applied Science and Manufacturing, 2007. **38**(6): pp. 1525-1532.
[68] Morgeneyer, T.F., Helfen, L., Sinclair, I., Proudhon, H., Xu, F., and Baumbach, T., *Ductile crack initiation and propagation assessed via in situ synchrotron radiation-computed laminography.* Scripta Materialia, 2011. **65**(11): pp. 1010-1013.
[69] Williams, G.J., Bond, I.P., and Trask, R.S., *Compression after impact assessment of self-healing CFRP.* Composites Part a-Applied Science and Manufacturing, 2009. **40**(9): pp. 1399-1406.
[70] Kessler, M.R., Sottos, N.R., and White, S.R., *Self-healing structural composite materials.* Composites Part a-Applied Science and Manufacturing, 2003. **34**(8): pp. 743-753.
[71] Soutis, C., *Carbon fiber reinforced plastics in aircraft construction.* Materials Science and Engineering a-Structural Materials Properties Microstructure and Processing, 2005. **412**(1-2): pp. 171-176.
[72] Pearson, R.A., *Toughening Epoxies Using Rigid Thermoplastic Particles - a Review.* Advances in Chemistry Series, 1993(233): pp. 405-425.
[73] Morita, H., Adachi, T., Tateishi, Y., and Matsumoto, H., *Characterization of impact damage resistance of CF/PEEK and CF/toughened epoxy laminates under low and high velocity impact tests.* Journal of Reinforced Plastics and Composites, 1997. **16**(2): pp. 131-143.
[74] Scott, J.M. and Phillips, D.C., *Carbon-Fiber Composites with Rubber Toughened Matrices.* Journal of Materials Science, 1975. **10**(4): pp. 551-562.
[75] Kim, J.K., Mackay, D.B., and Mai, Y.W., *Drop-Weight Impact Damage Tolerance of Cfrp with Rubber-Modified Epoxy Matrix.* Composites, 1993. **24**(6): pp. 485-494.
[76] Viana, J.C., *Polymeric materials for impact and energy dissipation.* Plastics Rubber and Composites, 2006. **35**(6-7): pp. 260-267.
[77] Onchi, T., Dohi, K., Soneda, N., Cowan, J.R., Scowen, R.J., and Castano, M.L., *Fractographic and microstructural characterization of irradiated 304 stainless steel intergranularly fractured in inert gas.* Journal of Nuclear Materials, 2003. **320**(3): pp. 194-208.
[78] Sun, L.Y., Gibson, R.F., Gordaninejad, F., and Suhr, J., *Energy absorption capability of nanocomposites: A review.* Composites Science and Technology, 2009. **69**(14): pp. 2392-2409.
[79] Odagiri, N., Kishi, H., Nakane, T., *T800H/3900-2 Toughened Epoxy Prepreg System : Toughening Concept and Mechanism.* Proc. American Society of Composites 6th Tech. Conf, 1988: pp. 46-52.
[80] Friedrich, K., *Application of fracture mechanics to composite materials*. 1989: Elsevier.
[81] Partridge, I.K., *Advanced composites*. 1989: Elsevier Applied Science.

[82] Sue, H.J., Jones, R.E., and Garciameitin, E.I., *Fracture-Behavior of Model Toughened Composites under Mode-I and Mode-Ii Delaminations.* Journal of Materials Science, 1993. **28**(23): pp. 6381-6391.
[83] Fu, S.Y., Feng, X.Q., Lauke, B., and Mai, Y.W., *Effects of particle size, particle/matrix interface adhesion and particle loading on mechanical properties of particulate-polymer composites.* Composites Part B-Engineering, 2008. **39**(6): pp. 933-961.
[84] Spanoudakis, J. and Young, R.J., *Crack-Propagation in a Glass Particle-Filled Epoxy-Resin .2. Effect of Particle Matrix Adhesion.* Journal of Materials Science, 1984. **19**(2): pp. 487-496.
[85] Hsueh, C.H., *Effects of Aspect Ratios of Ellipsoidal Inclusions on Elastic Stress Transfer of Ceramic Composites.* Journal of the American Ceramic Society, 1989. **72**(2): pp. 344-347.
[86] Groleau, M.R., Shi, Y.B., Yee, A.F., Bertram, J.L., Sue, H.J., and Yang, P.C., *Mode II fracture of composites interlayered with nylon particles.* Composites Science and Technology, 1996. **56**(11): pp. 1223-1240.
[87] Spanoudakis, J. and Young, R.J., *Crack-Propagation in a Glass Particle-Filled Epoxy-Resin .1. Effect of Particle-Volume Fraction and Size.* Journal of Materials Science, 1984. **19**(2): pp. 473-486.
[88] Gao, F., Jiao, G.Q., Lu, Z.X., and Ning, R.C., *Mode II delamination and damage resistance of carbon/epoxy composite laminates interleaved with thermoplastic particles.* Journal of Composite Materials, 2007. **41**(1): pp. 111-123.
[89] Garg, A.C. and Mai, Y.W., *Failure Mechanisms in Toughened Epoxy-Resins - a Review.* Composites Science and Technology, 1988. **31**(3): pp. 179-223.
[90] Chai, G.B. and Zhu, S., *A review of low-velocity impact on sandwich structures.* Proceedings of the Institution of Mechanical Engineers Part L-Journal of Materials-Design and Applications, 2011. **225**(L4): pp. 207-230.
[91] Moloney, A.C., Kausch, H.H., Kaiser, T., and Beer, H.R., *Parameters determining the strength and toughness of particulate filled epoxide resins.* Journal of Materials Science, 1987. **22**(2): pp. 381-393.
[92] Fu, S.-Y., Feng, X.-Q., Lauke, B., and Mai, Y.-W., *Effects of particle size, particle/matrix interface adhesion and particle loading on mechanical properties of particulate–polymer composites.* Composites Part B: Engineering, 2008. **39**(6): pp. 933-961.
[93] Ou, Y., Yang, F., and Yu, Z.-Z., *A new conception on the toughness of nylon 6/silica nanocomposite prepared via in situ polymerization.* Journal of Polymer Science Part B: Polymer Physics, 1998. **36**(5): pp. 789-795.
[94] Guo, T., Wang, L., Zhang, A., and Cai, T., *Effects of nano calcium carbonate modified by a lanthanum compound on the properties of polypropylene.* Journal of Applied Polymer Science, 2005. **97**(3): pp. 1154-1160.
[95] Spanoudakis, J. and Young, R.J., *Crack propagation in a glass particle-filled epoxy resin.* Journal of Materials Science, 1984. **19**(2): pp. 487-496.
[96] Broutman, L.J. and Sahu, S., *The effect of interfacial bonding on the toughness of glass filled polymers.* Materials Science and Engineering, 1971. **8**(2): pp. 98-107.

[97] Kruzic, J., Nalla, R.K., Kinney, J.H., and Ritchie, R.O., *Crack blunting, crack bridging and resistance-curve fracture mechanics in dentin: effect of hydration.* Biomaterials, 2003. **24**(28): pp. 5209-5221.
[98] Yamini, S. and Young, R.J., *The Mechanical-Properties of Epoxy-Resins .1. Mechanisms of Plastic-Deformation.* Journal of Materials Science, 1980. **15**(7): pp. 1814-1822.
[99] Yamini, S. and Young, R.J., *The Mechanical-Properties of Epoxy-Resins .2. Effect of Plastic-Deformation Upon Crack-Propagation.* Journal of Materials Science, 1980. **15**(7): pp. 1823-1831.
[100] Yee, A.F. and Pearson, R.A., *Toughening mechanisms in elastomer-modified epoxies.* Journal of Materials Science, 1986. **21**(7): pp. 2462-2474.
[101] Moloney, A.C., Kausch, H.H., Kaiser, T., and Beer, H.R., *Parameters Determining the Strength and Toughness of Particulate Filled Epoxide-Resins.* Journal of Materials Science, 1987. **22**(2): pp. 381-393.
[102] Pearson, R.A. and Yee, A.F., *Toughening Mechanisms in Thermoplastic-Modified Epoxies .1. Modification Using Poly(Phenylene Oxide).* Polymer, 1993. **34**(17): pp. 3658-3670.
[103] Faber, K.T. and Evans, A.G., *Crack Deflection Processes .1. Theory.* Acta Metallurgica, 1983. **31**(4): pp. 565-576.
[104] Rao, K.T.V., Soboyejo, W.O., and Ritchie, R.O., *Ductile-phase toughening and Fatigue-Crack Growth in Nb-Reinforced Molybdenum Disilicide Intermetallic Composites.* Metallurgical Transactions A, 1992. **23**(8): pp. 2249-2257.
[105] Chan, K.S., Lee, Y.D., Nicolella, D.P., Furman, B.R., Wellinghoff, S., and Rawls, R., *Improving fracture toughness of dental nanocomposites by interface engineering and micromechanics.* Engineering Fracture Mechanics, 2007. **74**(12): pp. 1857-1871.
[106] Ritchie, R.O., *Mechanisms of Fatigue Crack-Propagation in Metals, Ceramics and Composites - Role of Crack Tip Shielding.* Materials Science and Engineering a-Structural Materials Properties Microstructure and Processing, 1988. **103**(1): pp. 15-28.
[107] Cotterell, B. and Rice, J.R., *Slightly Curved or Kinked Cracks.* International Journal of Fracture, 1980. **16**(2): pp. 155-169.
[108] Ruf, H. and Evans, A.G., *Toughening by Monoclinic Zirconia.* Journal of the American Ceramic Society, 1983. **66**(5): pp. 328-332.
[109] Shang, J.K. and Ritchie, R.O., *Crack Bridging by Uncracked Ligaments during Fatigue-Crack Growth in Sic-Reinforced Aluminum-Alloy Composites.* Metallurgical Transactions a-Physical Metallurgy and Materials Science, 1989. **20**(5): pp. 897-908.
[110] Ahmad, Z.B., Ashby, M.F., and Beaumont, P.W.R., *The Contribution of Particle-Stretching to the Fracture-Toughness of Rubber Modified Polymers.* Scripta Metallurgica, 1986. **20**(6): pp. 843-848.
[111] Rose, L.R.F., *Toughening Due to Crack-Front Interaction with a 2nd-Phase Dispersion.* Mechanics of Materials, 1987. **6**(1): pp. 11-15.
[112] Aksoy, A. and Carlsson, L.A., *Interlaminar Shear Fracture of Interleaved Graphite Epoxy Composites.* Composites Science and Technology, 1992. **43**(1): pp. 55-69.
[113] Ishikawa, T., Hayashi, Y., and Matsushima, M., *Compression after Impact (Cai) Properties of Cf/Peek (Apc-2) and Conventional Cf-Epoxy Stiffened Panels.* Icas Proceedings 1992, Vols 1 and 2, 1992: pp. 1225-1234.

[114] Wright, P., Fu, X., Sinclair, I., and Spearing, S.M., *Ultra high resolution computed tomography of damage in notched carbon fiber-epoxy composites.* Journal of Composite Materials, 2008. **42**(19): pp. 1993-2002.
[115] Williams, J.G., *Particle toughening of polymers by plastic void growth.* Composites Science and Technology, 2010. **70**(6): pp. 885-891.
[116] Singh, R.P., Zhang, M., and Chan, D., *Toughening of a brittle thermosetting polymer: Effects of reinforcement particle size and volume fraction.* Journal of Materials Science, 2002. **37**(4): pp. 781-788.
[117] ASTM-International. *ASTM Int'l Approves Compression-After-Impact Standards*. 1995. Available from: http://www.ihs.com/news/2005/astm-compression-after-impact-standards.htm. Accessed 18th July 2013.
[118] Adams, D. *Testing Tech: Compression After Impact Testing*. 2007. Available from: http://www.compositesworld.com/articles/testing-tech-compression-after-impact-testing. Accessed
[119] Rio, T.G.D., Zaera, R., Barbero, E., and Navarro, C., *Damage in CFRPs due to low velocity impact at low temperature.* Composites Part B-Engineering, 2005. **36**(1): pp. 41-50.
[120] Heimbs, S., Heller, S., Middendorf, P., Hahnel, F., and Weisse, J., *Low velocity impact on CFRP plates with compressive preload: Test and modelling.* International Journal of Impact Engineering, 2009. **36**(10-11): pp. 1182-1193.
[121] Cantwell, W.J. and Morton, J., *Comparison of the Low and High-Velocity Impact Response of Cfrp.* Composites, 1989. **20**(6): pp. 545-551.
[122] Sutcliffe, M.P.F., Aceves, C.M., Stronge, W.J., Choudhry, R.S., and Scott, A.E., *Moderate speed impact damage to 2D-braided glass-carbon composites.* Composite Structures, 2012. **94**(5): pp. 1781-1792.
[123] Davies, G.A.O., Zhang, X., Zhou, G., and Watson, S., *Numerical Modeling of Impact Damage.* Composites, 1994. **25**(5): pp. 342-350.
[124] Recker, H.G., Altstadt, V., Eberle, W., Folda, T., Gerth, D., Heckmann, W., Ittemann, P., Tesch, H., and Weber, T., *Toughened Thermosets for Damage Tolerant Carbon-Fiber Reinforced Composites.* Advanced Materials : The Big Payoff, 1989. **21**: pp. 283-293.
[125] Kim, N. and Achenbach, J.D., *Quantitative characterization of multiple delaminations in laminated composites using the compton backscatter technique.* Journal of Nondestructive Evaluation, 1998. **17**(2): pp. 53-65.
[126] Aymerich, F. and Meili, S., *Ultrasonic evaluation of matrix damage in impacted composite laminates.* Composites Part B-Engineering, 2000. **31**(1): pp. 1-6.
[127] de Freitas, M., Silva, A., and Reis, L., *Numerical evaluation of failure mechanisms on composite specimens subjected to impact loading.* Composites Part B-Engineering, 2000. **31**(3): pp. 199-207.
[128] Aymerich, F., Pani, C., and Priolo, P., *Damage response of stitched cross-ply laminates under impact loadings.* Engineering Fracture Mechanics, 2007. **74**(4): pp. 500-514.
[129] Tan, K.T., Watanabe, N., and Iwahori, Y., *Effect of stitch density and stitch thread thickness on low-velocity impact damage of stitched composites.* Composites Part a-Applied Science and Manufacturing, 2010. **41**(12): pp. 1857-1868.

[130] Perrot, Y., Baley, C., Grohens, Y., and Davies, P., *Damage resistance of composites based on glass fibre reinforced low styrene emission resins for marine applications.* Applied Composite Materials, 2007. **14**(1): pp. 67-87.
[131] Appleby-Thomas, G.J., Hazell, P.J., and Dahini, G., *On the response of two commercially-important CFRP structures to multiple ice impacts.* Composite Structures, 2011. **93**(10): pp. 2619-2627.
[132] *ASTM D6264 / D6264M - 07 Standard Test Method for Measuring the Damage Resistance of a Fiber-Reinforced Polymer-Matrix Composite to a Concentrated Quasi-Static Indentation Force*. 2007, ASTM International.
[133] Wardle, B.L. and Lagace, P.A., *On the use of quasi-static testing to assess impact damage resistance of composite shell structures.* Mechanics of Composite Materials and Structures, 1998. **5**(1): pp. 103-121.
[134] Baucom, J.N. and Zikry, M.A., *Evolution of failure mechanisms in 2D and 3D woven composite systems under quasi-static perforation.* Journal of Composite Materials, 2003. **37**(18): pp. 1651-1674.
[135] Kwon, Y.S. and Sankar, B.V., *Indentation-Flexure and Low-Velocity Impact Damage in Graphite-Epoxy Laminates.* Journal of Composites Technology & Research, 1993. **15**(2): pp. 101-111.
[136] Kaczmarek, H. and Maison, S., *Comparative Ultrasonic Analysis of Damage in Cfrp under Static Indentation and Low-Velocity Impact.* Composites Science and Technology, 1994. **51**(1): pp. 11-26.
[137] Lee, S.M. and Zahuta, P., *Instrumented Impact and Static Indentation of Composites.* Journal of Composite Materials, 1991. **25**(2): pp. 204-222.
[138] Tan, K.T., Watanabe, N., Yoshimura, A., Iwahori, Y., and Ishikawa, T. *Progressive damage in stitched composites under impact loading* in 18th International conference on composite materials, 2011. South Korea.
[139] Tan, K.T., Yoshimura, A., Watanabe, N., Iwahori, Y., and Ishikawa, T., *Effect of stitch density and stitch thread thickness on damage progression and failure characteristics of stitched composites under out-of-plane loading.* Composites Science and Technology, 2013. **74**: pp. 194-204.
[140] Yokozeki, T., Kuroda, A., Yoshimura, A., Ogasawara, T., and Aoki, T., *Damage characterization in thin-ply composite laminates under out-of-plane transverse loadings.* Composite Structures, 2010. **93**(1): pp. 49-57.
[141] Olsson, R., *Mass criterion for wave controlled impact response of composite plates.* Composites Part a-Applied Science and Manufacturing, 2000. **31**(8): pp. 879-887.
[142] Sun, C.T. and Jih, C.J., *Quasi-Static Modeling of Delamination Crack-Propagation in Laminates Subjected to Low-Velocity Impact.* Composites Science and Technology, 1995. **54**(2): pp. 185-191.
[143] Abdallah, E.A., Bouvet, C., Rivallant, S., Broll, B., and Barrau, J.J., *Experimental analysis of damage creation and permanent indentation on highly oriented plates.* Composites Science and Technology, 2009. **69**(7-8): pp. 1238-1245.
[144] Symons, D.D., *Characterisation of indentation damage in 0/90 lay-up T300/914 CFRP.* Composites Science and Technology, 2000. **60**(3): pp. 391-401.
[145] Zhou, G. and Rivera, L.A., *Investigation on the reduction of in-plane compressive strength in thick preconditioned composite panels.* Journal of Composite Materials, 2007. **41**(16): pp. 1961-1994.

[146] de Freitas, M. and Reis, L., *Failure mechanisms on composite specimens subjected to compression after impact.* Composite Structures, 1998. **42**(4): pp. 365-373.
[147] Chen, P.H., Shen, Z., and Wang, J.Y., *A new method for compression after impact strength prediction of composite laminates.* Journal of Composite Materials, 2002. **36**(5): pp. 589-610.
[148] Sanchez-Saez, S., Barbero, E., and Navarro, C., *Compressive residual strength at low temperatures of composite laminates subjected to low-velocity impacts.* Composite Structures, 2008. **85**(3): pp. 226-232.
[149] Shivakumar, K.N. and Whitcomb, J.D., *Buckling of a Sublaminate in a Quasi-Isotropic Composite Laminate.* Journal of Composite Materials, 1985. **19**(1): pp. 2-18.
[150] Sztefek, P. and Olsson, R., *Nonlinear compressive stiffness in impacted composite laminates determined by an inverse method.* Composites Part a-Applied Science and Manufacturing, 2009. **40**(3): pp. 260-272.
[151] Yin, W.L., *The Effects of Laminated Structure on Delamination Buckling and Growth.* Journal of Composite Materials, 1988. **22**(6): pp. 502-517.
[152] Rhead, A.T., Butler, R., and Hunt, G.W., *Post-buckled propagation model for compressive fatigue of impact damaged laminates.* International Journal of Solids and Structures, 2008. **45**(16): pp. 4349-4361.
[153] Xiong, Y., Poon, C., Straznicky, P.V., and Vietinghoff, H., *A Prediction Method for the Compressive Strength of Impact Damaged Composite Laminates.* Composite Structures, 1995. **30**(4): pp. 357-367.
[154] Aktas, M., Karakuzu, R., and Arman, Y., *Compression-after impact behavior of laminated composite plates subjected to low velocity impact in high temperatures.* Composite Structures, 2009. **89**(1): pp. 77-82.
[155] Olsson, R., *Modelling of impact damage zones in composite laminates for strength after impact.* Aeronautical Journal, 2012. **116**(1186): pp. 1349-1365.
[156] Chai, H., Knauss, W.G., and Babcock, C.D., *Observation of Damage Growth in Compressively Loaded Laminates.* Experimental Mechanics, 1983. **23**(3): pp. 329-337.
[157] Yan, H., Oskay, C., Krishnan, A., and Xu, L.R., *Compression-after-impact response of woven fiber-reinforced composites.* Composites Science and Technology, 2010. **70**(14): pp. 2128-2136.
[158] Soutis, C. and Curtis, P.T., *Prediction of the post-impact compressive strength of CFRP laminated composites.* Composites Science and Technology, 1996. **56**(6): pp. 677-684.
[159] Pavier, M.J. and Clarke, M.P., *Experimental-Techniques for the Investigation of the Effects of Impact Damage on Carbon-Fiber Composites.* Composites Science and Technology, 1995. **55**(2): pp. 157-169.
[160] Berbinau, P., Soutis, C., and Guz, I.A., *Compressive failure of 0° unidirectional carbon-fibre-reinforced plastic (CFRP) laminates by fibre microbuckling.* Composites Science and Technology, 1999. **59**(9): pp. 1451-1455.
[161] Kyriakides, S., Arseculeratne, R., Perry, E.J., and Liechti, K.M., *On the Compressive Failure of Fiber-Reinforced Composites.* International Journal of Solids and Structures, 1995. **32**(6-7): pp. 689-738.

[162] Hahn, H.T. and Williams, J.G. *Compression failure mechanisms in unidirectional composites* in Composite Materials: Testing and Design (Seventh Conference), ASTM STP, 1986.
[163] Obdržálek, V. and Vrbka, J., *On Buckling of a Plate with Multiple Delaminations.* Engineering Mechanics, 2010. **17**(1): pp. 37-47.
[164] Hinton, M.J.E., Soden, P.D.E., and Kaddour, A.S.E., *Failure criteria in fibre-reinforced-polymer composites*. 1998: Elsevier.
[165] Orifici, A.C., Herszberg, I., and Thomson, R.S., *Review of methodologies for composite material modelling incorporating failure.* Composite Structures, 2008. **86**(1-3): pp. 194-210.
[166] Mishnaevsky, L. and Brondsted, P., *Micromechanical modeling of damage and fracture of unidirectional fiber reinforced composites: A review.* Computational Materials Science, 2009. **44**(4): pp. 1351-1359.
[167] Tsai, S.W. and Wu, E.M., *A general theory of strength for anisotropic materials.* Journal of Composite Materials, 1971. **5**(1): pp. 58-80.
[168] Tsai, S.W., *Theory of composites design*. 1992: Think composites Dayton.
[169] Kress, G., *Examination of Hashin's failure criteria for the second world-wide failure exercise.* Journal of Composite Materials, 2012. **46**(19-20): pp. 2539-2561.
[170] Kress, G., *Examination of Hashin's failure criteria for Part B of the second world-wide failure exercise: Comparison with test data.* Journal of Composite Materials, 2013. **47**(6-7): pp. 867-891.
[171] Hashin, Z., *Failure Criteria for Unidirectional Fiber Composites.* Journal of Applied Mechanics-Transactions of the Asme, 1980. **47**(2): pp. 329-334.
[172] Puck, A. and Schurmann, H., *Failure analysis of FRP laminates by means of physically based phenomenological models.* Composites Science and Technology, 1998. **58**(7): pp. 1045-1067.
[173] Soden, P.D., Hinton, M.J., and Kaddour, A.S., *A comparison of the predictive capabilities of current failure theories for composite laminates.* Composites Science and Technology, 1998. **58**(7): pp. 1225-1254.
[174] Hinton, M.J. and Kaddour, A.S., *The background to Part B of the Second World-Wide Failure Exercise: Evaluation of theories for predicting failure in polymer composite laminates under three-dimensional states of stress.* Journal of Composite Materials, 2013. **47**(6-7): pp. 643-652.
[175] Hinton, M.J. and Kaddour, A.S., *Triaxial test results for fibre-reinforced composites: The Second World-Wide Failure Exercise benchmark data.* Journal of Composite Materials, 2013. **47**(6-7): pp. 653-678.
[176] Hinton, M.J., Kaddour, A.S., and Soden, P.D., *A comparison of the predictive capabilities of current failure theories for composite laminates, judged against experimental evidence.* Composites Science and Technology, 2002. **62**(12-13): pp. 1725-1797.
[177] Hinton, M.J., Kaddour, A.S., and Soden, P.D., *Failure criteria in fibre reinforced polymer composites : the World-Wide Failure Exercise*. 2004, Amersterdam ; London: Elsevier.
[178] Hinton, M.J. and Soden, P.D., *Predicting failure in composite laminates: The background to the exercise.* Composites Science and Technology, 1998. **58**(7): pp. 1001-1010.
[179] Rybicki, E.F. and Kanninen, M.F., *Finite-Element Calculation of Stress Intensity Factors by a Modified Crack Closure Integral.* Engineering Fracture Mechanics, 1977. **9**(4): pp. 931-938.

[180] Wisnom, M.R., *Modelling discrete failures in composites with interface elements.* Composites Part a-Applied Science and Manufacturing, 2010. **41**(7): pp. 795-805.
[181] Park, K. and Paulino, G.H., *Cohesive Zone Models: A Critical Review of Traction-Separation Relationships Across Fracture Surfaces.* Applied Mechanics Reviews, 2011. **64**(6).
[182] Benzeggagh, M.L. and Kenane, M., *Measurement of mixed-mode delamination fracture toughness of unidirectional glass/epoxy composites with mixed-mode bending apparatus.* Composites Science and Technology, 1996. **56**(4): pp. 439-449.
[183] Song, K., Dávila, C.G., and Rose, C.A. *Guidelines and parameter selection for the simulation of progressive delamination*.
[184] Suemasu, H., Sasaki, W., Ishikawa, T., and Aoki, Y., *A numerical study on compressive behavior of composite plates with multiple circular delaminations considering delamination propagation.* Composites Science and Technology, 2008. **68**(12): pp. 2562-2567.
[185] Rhead, A.T. and Butler, R., *Compressive static strength model for impact damaged laminates.* Composites Science and Technology, 2009. **69**(14): pp. 2301-2307.
[186] Aoki, Y., Kondo, H., and Hatta, H., *Effect of delamination propagation on mechanical behavior in compression after impact*, in *16th International Conference on Composite Materials*. 2007.
[187] Soden, P.D., Hinton, M.J., and Kaddour, A.S., *Lamina properties, lay-up configurations and loading conditions for a range of fibre-reinforced composite laminates.* Composites Science and Technology, 1998. **58**(7): pp. 1011-1022.
[188] Suemasu, H., Sasaki, W., Aoki, Y., and Ishikawa, T. *Compressive behavior of impact damaged composite laminates* in 16th International Conference on Composite Materials, 2007. Kyoto, Japan.
[189] Melin, L.G. and Schon, J., *Buckling behaviour and delamination growth in impacted composite specimens under fatigue load: an experimental study.* Composites Science and Technology, 2001. **61**(13): pp. 1841-1852.
[190] Hwang, S.F. and Liu, G.H., *Buckling behavior of composite laminates with multiple delaminations under uniaxial compression.* Composite Structures, 2001. **53**(2): pp. 235-243.
[191] Rhead, A.T., Butler, R., and Baker, N., *Analysis and Compression Testing of Laminates Optimised for Damage Tolerance.* Applied Composite Materials, 2011. **18**(1): pp. 85-100.
[192] Williams, F.W., Kennedy, D., Butler, R., and Anderson, M.S., *Viconopt - Program for Exact Vibration and Buckling Analysis or Design of Prismatic Plate Assemblies.* Aiaa Journal, 1991. **29**(11): pp. 1927-1928.
[193] Nilsson, K.F., Asp, L.E., Alpman, J.E., and Nystedt, L., *Delamination buckling and growth for delaminations at different depths in a slender composite panel.* International Journal of Solids and Structures, 2001. **38**(17): pp. 3039-3071.
[194] Chai, H. and Babcock, C.D., *Two-Dimensional Modeling of Compressive Failure in Delaminated Laminates.* Journal of Composite Materials, 1985. **19**(1): pp. 67-98.

[195] Kardomateas, G.A., *The Initial Postbuckling and Growth-Behavior of Internal Delaminations in Composite Plates.* Journal of Applied Mechanics-Transactions of the Asme, 1993. **60**(4): pp. 903-910.
[196] Hounsfield, G.N., *Computerized transverse axial scanning (tomography): Part 1. Description of system.* British Journal of Radiology, 1973. **46**(552): pp. 1016-1022.
[197] Baruchel, J., Buffiere, J.-Y., and Maire, E., *X-ray tomography in material science.* 2000.
[198] Maire, E., Buffiere, J.Y., Salvo, L., Blandin, J.J., Ludwig, W., and Letang, J.M., *On the application of X-ray microtomography in the field of materials science.* Advanced Engineering Materials, 2001. **3**(8): pp. 539-546.
[199] Kak, A.C., *Computerized Tomography with X-Ray, Emission, and Ultrasound Sources.* Proceedings of the Ieee, 1979. **67**(9): pp. 1245-1272.
[200] Ritman, E.L., *Micro-computed tomography-current status and developments.* Annual Review of Biomedical Engineering, 2004. **6**: pp. 185-208.
[201] Brooks, R.A. and Dichiro, G., *Theory of Image Reconstruction in Computed Tomography.* Radiology, 1975. **117**(3): pp. 561-572.
[202] Stock, S.R., *Microcomputed tomography: methodology and applications*. 2010: CRC press.
[203] Baruchel, J., Buffiere, J.Y., Cloetens, P., Di Michiel, M., Ferrie, E., Ludwig, W., Maire, E., and Salvo, L., *Advances in synchrotron radiation microtomography.* Scripta Materialia, 2006. **55**(1): pp. 41-46.
[204] Helfen, L., Morgeneyer, T.F., Xu, F., Mavrogordato, M.N., Sinclair, I., Schillinger, B., and Baumbach, T., *Synchrotron and neutron laminography for three-dimensional imaging of devices and flat material specimens.* International Journal of Materials Research, 2012. **103**(2): pp. 170-173.
[205] Helfen, L., Myagotin, A., Rack, A., Pernot, P., Mikulik, P., Di Michiel, M., and Baumbach, T., *Synchrotron-radiation computed laminography for high-resolution three-dimensional imaging of flat devices.* Physica Status Solidi a-Applications and Materials Science, 2007. **204**(8): pp. 2760-2765.
[206] Barrett, J.F. and Keat, N., *Artifacts in CT: Recognition and avoidance.* Radiographics, 2004. **24**(6): pp. 1679-1691.
[207] Meganck, J.A., Kozloff, K.M., Thornton, M.M., Broski, S.M., and Goldstein, S.A., *Beam hardening artifacts in micro-computed tomography scanning can be reduced by X-ray beam filtration and the resulting images can be used to accurately measure BMD.* Bone, 2009. **45**(6): pp. 1104-1116.
[208] Archer, E., King, S, Quinn, JP, Buchanan, S and McIlhagger. *Impact damage analysis of 3D woven carbon fibre composites using computed tomography* in 18th international conference on composite materials, 2011. South Korea: The Korean society for composite materials.
[209] Tan, K.T., Watanabe, N., and Iwahori, Y., *X-ray radiography and micro-computed tomography examination of damage characteristics in stitched composites subjected to impact loading.* Composites Part B-Engineering, 2011. **42**(4): pp. 874-884.
[210] Crupi, V., Epasto, G., and Guglielmino, E., *Computed Tomography analysis of damage in composites subjected to impact loading.* V. Crupi et alii, Frattura ed Integrità Strutturale, 2011. **17**: pp. 32-41.
[211] Schilling, P.J., Karedla, B.P.R., Tatiparthi, A.K., Verges, M.A., and Herrington, P.D., *X-ray computed microtomography of internal damage in*

fiber reinforced polymer matrix composites. Composites Science and Technology, 2005. **65**(14): pp. 2071-2078.
[212] Hufenbach, W., Böhm, R., Gude, M., Berthel, M., Hornig, A., Ručevskis, S., and Andrich, M., *A test device for damage characterisation of composites based on in situ computed tomography.* Composites Science and Technology, 2012. **72**(12): pp. 1361-1367.
[213] Sket, F., Seltzer, R., Molina-Aldareguia, J.M., Gonzalez, C., and LLorca, J., *Determination of damage micromechanisms and fracture resistance of glass fiber/epoxy cross-ply laminate by means of X-ray computed microtomography.* Composites Science and Technology, 2012. **72**(2): pp. 350-359.
[214] Lambert, J., Chambers, A.R., Sinclair, I., and Spearing, S.M., *3D damage characterisation and the role of voids in the fatigue of wind turbine blade materials.* Composites Science and Technology, 2012. **72**(2): pp. 337-343.
[215] Xu, F., Helfen, L., Moffat, A.J., Johnson, G., Sinclair, I., and Baumbach, T., *Synchrotron radiation computed laminography for polymer composite failure studies.* Journal of Synchrotron Radiation, 2010. **17**: pp. 222-226.
[216] Scott, A.E., Mavrogordato, M., Wright, P., Sinclair, I., and Spearing, S.M., *In situ fibre fracture measurement in carbon-epoxy laminates using high resolution computed tomography.* Composites Science and Technology, 2011. **71**(12): pp. 1471-1477.
[217] Moffat, A.J., Wright, P., Buffiere, J.Y., Sinclair, I., and Spearing, S.M., *Micromechanisms of damage in 0 degrees splits in a [90/0](s) composite material using synchrotron radiation computed tomography.* Scripta Materialia, 2008. **59**(10): pp. 1043-1046.
[218] Muller, B.R., Lange, A., Harwardt, M., Hentschel, M.P., Illerhaus, B., Goebbels, J., Bamberg, J., and Heutling, F., *Synchrotron-Refraction-Computed-Tomography for NDT and characterisation of lightweight composite materials.* Emerging Technologies in Non-Destructive Testing, 2008: pp. 217-221.
[219] Yoshimura, A., Nakao, T., Yashiro, S., and Takeda, N., *Improvement on out-of-plane impact resistance of CFRP laminates due to through-the-thickness stitching.* Composites Part a-Applied Science and Manufacturing, 2008. **39**(9): pp. 1370-1379.
[220] Moffat, A.J., Wright, P., Helfen, L., Baumbach, T., Johnson, G., Spearing, S.M., and Sinclair, I., *In situ synchrotron computed laminography of damage in carbon fibre-epoxy [90/0](s) laminates.* Scripta Materialia, 2010. **62**(2): pp. 97-100.
[221] Buffiere, J.Y., Maire, E., Adrien, J., Masse, J.P., and Boller, E., *In Situ Experiments with X ray Tomography: an Attractive Tool for Experimental Mechanics.* Experimental Mechanics, 2010. **50**(3): pp. 289-305.
[222] Maire, E. and Withers, P.J., *Quantitative X-ray tomography.* International Materials Reviews, 2014. **59**(1): pp. 1-43.

Chapter 3

Experimental materials and methods

This chapter presents details of the materials and experimental procedures used in this thesis. To avoid repetition describing the experimental procedures used in the technical chapters, sections contained in this chapter are referred to for further details.

3.1 Materials

Two laminate thicknesses were used in this thesis corresponding to ~1 mm and ~4.5 mm. The use of 1 mm thick specimens was driven by laminography work which has been found in previous trials to perform well with 1 mm thick carbon fibre plates [1]. The thicker (4.5 mm) laminates were used to conform to ASTM D7136M [2] and ASTM D7137M [3] standards for impact and subsequent compression testing respectively. In all cases, proprietary unidirectional carbon fibre prepreg provided by Cytec was used. These were stacked in a quasi-isotropic layup (see below) and cured in an autoclave according to the manufacturer's specifications. All test coupons were subjected to an ultrasonic C-scan to check for manufacturing defects and damage. The C-scan equipment enabled defects (delaminations and groups of voids) larger than 1x1 mm to be detected. Coupons containing any detected defects were rejected.

3.1.1 Test coupons - 1 mm thick

Unidirectional carbon fibre prepreg material with an 8 ply quasi-isotropic $[45/0/-45/90]_S$ layup was used to form coupons with an approximate thickness of 1 mm. Two resin systems were manufactured encompassing a proprietary particle-toughened

and an untoughened matrix system (Cytec Engineered Materials Ltd). The former system incorporated thermoplastic particles within the epoxy matrix that were concentrated at the interface of the prepreg. For direct comparison, the untoughened system used the same intermediate modulus carbon fibre and base resin as the particle-toughened system and the same fibre to matrix (resin plus particles) ratio by weight were used. Plates were laid up and cured in an autoclave using an aerospace industry-standard cure cycle before being cut to 80 x 80 mm test coupons.

3.1.2 Test coupons - 4.5 mm thick

Five proprietary unidirectional carbon fibre prepreg material systems were manufactured for use in these studies. These systems used a different resin and particle system to that of the 1 mm thick test coupons. These materials encompassed one untoughened epoxy system (UT) without particles and four particle-toughened systems (T1-T4), labelled in order of damage resistance (T1 being the least damage resistant and T4 the most, as measured by ultrasonic C-scan of the projected damage areas after impact). For the particle-toughened systems, thermoplastic particles were introduced to the base epoxy resin to form the matrix. Different particles (particle size and chemistry) were used in each of the particle-toughened systems and the same base resin was used across all five systems. Across all systems, the same fibre to matrix ratio by weight was used. For the particle systems the same ratio of particles to resin by weight was used to form the matrix. The same intermediate modulus fibre type was used in all five cases. The mode II fracture toughness supplied by the manufacturer was normalised by dividing the corresponding fracture toughness by the system with the largest fracture toughness. This led to normalised mode II fracture toughness values for the UT, T1, T2, T3 and T4 systems of 0.4, 0.8, 0.3, 0.6 and 1 respectively. These toughness values are of the composite system with the matrix.

For each material system, ASTM D7136M standard panels were manufactured consisting of a 24 ply layup with a $[45/0/-45/90]_{3S}$ stacking sequence. Panels were vacuum-bagged and fully cured under pressure in an autoclave to the

manufacturer's specifications. Panel thickness was approximately 4.5 mm ±0.2 mm across the systems tested. Panels were cut using a water jet followed by end milling on a CNC machine to create test coupons measuring 100 x 150 mm to within the tolerances of D7136M.

3.2 Instrumented Impact testing

Impact tests were performed in general accordance with the ASTM D7136M standard for the 4.5 mm thick test coupons [2]. However to perform tests on the thinner 1 mm samples, a non-standard base plate was used, shown later. Instrumented tests were not carried out on 1 mm specimens but were performed on the thicker 4.5 mm samples; this was due to instrumentation hardware being added later on in the project.

3.2.1 Impact apparatus

A steel drop weight indenter guided by two vertical rails was built by the author and used to impact carbon fibre test coupons. A 4.9 kg, 16 mm diameter hemispherical impactor (tup), with a hardness between 60 and 62 HRC, was set to a predetermined height to achieve the desired impact energy, see Figure 3.1. After the impact event, the crosshead was caught on the rebound preventing multiple strikes.

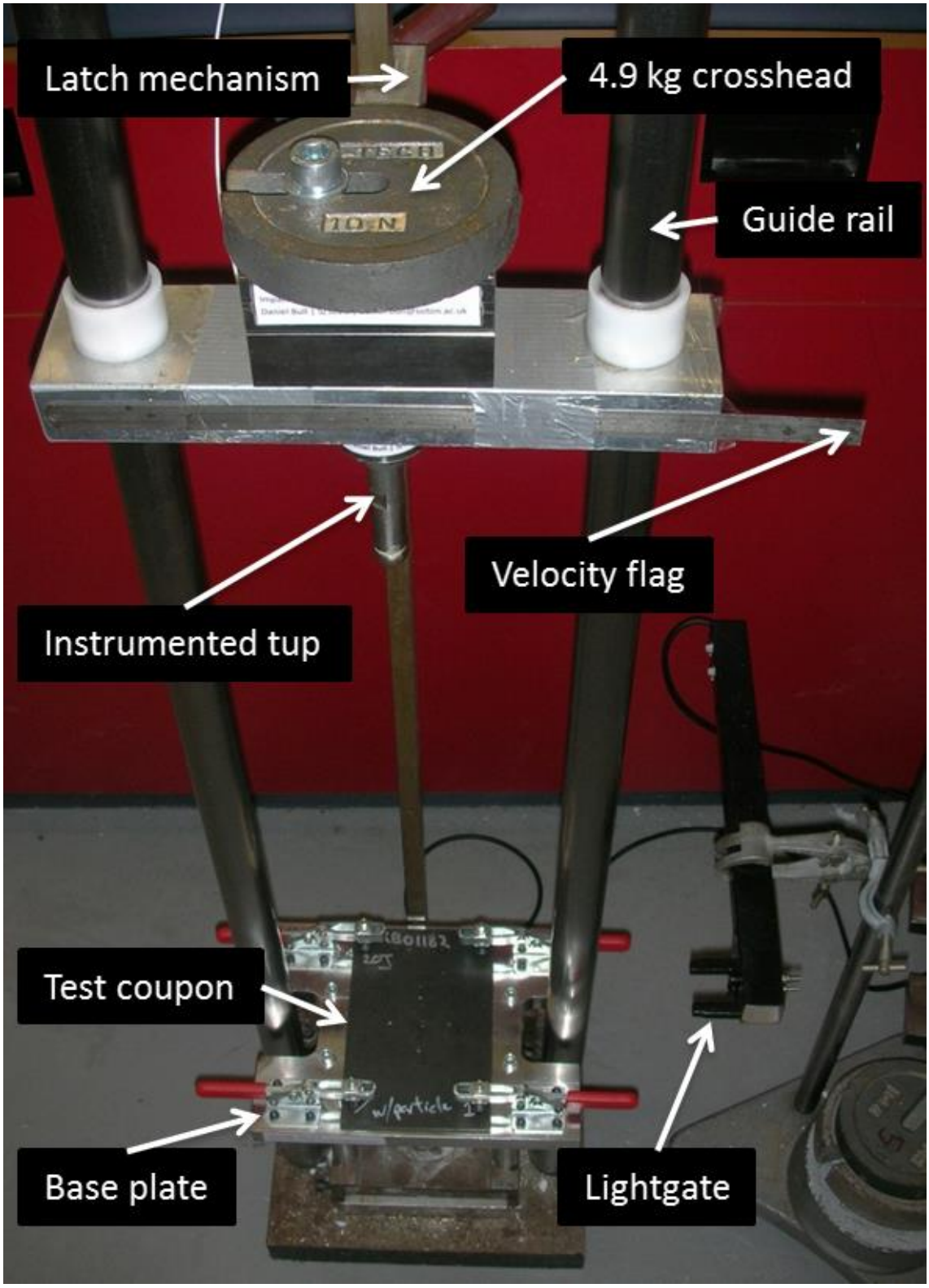

Figure 3.1: Impact testing apparatus.

Two base plates were used to accommodate both specimen geometries. For the 1 mm thick coupons, a non-standard base plate was used encompassing a 60 mm

diameter hole over which the coupon was loosely clamped using a ring of the same diameter. This is of a similar setup (base plate and impact conditions) to another study which performed impacts on 1 mm thick coupons [4]. The 4.5 mm specimens used a standard base plate with a rectangular window measuring 125 x 75 mm with four toggle clamps at the corners providing a loose support for the specimen in accordance to the ASTM standard.

To capture the velocity of impact, a combination of a 10 mm wide flag and a lightgate circuit was used. This was positioned so the circuit was triggered when the tup was between 3.0 and 6.0 mm above the coupon, in accordance with the standard. The lightgate was wired to a control circuit which sent a 5 V signal to an Arduino Uno microcontroller used to measure the impact and rebound velocity when it was interrupted. At the same time, the microcontroller also sent a 5 V trigger signal to the data-acquisition (DAQ) hardware to start capturing the data as shown in Figure 3.2. A flowchart describing the signal chain is shown in Figure 3.3.

A piezoelectric load cell with a working compressive range of 22 kN was connected within the impact loading chain. The positioning of the load cell ensured that at least 95 % of the impactor mass was located above it. The load cell was connected to an amplifier and one of the channels on the DAQ card shown in Figure 3.2. Data-acquisition from the impact event was captured using a sample rate of 100 kHz to ensure the entire impact event was recorded with at least 100 data points.

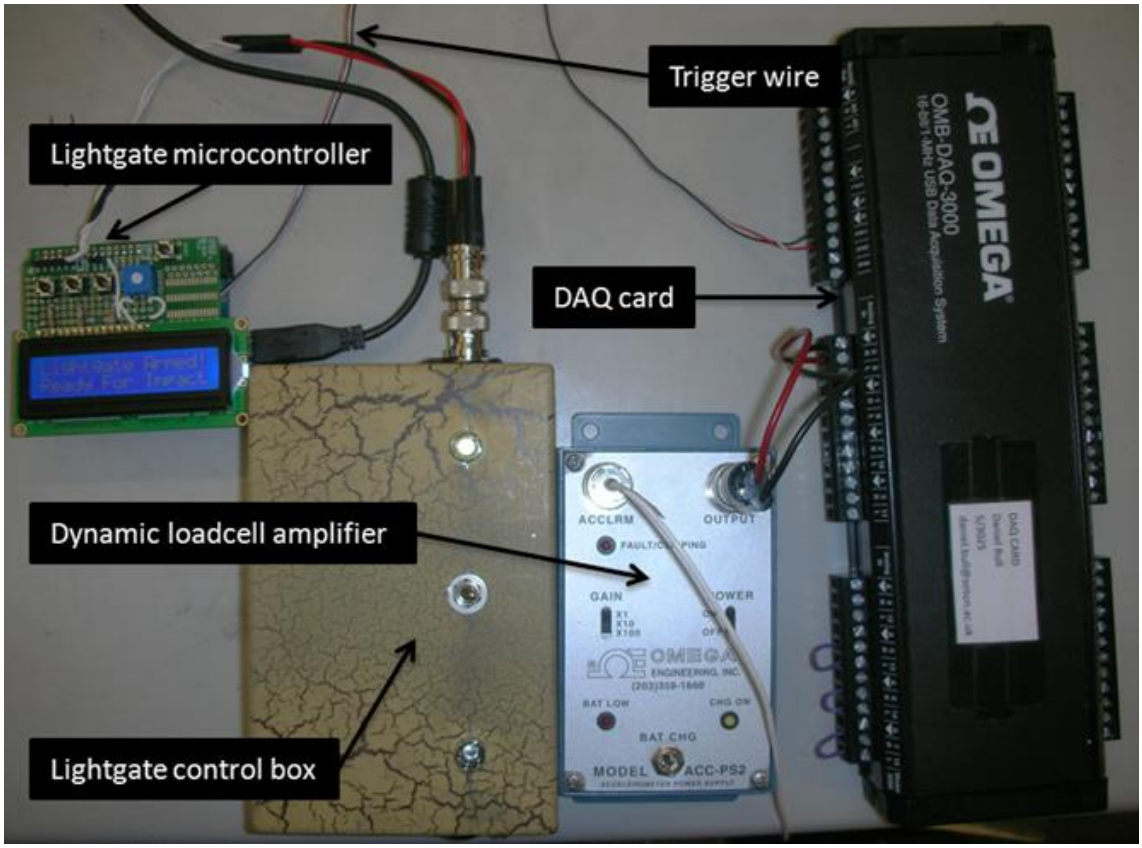

Figure 3.2: Instrumentation hardware and setup.

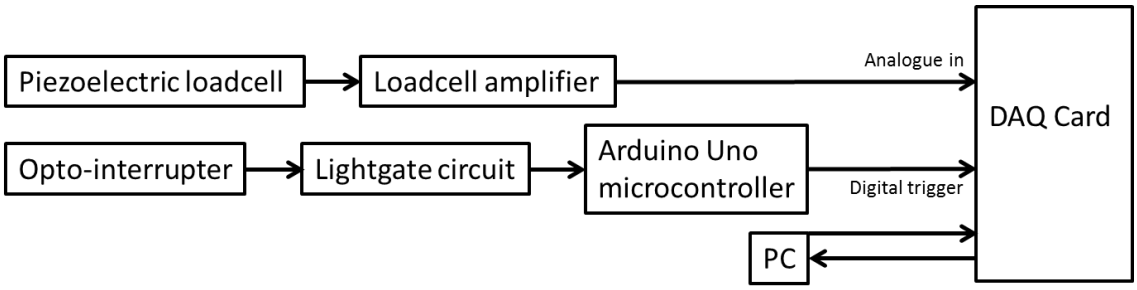

Figure 3.3: Flowchart of drop tower instrumentation.

3.2.2 Impact test procedure

Coupons were loosely clamped onto their respective support fixtures. The impact device was then prepared to the required drop height to create the desired impact energy according to simple gravitational potential energy equations.

The impactor was released so that out-of-plane impact occurred at the centre of the coupon. Information recorded from the load cell consisted of force-time data that was combined with the initial velocity calculated from the lightgate and the

mass of the impactor, *m*. This information in accordance to the ASTM standard was used to derive displacement, velocity, acceleration and energy as a function of time using equations (3-1) to (3-5) allowing any combination of these to be plotted against each other. A Matlab code was created to achieve this.

Impact velocity

$$v_i = \frac{W_{12}}{(t_2 - t_1)} + g\left(t_i - \frac{(t_1 + t_2)}{2}\right) \tag{3-1}$$

Impactor displacement vs. time

$$\delta(t) = \delta_i + v_i t + \frac{gt^2}{2} - \int_0^t \left(\int_0^t \frac{F(t)}{m} dt \right) \tag{3-2}$$

Impactor velocity vs. time

$$v(t) = v_i + gt - \int_0^t \frac{F(t)}{m} dt \tag{3-3}$$

Impactor acceleration vs. time

$$a(t) = \frac{F(t)}{m} \tag{3-4}$$

Absorbed Energy vs. time

$$E_a(t) = \frac{m(v_i^2 - v(t)^2)}{2} + mg\delta(t) \tag{3-5}$$

where v_i is the impact velocity of the impactor as it makes first contact with the test coupon, W_{12} is the distance between leading edges of the first (lower) and second (upper) flag prongs, t_1 is the time the first (lower) flag prong passes the lightgate detector, t_2 is the time the second (upper) flag prong passes the lightgate detector, t_i is the time of initial contact obtained from the force-time curve, t is the time during the test in which $t = 0$ is the time when the impactor first made contact with the test coupon. $F(t)$ is the force measured from the dynamic load cell as a function of time, δ_i is the impactor displacement from the reference location at

$t = 0$, δ is the impactor displacement at time t, a is the acceleration of the impactor, and E_a is the absorbed energy at time t.

After impact, the dent depth and the projected C-scan damage area of the coupons was measured. This was achieved using a TaiCaan laser profilometer (see section 3.6), and ultrasonic C-scan (see section 3.5) for the respective testing procedures.

3.3 Compression-after-impact testing

There are two procedures of the compression-after-impact (CAI) test method used in this work. The first follows the ASTM D7137 [3] standard, in which impacted plates were subjected to quasi-static in-plane compression until failure. The second used a modified mechanical compression frame to apply stepped loads for *ex situ* µCT experiments.

3.3.1 Compression apparatus

A compression support fixture shown in Figure 3.4 was used as an anti-buckling guide to support the sample when loaded. The side supports encompassed knife-edges to prevent global buckling, as per ASTM D7137M. The top and bottom side supports were square and provided no clamping forces, but enabled some rotational restraint due to the fixture geometry.

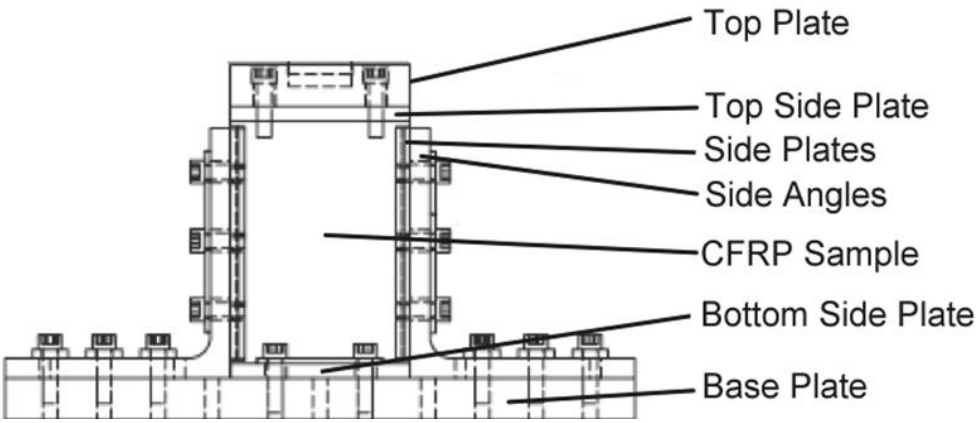

Figure 3.4: Anti-buckling compression support fixture.

To perform conventional compression tests, a standard servo-hydraulic testing machine was used (Instron 8800 series). The machine applied a continuous load at a speed of 1.25 mm/min (displacement control). For *ex situ* CT work, a custom-built compression frame was used, see Figure 3.5 allowing loads to be applied at various incremental steps.

In both continuous and incrementally-stepped load testing conditions, a load cell measured the total force being carried by the test coupon with the critical failure load reported, and position was recorded via a linear variable displacement transducer (LVDT).

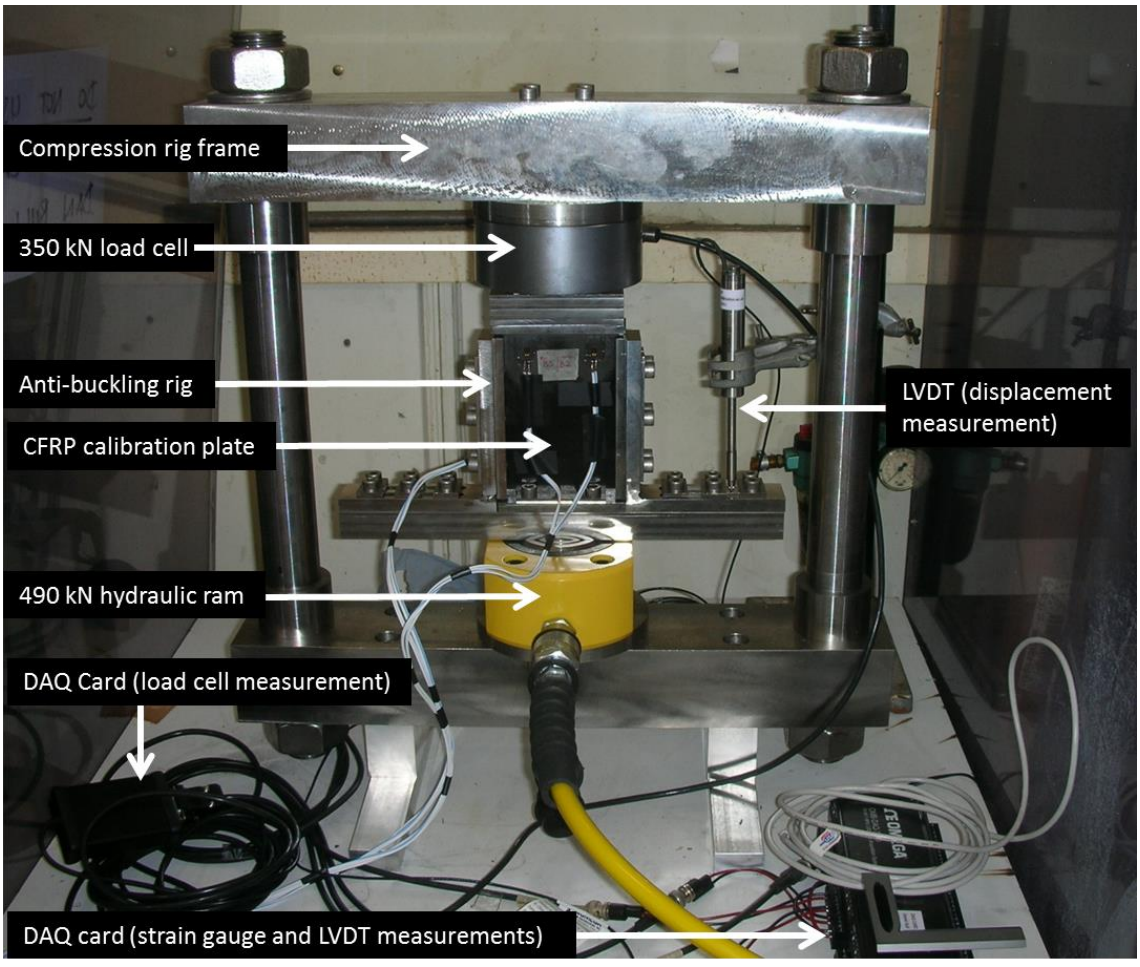

Figure 3.5: Compression frame used to apply stepped loads for *ex situ* µCT work.

To ensure the anti-buckling guide was set up correctly, a calibration plate with four strain gauges was used. This ensured the anti-buckling guide was set up to

minimise the amount of bending being introduced onto the test coupon. The calibration plate was made from the untoughened material system with the strain gauges positioned at two locations on each side as shown in Figure 3.6, orientated in the 0° direction. Calibration plates were placed in the anti-buckling guide and loaded to 450 N. The misalignment was characterised by calculating the "percentage bending" on the plates by comparing the average back-to-back strain values using equation (3-6), where ϵ_1 is the indicated strain of the gauge on one of the faces, and ϵ_2 is the indicated strain on the opposite face. If the percentage bending was less than 10 %, the calibration plate was swapped with the test coupon and the full CAI test performed. A percentage bending over 10 % required re-examination and realignment of the fixture in accordance with the ASTM standard [3].

$$B_y = Percent\ Bending = \frac{\epsilon_1 - \epsilon_2}{\epsilon_1 + \epsilon_2} \cdot 100 \tag{3-6}$$

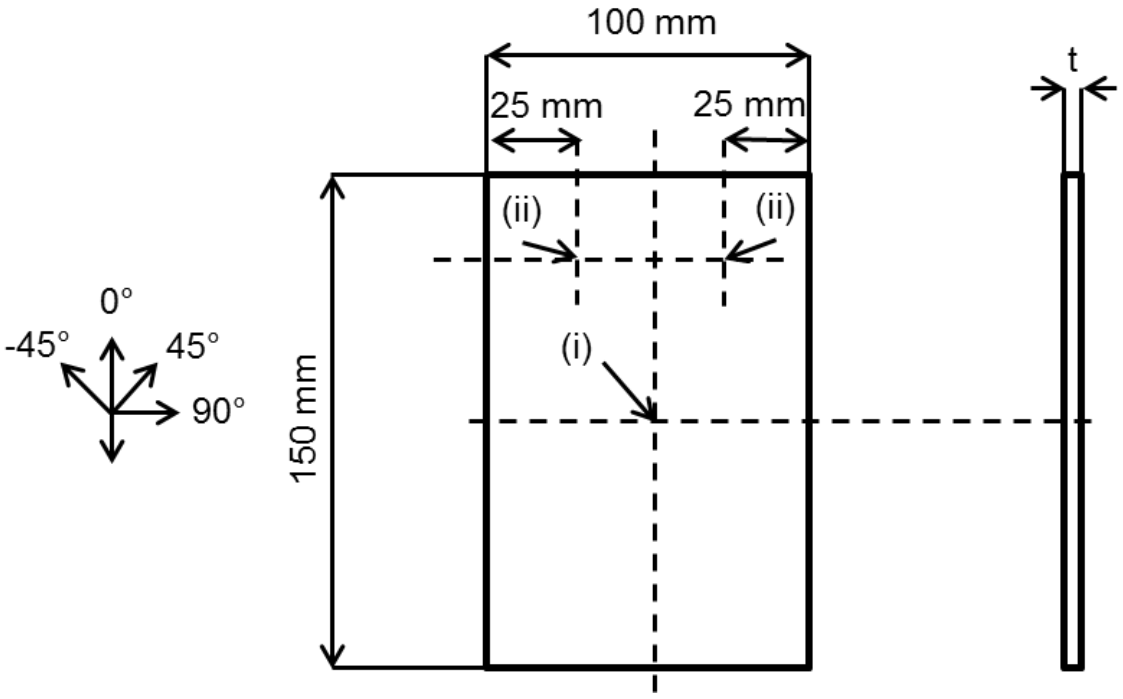

Figure 3.6: Diagram of CFRP coupon to be tested; (i) represents the impact point and (ii) represents the locations of the strain gauges for the calibration plate.

3.3.2 Compression-after-impact test procedure

Prior to testing, the thickness and width of the coupon was measured at five locations using callipers to determine the average cross-sectional area. Coupons were then placed in the anti-buckling guide and positioned between two flat platens. The test was started and concluded once the coupon reached critical compression failure (>50 % loss in peak load). After the coupon was loaded to failure, it was removed from the anti-buckling guide and checked for a valid failure mode; non-acceptable failure modes include end-crushing and edge-restrained delamination growth. The ultimate compressive residual strength of the coupon was calculated using equation (3-7):

$$\sigma^{CAI} = \frac{F_{max}}{A} \tag{3-7}$$

where σ^{CAI} is the ultimate compressive residual strength (MPa), F_{max} is the maximum force reached during the test (N), and A is the cross-sectional area calculated by $t \cdot w$ (mm^2), t being the average thickness and w the average width of the material.

3.4 Quasi-static indentation testing

Quasi-static indentation testing was undertaken in accordance to the ASTM D6264M [5] standard on the 150 x 100 x 4.5 mm coupons. The same rectangular base plate (125 x 75 mm) and indenter tup geometry (16 mm hemispherical) as in section 3.2.1 was used. Coupons were loosely clamped to the centre of the baseplate which was secured to the base of a mechanical testing machine. An out-of-plane displacement was applied to the centre of the coupon with a cross head displacement speed of 2 mm-min^{-1}. Force-displacement data were recorded during the loading stages of the test. Interrupted tests were performed on the coupons at increasing out-of-plane nominal displacements of 2, 2.5, 3, 4 and 5 mm using the same coupon on each material system. Since each subsequent loading step was applied by positioning the tup to make initial contact with the coupon, the total displacement reported took into account the offset by the dent measured immediately prior to the subsequent loading stage. After each

loading step, C-scan, dent depth and µCT was performed. This process was repeated on three samples of each material system in the case of C-scan and dent depth measurements. Due to time constraints, µCT scans of the incremental loading process were conducted with no repeats and were carried out on all material systems with the exception of T2.

3.5 Ultrasonic C-scan

Ultrasonic C-scanning was used to check for manufacturing defects and to measure the projected damage area. A 5 MHz probe was used with signal gains set to 14 dB and 26 dB for the 1 mm and 4.5 mm thick coupons respectively. Figure 3.7 represents schematically the setup used to scan the coupons. A tank containing deionised water was used to couple the signal to and from the ultrasonic probe. The coupon was placed on a standoff, *i.e.* on Perspex blocks 50 mm above a glass sheet. In this setup, a double through-transmission method was used. The glass sheet reflected the ultrasonic signal causing it to travel through the coupon twice. Should the coupon contain voids or delaminations (air), the reflected signal would be heavily attenuated with a reduction in amplitude, enabling the presence of a defect to be detected [6].

Figure 3.8 shows a comparison of two A-scans (ultrasound measurements) at two specific locations consisting of; (a) the probe over an undamaged coupon and (b) over a damaged coupon. The Y-axis represents signal amplitude and X-axis represents the time of the reflections relative to the initial pulse sent from the probe. Highlighted at (i) is the main signal reflection off the surface of the coupon. At (ii), the reflected signal that has passed through the coupon, reflected off the glass, and then passed through the coupon a second time, is detected on the probe. Should this signal pass through a damaged region in the coupon, it is attenuated as shown in (iii). The remaining peaks detected by the probe represent reflections off the bottom of the tank, and secondary reflections.

To capture the attenuated regions representing damage, gates are applied both to the main reflection (i) and the reflection off the glass (ii) in order to detect the amplitude of these signals. During a C-scan, the probe is moved through a predetermined path over the coupon along the X and Y axes, capturing the

attenuation at these gates. This ultimately produces a projected damage area of the coupon as an image. In this work the X-Y measurements of the equipment had a resolution of approximately 1 mm. ImageJ ^{TM} software was used to measure the projected damage area.

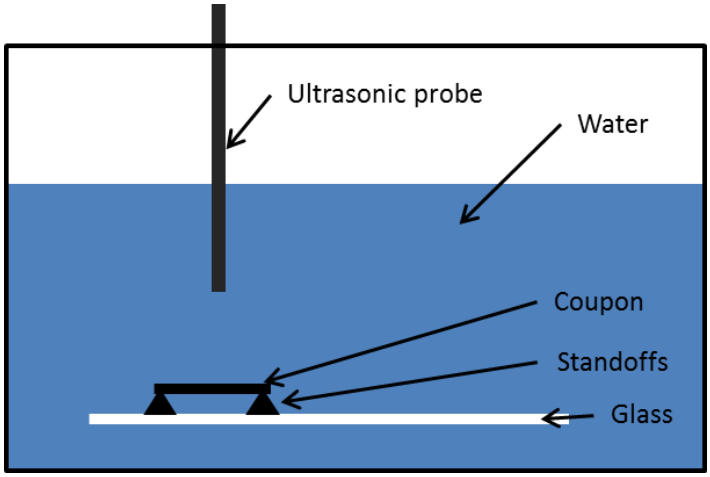

Figure 3.7: Ultrasonic C-scan setup.

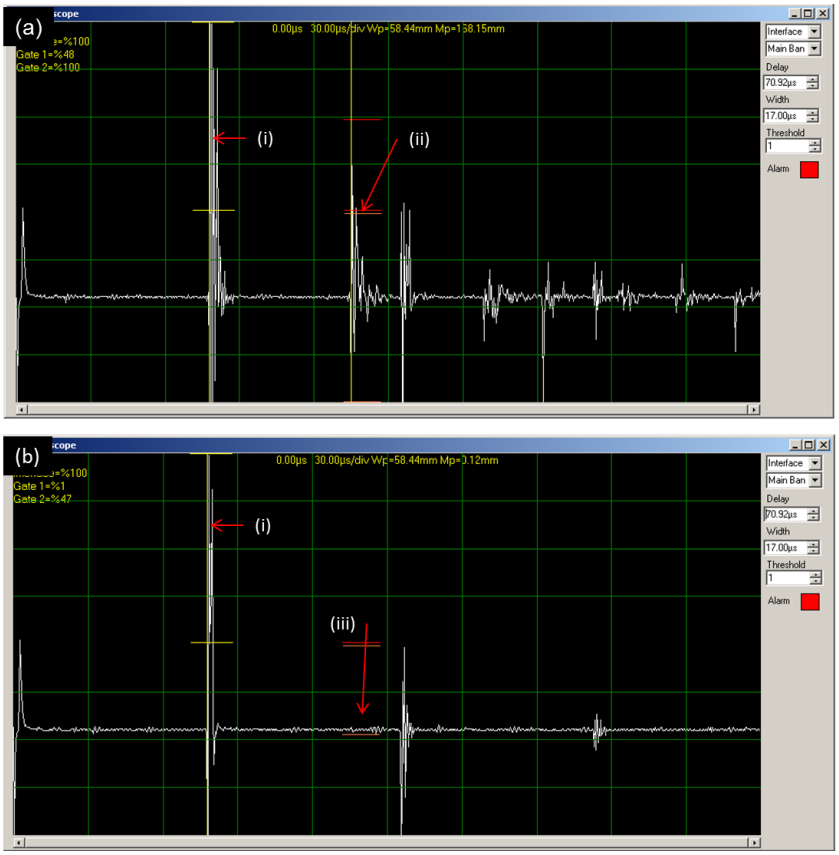

Figure 3.8: A-scan signal representing the position of the probe over (a) an undamaged and (b) a damaged region of the coupon. Y-axis indicates amplitude of reflected signals detected by the probe, and x-axis represents time of reflected signals.

3.6 Dent depth measurements

ASTM methods [2] to measure dent depth required use of a mechanical dial gauge that made physical contact on the coupon. From experience it was fairly difficult to achieve repeatable measurements with this technique due to the surface roughness caused by the material peel ply. To avoid these issues, a Tai-Caan Xyris 4000 confocal laser surface profilometer was used to obtain a non-contact measurement of the dent depth as shown in Figure 3.9. A 20 mm thick stainless steel block with a 60 mm diameter window was used to mount the specimen allowing it to sit reasonably flat despite the presence of back-face protrusions in some cases. A 30 x 30 mm region across the impact crater was scanned using 201 x 201 data samples, *i.e.* ~150 µm in-plane spacing, a depth resolution of 0.1 µm and a measurement spot size of ~2 µm diameter. After scanning, BODDIES ^{TM} software [7] was used to create a reference plane of the surface of the material that was used as a datum point for measuring the depth of the dent.

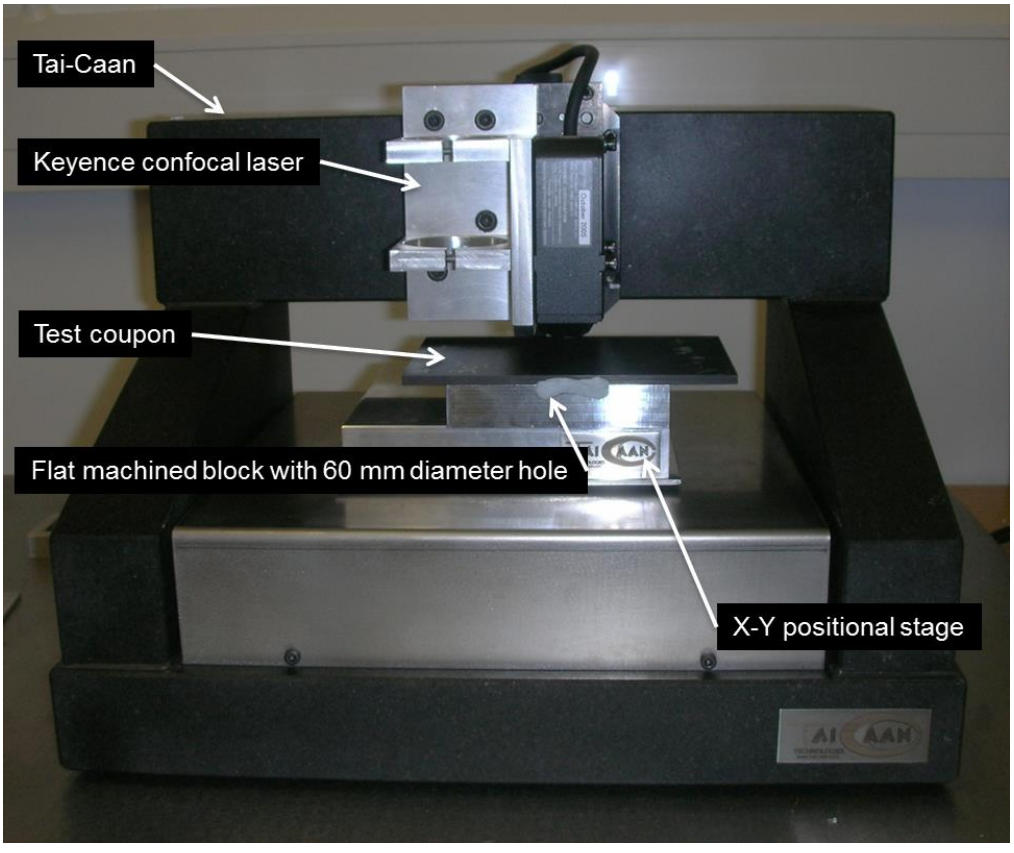

Figure 3.9: Tai-Caan surface profilometer setup.

3.7 Optical microscopy

In some cases, cross-sections of material were studied using standard optical microscopy. To achieve this, regions of interests approximately 4.5 x 4.5 x 20 mm were cut using a low speed diamond cutting wheel (Struers Minitom) to minimise sectioning damage. These were then cold-mounted in epoxy and polished via standard materialographic methods and imaged on an Olympus BX51 microscope.

3.8 3D X-ray tomography

3D X-ray tomography was used extensively in this project allowing internal damage at multiple scales to be detected. Three specific methods were used: synchrotron radiation computed tomography (SRCT), synchrotron radiation computed laminography (SRCL) and micro-focus computed tomography (µCT). All three techniques followed essentially identical principles of collecting multiple radiographs at different angles of rotation and reconstructing these to form a 3D volume.

3.8.1 Micro-focus CT

Micro-focus CT scans were carried out at the University of Southampton µVIS Centre using Benchtop and HMX facilities. A simplified µCT layout is shown in Figure 3.10 consisting of a micro-focus X-ray source, created by a focused electron beam hitting a molybdenum target, a manipulator that rotates the sample through 360°, and a digital X-ray detector. As the object rotates, a sequence of 2D X-ray radiographs is collected at the detector. Filtered back-projection (FBP) was then performed on these radiographs to reconstruct a 3D volume; this was achieved using CT-Pro software. The cone beam geometry allowed the voxel size to be increased by bringing the object closer to the source, however by doing so, the field of view decreases.

To achieve the highest resolution scans, regions of interest are typically cut from the coupons forming ‘matchsticks’ with square cross-sections. This is to achieve a better scanning geometry [8], allowing the object to be positioned closer to the X-

ray source, achieving usable spatial resolutions down to ~3 µm (reflection X-ray source) or ~1 µm (transmission X-ray source). This technique was performed on 1 mm thick coupons to capture the entire damage area; the schematic diagram in Figure 3.11 describes how this was achieved. Approximately 4 mm wide strips were cut along the coupon across the damage area to form matchsticks. These matchsticks were stacked together and several µCT scans were performed along the length of the matchstick. Once reconstructed, realignment of the volumes and stacked matchsticks was carried out in VG Studio Max ^{TM} software to generate a new volume representing the entire damaged region.

To achieve a non-destructive assessment of damage, local µCT scans of intact 4.5 mm thick impact coupons were also undertaken; this is referred to in this thesis as 'local full plate scans'. A schematic of this setup is shown in Figure 3.12 with local scanned regions highlighted. An important distinction here is that the sample is, in some directions at least, larger than the field of view of the detector, *i.e.* 'local' scanning has to be carried out, see [9]. To maximise filling the actual volume of material scanned at one time, two coupons were stacked together and scanned at a time. In setting up the scans, self-adhesive putty markers (Blu-tack^{TM}) were used to position the coupon and to ensure the region of interest was positioned over the axis of rotation. Once positioned, the putty was removed prior to running the scan. This type of local scanning was performed for a more truly non-destructive assessment of impact panels, at the expense of additional noise and artefacts due to variations in beam transmission distance and partially out-of-view material caused by the high aspect ratio of the coupon as it is rotated. Alternatively, SRCL is a scanning technique better suited to such a planar extended sample geometry, allowing local regions to be scanned at high resolution with uniform beam transmission distances at all angles [10], see section 3.8.3.

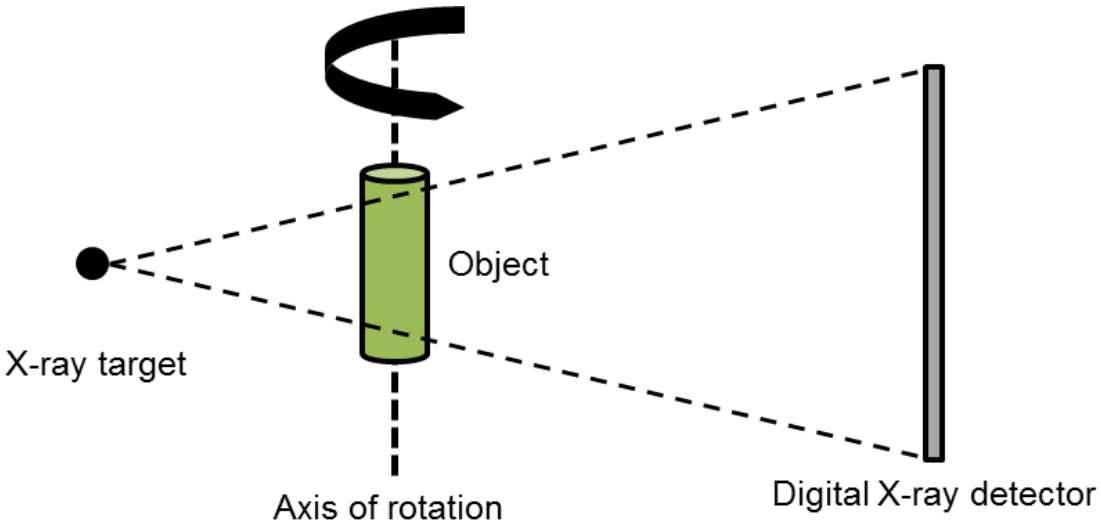

Figure 3.10: Simplified layout of a micro-focus CT scanner.

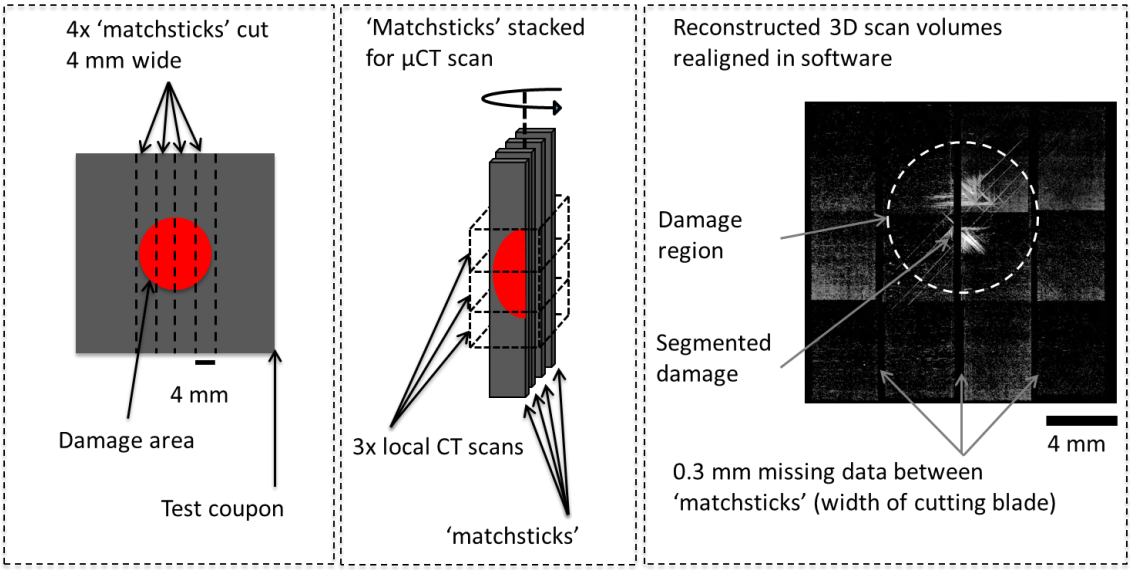

Figure 3.11: Schematic showing 1 mm thick coupons prepared for µCT scans and rearrangement of the volumes.

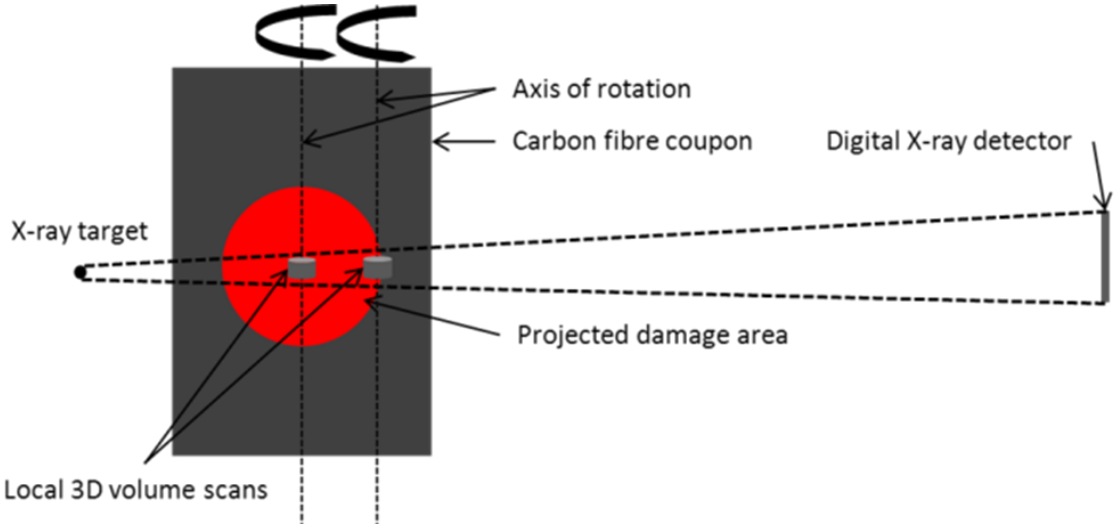

Figure 3.12: Local µCT scans of 4.5 mm thick intact plates.

Striking the right balance between the quality and scan time was important as there is usually a trade-off between the two. Typically the signal to noise, contrast to noise and ring artefacts are issues to consider [11]. Factors that affect scan time include radiograph exposure time, averaging of multiple radiographs, the number of projections (angular positions) used, and hardware settings such as the use of shuttling to minimise ring artefacts. Whilst it is desirable to achieve the best quality scans possible, time constraints on the equipment may make this impractical, for example the requirement to achieve a high throughput of coupons. Striking the balance between scanning work-load and image quality has therefore been a practical consideration in this work with time series experiments, both *in situ* and *ex situ*, requiring higher scan throughput.

3.8.2 Synchrotron Radiation CT

In this work, two synchrotron radiation facilities were used. Early work which focused on 1 mm thick material systems was undertaken at the European Synchrotron Radiation Facility (ESRF) in Grenoble, France on beamline ID19. Later work on the thicker 4.5 mm coupons was undertaken at the Swiss Light Source (SLS), Villigen, Switzerland on the TOMCAT CT beamline. ESRF and SLS scans were conducted at 1.4 µm and 1.5 µm voxel resolutions respectively.

SRCT typically offers greater spatial resolution and higher quality scans (*e.g.* contrast-to-noise-ratio, artefact control) than can be achieved from standard lab µCT systems with significantly shorter scan times in the region of minutes rather than hours. The key difference between laboratory CT and SRCT is the X-ray source whereby a synchrotron radiation beamline produces very bright, coherent monochromatic X-rays that are tuneable and collimated [12]. The parallel beam geometry means a full scan can be achieved from just 180° of rotation instead of the full 360° and all planes within the sample are radiographed at an ideal 90° orientation to the beam, as opposed to the non-90° angles obtained in all but the centre plane of a cone beam µCT system. To achieve high resolutions, SRCT systems typically employ a microscopic scintillator detector system, essentially an optical microscope and CCD camera coupled to a thin scintillator as opposed to the large panel detectors now commonly employed in lab µCT systems. To allow better detectability of edges, phase contrast imaging may be performed by adjusting the sample-to-detector distance to achieve near-field Fresnel diffraction effects [13, 14]. Reconstructions of synchrotron CT data in this work were achieved using a conventional filtered back-projection algorithm at the ESRF, whilst a GRIDREC approach [15] was used at the Swiss Light Source.

In preparing physically extracted regions of interest (ROI) of the 1 mm thick impacted coupons, matchsticks were cut across the impacted region and stacked together prior to scanning at the ESRF, see Figure 3.13. For the 4.5 mm coupons, a 5 x 5 x 4.5 mm ROI ‘cube’ at the edge of damage was cut and mounted to the centre of an SEM stub prior to SRCT scanning at the SLS.

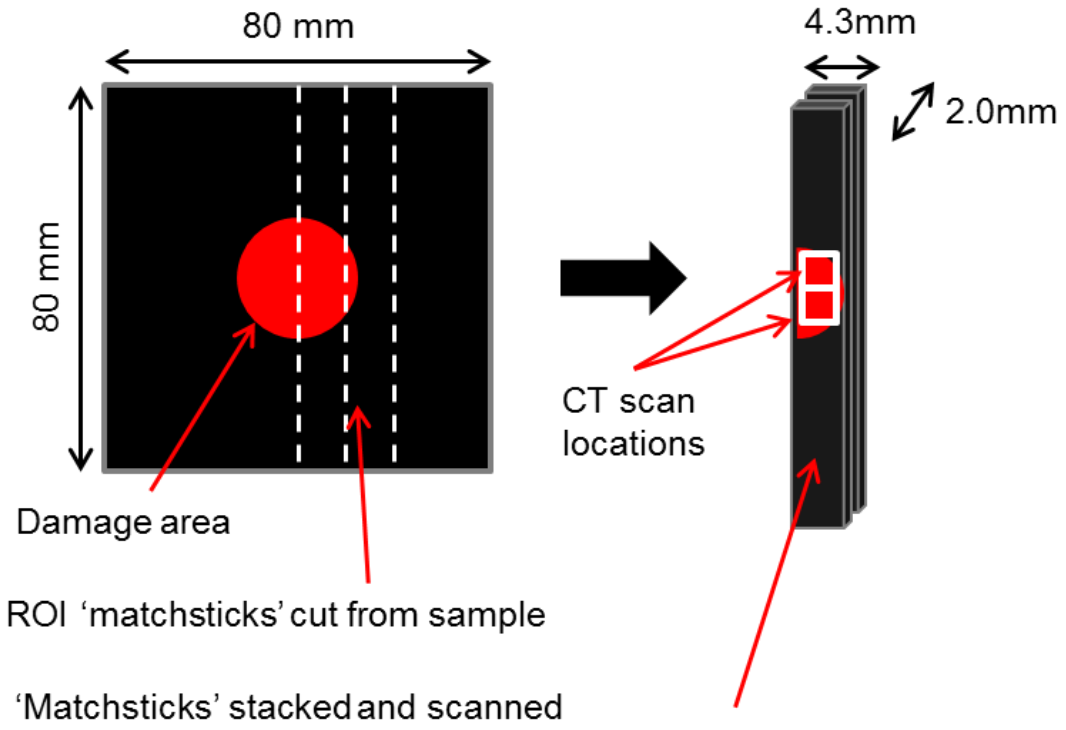

Figure 3.13: Schematic of 1mm thick sample cut to 'matchsticks' and stacked together for SRCT scanning.

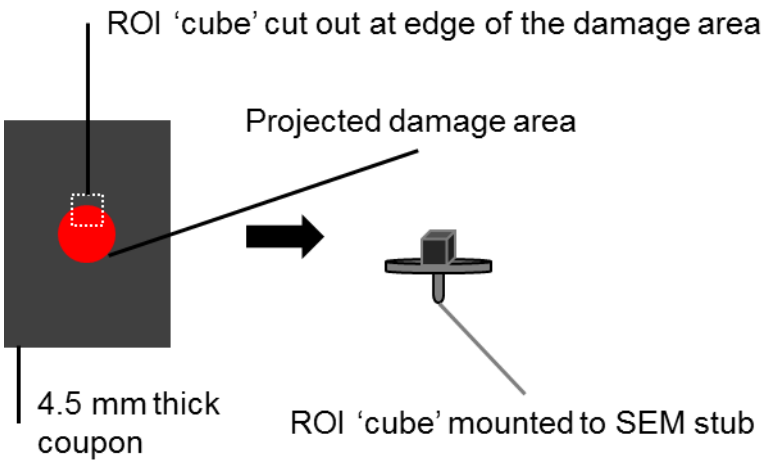

Figure 3.14: Schematic of region of interest 'cube' cut out of a 4.5 mm coupon and mounted to an SEM stub in preparation for SRCT scanning.

3.8.3 Synchrotron Radiation Computed Laminography (SRCL)

SRCL was carried out at the ESRF on Beamline ID19 using a voxel size of 0.7 µm. The key difference between SRCL and SRCT is that the axis of rotation is inclined at an angle to the incident beam rather than perpendicular as in standard CT, see Figure 3.15 and Figure 3.16. It is this difference that make SRCL better suited for high resolution scanning of laterally extended objects by minimising two issues highlighted in (a): firstly, the large variations of X-ray path length which occur as the object is rotated yields non-optimised signal-to-noise conditions for the majority of projections and an effectively incomplete set of projections for the largest path lengths; secondly, material outside the volume of the scan moves in and out of view creating local CT artefacts, typically a bright band at the edges of the reconstructed volume. Whilst steps may be taken to limit these effect such as using angle dependent X-ray energy, or modified reconstruction methods [16](REF) these carry experimental and computational load and are of varying efficacy [17]. By tilting the specimen as shown in Figure 3.15(b), minimal variations in X-ray path is achieved when local scans are undertaken.

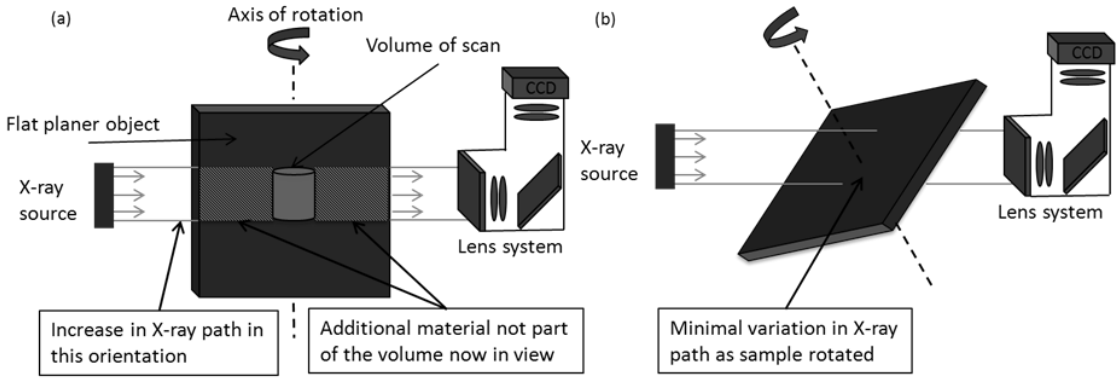

Figure 3.15: Schematic comparing scanning techniques of a flat planar object using (a) SRCT and (b) SRCL.

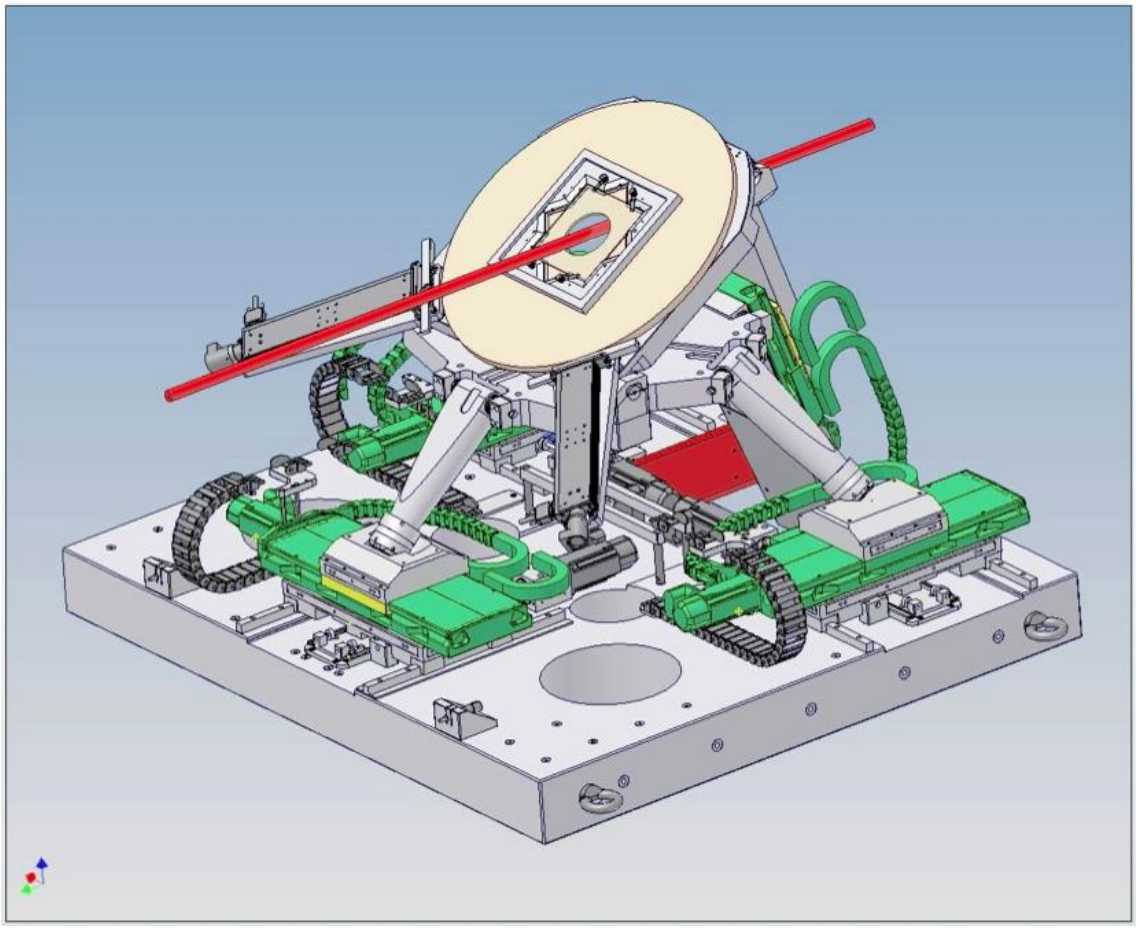

Figure 3.16: Schematic of laminography apparatus. Red line indicates synchrotron X-ray path [18].

Since local scans are produced within a large coupon ‘space’, positioning is critical. The centre point of the volume of the scan is formed at the intersection between the axis of rotation and the X-ray source. To locate the regions of interest on the coupon to this position, a glass slide was fixed to the surface; this is illuminated by fluorescence when synchrotron radiation passes through the glass, indicating the location of the beam on the coupon. Overall, scans took approximately 15 minutes each to perform and about 60 minutes per coupon changeover.

Local scans on 1 mm thick impacted coupons were undertaken across the length of the coupon to form four regions, see Figure 3.17. Scanning of region ‘A’ as highlighted in Figure 3.17 was undertaken at the impact site determined from the centre of the coupon. Scanning of regions ‘B-D’ was carried out 2 to 4 mm from the impact site to ensure the edge of the damage area would be captured.

Beamline time constraints restricted the study to focus on one toughened and one untoughened coupon at the four regions described.

Laminography was also performed on a proof-of-concept basis on a 4.5 mm thick toughened coupon. This was scanned 20 mm away from the centre of the impact region and below the mid-plane in the through-thickness direction. This was to test the feasibility of locally scanning such thickness of material.

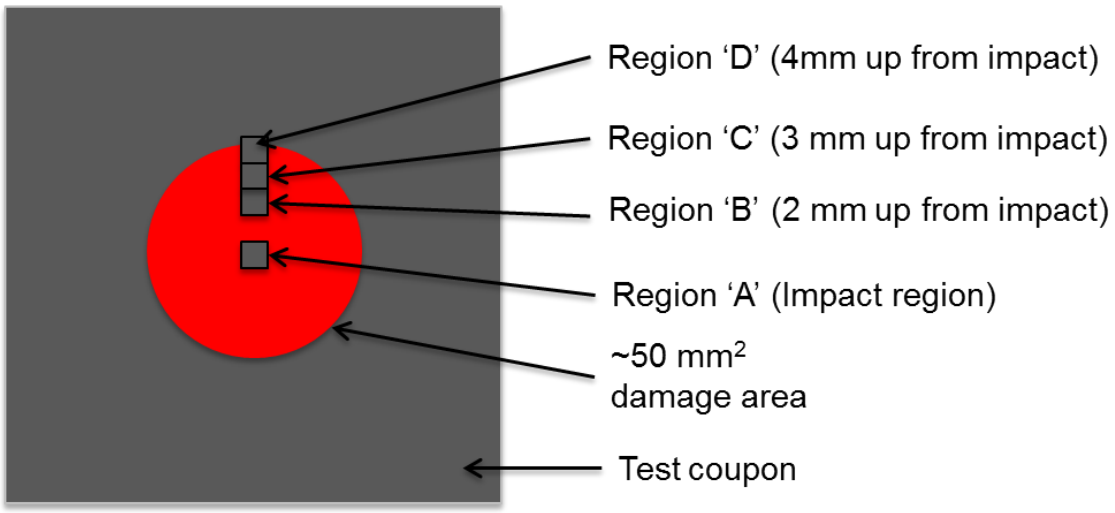

Figure 3.17: SRCL scan locations on 1 mm thick impacted coupons.

3.8.4 X-ray tomography settings

Table 3.1 summarises settings used for the high-resolution synchrotron work, whilst Table 3.2 shows settings used for matchstick specimens undertaken on the µCT equipment.

Table 3.3 lists the settings used for scanning full plates on the Benchtop and HMX scanners. In all µCT scans, these were undertaken using a molybdenum target with no filtering.

Table 3.1: Synchrotron radiation imaging settings.

	SRCT (ESRF)	**SRCT (SLS)**	**SRCL (ESRF)**
Sample thickness tested	1 mm 'matchsticks'	4.5 mm 'cubes'	1 mm 'full plates'
Beam energy (keV)	19 (monochromatic)	20 (monochromatic)	19 (monochromatic)
Voxel resolution (µm)	1.4	1.5	0.7
Detector dimensions (pixels)	2048 x 2048	2048 x 2048	2048 x 2048
Number of radiographs	1500 (180°)	1501	1500 (180°)
Number of frames	2	2	2
Exposure time (ms)	100	200	100
Scan time (minutes)	5	10	11

Table 3.2: µCT scans settings for 'matchstick' specimens.

	µCT Benchtop	**µCT HMX**
Sample thickness tested	1 mm and 4.5 mm 'matchsticks'	1 mm and 4.5 mm 'matchsticks'
Acceleration voltage (kV)	75	65
Beam current (µA)	80	70
Voxel resolution (µm)	5.2	4.3
Detector dimensions (pixels)	1024 x 1024	2048 x 2048
Number of radiographs	2000	2000
Number of frames	2	2
Exposure time (ms)	2000	2000
Scan time (hours)	2.5	2.5

Table 3.3: µCT scans settings for 'full plate' specimens

	µCT Benchtop	**µCT HMX**
Sample thickness tested	4.5 mm	2x 4.5 mm (double stack)
Acceleration voltage (kV)	95	115
Beam current (µA)	95	100
Voxel resolution (µm)	12.6	14.2
Detector dimensions (pixels)	1024 x 1024	2048 x 2048
Number of radiographs	1813	1301
Number of frames	1 (minimise ring artefacts setting enabled)	2
Exposure time (ms)	1000	1000
Scan time (hours)	2	0.75

3.9 Analysis of CT data

3.9.1 Data conversion from 32-bit to 8-bit

To make processing and data handling more practical, the dynamic greyscale range of the reconstructed volumes were converted from 32-bit to an 8-bit format reducing the volume file size by a factor of four. As there is a clear contrast between cracks and background material this was done without any compromise to the data. Chapter 5 discusses the issues of accuracy and interpolation of CT data for crack measurement. This conversion was done using ImageJ software [19].

3.9.2 Segmentation

Segmentation of cracks from the background material was required to create a 3D view of the extent of damage; this was achieved using VG studio Max 2.1 software. In cases where there is good contrast between crack and material, particularly at high resolution scans, global thresholding applied to the histogram can segment these features relatively quickly [20].

Where interactions between different damage modes and their corresponding locations were required, the seeded region growing tool [21] was used to segment these features separately allowing different colours to be used to distinguish between different modes of damage. Whilst this technique worked well for segmenting features, it was only a semi-automated (*i.e.* semi-manual) process and therefore time-consuming in many cases.

For features with minimal contrast, segmentation was also achieved manually using a graphics tablet in some cases. Given the number of slices making up a 3D volume and the manual effort involved, this was typically performed on smaller regions of interest. For example in chapter 7, segmentation of particles in a region 300 x 200 x 50 px.

3.9.3 Quantification of micro-mechanisms

Quantification of crack bridging and deflection was applied to SLS SRCT data in chapter 7. A schematic illustration of how this was achieved is shown in Figure 3.18.

To quantify bridging behaviour, the sampled region was orientated so slices were perpendicular to the nominal crack front, Figure 3.17(b). Cross-sectional slices were spaced at one voxel intervals, *i.e.* adjacent slices. The crack was “binarised” by simple 2D grey-scale thresholding (c) with the threshold value being determined and checked by thorough visual inspection. Any binarised noise surrounding the crack was removed manually using a graphics tablet. A MATLAB ^{TM} script was prepared to read the binarised image slices and used to determine the shortest interconnected distance between crack segments in regions of bridging (d). A series of 200 voxel (*i.e.* 300 μm) sub-areas from the crack tip towards the wake of the crack was used to produce local averages along the crack wake. This dimension is essentially nominal, being selected to average ligament characteristics to some extent, whilst mapping the wake: a distance of 300 μm was seen to capture at least five bridged regions within the sub-areas near the crack tip in each of the material systems. The lengths of bridged regions within each sub-area were summed to give a total accumulated length of interconnectivity for that sub-area and averaged across all 300 cross-sectional slices for that sub-area position relative to the crack tip.

In addition to the extent of bridging along the crack wakes, the average number of bridging ligaments was also measured within each 300 μm region. Crack bridging was furthermore noted to occur in two distinct geometries, with either overlapping or non-overlapping crack sections, see Figure 3.18, which are identified here as ‘oblique’ and ‘perpendicular’ respectively. In the overlapping case, this is defined where one crack segment extends over another crack segment in the through-thickness direction and is indicated by the shaded region in (e).

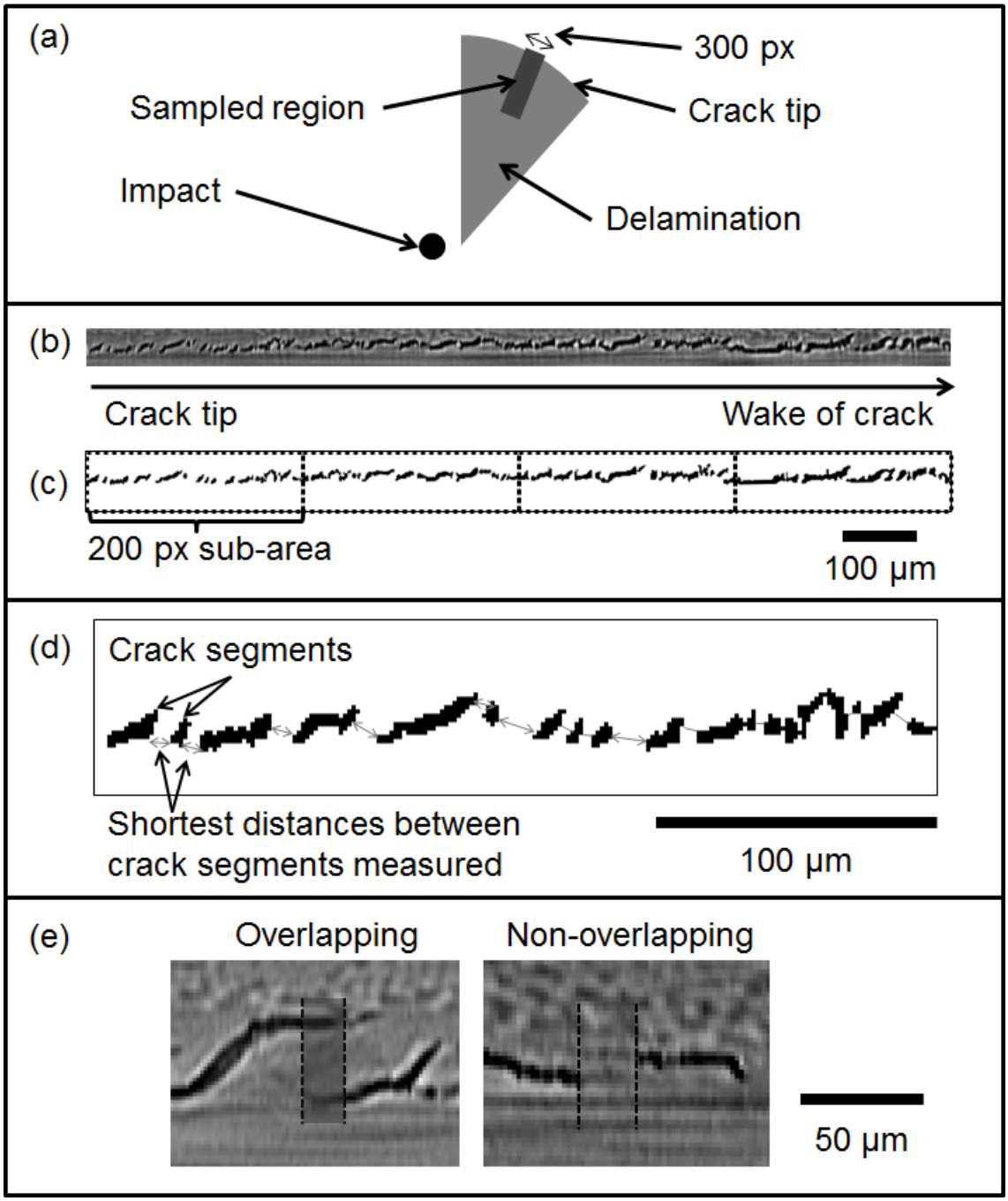

Figure 3.18: Crack bridging measurement process. (a) Schematic showing the location of the sampled region within a segment of delamination. (b) SRCT cross-section of the side of a delamination. (c) Binarization of the crack with the crack profile divided into 200 px sub-areas. (d) Close up of a sub-area with shortest distances between crack segments measured. The distances are summed together within each sub-area. (e) Example of overlapping (oblique) and non-overlapping (perpendicular) crack segments highlighted with dashed lines.

Quantification of crack deflection was carried out on a 500 x 500 voxel (750 µm x 750 µm) area at the wake of a given crack, ~2 mm from the crack tip; see Figure 3.19. A manual process of tracing a line profile along the fracture surface was undertaken using a graphics tablet (a). The cross-section was orientated with the side of the crack perpendicular to the normal crack front. Due to the laborious nature of this task, this was done at 25 cross-section intervals (30 µm spacing) to obtain a reasonable representation of the crack.

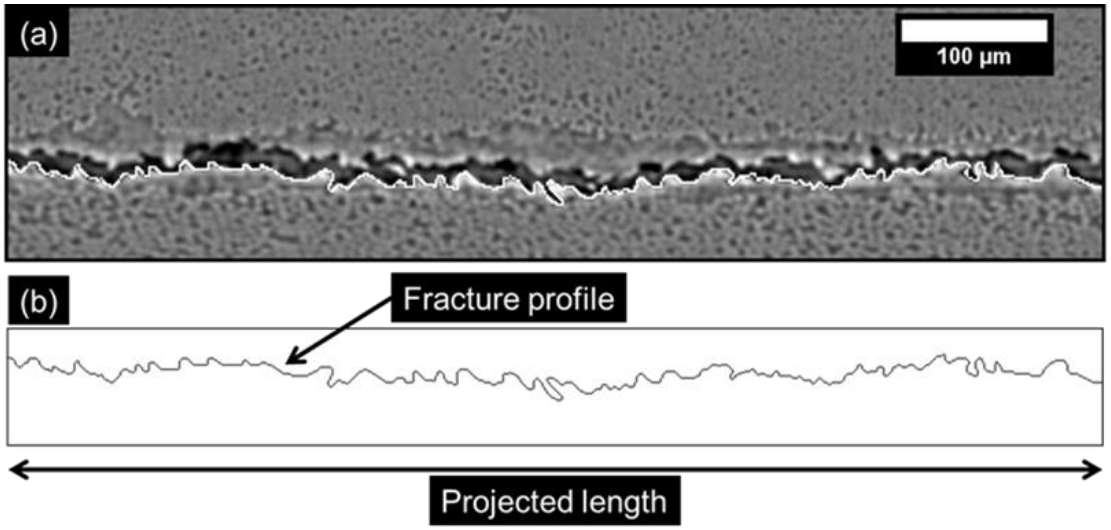

Figure 3.19: SRCT cross-section of delamination in the wake of the crack. (a) shows an overlay of the lower fracture profile, (b) shows the fracture profile segmented from (a) where the length of the profile is divided by the projected length to calculate the increase in crack path length as a ratio.

For each cross-section, the length of this fracture profile, Figure 3.19 (b), was measured and divided by the projected length to indicate the increase in path length as a ratio. This was achieved by calculating the distances between the pixel centres representing the profile. A conventional description of surface roughness was also obtained in terms of the R_a arithmetic average value, equation (3-8):

$$R_a = \frac{1}{n}\sum_{i=1}^{n}|y_i| \qquad (3\text{-}8)$$

where n represents points along the trace of the fracture profile, y_i is the vertical distance from the mean line to the i^{th} data point. In both sets of measurements the standard error in the mean was calculated for path length and roughness measurements.

3.9.4 Measurement of cracks and delaminations

Measurements of features such as crack lengths, delaminations and crack-segments were undertaken using the ruler tools in ImageJ and VG Studio Max software.

To measure the projected delamination area on each ply in a material system, semi-automated segmentation was required. To balance the workload, the majority of delamination measurements were performed by taking the projected length. This enabled the extent of the through-thickness distribution of delaminations and delamination growth to be studied. Measurements were achieved by locating the start and furthest detectable tip of the delaminations on the 2D slices, positioned to show the delamination crack front. The precision of the measurements were less than 10 voxels. Figure 3.20 shows how two different delamination characteristics were measured in this study. The majority of delaminations consisted of 45° segments as shown in white in Figure 3.20(i). The total delamination length within this ply was calculated by combining measurements of both sides of the delamination. This was similarly done for delaminations that occurred between 45° segments shown in red (ii).

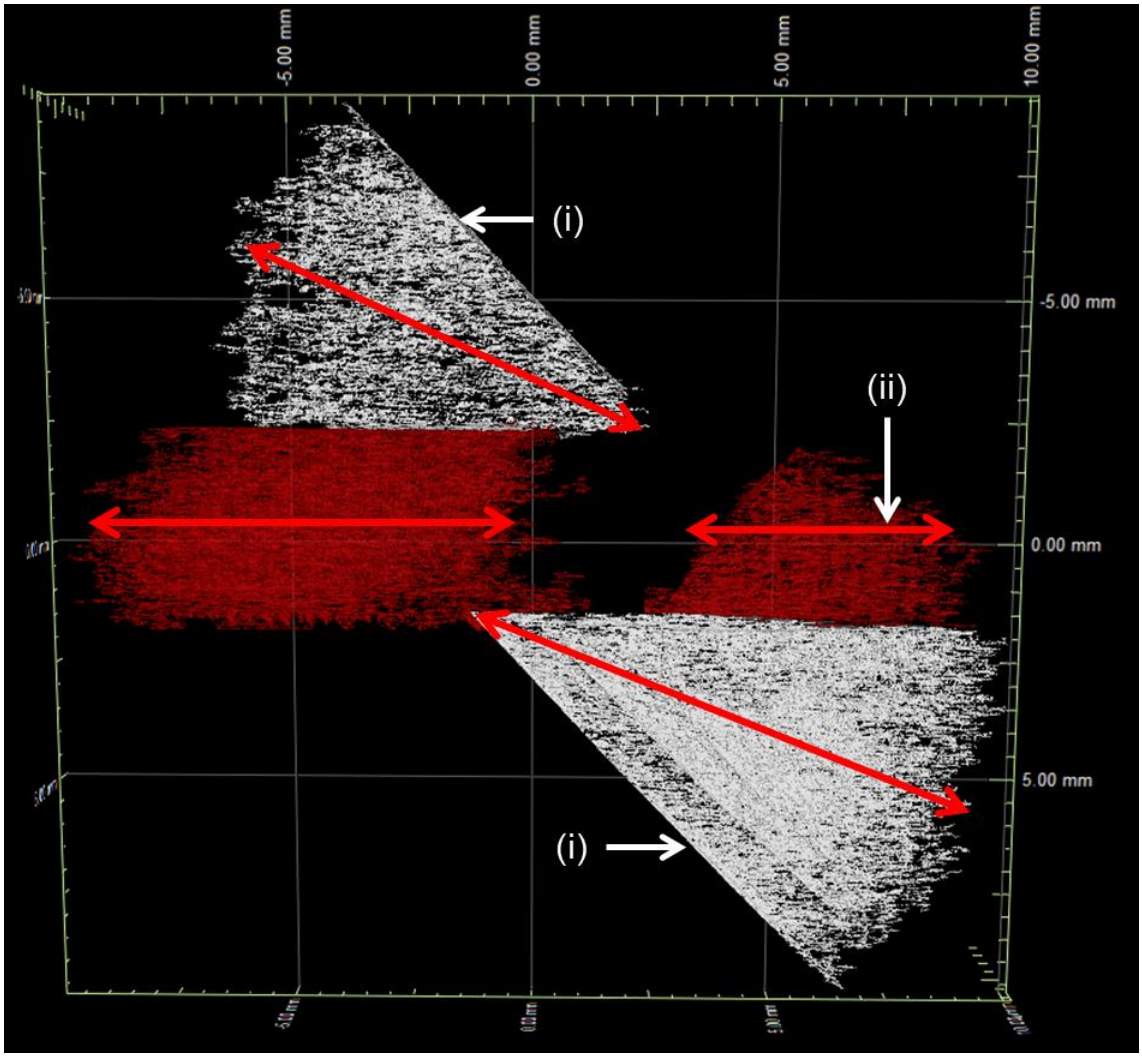

Figure 3.20: Schematic showing how the lengths of two types of delaminations were measured. These consisted of (i) 45° delamination segments and (ii) delaminations which occurred between segments.

3.10 References

[1] Moffat, A.J., Wright, P., Helfen, L., Baumbach, T., Johnson, G., Spearing, S.M., and Sinclair, I., *In situ synchrotron computed laminography of damage in carbon fibre-epoxy [90/0](s) laminates.* Scripta Materialia, 2010. **62**(2): pp. 97-100.

[2] *ASTM D 7136/D 7136M 07 standard test method for measuring the damage resistance of a fiber-reinforced polymer matrix composite to a drop-weight impact event*. 2007, ASTM International.

[3] *ASTM D7137 / D7137M - 07 Standard Test Method for Compressive Residual Strength Properties of Damaged Polymer Matrix Composite Plates*. 2007, ASTM International.

[4] Sanchu-Saez, S., Barbero, E., Zaera, R., and Navarro, C., *Compression after impact of thin composite laminates.* Composites Science and Technology, 2005. **65**(13): pp. 1911-1919.

[5] *ASTM D6264 / D6264M - 07 Standard Test Method for Measuring the Damage Resistance of a Fiber-Reinforced Polymer-Matrix Composite to a Concentrated Quasi-Static Indentation Force*. 2007, ASTM International.
[6] Boarden, J. *A Guide to Double Through Transmission Inspection*.
[7] *BODDIES surface analysis software, roughness, measurement and analysis*. Available from: http://www.taicaan.com/soft_bod_eng.html. Accessed 13/06/13.
[8] Salvo, L., Cloetens, P., Maire, E., Zabler, S., Blandin, J.J., Buffiere, J.Y., Ludwig, W., Boller, E., Bellet, D., and Josserond, C., *X-ray micro-tomography an attractive characterisation technique in materials science.* Nuclear Instruments & Methods in Physics Research Section B-Beam Interactions with Materials and Atoms, 2003. **200**: pp. 273-286.
[9] Kyrieleis, A., Titarenko, V., Ibison, M., Connolley, T., and Withers, P.J., *Region-of-interest tomography using filtered backprojection: assessing the practical limits.* Journal of Microscopy, 2011. **241**(1): pp. 69-82.
[10] Helfen, L., Baumbach, T., Mikulik, P., Kiel, D., Pernot, P., Cloetens, P., and Baruchel, J., *High-resolution three-dimensional imaging of flat objects by synchrotron-radiation computed laminography.* Applied Physics Letters, 2005. **86**(7): pp. 071915.
[11] Ritman, E.L., *Micro-computed tomography-current status and developments.* Annual Review of Biomedical Engineering, 2004. **6**: pp. 185-208.
[12] Baruchel, J., Buffiere, J.Y., Cloetens, P., Di Michiel, M., Ferrie, E., Ludwig, W., Maire, E., and Salvo, L., *Advances in synchrotron radiation microtomography.* Scripta Materialia, 2006. **55**(1): pp. 41-46.
[13] Snigirev, A., Snigireva, I., Kohn, V., Kuznetsov, S., and Schelokov, I., *On the possibilities of x-ray phase contrast microimaging by coherent high-energy synchrotron radiation.* Review of Scientific Instruments, 1995. **66**(12): pp. 5486-5492.
[14] Spanne, P., Raven, C., Snigireva, I., and Snigirev, A., *In-line holography and phase-contrast microtomography with high energy x-rays.* Physics in Medicine and Biology, 1999. **44**(3): pp. 741-749.
[15] Marone, F. and Stampanoni, M., *Regridding reconstruction algorithm for real-time tomographic imaging.* Journal of Synchrotron Radiation, 2012. **19**: pp. 1029-1037.
[16] Rouse, J.E., *Characterisation of Impact Damage in Carbon Fibre Reinforced Plastics by 3D X-Ray Tomography.* Ph. D. Thesis. University of Manchester: U.K., 2012.
[17] Helfen, L., Myagotin, A., Rack, A., Pernot, P., Mikulik, P., Di Michiel, M., and Baumbach, T., *Synchrotron-radiation computed laminography for high-resolution three-dimensional imaging of flat devices.* Physica Status Solidi a-Applications and Materials Science, 2007. **204**(8): pp. 2760-2765.
[18] Helfen, L. *IPS-ANKAIPS - nano & micro characterization - imaging group - laminography*. Available from: http://www.ips.kit.edu/english/974_1109.php. Accessed 05/02/13.
[19] Schneider, C.A., Rasband, W.S., and Eliceiri, K.W., *NIH Image to ImageJ: 25 years of image analysis.* Nature Methods, 2012. **9**(7): pp. 671-675.
[20] Nixon, M.S. and Aguado, A.S., *Feature extraction and image processing*. 2nd ed. ed. 2008, Amsterdam ; London: Elsevier/Academic Press.

[21] Justice, R.K., Stokely, E.M., Strobel, J.S., Ideker, R.E., and Smith, W.M., *Medical image segmentation using 3D seeded region growing.* 1997: pp. 900-910.

Chapter 4

A Comparison of multi-scale 3D X-ray tomographic inspection techniques for assessing carbon fibre composite impact damage

This chapter explores the use of three imaging facilities to assess impact damage in CFRP materials. Tomographic imaging using both laboratory sources and synchrotron radiation (SR) were performed to achieve a multi-scale damage assessment of carbon fibre composites subjected to low velocity impact damage, allowing various internal damage modes to be studied in 3D. The focus of this study is the comparison of different tomographic methods, identifying their capabilities and limitations, and their use in a complementary manner for creating an overall 3D damage assessment at both macroscopic and microscopic levels. Having a clear understanding of the imaging techniques enabled a better understanding of their capabilities to be applied to the studies in the later chapters of this thesis. Overall, microfocus laboratory computed tomography (µCT) offers efficient routine assessment of damage at mesoscopic and macroscopic levels in engineering-scale test coupons and relatively high spatial resolutions on trimmed-down samples; whilst synchrotron radiation computed tomography (SRCT) and computed laminography (SRCL) offer scans with the highest image quality, particularly given the short acquisition times, allowing damage micromechanisms to be studied in detail.

4.1 Introduction

Recent studies have used µCT to study impact damage on composite laminate materials and have detected interlaminar and intralaminar damage throughout the laminate thickness. In some cases contrast agents have been used to detect the

presence of damage [1]; this however has a limitation requiring interconnectivity between all cracks to absorb the agent, which cannot be guaranteed [2]. Other studies have successfully captured 3D damage without the use of contrast agents [3-5]. A major challenge in standard µCT imaging using a large-area (*e.g.* flat panel) detector is that to reach high spatial resolutions (15 µm and less), flat specimens cannot be fully turned due to collision with the X-ray tube housing, which effectively limits the angular acquisition range. In most studies the specimens are hence cut to smaller sample sizes. To our knowledge, no work using SRCT or SRCL to study composite impact damage has been published so far.

SRCL, SRCT and µCT operate on similar principles: a large number of 2D radiographic projections are taken as the sample in question is rotated. These radiographs undergo an inverse Radon Transform via a variety of possible methods to form a 3D volume. The two key differences between these techniques are the X-ray sources - use of synchrotron vs. micro-focus tube - and the axis of rotation for scan acquisition; this is perpendicular to the X-ray beam in computed tomography (CT), and tilted to less than 90˚ in computed laminography (CL). Key benefits of synchrotron imaging include fast acquisition speed with high signal-to-noise, convenient exploitation of phase contrast effects particularly propagation methods for enhanced edge detection [6], and sub-micrometer resolutions, when compared to conventional micro-focus sources [7].

The present chapter specifically explores the use of SRCT, SRCL and µCT on relatively thin (1 mm) impacted coupons of CFRP laminate, to evaluate their uses in a complementary manner. The feasibility of scanning intact 4.5 mm thick coupons is also studied using coupons conforming to the ASTM D7136M [8] impact standard; this was performed using µCT and SRCL. This work differs from previous work by forming a direct comparison of 3D imaging methods on impacted CFRP panels.

4.2 Results and discussion

4.2.1 Initial observations

All three imaging techniques yield reasonably clear imaging of overall larger-scale damage modes associated with impact loading, particularly interlaminar and intralaminar cracking: a cross-sectional slice of the reconstructed volumes shows representative image qualities in Figure 4.1(a-c) for µCT, SRCT and SRCL respectively. All results are shown in a mostly unprocessed state, *i.e.* no image-domain filtering or enhancements are applied. For direct comparison, Figure 4.1 (a and b) show the same location within the same sample, and (c) is of a different sample at a similar damage region. Whilst both CT techniques involved specimen cutting, comparing this data to the non-destructive SRCL technique shows qualitatively comparable quality of damage visualisation, with similar damage morphologies and apparent crack-opening displacements (COD). There was limited evidence of additional damage being introduced to the CT specimen volumes during cutting, although it is possible that some surface damage is introduced, particularly where sectioning across areas that are severely damaged during impact.

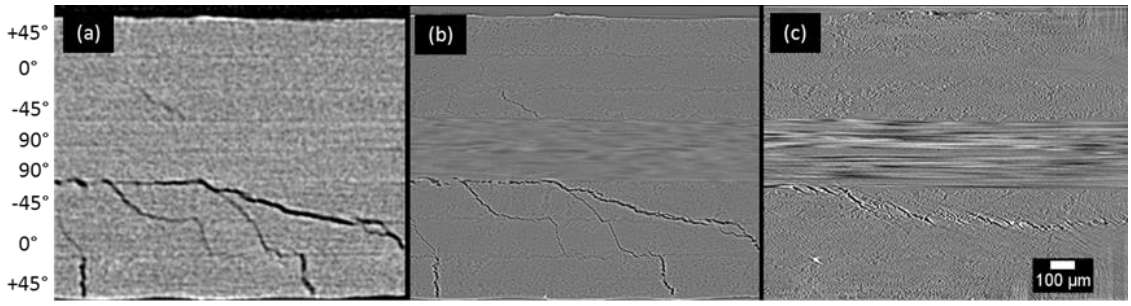

Figure 4.1: Cross-sectional views of impact damage via: (a) µCT, (b) SRCT and (c) SRCL. Images (a) and (b) are of the same sample at the same location, whilst (c) is of a similar damage region of a different sample.

Although individual fibres could not be detected in the µCT scans at the moderate voxel resolution selected here, individual plies and their interfaces could be distinguished as well as the presence of cracks, including those with CODs less

than the voxel size used in the scan. The two SR methods shown in Figure 4.1(b) and (c) demonstrate the benefits of phase-enhanced edge contrast and increased resolution: details of individual fibres and resin-rich regions are clearly visible, with damage micromechanisms clearly delineated. SRCT and SRCL yield qualitatively similar damage visualisation employing the edge-enhancing phase contrast [6, 9], with the benefit of SRCL being the intact coupon geometry. However in the case of SRCL, artefacts resulting from incomplete Fourier-space sampling can arise: an exact inversion of the modulation transfer function (MTF) is not possible. Using a filtering step for the 2D projection prior to back-projection data minimises artefacts in the 3D reconstructed volume [9, 10]. Additional artefacts appearing in this study were particularly evident at the edges of the volume in places where not all projections contribute to the reconstructed image. Additional artefacts in the reconstructed 3D images of SRCL will have direct implications for automated segmentation and feature extraction processes, inevitably increasing the complexity of such processes.

Delaminations are a key damage mode in impact loading, in which micro-scale data for the crack morphology and shear and opening displacements is important [11, 12]. A comparison of the same delamination shown in Figure 4.2(a/b) obtained using µCT and SRCT techniques respectively, and a similar delamination obtained with SRCL in Figure 4.2(c) highlights the role of multi-scale imaging. Assessment of the delamination via µCT at moderate resolution suggests the presence of a continuous crack with a single bridged section. The greater level of detail obtained from both SR techniques shows that the micromechanisms are more complicated, with significant incidence of fine-scale crack bridging within the resin-rich regions.

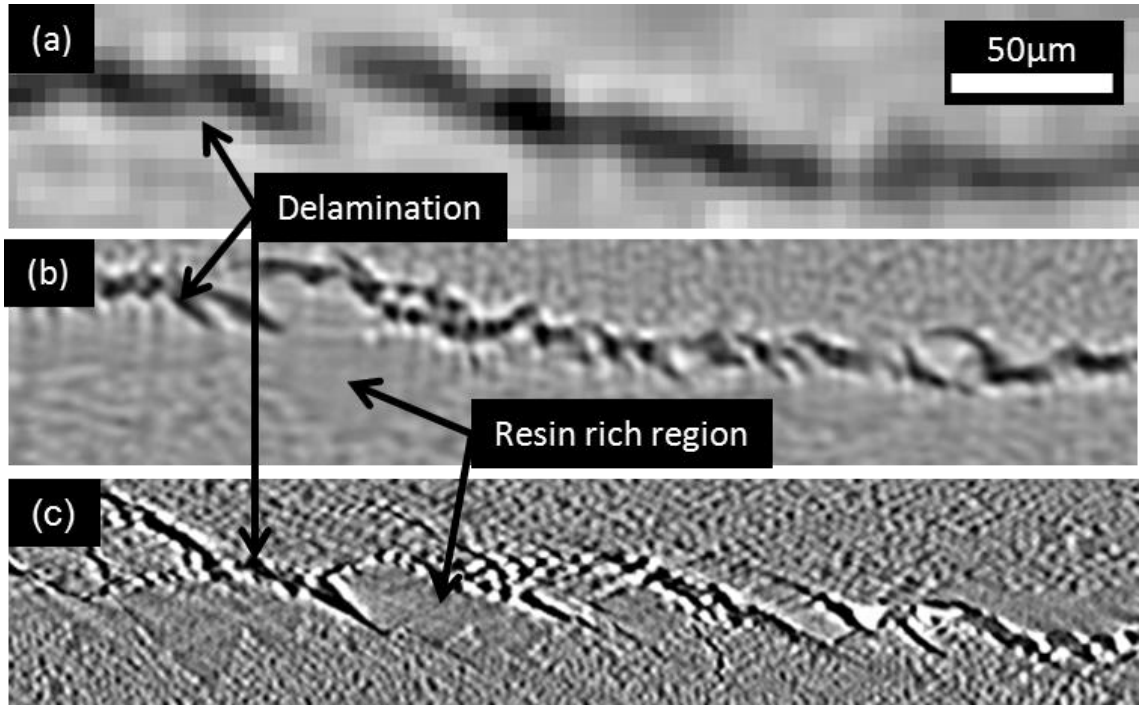

Figure 4.2: Close up of a delaminated region obtained using (a) µCT (b) SRCT (c) and SRCL. (a) and (b) are of the same specimen at approximately the same location, (c) is representative of similar damage on a separate specimen.

4.2.2 Sub-voxel assessment of µCT data

It is reported that sub-voxel data may be captured from CT data [13], as illustrated in Figure 4.3(a i-ii). Direct comparison with the SRCT data for the low resolution µCT data indicated that cracks with an opening displacement as low as 30 % of the voxel resolution were reliably captured with µCT, in keeping with previous comparisons between µCT and conventional microscopy [2, 14]. Figure 4.4 illustrates the significance of partial volume effect on crack detection via grey-scale plots across the crack-openings, indicated by the lines in Figure 4.3(a i-iv). The presence of a crack is indicated by a minimum on the line plot and, in the case of sub-voxel data, this minimum falls between the bounds of the mean grey-scale values of air and material. In the presence of complex crack-bridging ligaments, it is clear that whilst the CODs from these cracks cannot be measured via µCT to high accuracy, for example by exploiting weighted averages of bulk greyscale values to deduce partial volume effects [13], they show the locations and extent of damage. This informs the general mechanics of failure, in addition to identifying

ROIs for more detailed analysis. It may be noted that to achieve greater effective contrast in crack detection penetrant dyes may be employed [1, 2, 15]; however impact damage analysis presents limited scope for penetrant use given the presence of many non-surface breaking cracks, particularly in the critical Barely Visible Impact Damage (BVID) regime.

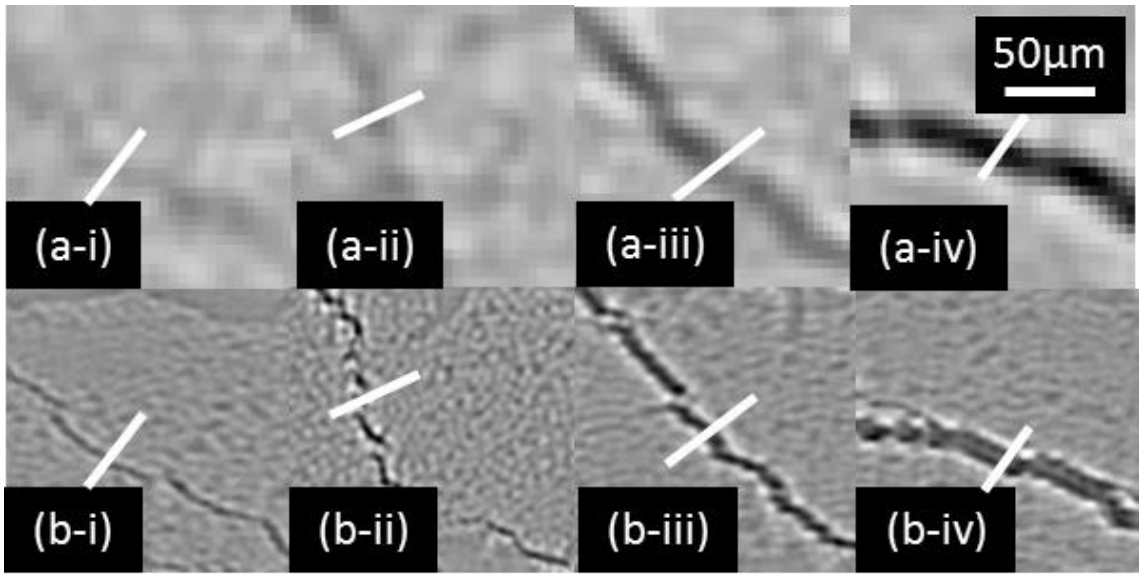

Figure 4.3: Cracks of varying COD level (approximate) (i-iv) <1.4, 3, 4, and 8 µm respectively, comparisons of image quality between (a) µCT and (b) SRCT.

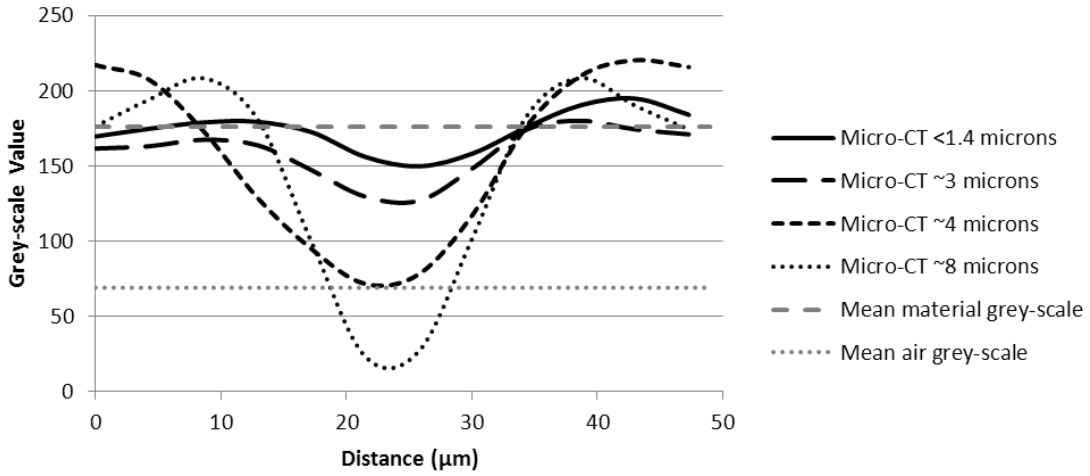

Figure 4.4: Line-plot showing the corresponding µCT grey-scale values across the opening of cracks ranging from crack-opening displacements of <1.4 to ~8 µm.

4.2.3 3D segmentation

The 3D morphology of impact damage was segmented via the semi-automatic 'seed growth' approach [16] in the same 'matchstick' specimen using µCT and SRCT data, as shown in Figure 4.5(a/b). The field of view for SRCT was smaller than that of µCT, hence the smaller segmented volume. µCT and SRCT both give a reasonable mechanistic representation of 3D damage, nonetheless the reduced resolution of µCT means that even though sub-voxel information can be extracted to some extent, information is lost when crack-opening displacements (COD) start approaching the lower limits of detection.

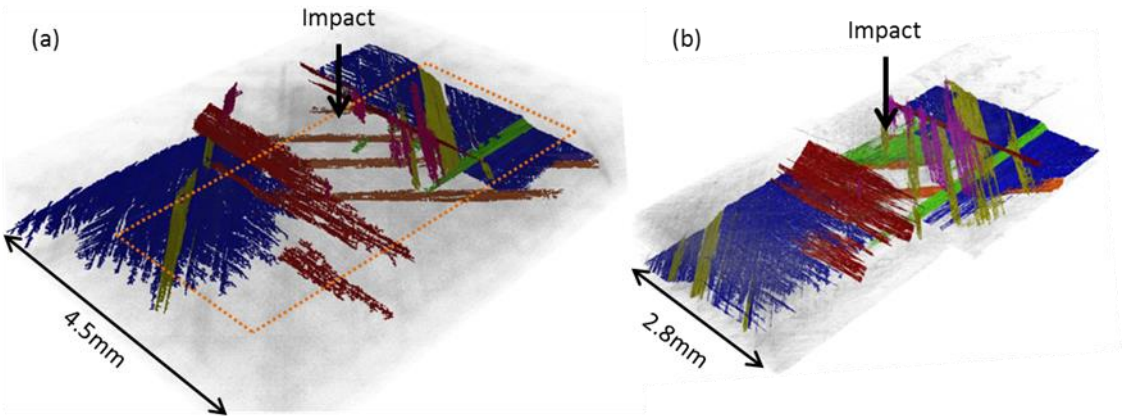

Figure 4.5: 3D segmentation revealing the damage morphology surrounding the impact region within the same specimen obtained by (a) µCT with the dotted region indicating the region obtained using (b) SRCT. Blue is representative of delaminations whilst other colours indicate matrix cracking occurring on each respective ply.

A compromise between resolution and the overall size of the volume needs to be met. At the 4.3 micrometer voxel resolution used in this study, µCT gives damage representation over a sample volume cross-section of approximately 10 mm. Additionally measurements of crack lengths can be approximated, although information towards the tips of the crack will be missed where crack-openings are down to 30 % of the voxel resolution, leading to an underestimation of the crack length. To achieve the microscopic detail required to capture the undetected or non-segmentable damage, SR techniques are clearly of significant value (*e.g.* in identifying the role of traction forces due to ligament formation across cracks) at the expense of reduced overall fields of view. Multiple scans may of course be

taken to capture a larger proportion of damage; however increased computational costs in terms of data-set size and post-processing load are non-trivial.

4.2.4 SRCL: analysis of thick specimen

Whilst the above results are based on 1 mm thick laminate samples, to study impact damage within a conventional engineering context it is desirable to achieve high resolution non-destructive scans of specimens meeting standard impact test conditions such as ASTM D7136. For a D7136 compliant coupon thickness of 4.5 mm, the SRCL conditions noted above led to a scanning condition that is local in terms of both in-plane, and through-thickness position. As such, by adjusting the location of the specimen so that the ROI lies at the point where the tilted centre of rotation intercepts the beam, localised volumes through the thickness of the material may be generated within the specimen.

Figure 4.6(a) illustrates such a typical 'local' SRCL result for a 4.5 mm thick CFRP plate, demonstrating that high-resolution imaging is indeed possible for such a full-thickness intact impact coupon. Artefacts consisting of vertical streaks are present towards the image corners as indicated by arrows, as these regions are increasingly out of view across the full scan rotation. These artefacts occur at similar image locations with the 1 mm specimens shown in Figure 4.1(c).

A direct comparison of this local SRCL region shown in Figure 4.6(a) is compared with a μCT 'matchstick' scan of the same region in (b) with the corresponding SRCL location indicated by the box. The overall image quality from SRCL is sufficient to identify individual fibres, cracking and small voids, with the latter two features also being detected with μCT. Limited contrast is particularly noticeable for the large continuous delamination crack seen in the upper half of Figure 4.6(a) and the corresponding boxed area of Figure 4.6(b), consistent with this crack lying in a plane which is not directly sampled by the tilted rotation axis used for CL, highlighting the direction-dependence of image quality in a limited angular access geometry, such as CL. Reasonably similar image qualities in detecting intralaminar cracking in 4.5 mm and 1 mm thick sample are illustrated in Figure

4.7, consistent with the modest absorption of CFRP for these thicknesses at the associated X-ray energy level.

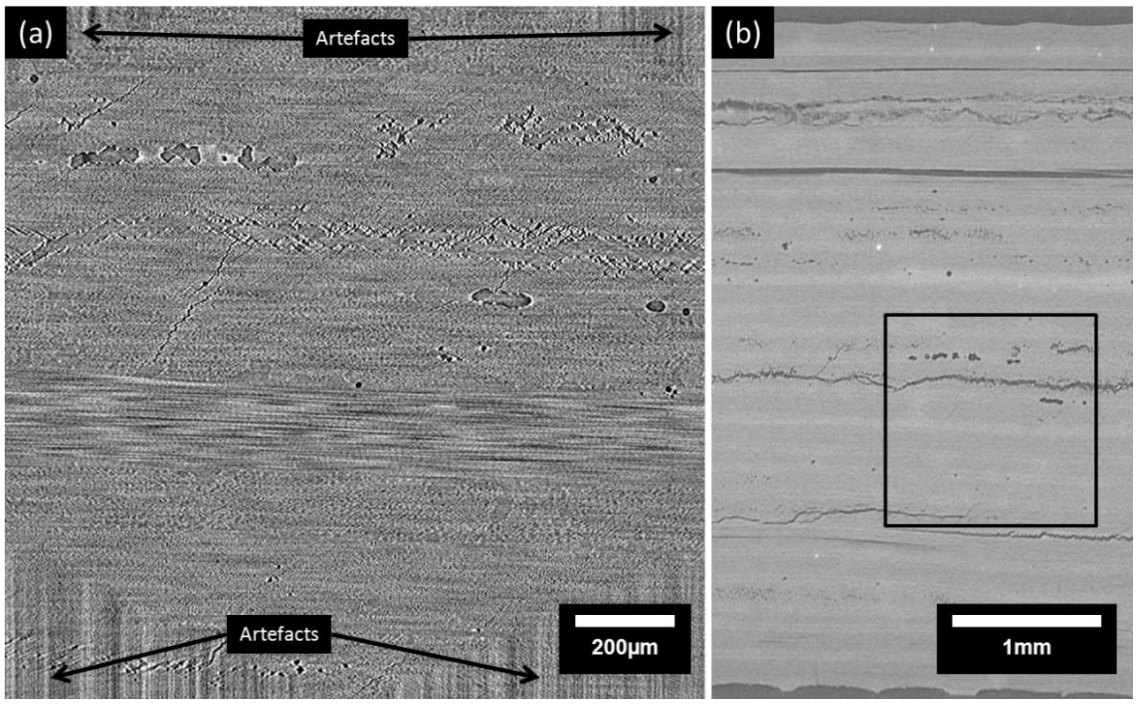

Figure 4.6: Cross-sectional view of an impacted 4.5 mm thick specimen, (a) mid-way through the cross-sectional thickness obtained using SRCL (voxel size = 0.7 µm) and (b) corresponding µCT slice (voxel size = 4.3 µm), with box showing the location of the SRCL scan within the through thickness.

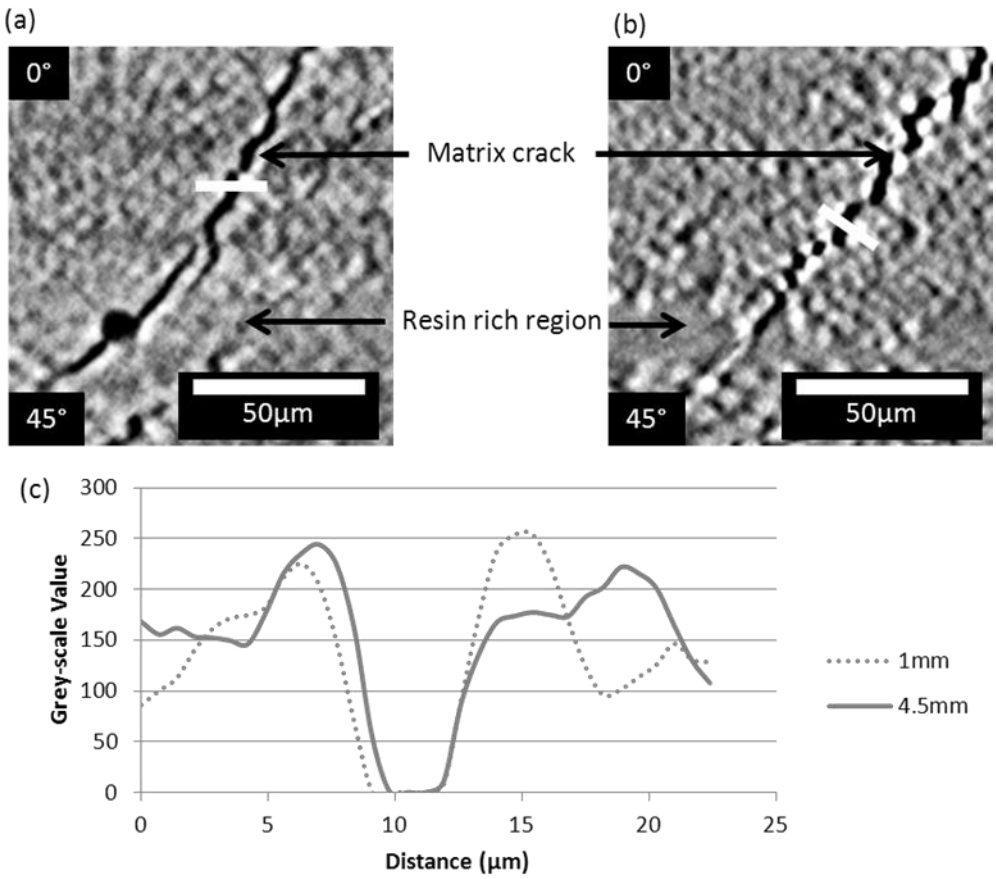

Figure 4.7: Close up of a crack obtained using SRCL of 4.5mm thick specimen (a) and 1mm specimen (b), the white lines indicate a region across the crack to obtain the line plots shown in (c).

Considering that SRCL allows for truly non-destructive, high resolution testing on ASTM standard panels, one may identify SRCL as a preferred analysis method for materials performance analysis under standard impact conditions. However, high resolution SRCL carried out over the large areas that may be associated with an impact event clearly requires a high synchrotron beamtime and large computational/data handling load.

4.2.5 µCT: local scan on intact thick specimen

Whilst SRCL offers non-destructive assessment of full ASTM standard panels, time and beam access constraints apply. As an alternative, µCT scans of complete intact panels are also of interest and offer rapid global assessment at intermediate

voxel resolutions, as obtained in [17] and [5]. The voxel resolution was limited by how close the specimen could be positioned to the X-ray target source. Local scans of full plates were tested using µCT and importantly this was achieved using relatively fast micro-focus CT settings. A cross-sectional slice of such a scan is shown in Figure 4.8. Despite the non-ideal geometry of the sample for CT assessment compared to the near 'matchstick' samples and the lower 14.3 µm voxel resolution used, primary damage mechanisms were clearly detected. Whilst limited in resolution, the ability to image meso- to macro-scale damage characteristics in the absence of synchrotron access remains a valuable complementary approach. In particular, extended time-resolved studies of damage propagation under incrementally increasing compressive loads, where truly global assessment across a complete damage zone in the order of centimetres in diameter via SRCL would be excessive in both beamtime and the amount of data generated.

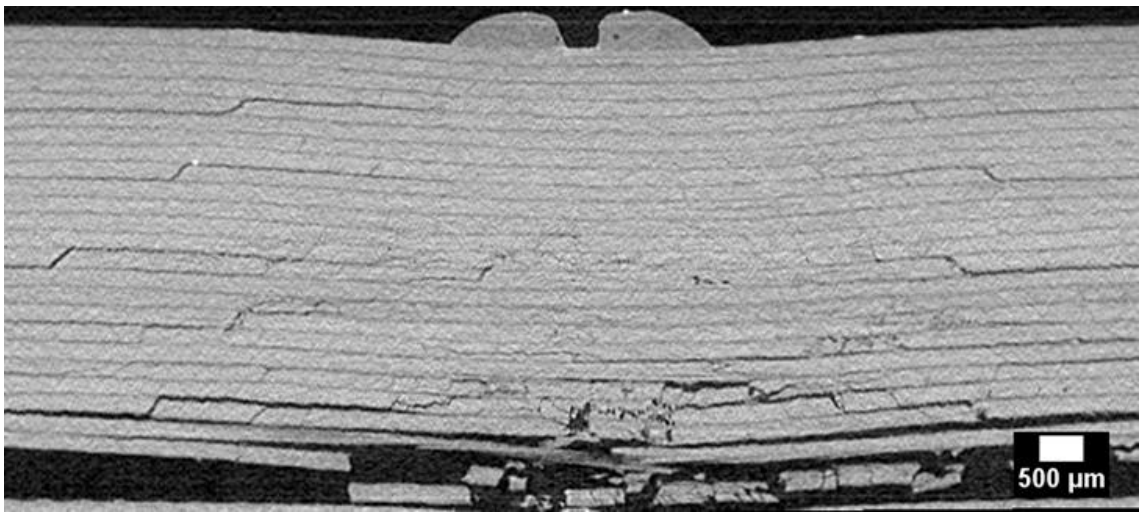

Figure 4.8: Cross-section of a ~4.5mm thick CFRP laminate sample obtained by a local µCT scan of the whole panel.

4.3 Conclusions

It is evident that for the mixed length scales associated with impact events, different X-ray imaging methods offer alternative and complementary combinations of image resolution and fidelity, sample preparation requirements, limitations and hardware availability.

At routinely achievable voxel resolutions laboratory µCT offers valuable detail for understanding the three-dimensional macro and mesoscopic extent of impact damage, with reliable sub-voxel detection of the extent of cracks being illustrated. SR techniques (SRCT and SRCL) allow for rapid scanning of 3D micro-scale damage down to the scale of individual fibres. Laboratory µCT systems alternatively offer scan volumes up to hundreds of millimetres, capturing entire impact sites in a single scan on complete panels. This coupled with a fast scan setting make it feasible to perform *ex situ* time series work, enabling 3D damage propagation to be monitored.

Comparing the damage morphologies of the 3D segmentation of the same sample obtained using µCT and SRCT, both techniques show similar results for capturing the overall extent of damage. However, where greater mechanistic detail is required, SR techniques are clearly superior, particularly in terms of the speed at which low noise, high resolution scans may be obtained.

The potential for local, very high resolution 3D analysis of complete, engineering-scale impact test panels is demonstrated for synchrotron laminography, offering unique opportunities for 'through-process' assessment of compression-after-impact analysis; *i.e.* intact impacted panels being examined non-destructively at high resolution, prior to compression testing. However, integration within a program of more conventional and accessible testing and imaging modalities is likely to be required for effective use of such limited, specialised capabilities.

4.4 References

[1] Tan, K.T., Watanabe, N., and Iwahori, Y., *X-ray radiography and micro-computed tomography examination of damage characteristics in stitched composites subjected to impact loading.* Composites Part B-Engineering, 2011. **42**(4): pp. 874-884.

[2] Schilling, P.J., Karedla, B.P.R., Tatiparthi, A.K., Verges, M.A., and Herrington, P.D., *X-ray computed microtomography of internal damage in fiber reinforced polymer matrix composites.* Composites Science and Technology, 2005. **65**(14): pp. 2071-2078.

[3] Archer, E., King, S, Quinn, JP, Buchanan, S and McIlhagger. *Impact damage analysis of 3D woven carbon fibre composites using computed tomography*. in *18th international conference on composite materials*. 2011. South Korea: The Korean society for composite materials.

[4] Crupi, V., Epasto, G., and Guglielmino, E., *Computed Tomography analysis of damage in composites subjected to impact loading.* V. Crupi et alii, Frattura ed Integrità Strutturale, 2011. **17**: pp. 32-41.
[5] McCombe, G.P., Rouse, J., Trask, R.S., Withers, P.J., and Bond, I.P., *X-ray damage characterisation in self-healing fibre reinforced polymers.* Composites Part a-Applied Science and Manufacturing, 2012. **43**(4): pp. 613-620.
[6] Cloetens, P., PateyronSalome, M., Buffiere, J.Y., Peix, G., Baruchel, J., Peyrin, F., and Schlenker, M., *Observation of microstructure and damage in materials by phase sensitive radiography and tomography.* Journal of Applied Physics, 1997. **81**(9): pp. 5878-5886.
[7] Baruchel, J., Buffiere, J.Y., Cloetens, P., Di Michiel, M., Ferrie, E., Ludwig, W., Maire, E., and Salvo, L., *Advances in synchrotron radiation microtomography.* Scripta Materialia, 2006. **55**(1): pp. 41-46.
[8] *ASTM D 7136/D 7136M 07 standard test method for measuring the damage resistance of a fiber-reinforced polymer matrix composite to a drop-weight impact event*. 2007, ASTM International.
[9] Helfen, L., Myagotin, A., Rack, A., Pernot, P., Mikulik, P., Di Michiel, M., and Baumbach, T., *Synchrotron-radiation computed laminography for high-resolution three-dimensional imaging of flat devices.* Physica Status Solidi a-Applications and Materials Science, 2007. **204**(8): pp. 2760-2765.
[10] Helfen, L., Baumbach, T., Mikulik, P., Kiel, D., Pernot, P., Cloetens, P., and Baruchel, J., *High-resolution three-dimensional imaging of flat objects by synchrotron-radiation computed laminography.* Applied Physics Letters, 2005. **86**(7): pp. 071915.
[11] Greenhalgh, E. and Hiley, M., *The assessment of novel materials and processes for the impact tolerant design of stiffened composite aerospace structures.* Composites Part a-Applied Science and Manufacturing, 2003. **34**(2): pp. 151-161.
[12] Takeda, N., Sierakowski, R.L., and Malvern, L.E., *Microscopic observations of cross sections of impacted composite laminates* Composites Technology Review, 1982. **4**(2): pp. 40-44.
[13] Guvenilir, A., Breunig, T.M., Kinney, J.H., and Stock, S.R., *New direct observations of crack closure processes in Al-Li 2090 T8E41.* Philosophical Transactions of the Royal Society of London Series a-Mathematical Physical and Engineering Sciences, 1999. **357**(1761): pp. 2755-2775.
[14] Wright, P., Moffat, A., Sinclair, I., and Spearing, S.M., *High resolution tomographic imaging and modelling of notch tip damage in a laminated composite.* Composites Science and Technology, 2010. **70**(10): pp. 1444-1452.
[15] Bathias, C. and Cagnasso, A., *Application of X-Ray Tomography to the Nondestructive Testing of High-Performance Polymer Composites.* Damage Detection in Composite Materials, 1992. **1128**: pp. 35-54.
[16] Scott, A.E., Mavrogordato, M., Wright, P., Sinclair, I., and Spearing, S.M., *In situ fibre fracture measurement in carbon-epoxy laminates using high resolution computed tomography.* Composites Science and Technology, 2011. **71**(12): pp. 1471-1477.
[17] Enfedaque, A., Molina-Aldareguia, J.M., Galvez, F., Gonzalez, C., and Llorca, J., *Effect of Glass Fiber Hybridization on the Behavior Under Impact*

of Woven Carbon Fiber/Epoxy Laminates. Journal of Composite Materials, 2010. **44**(25): pp. 3051-3068.

Chapter 5

Partial volume correction for approximating crack-opening displacements in CFRP material obtained from micro-focus X-ray CT scans

This chapter presents a partial volume correction technique that applies a measurement weighting based on grey scale intensity values, allowing crack-opening displacements (CODs) to be better estimated in micro-focus computed tomography (µCT) scans. These were tested on 3D data obtained from two separate µCT scanners on particle-toughened and untoughened carbon fibre material subjected to low velocity impact. Direct comparisons of COD estimations were made with higher resolution measurements obtained using synchrotron radiation computed tomography (SRCT) scans taken at the European Synchrotron Radiation Facility (ESRF). In this study, partial volume correction is reported to improve the accuracy of these measurements to within 20 % of SRCT measurements, whereas measurements based on counting interconnected voxels representing a detectable crack are reported to consistently overestimate crack-openings by up to 500 %. Scatter in estimations was dependent on material type, noise, and artefacts associated with µCT volumes. The development and understanding of this technique enabled crack-opening displacements to be better measured in chapter 9.

5.1 Introduction

Industrial CT scanners have made it possible to routinely extract 3D damage features in structural materials such as carbon fibre composites [1]. Common operating voxel resolutions of the order of 5 microns have been used in previous

studies on impacted composites [2-7]; the significant limiting factor affecting resolution is the X-ray focal spot size and specimen size [8]. Whilst this resolution is useful for identifying the components of composite damage, quantification of key features, such as crack-opening displacements (CODs) within impacted carbon fibre materials requires a higher fidelity. Informed use of the partial volume effect provides a means so that sub-resolution features may still be detected and quantified [2]. Crack-opening and crack shear displacements are important parameters in micromechanical modelling of composite damage and failure. Accurate experimental measurement of these parameters in three-dimensions (3D) is enabled by computed tomography, and allows the validation and calibration of models [9] and to calculate effective stress intensities at the crack tip [10].

The partial volume effect occurs when two or more phases with differing density are represented within a single voxel leading to an effective averaging of attenuation coefficients; this is typically critical if the object or region's dimensions are at the voxel resolution or less (assuming other forms of un-sharpness are under-sampled by the voxel dimensions) [11-13]. Depending on the contrast difference between the two phases, this has an influence on the smallest detectable feature. For the detectability of cracks in composites it has been reported that openings down to 20 % of the voxel resolution in CT scans can be detected, and by using contrast enhancement agents, this may be further reduced to 5 %. Contrast agents require all cracks to be interconnected up to the surface of the material to allow full penetration of the dye [2]. For internal damage, such as that sustained in impact loading, this is often not the case. Furthermore, in cases for which *in situ* load-stepped CT experiments are combined with digital volume correlation (DVC), the detectability of cracks can be greatly improved by quantifying the mechanical effects of cracking in addition to direct physical imaging [14, 15]. However, these rely on comparisons between multiple scans rather than a single volume.

The partial volume averaging effect may lead to inaccuracies in the estimation of object sizes due to the dependence on the feature's location on the image grid. Figure 5.1(a and b) shows schematically how this affects crack-opening measurements. Since a crack that partially fills a voxel may be treated as occupying a full voxel when interconnected measurements are taken,

overestimations in measurements occur [16-18]. This phenomenon is particularly noticeable at phase boundaries that fall within a voxel, leading to intermediate voxel intensities dependant on the percentage of “fill” between both phases [16, 19, 20].

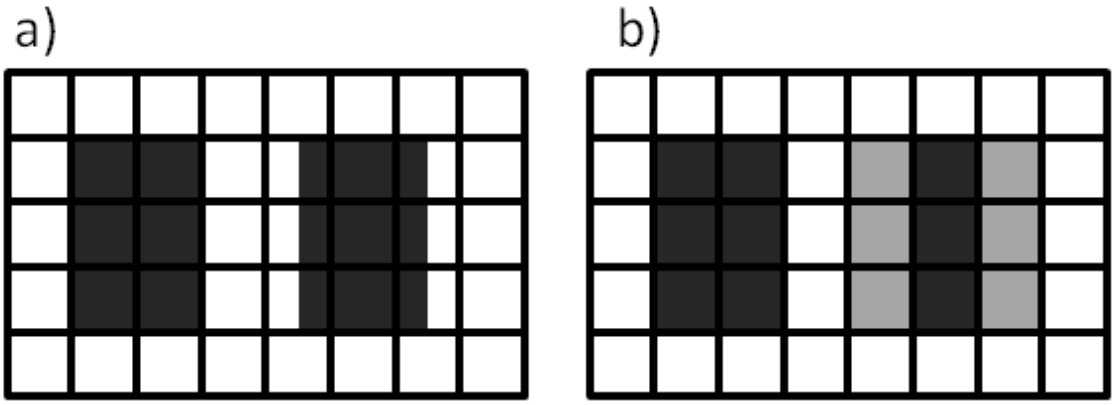

Figure 5.1: Schematic showing (a) positions of an actual crack relative to the image grid, (b) corresponding rendered image. The crack boundaries that partially spill over and fill neighbouring voxels are rendered with less intensity at the edges and result in an inaccurate width estimate, this leads to consistent overestimates when measured by counting interconnected voxels.

Where the crack-opening approaches the limit of detectability, in reported cases down to 20 % of the voxel resolution, measurements of counting interconnected regions will overestimate the crack-opening by up to ten times. If the smallest detectable crack were to fill partially two neighbouring voxels, measurements would include the crack as fully occupying both voxels leading to a large overestimation. Scanning at higher voxel resolutions does reduce these errors [16], however the trade-off between resolution and field of view [8], and the high barriers to entry to equipment capable of higher resolution such as synchrotron radiation computed tomography (SRCT) often limits this option.

A partial volume correction algorithm has been used in previous studies to estimate crack-openings on Al-Li fatigue cracks in work by Ignatiev *et al*. [21] and Guvenilir *et al* [22, 23]. This work utilised attenuation coefficients to calculate an estimate for the measured fraction of crack-opening. Work similar to this by Heckel *et al*. [19] utilised linear interpolation based on intensity and applied a weighting on the voxel volume at feature boundaries; this has been reported to increase

accuracy and repeatability in volume measurements of liver metastases and lymph nodes obtained in CT scans.

The work presented in the present chapter uses the same techniques by mapping grey scale intensities to a linear relationship between the material and crack levels to allow an adjusted length to be calculated for that voxel representing a crack-opening. To the author's knowledge, this is the first study applying this technique on cracks in carbon fibre composite materials and unlike previous work on this topic, this chapter calibrates partial volume correction estimates to higher voxel resolution SRCT scans enabling this technique to be tested more rigorously.

5.2 Test procedure

The testing procedures are briefly outlined here. For further details on the materials and testing procedures, refer to chapter 3.

Two 1 mm thick carbon fibre reinforced epoxy materials were tested, consisting of a particle-toughened and untoughened systems. Coupons were impacted at 0.6 J and 1.2 J for the particle-toughened and untoughened systems respectively. In preparation for SRCT and µCT scans, two 4.5 mm wide 'matchsticks' were cut along the length of the coupon; one through the impact centre and one to the right of the previous cut. For each system, 'matchsticks' were stacked in pairs and scanned at the impact site. Two µCT machines were used in this study and consisted of a Nikon^{TM} HMX and Benchtop system. For comparison of measurements, a higher resolution SRCT scan was performed at the ESRF on Beamline ID19. The settings used can be found in section 3.8.4.

The same test coupons were scanned for all three imaging facilities and no penetrants or any other treatment was applied to the specimens. Whilst the full lengths of the cracks were not captured due to the limited field of view, the same regions of interest were obtained with each of the three imaging facilitates. This enabled the same cracks from the same specimens to be directly compared across the different imaging facilities.

5.3 Partial volume COD approximation technique

As the size of the crack-opening approaches the voxel resolution, a combination of background material and crack features are sampled and averaged within a voxel. Visually, the crack may appear faint, with a limited contrast against the surrounding material. This effect is shown in the lower resolution HMX scan in Figure 5.2(c) with a higher resolution SRCT scan of the same crack shown in Figure 5.2(b). Figure 5.3 illustrates this behaviour; a line plot across a ~3 micron crack exhibits a dip in grey scale value centred at 23 μm, which is indicative of the presence of a crack. The SRCT scan shows a sharp contrast between the crack and background material over a narrow band of voxels. In the example given in Figure 5.2(b) white fringes are present at the edge of the crack representing the edge detection regime. In this particular case, the fringe was more pronounced on the left hand side of the crack due to slight variations in path length through irregular material containing multiple phases, which has a control on the interference effect when reconstructed. With the lower resolution μCT scans, the crack intensity diminishes towards the background material mean grey scale, with the dip spread over a wider range of voxels, due to the crack partially filling the voxels.

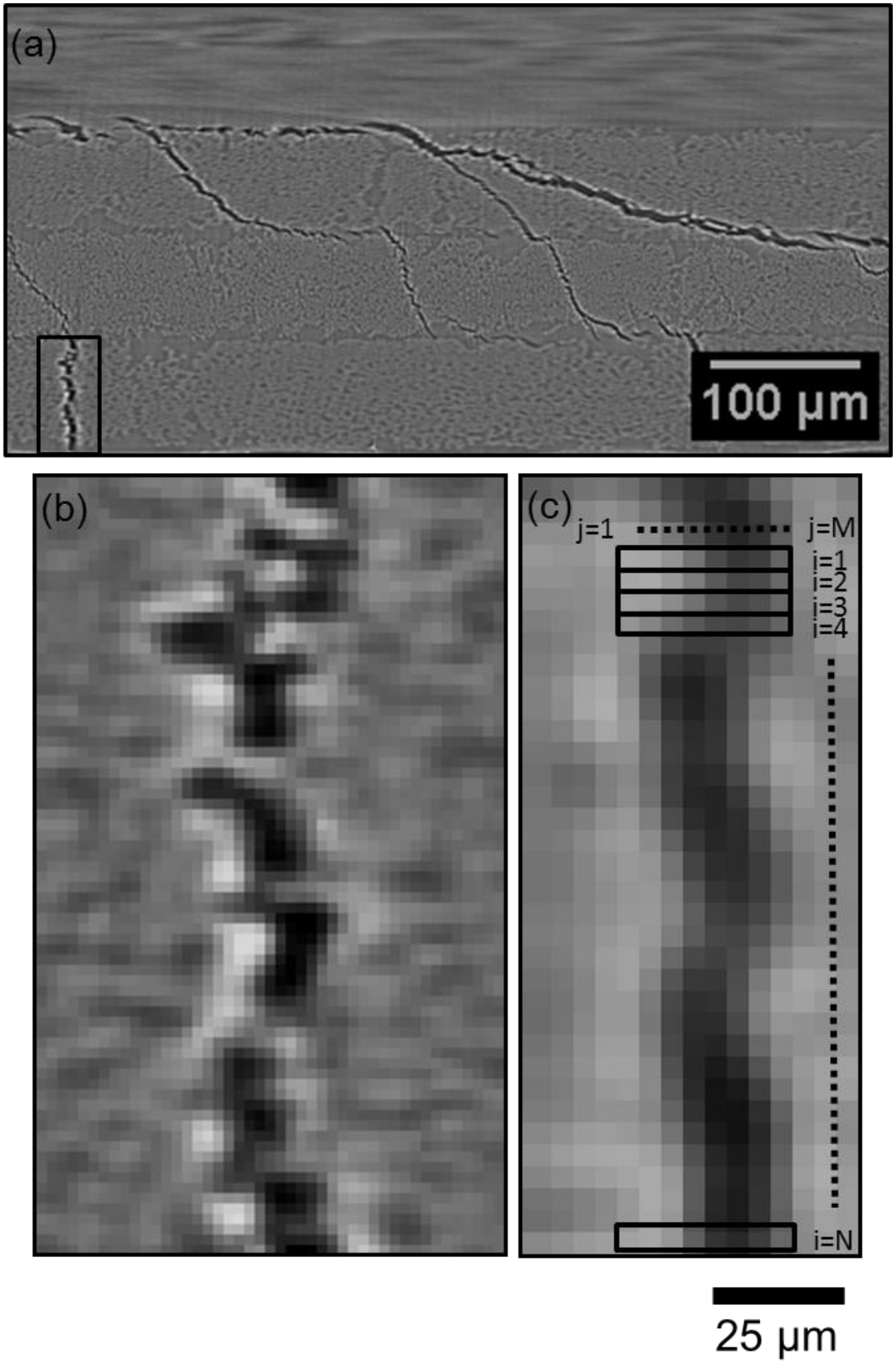

Figure 5.2: (a) SRCT cross-section showing matrix cracks and delaminations, the box highlights a close up of this region in (b) and for an HMX scan of the same crack in (c). A schematic in (c) also shows the sampled rows and columns used to estimate the COD in equation 1.

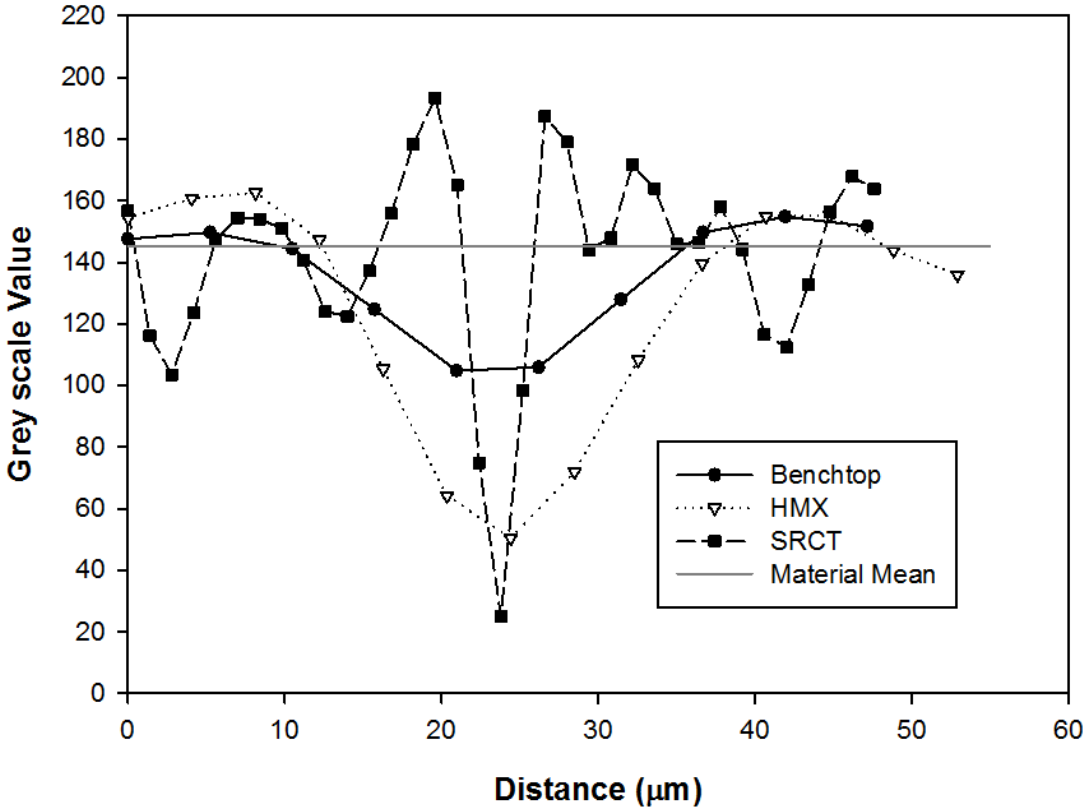

Figure 5.3: Grey scale intensity line plot across the same crack obtained from three different µCT scans.

By taking the grey scale intensity of a voxel partially containing a crack, the percentage of crack and material occupied within the voxel can be approximated as a linear combination of grey scales representing the crack (*i.e.* air) and material. Provided isotropic voxels are used, this calculated percentage can be weighted to the corresponding length of the voxel. A linear relationship between the adjusted length of a voxel and the two grey scale intensity values consisting of the crack (air) and the material is represented by the relationship in equation (5-1):

$$\delta_{ij} = \begin{cases} \delta_{res}, & \text{if } g_{ij} \leq g_{air} \\ 0, & \text{if } g_{ij} \geq g_{mat} \\ \delta_{res} - \delta_{res}\left(\dfrac{g_{ij} - g_{air}}{g_{mat} - g_{air}}\right), & \text{if } g_{air} < g_{ij} < g_{mat} \end{cases} \quad (5\text{-}1)$$

This relationship can be applied to approximate the adjusted length δ_{ij} at voxel ij where δ_{res} represents the length of one voxel resolution and g_{ij} is the grey scale value at voxel ij. To obtain the grey scale constant of the material, g_{mat}, a region representing material away from the crack is selected and the mean grey scale value is used; for the grey scale constant of the crack, g_{air} , the grey scale value of air at the centre of a large crack-opening known not to be affected by any partial volume effects is used. When the sampled grey scale value is equal to or less than g_{air}, it is assumed that the whole voxel contains a crack and an adjusted width is applied equal to the width of the voxel resolution. Similarly if the voxel grey scale is equal to or greater than g_{mat}, it is assumed that no cracks are contained within that voxel and a zero length is applied. A grey scale value between the two limiting values will result in an adjusted length being applied based on the proportion of crack and material contained within the voxel.

After calculation of the adjusted length δ_{ij} at voxel ij, these adjustments can be applied to approximate the mean local COD, $\bar{\delta}$, using equation (5-2):

$$\bar{\delta} = \frac{1}{N}\sum_{i=1}^{N}\sum_{j=1}^{M}\delta_{ij} \qquad (5\text{-}2)$$

In the case of a vertical crack such as that shown with a schematic in Figure 5.2(c), the crack-opening on each horizontal row of voxels, *i,* is calculated by summing the adjusted lengths δ_{ij} at each voxel position along the row, *j*, in which M represents the total number of voxels in the row. The CODs from each respective row are then summed together and divided by the number of rows N to give the mean estimated COD value $\bar{\delta}$ across all the rows. It is acknowledged that the COD varies at different positions along a crack; hence a local region was cropped and sampled to determine the mean COD at a particular position, *e.g.* the cropped selection indicated by the box in Figure 5.2(a).

To estimate the COD profile along the length of the crack in the k direction (*i.e.* perpendicular to the plane of an image “slice” such as shown in Figure 5.2), and to give a 3D representation, the equation was applied to one 2D slice at a time, thus

obtaining a displacement for each slice along the length of the crack, equal to the voxel depth.

5.3.1 Measurements of CODs by counting interconnected voxels

To achieve COD measurements from µCT (HMX and Benchtop) image volumes, both matrix cracks and delaminations were segmented and binarised by thresholding. In a conventional approach, an ISO50% threshold value is used consisting of a value exactly halfway between the mean air and material grey scale values [24]. The ISO50% approach was used on SRCT scans using a threshold value halfway between the light and dark fringes of the crack.

In this study, the majority of crack-openings in µCT scans were around or below the voxel resolution leading to partially filled cracks. Segmentation by the ISO50% approach would exclude all partially filled cracks with voxels containing more than 50% material, therefore, although the cracks could be detected, it will show zero crack-opening displacement using the ISO50% method.

To segment all detectable cracks in µCT scans, a threshold value was chosen to exclude the material. This was achieved by measuring the grey scale values within a region of composite material containing no cracks and taking the mean minus two standard deviations of the grey scale values, excluding ~95 % of the material. The crack was segmented by including values less than this calculated threshold value.

Voxels representing the segmented cracks were measured across the opening at all points across the crack and then averaged to calculate the mean crack-opening; this is referred to in this study as the ‘counting’ method. In SRCT scans, due to COD measurement variations at different points across the crack, error bars representing the standard error of the mean COD are reported. This technique was applied to both the 2D and 3D COD measurements. It should be noted that the edge detection fringes and partial volume effects on the SRCT scans can also influence the accuracy of these measurement, up to the length of a

single voxel; therefore the COD is taken as an average across multiple measurements.

5.3.2 Comparisons between measured COD mean values

In order to allow consistent comparisons, no modifications were made such as rotating, tilting, or repositioning the reconstructed volumes; which could affect the results by resampling the voxel intensities and positions. Direct comparisons were made from raw 8-bit reconstructions on cracks obtained at identical positions between scans; with both µCT locations within one voxel of the equivalent position in the SRCT scan. This was achieved by measurements of the crack's position relative to fiducial features present in the scan such as small voids, inclusions, and other crack positions present in the volume.

By taking the mean COD obtained from SRCT measurements as the benchmark value, error values were calculated for the estimates obtained from the two µCT scans for each crack location. This allowed an assessment to be made of the partial volume COD approximation technique and also allowed comparisons with the method of counting interconnected voxels. Percentage errors were not calculated along 3D crack lengths. This is due to the different voxel resolutions used between the three CT scans resulting in the cross-sectional spacing no longer coinciding beyond the first slice, therefore preventing direct COD comparison using this method in the through-thickness direction along the length of the crack. Instead the general trends between COD and crack length are presented and compared.

5.4 Results and discussion

5.4.1 Partial volume COD assessment

Figure 5.4(a) shows an example of a delamination as indicated by the box: close up SRCT and µCT (HMX System) images of this delamination are shown in (b-i)

and (c-i) respectively and has been binarised by thresholding in (b-ii) and (c-ii). It is clear that due to the crack partially filling neighbouring voxels, segmentation of detectable cracks (c-ii) has captured a region larger than the true opening of the crack shown in (c-i), and when the opening is measured as indicated by the arrow, it is overestimated.

Measurement of the CODs of the delamination in Figure 5.4 is shown in a plot in Figure 5.5 as a function of voxel position along the crack width. The COD measurement from µCT scanning is shown to overestimate the crack-opening by approximately three times. Applying the partial volume correction to the HMX scan, the estimated COD is comparable to SRCT measurements. Interestingly, some local variation in the SRCT COD measurements are observed depending on the position of the measurement due to the nature of the crack morphology; these variations have been smoothed by the partial volume correction estimation and fall within the peak to peak regions in the SRCT measurements. When the average CODs are considered consisting of 4.9 µm, 4.8 µm and 17.4 µm for the SRCT, µCT partial volume correction and µCT counting measurements respectively, it is clear that simple linear partial volume considerations provide a good estimation of crack-opening from the lower resolution the µCT scan.

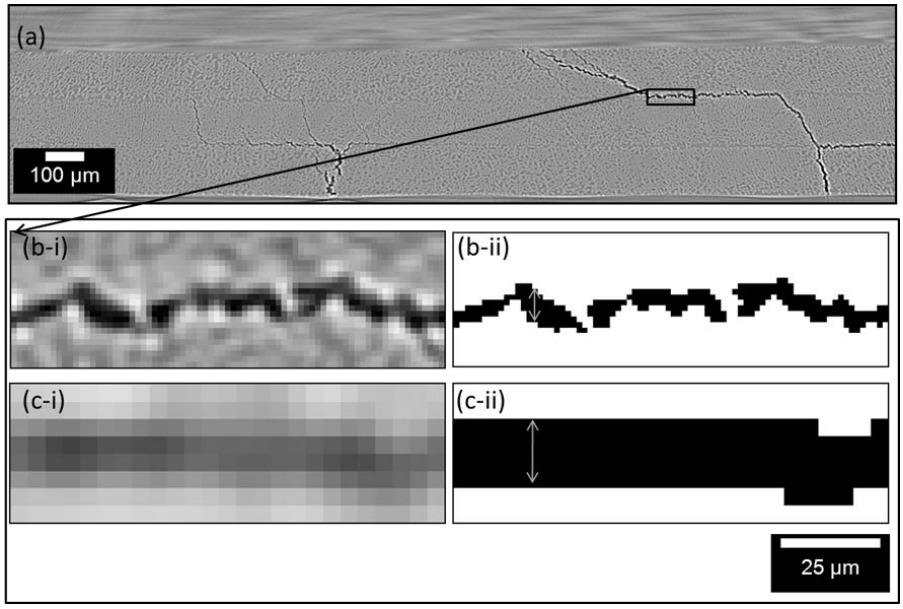

Figure 5.4: An example of counting interconnected voxels to measure the COD. A cross-section of this damage is shown in the SRCT scan in (a), the box indicates a close up of this SRCT region in (b-i) and for an HMX scan in (c-i). Binarised images from these cracks are shown in (b-ii) and (c-ii), the arrow indicating the method of counting interconnected voxels representing the COD.

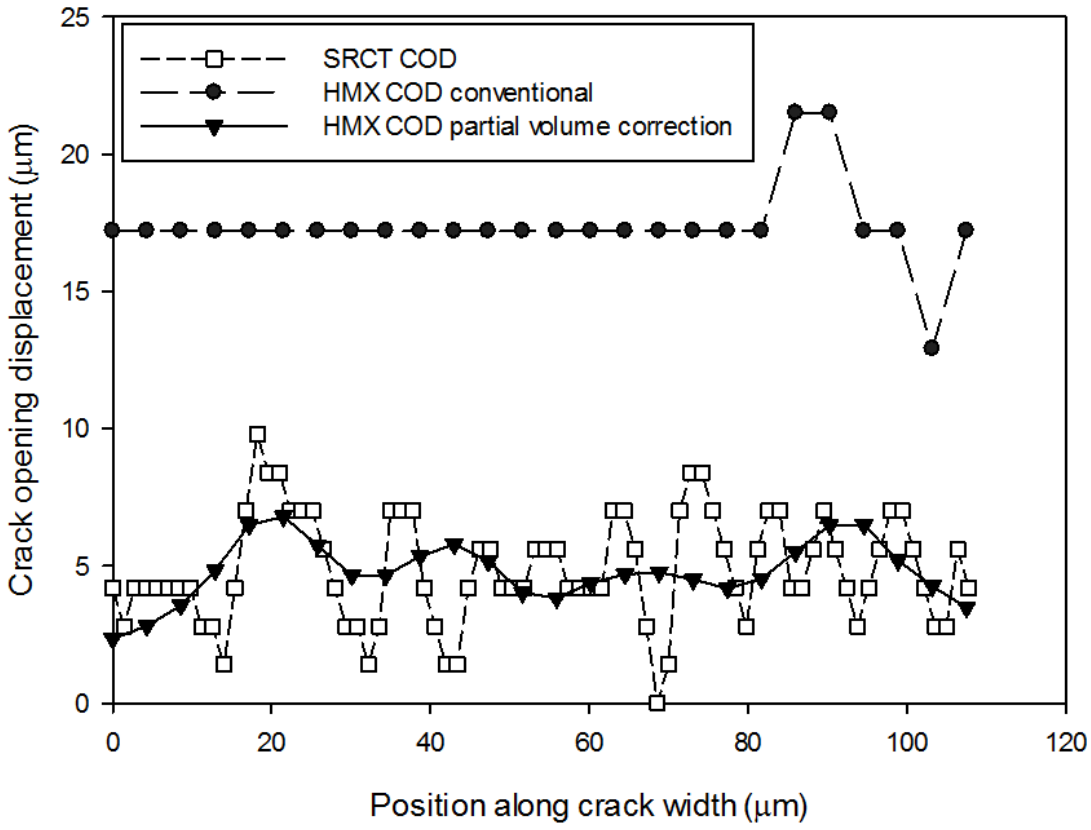

Figure 5.5: COD measurements of the delamination shown in Figure 5.4. SRCT and HMX COD were measured at each voxel along the width of the crack. A partial volume correction shows an improvement to the HMX COD measurement.

5.4.2 Average COD comparisons on single slice cracks

The partial volume correction algorithm was applied to μCT scans to estimate the average CODs on several 2D matrix cracks and delaminations. These were compared to counting COD measurements and SRCT measurements. The results of crack-opening measurements are shown in Figure 5.6(a) for particle-toughened and Figure 5.6(b) untoughened resin systems. Standard error bars indicated on SRCT COD measurements were larger in cases in which the cracks were more open, suggesting larger variations in crack-openings at these levels. R-squared values on partial volume correction estimates were 0.68 and 0.87 for the toughened and non-toughened systems respectively. This scatter is believed to be principally caused by the ligamented and non-continuous delaminations, characteristic of particle-toughening that could be detected in the SRCT scan but not in the μCT scans. This led to bridged sites that were included in the partial

volume correction leading to underestimations of the mean crack-opening. Additional sources of scatter in the data include noise, beam hardening, ring artefacts, non-linearity in X-ray detector response and the simplicity of the algorithm which neglects the three-dimensionality of the partial volume effect.

It should be noted that due to the use of different voxel resolutions across the three imaging facilities, there are approximately three to four SRCT cross-sectional slices to one µCT slice. Despite this issue, this has been shown not to have affected the partial volume correction results. It is probable that as the crack path moves through the µCT slice, the crack-opening does not vary significantly at these voxel sizes, therefore voxels contain similar proportions of crack and material between µCT and SRCT scans.

In comparison, COD measurements using the “counting” method on µCT scans overestimated CODs by up to five times. There is no correlation between the measurements obtained through counting connected voxel measurements in HMX and Benchtop scans and the measured SRCT scan. This shows the unreliability in using the counting technique in detectable but partially-filled cracks to gauge crack-openings. The use of partial volume correction is shown to reduce these significant overestimations.

Percentage errors comparing µCT COD estimates to SRCT measurements are shown in Figure 5.7 and demonstrate good approximations within 20 % error. Discontinuities in the crack generally led to underestimations either when the COD was below approximately 4 µm, or in the particle-toughened system where delamination crack ligaments were present. The discontinuous behaviour of the cracks led to lower proportion of crack partially filling a voxel and hence an underestimation of the COD.

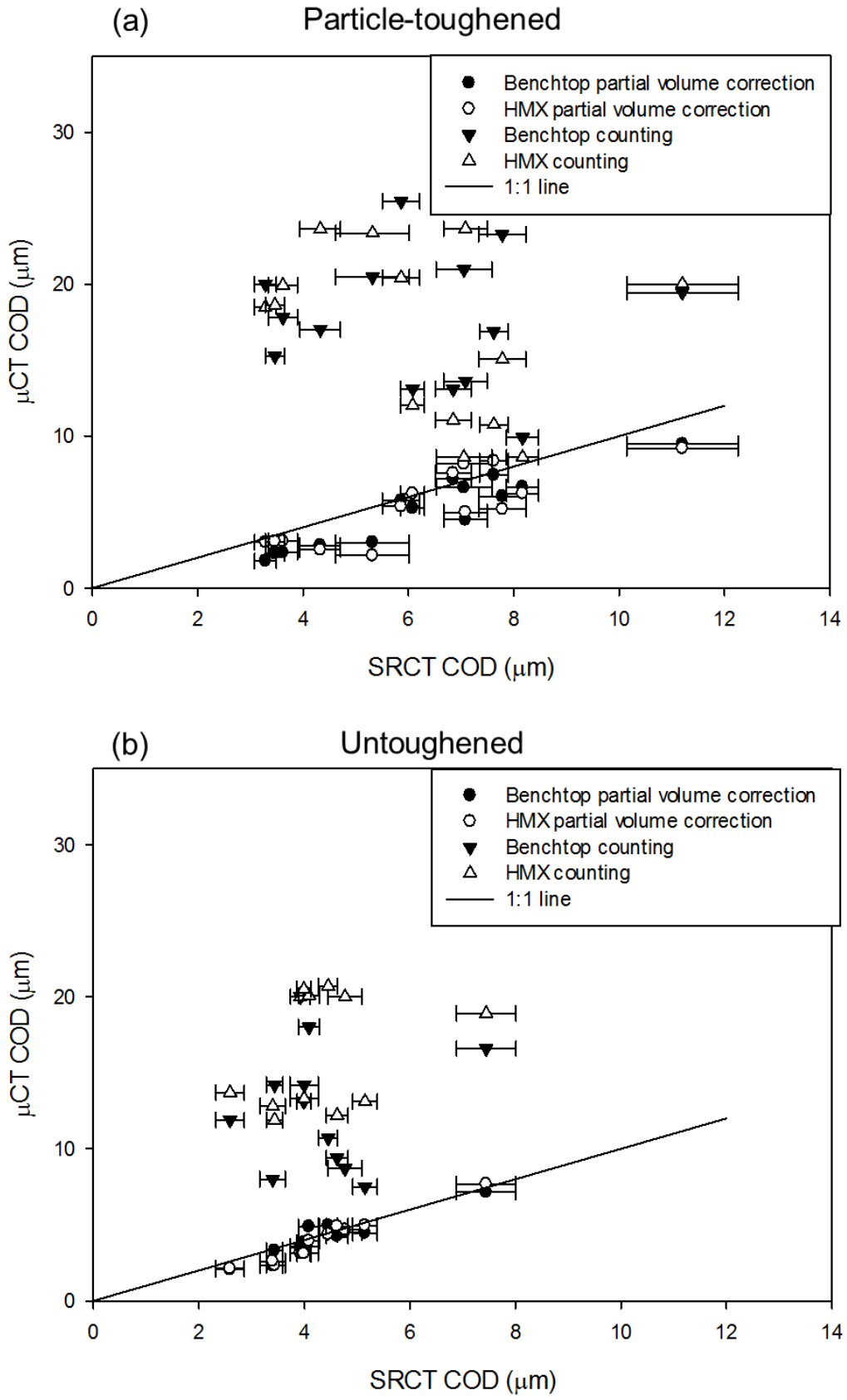

Figure 5.6: Graph showing partial volume corrected and counting COD measurements obtained from µCT scans directly compared to SRCT COD measurements for (a) toughened and (b) non-toughened specimens.

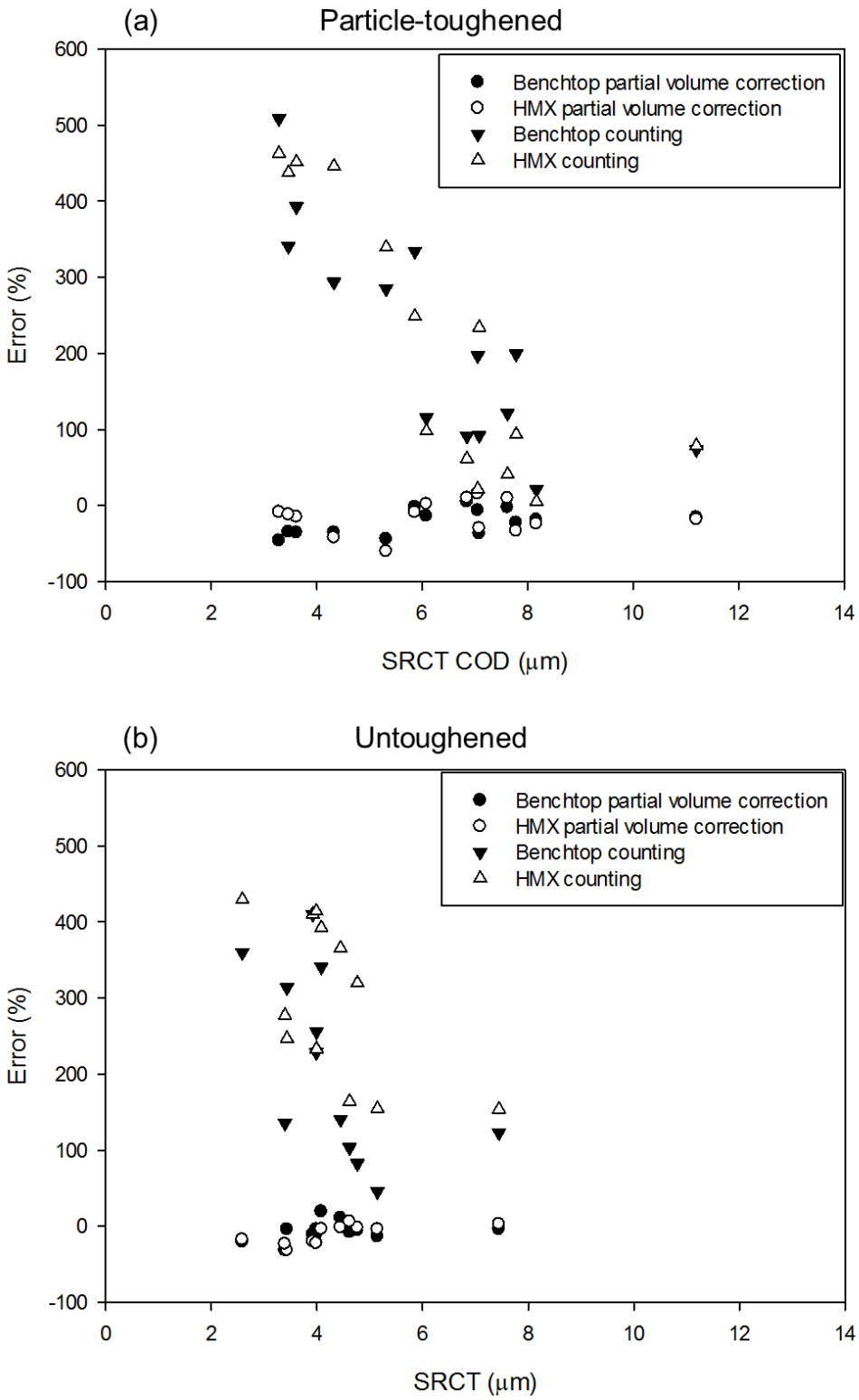

Figure 5.7: COD percentage errors for counting and partial volume corrected measurements compared to SRCT measurements for (a) particle-toughened and (b) untoughened material

For counting interconnected voxel measurements in µCT scans, the percentage errors increase with smaller crack-openings up to 500 % and all measurements were overestimated. This demonstrates the unreliability of this method for measuring crack-openings where the voxel resolution is within two to three voxels of the feature size, and the use of partial volume correction is shown it provide better accuracy.

5.4.3 3D COD assessments and comparisons

Multiple COD measurements were taken along the length of the crack at arbitrary starting and ending positions that fell within the field of view of the CT scans. These are shown in Figure 5.8(a-d) in which partial volume COD corrections are applied to HMX and Benchtop µCT scans, and the resulting estimates are compared to those obtained from SRCT data. Different crack types were measured consisting of delaminations as shown in Figure 5.8(a & b) and matrix cracks as shown in Figure 5.8(c & d). The COD measurements were made on the two materials; particle-toughened as shown in Figure 5.8(a & c) and untoughened as shown in Figure 5.8(b & d).

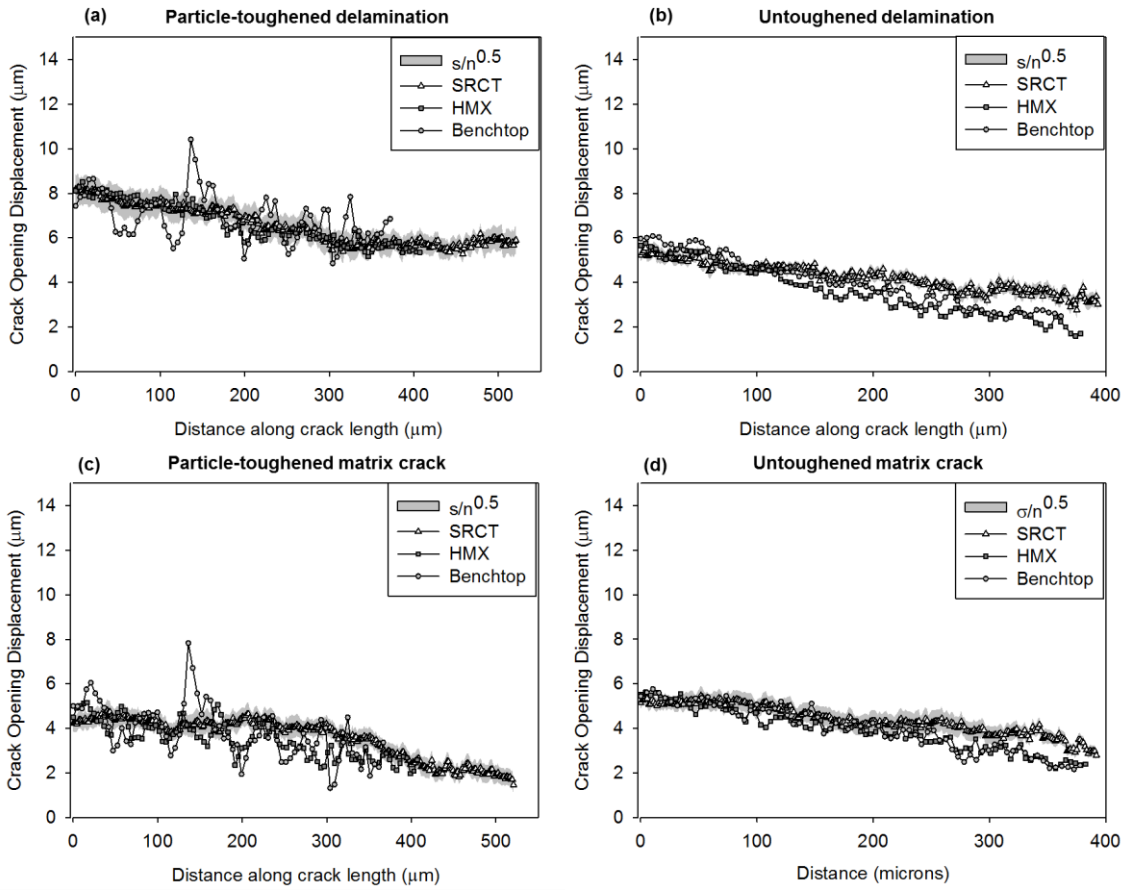

Figure 5.8: COD measurements along the length of a crack comparing partial volume correction techniques applied to HMX and Benchtop CT cracks to SRCT measurements.

All measurements show similarly decreasing crack-openings towards the crack tip. Comparisons between estimates from µCT observations to SRCT measurement show good COD correlations along the crack towards the crack tip. Divergence from the SRCT measurements started to occur when the COD was less than approximately 4 µm leading to underestimations of the COD. This again was attributed to cracks becoming discontinuous below this threshold. The delamination COD estimations for toughened material, as shown in Figure 5.8(c), had the greatest scatter for both Benchtop and HMX µCT; this was attributed to the ligamented, non-continuous delamination associated with particle-toughening.

The presence of ring artefacts created noticeable spiked peaks, particularly in the Benchtop µCT results in Figure 5.8(a & c). In this case the cracks were in a region of ring artefacts that affected the local grey scale intensity [13] which led to erroneous COD measurements. Care therefore needs to be taken to check the

presence of neighbouring artefacts when taking partial volume correction estimations that are dependent on grey scale intensity values.

Again, as discussed earlier, when the partial volume correction method is compared to the method of counting interconnected voxels representing the COD, improvements to the accuracy are achieved as illustrated in Figure 5.9.

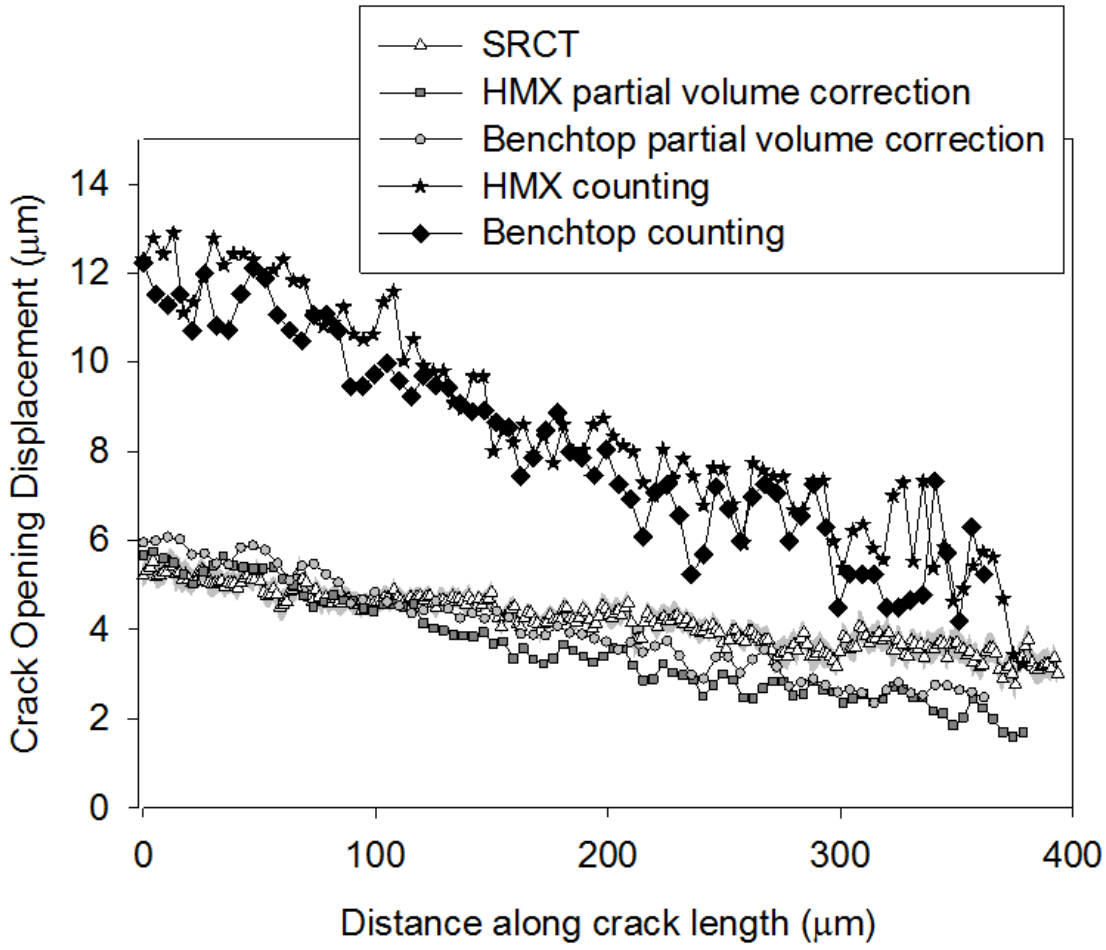

Figure 5.9: Comparison between both the counting and partial volume correction method to calculate COD on Benchtop and HMX CT scans for an untoughened delamination. It is clear the counting method vastly overestimates COD by up to a factor of two in this instance.

5.5 Conclusions

Crack-opening displacement measurements were estimated on µCT scans of impacted CFRP material by applying a partial volume correction based on grey scale intensities and weighting this to the voxel length. In 2D studies, partial volume estimates of CODs correlated well with measurements taken from higher resolution SRCT scans. This method is significantly more accurate (within 20 % of

SRCT measurements) than the more straightforward approach of simply counting interconnected voxels from detectable but partially-filled cracks, which overestimated CODs by up to 500 %. Underestimations occurred when the cracks became discontinuous, this was typically when the crack-openings were less than approximately 4 µm, and in the toughened system where particles created crack ligaments in the delamination. Additional contributions to errors also include noise, non-linearity in X-ray detector response, CT artefacts (ring artefacts and beam hardening), and the three-dimensional nature of the partial volume averaging process. The partial volume correction technique has been demonstrated as a means to obtain 3D crack-opening profiles along the length of cracks. Good correlations were obtained with SRCT data in estimating crack-openings along the length of the crack. Issues with the measured crack-opening being distorted by ring artefacts led to erroneous results indicated by large peaks in the measurements. Overall the use of partial volume corrections has been shown to be a viable method to obtain quantitative estimates of crack-opening displacements in composite materials using micro-focus computed tomography.

5.6 References

[1] Sugimoto, S., Aoki, T., Iwahori, Y., and Ishikawa, T., *Nondestructive evaluation of composites using Micro-Focused X-Ray CT Scanner.* Review of Progress in Quantitative Nondestructive Evaluation, Vols 24A and 24B, 2005. **760**: pp. 1081-1086.

[2] Schilling, P.J., Karedla, B.P.R., Tatiparthi, A.K., Verges, M.A., and Herrington, P.D., *X-ray computed microtomography of internal damage in fiber reinforced polymer matrix composites.* Composites Science and Technology, 2005. **65**(14): pp. 2071-2078.

[3] Tan, K.T., Watanabe, N., and Iwahori, Y., *X-ray radiography and micro-computed tomography examination of damage characteristics in stitched composites subjected to impact loading.* Composites Part B-Engineering, 2011. **42**(4): pp. 874-884.

[4] Girshovich, S., Gottesman, T., Rosenthal, H., Drukker, E., and Steinberg, Y., *Impact Damage Assessment of Composites.* Damage Detection in Composite Materials, 1992. **1128**: pp. 183-199.

[5] Bathias, C. and Cagnasso, A., *Application of X-Ray Tomography to the Nondestructive Testing of High-Performance Polymer Composites.* Damage Detection in Composite Materials, 1992. **1128**: pp. 35-54.

[6] Pandita, S.D., Falconet, D., and Verpoest, I., *Impact properties of weft knitted fabric reinforced composites.* Composites Science and Technology, 2002. **62**(7-8): pp. 1113-1123.

[7] Enfedaque, A., Molina-Aldareguia, J.M., Galvez, F., Gonzalez, C., and Llorca, J., *Effect of Glass Fiber Hybridization on the Behavior Under Impact of Woven Carbon Fiber/Epoxy Laminates.* Journal of Composite Materials, 2010. **44**(25): pp. 3051-3068.
[8] Arabi, H., Asl, A.R.K., and Aghamiri, S.M., *The effect of focal spot size on the spatial resolution of variable resolution X-ray CT scanner.* Iranian Journal of Radiation Research, 2010. **8**(1): pp. 37-43.
[9] Wright, P., Moffat, A., Sinclair, I., and Spearing, S.M., *High resolution tomographic imaging and modelling of notch tip damage in a laminated composite.* Composites Science and Technology, 2010. **70**(10): pp. 1444-1452.
[10] Withers, P.J., Bennett, J., Hung, Y.C., and Preuss, M., *Crack opening displacements during fatigue crack growth in Ti-SiC fibre metal matrix composites by X-ray tomography.* Materials Science and Technology, 2006. **22**(9): pp. 1052-1058.
[11] Hoffman, E.J., Huang, S.C., and Phelps, M.E., *Quantitation in Positron Emission Computed-Tomography .1. Effect of Object Size.* Journal of Computer Assisted Tomography, 1979. **3**(3): pp. 299-308.
[12] Plewes, D.B. and Dean, P.B., *The Influence of Partial Volume Averaging on Sphere Detectability in Computed-Tomography.* Physics in Medicine and Biology, 1981. **26**(5): pp. 913-919.
[13] Barrett, J.F. and Keat, N., *Artifacts in CT: Recognition and Avoidance.* Radiographics, 2004. **24**(6): pp. 1679-1691.
[14] Gates, M., Lambros, J., and Heath, M.T., *Towards High Performance Digital Volume Correlation.* Experimental Mechanics, 2011. **51**(4): pp. 491-507.
[15] Buffiere, J.Y., Maire, E., Adrien, J., Masse, J.P., and Boller, E., *In Situ Experiments with X ray Tomography: an Attractive Tool for Experimental Mechanics.* Experimental Mechanics, 2010. **50**(3): pp. 289-305.
[16] Soret, M., Bacharach, S.L., and Buvat, I., *Partial-volume effect in PET tumor imaging.* Journal of Nuclear Medicine, 2007. **48**(6): pp. 932-945.
[17] Oliveira, C.A.P., Meurer, M.I., Pascoalato, C., and Silva, S.R.C., *Cone-beam computed tomography analysis of the apical third of curved roots after mechanical preparation with different automated systems.* Brazilian Dental Journal, 2009. **20**: pp. 376-381.
[18] Pham, D.L., Xu, C.Y., and Prince, J.L., *Current methods in medical image segmentation.* Annual Review of Biomedical Engineering, 2000. **2**: pp. 315-+.
[19] Heckel, F., Dicken, V., Bostel, T., Fabel, M., Kiessling, A., and Peitgen, H.O., *Partial volume correction for volume estimation of liver metastases and lymph nodes in CT scans using spatial subdivision.* Medical Imaging 2010: Image Processing, 2010. **7623**.
[20] Conradi, S.H., Lutey, B.A., Atkinson, J.J., Wang, W., Senior, R.M., and Gierada, D.S., *Measuring Small Airways in Transverse CT Images: Correction for Partial Volume Averaging and Airway Tilt.* Academic Radiology, 2010. **17**(12): pp. 1525-1534.
[21] Ignatiev, K.I., Davis, G.R., Elliott, J.C., and Stock, S.R., *MicroCT (microtomography) quantification of microstructure related to macroscopic behaviour - Part 1 - Fatigue crack closure measured in situ in AA 2090*

compact tension samples. Materials Science and Technology, 2006. **22**(9): pp. 1025-1037.
[22] Guvenilir, A., Breunig, T.M., Kinney, J.H., and Stock, S.R., *New direct observations of crack closure processes in Al-Li 2090 T8E41.* Philosophical Transactions of the Royal Society of London Series a-Mathematical Physical and Engineering Sciences, 1999. **357**(1761): pp. 2755-2775.
[23] Guvenilir, A., Breunig, T.M., Kinney, J.H., and Stock, S.R., *Direct observation of crack opening as a function of applied load in the interior of a notched tensile sample of Al-Li 2090.* Acta Materialia, 1997. **45**(5): pp. 1977-1987.
[24] Kiekens, K., Welkenhuyzen, F., Tan, Y., Bleys, P., Voet, A., Kruth, J.P., and Dewulf, W., *A test object with parallel grooves for calibration and accuracy assessment of industrial computed tomography (CT) metrology.* Measurement Science & Technology, 2011. **22**(11).

Chapter 6

Three-dimensional assessment of low velocity impact damage in thin particle-toughened composite laminates

Results are presented studying the contribution of particle-toughening to impact damage resistance in carbon fibre reinforced polymer materials. Micro-focus X-ray computed tomography and synchrotron radiation computed laminography were used to provide a novel, multiscale approach for assessing impact damage. Thin (1 mm thick) composite plates containing either untoughened or particle-toughened resin systems were subjected to low velocity impact. Damage was assessed three-dimensionally at voxel resolutions of 0.7 µm and 4.3 µm using SRCL and µCT respectively, the former being an innovative approach to the laterally extended geometry of CFRP plates. Observations and measurements taken from µCT scans captured the full extent of impact damage on both material systems revealing an interconnected network of intra- and inter-laminar cracks. These lower resolution images revealed that particle-toughened systems suppress delaminations with little effect on intra-laminar damage. The higher resolution images revealed the contribution of particle toughening by crack deflection and bridging. The understanding of the key toughening micromechanisms in this chapter enabled regions of interest to be identified for work in chapter 7 and led to the development of quantification techniques.

6.1 Introduction

It has been shown that the inclusion of thermoplastic toughening particles in the resin of carbon fibre composites can lead to improved toughness in simple delamination fracture tests [1]. The mechanisms of particle-toughening include: crack deflection, crack bridging, crack-tip blunting, particle-matrix interface

debonding, and particle-induced localised yielding [2-9]. Whilst these toughening micromechanisms are understood, it is less clear as to what toughening mechanisms are present in particular systems and their relative contributions to the overall toughness. Additionally, it is less clear how such toughening strategies translate to the more complicated damage state associated with impact loading. This is exacerbated by the more commonly used techniques for impact damage characterisation which typically yield two-dimensional information; *e.g.* ultrasonic C-scan or cross-sectional microscopy. These obscure the three-dimensionality of the interacting damage modes associated with composite impact.

To accommodate the three-dimensional (3D) characteristics of impact damage and to study particle toughening micromechanisms, micro-focus computed tomography (µCT) [10] and synchrotron radiation computed laminography (SRCL) [11] using propagation-based phase contrast [12, 13] have been used in this chapter to understand better the role of particle-toughening and its toughening micromechanisms.

6.2 Materials and testing procedure

The materials and testing procedure are outlined in brief here. For further details please refer to chapter 3.

In this study 1 mm thick coupons were used and consisted of one particle-toughened and one untoughened system; details of which can be found in section 3.1.1. This thickness of material was chosen as it was known to yield good quality images, based on previous laminography studies [26].

To aid like-for-like comparison of microscopic and macroscopic behaviour in untoughened and particle-toughened systems, impact conditions were selected for an equivalent nominal projected damage area (approximately 50 mm^2, as measured by ultrasonic C-scan to result in a 4 *mm* damage radius that could be captured within relatively few CT scans).

To determine the impact energy required for producing the desired projected damage area; coupons were impacted at a range of impact energies between 0.3 J and 3.0 J, see Figure 6.1. This resulted in impact energies of 0.6 J and 1.2 J

being identified for the untoughened and particle-toughened coupons respectively to achieve the desired projected damage area (*i.e.* ~50 mm^2), although it should be noted that there is some scatter in the data as indicated by the 95 % prediction intervals. The damage areas exhibited by the particle-toughened system are clearly reduced in comparison to the untoughened sample tests. This is progressively more evident at impact energies of 2 J and above, corresponding to the increasing prevalence of delamination in the untoughened material at higher impact energies.

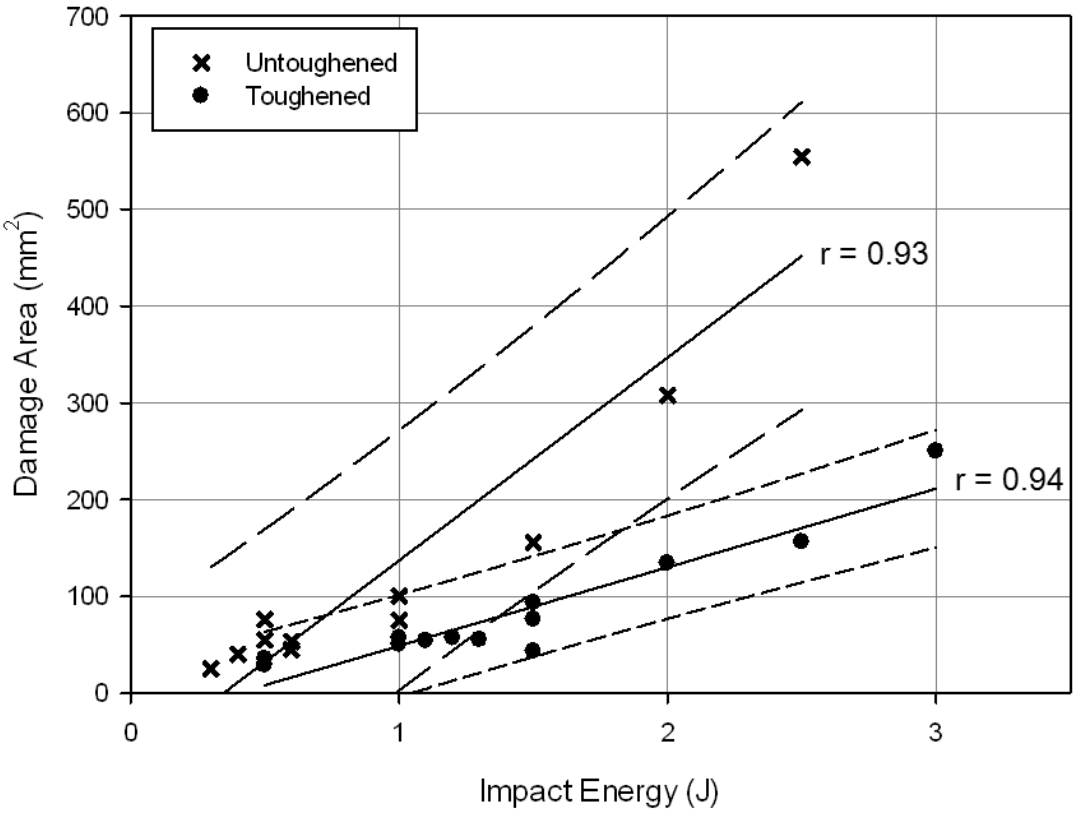

Figure 6.1: Scatter plot of C-scan projected damage area vs. impact energy for untoughened and particle-toughened specimens. Linear fits are shown along with dashed lines representing 95 % prediction intervals.

Post-impacted coupons were prepared for damage assessment by µCT and SRCL. Separate specimens were used for µCT and SRCL studies. µCT studies were performed on the material systems first to better understand the damage formation and identify regions of interest for SRCL work.

For each material system four regions of interest were imaged using SRCL of which the procedure can be found in section 3.8.3. The regions are labelled region ‘A’ through to ‘D’.

To capture the full extent of damage in impacted coupons, regions of interest were cut from across the damage region, stacked and μCT scanned at three locations using the HMX scanner. Details of this procedure are found in section 3.8.1.

Details of scan settings used for SRCL and μCT can be found in section 3.8.4.

Segmentation of cracks and measurements are described in sections 3.9.2 and 3.9.4 respectively.

6.3 Results and discussion

6.3.1 Impact damage mechanisms observed from μCT

A cross-sectional slice obtained from μCT is shown in Figure 6.2 for both material systems. A cone of internal damage is revealed at the impact region containing commonly observed modes of damage: (i) shear-induced matrix cracks, (ii) delaminations and (iii) bending-induced tensile matrix cracks towards the back-face [14, 15]. Some evidence of delamination crack ligamented behaviour in the toughened system is observed in (iv).

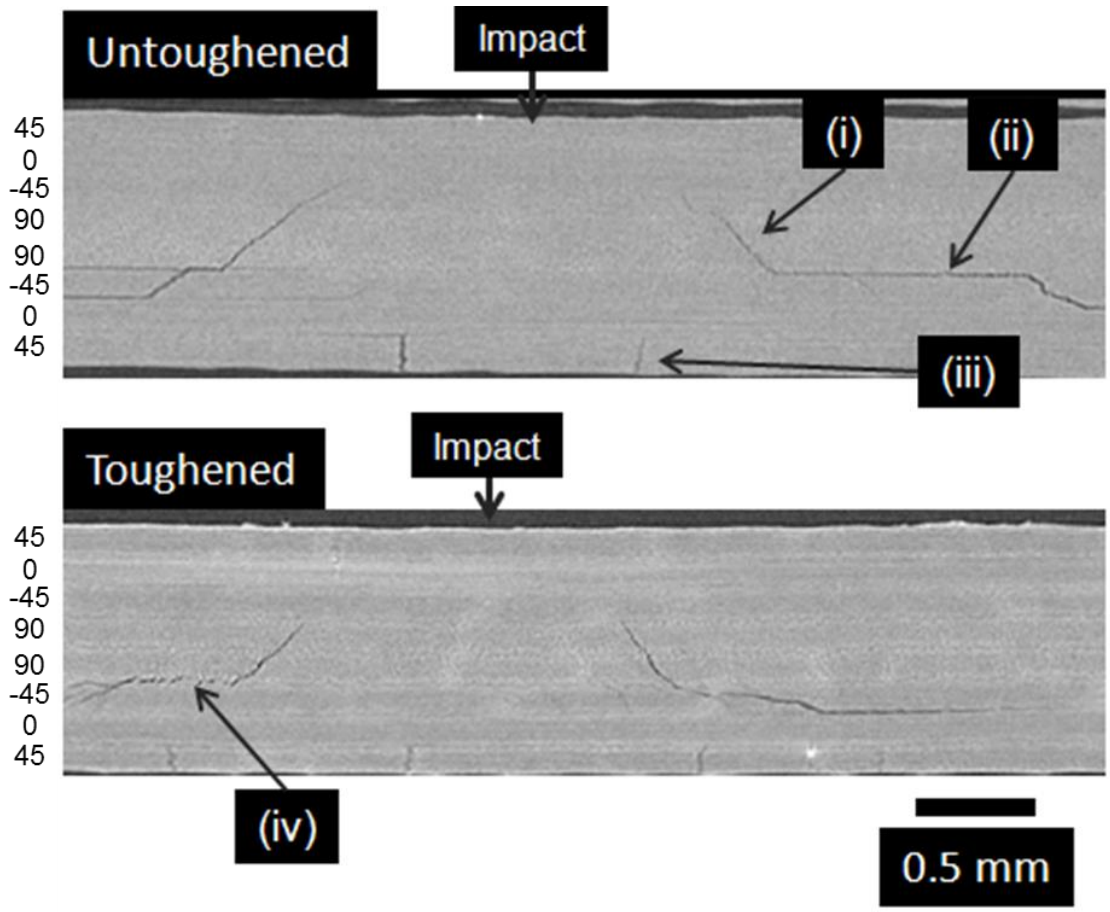

Figure 6.2: µCT 2D cross-section showing post-impact damage for untoughened (0.6J) and particle-toughened (1.2J) systems. Typical damage modes are identified (i) matrix crack, (ii) delaminations, (iii) tensile cracks and (iv) cracks exhibiting ligamented behaviour.

Segmentation of all detectable impact damage obtained from µCT scans revealed the 3D impact damage morphology and is shown in Figure 6.3. Based on previous observations, the crack-opening detectability limit of cracks was taken to be approximately 30 % of the voxel resolution used (*i.e.* just over 1 μm in this case) [16]. Due to the method of cutting 'matchsticks', some information representative of the width of the 0.3 *mm* blade is absent; despite this limitation, the overall internal 3D damage structure can be identified. A colour key is shown where blue represents the presence of delamination and each of the other colours represents intralaminar damage occurring in that particular ply. For clarity, the delaminations are labelled in Figure 6.3 i-iv at the 3/4, 5/6, 6/7 and 7/8 ply interface respectively. In both of the material systems, a similar damage interaction and morphology is observed on this scale. A characteristic "cone" of impact damage is formed around

the impact site, consisting of a network of delaminations interlinked by intralaminar matrix cracks. These intralaminar matrix cracks occur parallel to the direction of the fibres and form at tangents to a concentric ring surrounding the impact site. This leads to a “spiral staircase” of delaminations consisting of 45° segments that form between two matrix cracks of different orientations. This is consistent with other studies using quasi-isotropic layups *e.g.* [15, 17]. Delaminations always occur within the boundaries of matrix cracks on plies of different orientation, consistent with initiation of delaminations from critical matrix cracks, *e.g.* see [15].

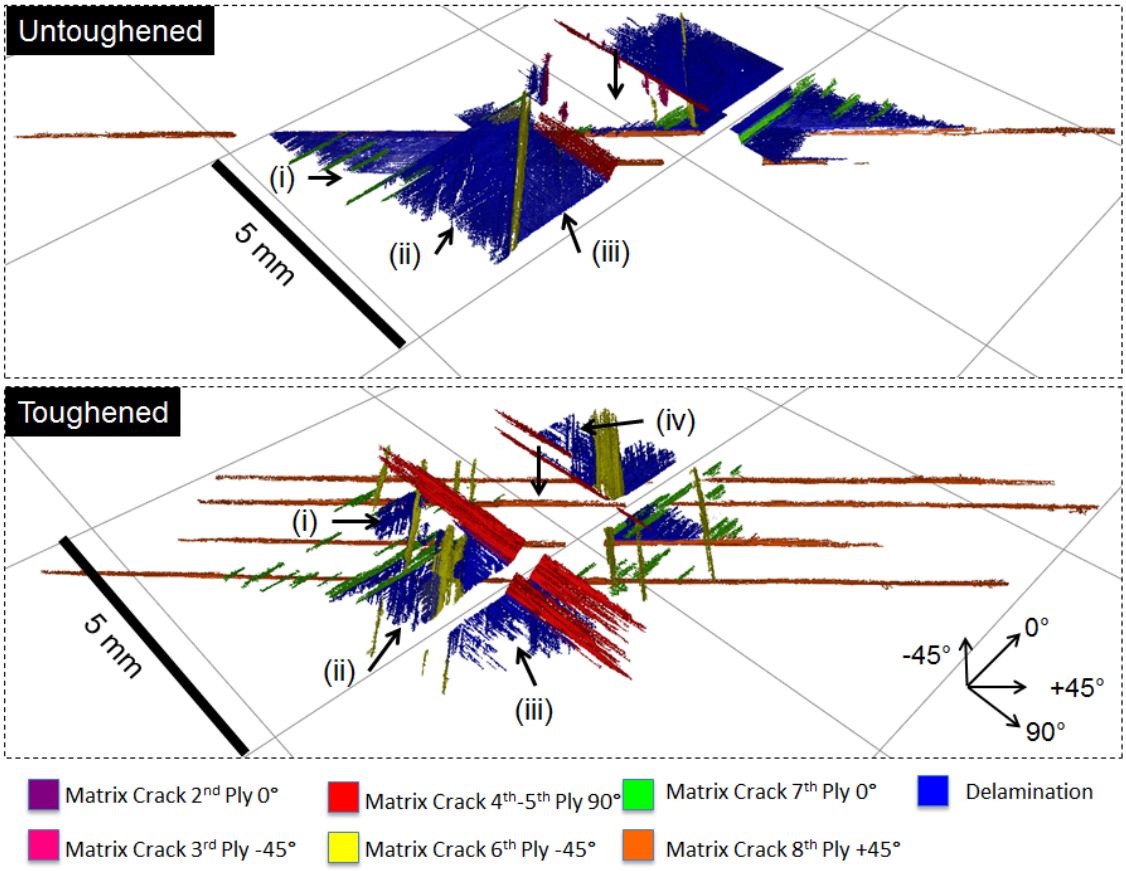

Figure 6.3: µCT 3D damage segmentation of impacted 8 ply coupons for untoughened (0.6 J) and particle-toughened material (1.2 J). Point of impact is indicated by the arrow and grid lines are spaced 5 mm apart.

The extent of the detectable delamination areas was measured at each ply interface and is plotted in Figure 6.4. The total delamination areas measured by µCT were typically lower than the projected damage areas measured by ultrasonic C-scan. There are two contributions to this; the 1 mm XY resolution of the C-scan has overestimated the damage area by including damage beneath the impact

cone. This is likely due to the ultrasonic probe partially detecting neighbouring cracks at these locations. Secondly, the detectability of cracks was limited to crack-openings above ~30 % of the voxel resolution; this typically underestimates the true extent of the damage areas and crack lengths. Nonetheless, relative comparisons to the extent of detectable damage between the two material systems can be made.

Delaminations in this study were observed occurring dominantly within the bottom three ply interfaces (non-impacted side) below the mid-plane on both the untoughened and toughened systems, although some delamination was also observed above the mid-plane in the untoughened system. It is probable that coupon bending, induced by the point impact load, led to the formation of tensile stresses below the midplane causing a greater incidence of damage on the lower half of the material.

Toughening particles clearly restricted delaminations and in this particular case, measurement of delamination areas taken from μCT data when plotted in Figure 6.4 show that the toughened coupon resulted in a lower extent of delaminations across all ply interfaces despite the higher impact energy. Observations in Figure 6.3 near the outer tips of delaminations in the toughened system show discontinuities in the crack, which are attributed to particle-toughening behaviour.

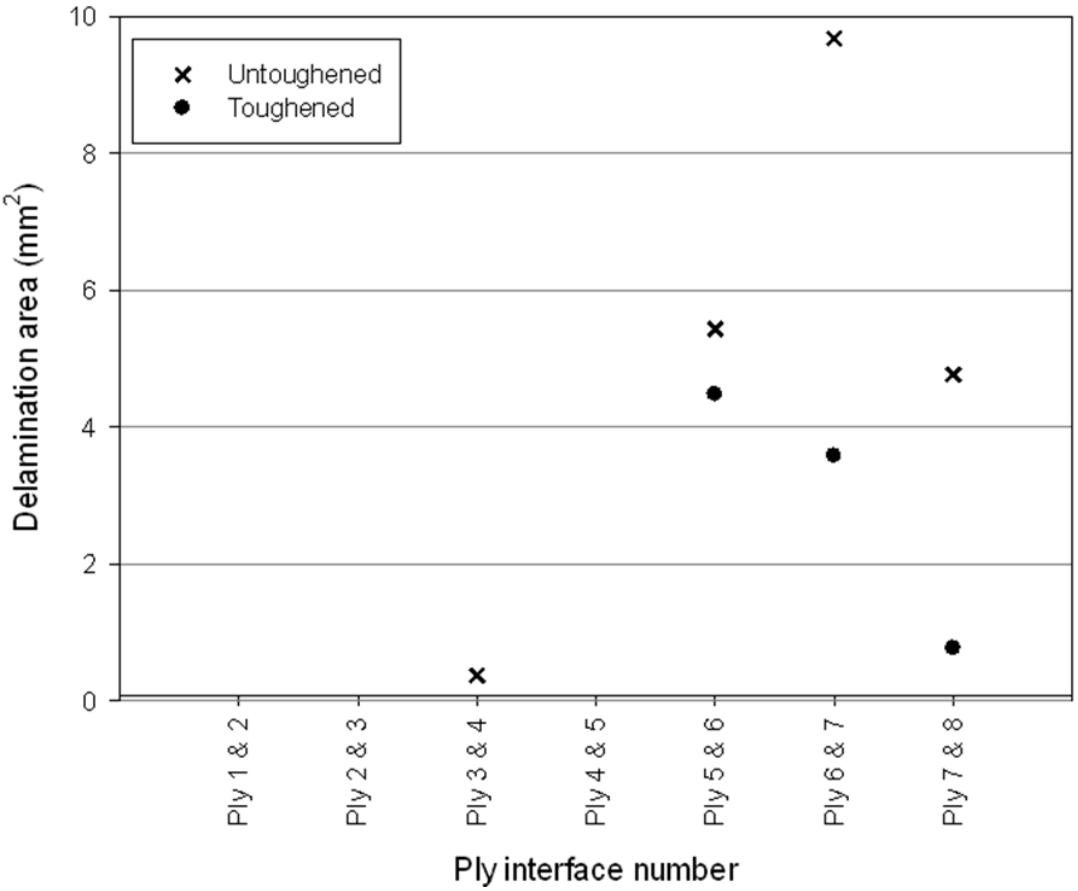

Figure 6.4: Delamination areas measured at each ply interface for untoughened (0.6 J) and toughened (1.2 J) systems.

Intralaminar crack lengths were measured from the μCT data and plotted in Figure 6.5 for both systems, for clarity these are plotted on two separate scatter plots with each point representing one crack and the number of cracks on each ply indicated. Between the untoughened and toughened systems, the incidence of intralaminar cracks did not appear to be equivalently suppressed as delaminations in the toughened system. Despite the lower level of delaminations, there is a significantly greater intralaminar crack density, although crack lengths are of similar lengths. It is possible that particle-toughening is most effective at the interlaminar regions between plies, consistent with the particles being constrained to these regions [18].

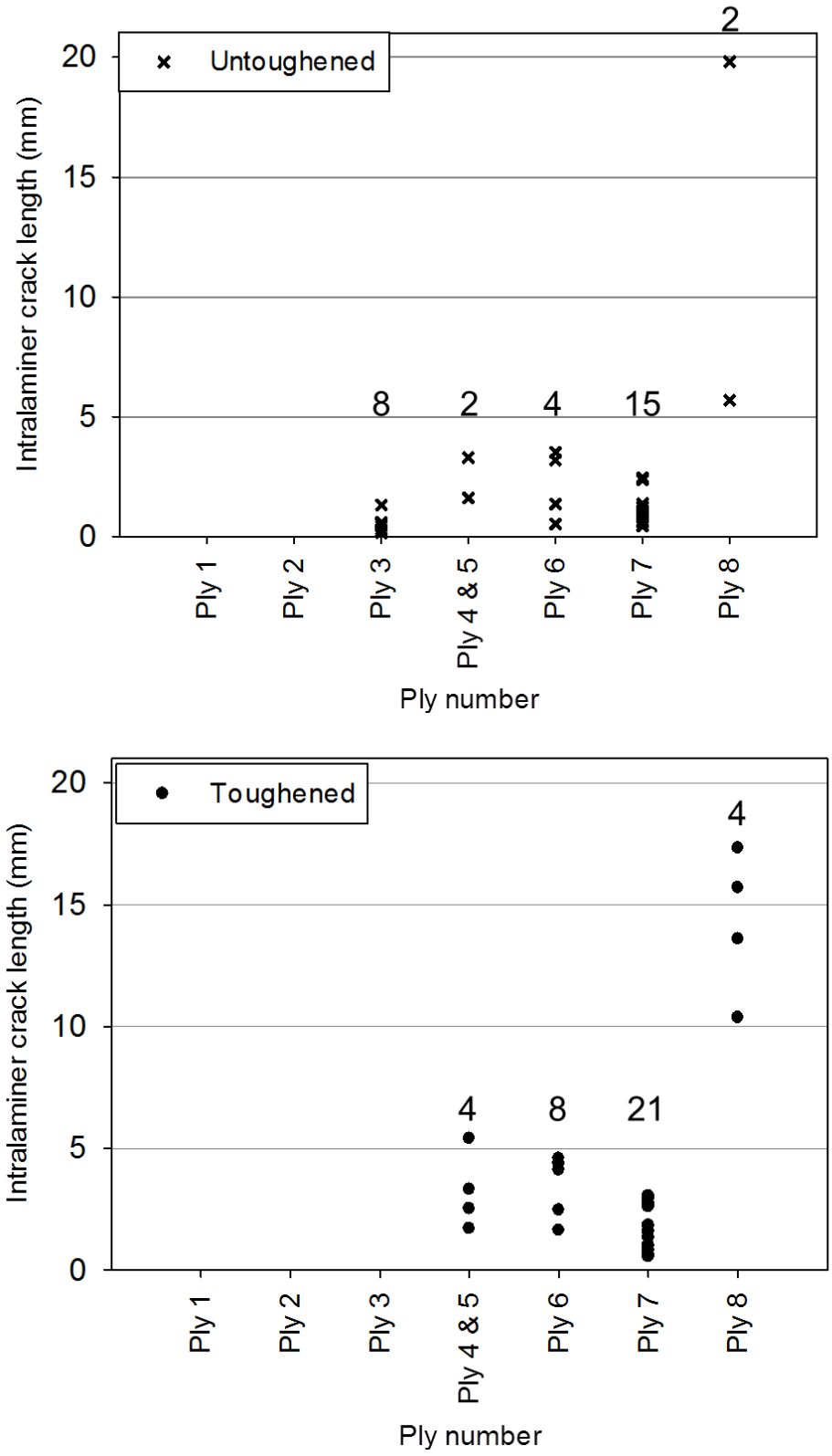

Figure 6.5: Scatter plot of the length of each individual intralaminar matrix crack on each ply measured from µCT volumes on the untoughened (0.6 J) and toughened (1.2 J) systems. Ply 1 represents the impact side and ply 8 the back-face. Numbers above scatter points indicates the number of matrix cracks detected and measured on each ply.

6.3.2 SRCL observation of toughening micromechanisms

To identify the micromechanisms of particle-toughening, higher resolution SRCL scans were utilised. As noted in the introduction, the non-destructive nature of this technique increases the confidence that the observed damage micromechanisms were solely caused by the impact event.

Figure 6.6 shows a 3D segmentation of matrix and delamination cracks at regions ‘A to D’ on both the untoughened and toughened systems, as viewed at an angle towards the back-face of the coupon. Whilst exact centring of the Region ‘A’ scans at the mid-point of the impacts was compromised in this case by a slight experimental error, ultrasonic C-scan confirmed that the ROIs in Region ‘C’ captured the delamination edge regions in both materials, whilst the tips of intralaminar cracks were captured in Region ‘D’.

To understand the role particle-toughening plays, cross-sectional slices from SRCL data are shown in Figure 6.7. Similarly to the µCT cross-sections, key damage features consist of (i) delaminations and (ii) intralaminar cracks. However, an additional level of detail is revealed, the untoughened and particle-toughened systems show distinct differences in the delamination micromechanisms and the presence of an approximately 20 µm thick resin-rich region (Figure 6.7(iii)) in the particle-toughened system. Although toughening particles cannot be directly visualised in the present scan data due to the particles being chemically closely related to the resin (in contrast to observations made on a different particle composition in a previous study with particle sizes of a similar diameter [34]); it is probable particles may have induced both crack deflection and crack-bridging which are clearly visible (Figure 6.7(iv)). The resulting ligamented behaviour of the delamination is consistent with crack deflection at the crack tip and subsequent bridging in the wake. Spacing of the order of ~20-80 µm is observed between crack segments. In comparison, delamination cracking in the untoughened system is restricted to deflections on the order of a few fibres diameters, < 14 µm. Such crack-shielding and bridging mechanisms within the particle-containing matrix are consistent with reducing delamination propagation: bridging creates traction between plies, reducing the stresses at the crack tip [19], whilst crack deflection

reduces the crack-tip stress intensity factor and increases the effective crack area [9]. These processes may act in conjunction with an increased process zone volume associated with the resin-rich layer [20], allowing greater energy absorption with crack propagation [5, 21, 22].

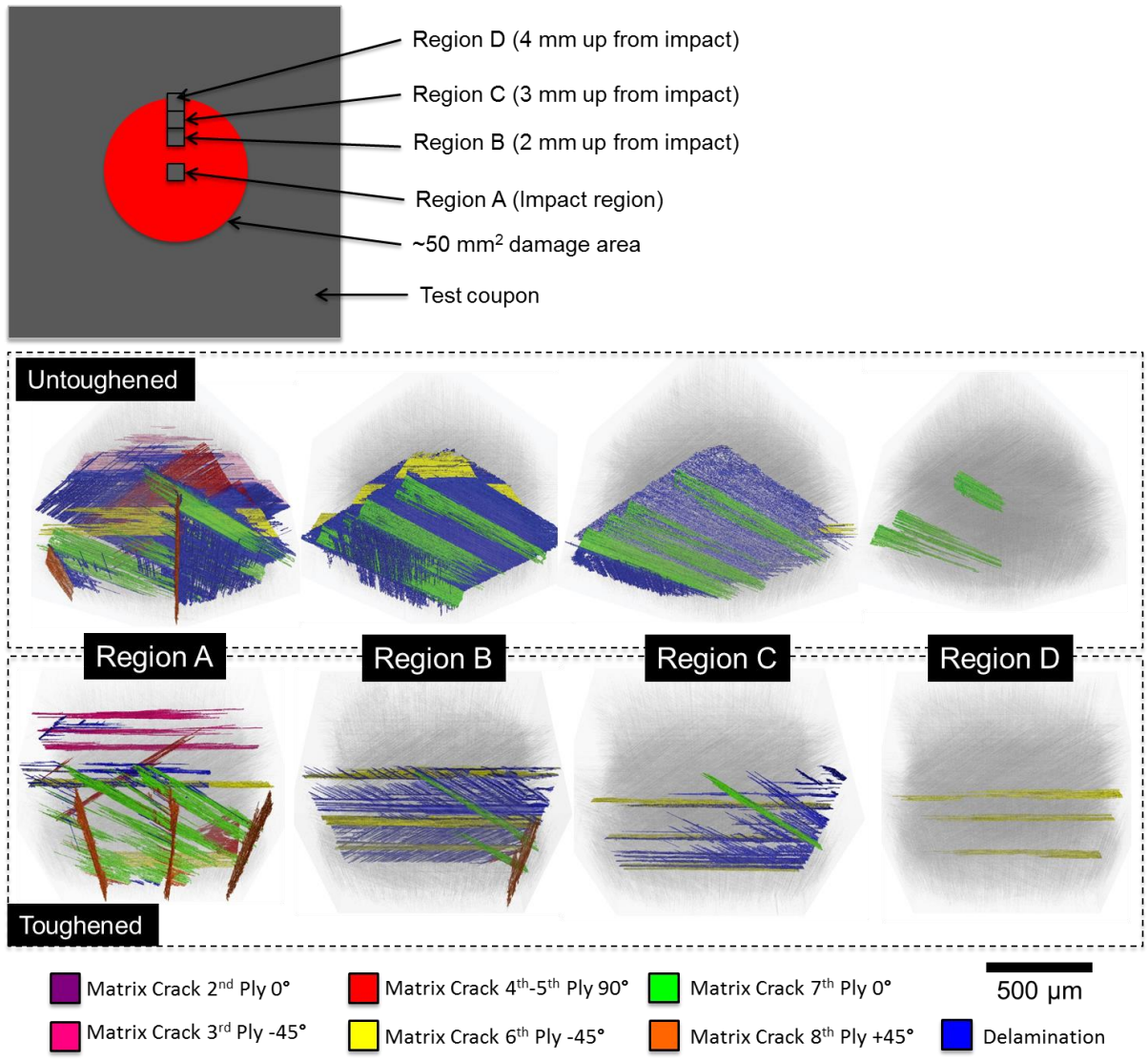

Figure 6.6: 3D segmentations of interlaminar and intralaminar cracks from SRCL scans taken at region A to D for untoughened (0.6 J upper row), and toughened (1.2 J bottom row) systems.

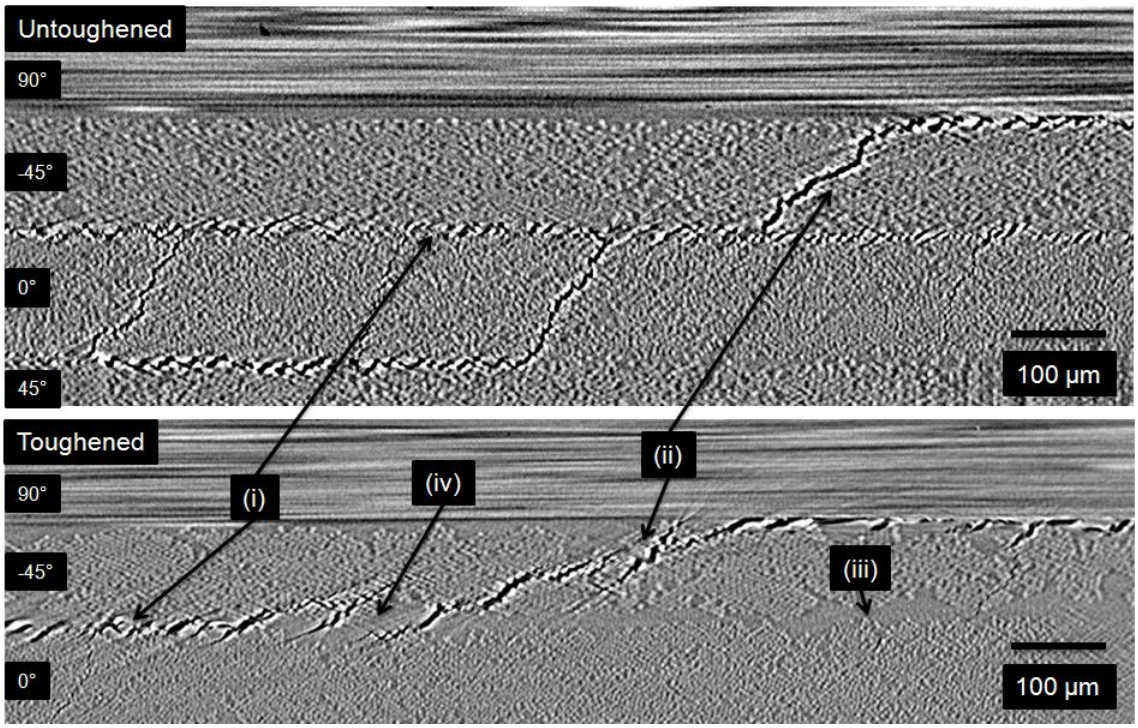

Figure 6.7: SRCL cross-section of untoughened (0.6 J) and toughened (1.2 J) taken from Region 'B'. The image shows a region below the mid-plane at the same interface plies in both systems. (i) indicates delaminations, (ii) matrix crack, (iii) ~20 µm resin-rich region and (iv) bridging ligaments.

In both material cases, the crack segments that separate the bridging ligaments in the delaminations are oriented at a range of angles between 30°- 45° to the plane of the plies, indicating their micro-scale formation is controlled by a combination of tensile and shear stresses; similar observations are made in [23]. Macroscopically the delaminations under low velocity impact conditions propagate by interlaminar shear, which is also consistent with earlier observations [14, 15].

In the untoughened system, some local resin-rich regions (> 10 µm thickness) were present between ply interfaces as shown in Figure 6.8(i). These were typically less than 5 % of the total interface surface area. This led to cracks with local deflections of similar characteristics to the toughened material. Such resin-rich variations during the manufacturing process will affect the local effective toughness and may be anticipated to contribute to variability in the impact response.

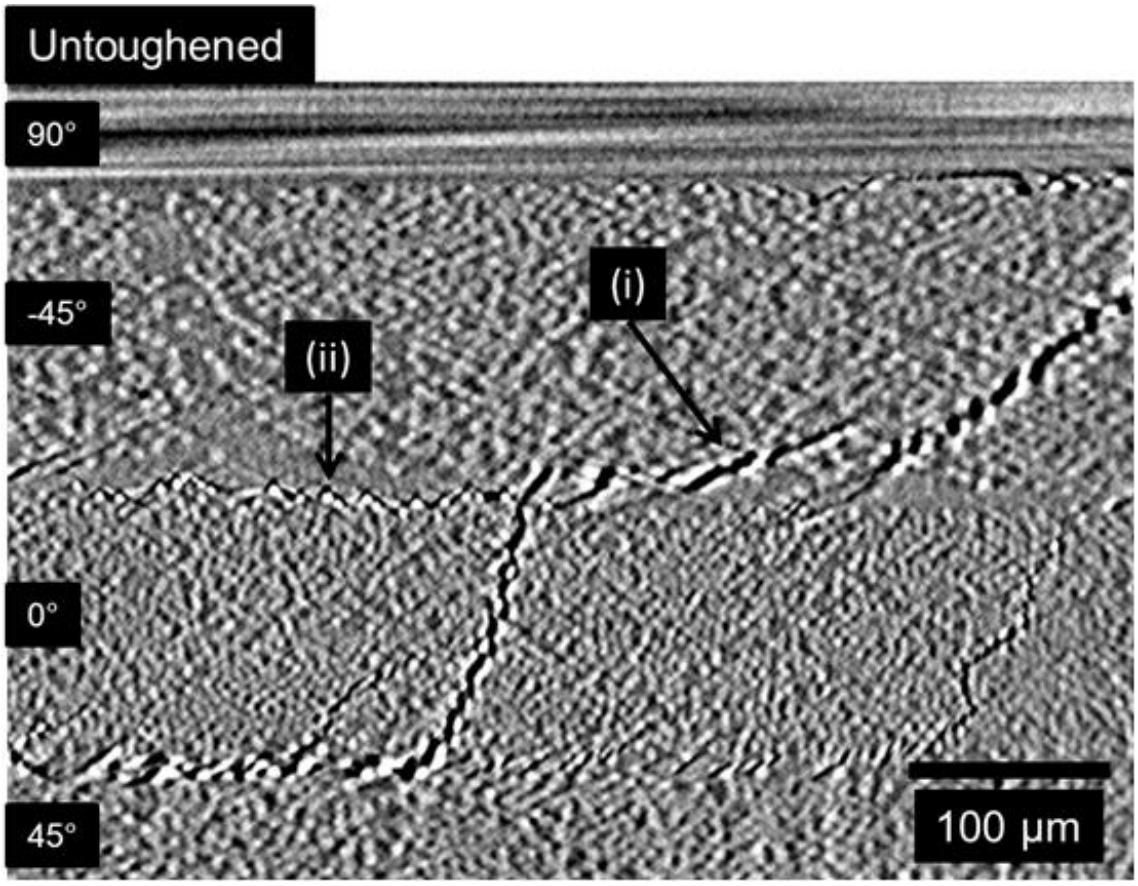

Figure 6.8: SRCL cross-section taken from Region ‘A’ in the untoughened material system. Variation in resin thickness led to a rich region present in (i) leading to ligaments with similar characteristics to the toughened system. (ii) show microscopic fibre-resin debonding.

SRCL cross-sectional images taken from the edge of the impact damage region in Figure 6.9 (Region ‘C’) reveal similar delamination micromechanisms as observed near the impact site, albeit with smaller crack-openings. This consists again of crack deflections of the order of a few fibre diameters (i) in the untoughened system and larger scale crack deflection and bridging (ii) in the toughened system, demonstrating toughening micromechanisms occurring throughout the damaged area.

Some fibre-resin debonding was observed in Figure 6.9(ii) between the -45° and 90° in the toughened system, similar behaviour is also shown in Figure 6.8(ii) in the untoughened material system. The observed frequency of this behaviour was less than 1 % of the total delamination area in the toughened material system and is therefore anticipated to have little effect on the key toughening mechanisms

discussed or the macroscale response. For the untoughened system, the lack of a thick resin-rich region made this observation difficult to distinguish from microcracking and could only be detected unambiguously in thick resin-rich areas (> 10 *μm* thick).

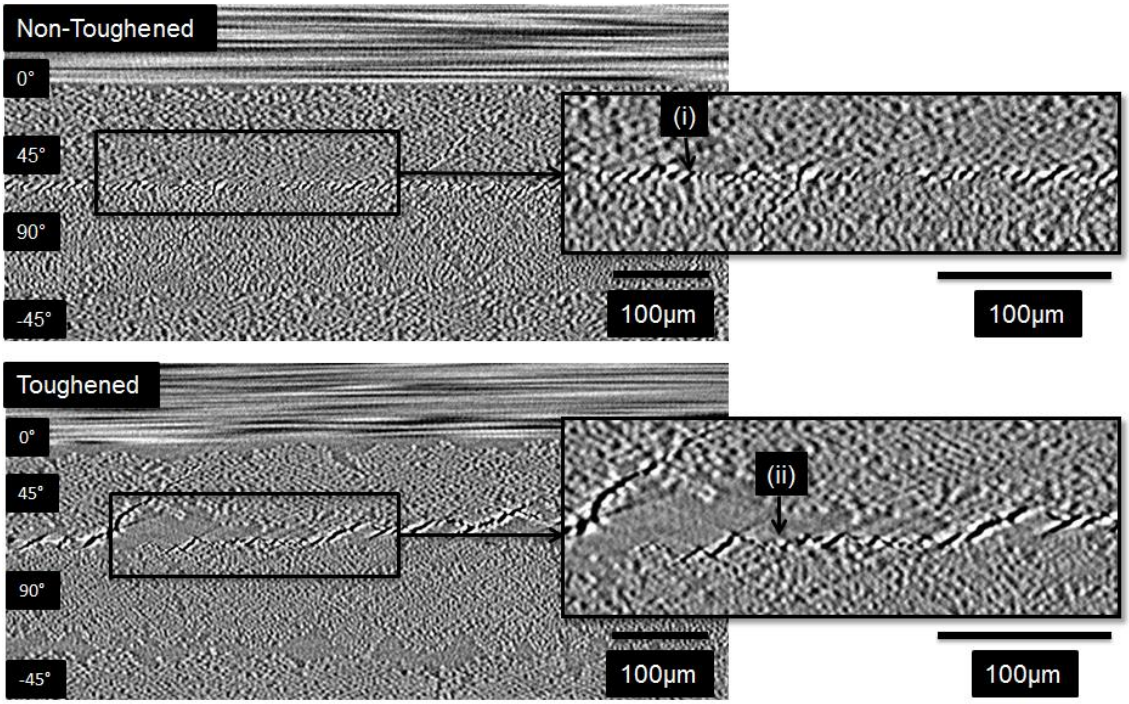

Figure 6.9: SRCL cross-section taken from the edge of the damaged area in Region 'C'. (i) crack deflection on the order of single fibre diameters and (ii) fibre-resin debonding.

6.4 Discussion and conclusions

The μCT and SRCL techniques have been applied to provide novel 3D insights as to the micro-mechanical damage mechanisms responsible for impact damage resistance in CFRP materials. The particle-toughened system tested exhibited clear improvements in delamination growth resistance where delamination suppression is critical to retaining post-impact compression strength. Toughening clearly induces extensive crack deflection and crack bridging within the ~20 *μm* thick inter-laminar resin-rich regions, which contain the great majority of toughening particles. Delaminations in the untoughened system were relatively planar, with little or no bridging, being constrained to local deflections of the order of a few fibre diameters within the relatively thin interlaminar region.

It is probable the presence of particles within the interlaminar region is highly effective at suppressing delaminations, but less so with intralaminar matrix cracks. Despite a larger impact energy used, the toughened system resulted in a lower extent of detectable delaminations in the µCT scans. However the lengths of intralaminar cracks were similar compared to the untoughened system. Further study comparing both systems impacted at the same energy would be required to confirm the influence of particles on matrix cracks. Such ineffectiveness of interlaminar particle toughening to reduce intralaminar damage may be identified as a weakness in cases where water ingress [24] or post-impact fatigue damage growth [25] are of concern.

Overall the work presented in this chapter highlights the potential for the use of complementary, multi-scale, 3D X-ray scanning methods to relate the micromechanical damage behaviour to the macroscopic mechanical responses of composite materials and structures.

6.5 References

[1] Singh, R.P., Zhang, M., and Chan, D., *Toughening of a brittle thermosetting polymer: Effects of reinforcement particle size and volume fraction.* Journal of Materials Science, 2002. **37**(4): pp. 781-788.

[2] Fu, S.Y., Feng, X.Q., Lauke, B., and Mai, Y.W., *Effects of particle size, particle/matrix interface adhesion and particle loading on mechanical properties of particulate-polymer composites.* Composites Part B-Engineering, 2008. **39**(6): pp. 933-961.

[3] Spanoudakis, J. and Young, R.J., *Crack-Propagation in a Glass Particle-Filled Epoxy-Resin .2. Effect of Particle Matrix Adhesion.* Journal of Materials Science, 1984. **19**(2): pp. 487-496.

[4] Hsueh, C.H., *Effects of Aspect Ratios of Ellipsoidal Inclusions on Elastic Stress Transfer of Ceramic Composites.* Journal of the American Ceramic Society, 1989. **72**(2): pp. 344-347.

[5] Groleau, M.R., Shi, Y.B., Yee, A.F., Bertram, J.L., Sue, H.J., and Yang, P.C., *Mode II fracture of composites interlayered with nylon particles.* Composites Science and Technology, 1996. **56**(11): pp. 1223-1240.

[6] Pearson, R.A., *Toughening Epoxies Using Rigid Thermoplastic Particles - a Review.* Advances in Chemistry Series, 1993(233): pp. 405-425.

[7] Spanoudakis, J. and Young, R.J., *Crack-Propagation in a Glass Particle-Filled Epoxy-Resin .1. Effect of Particle-Volume Fraction and Size.* Journal of Materials Science, 1984. **19**(2): pp. 473-486.

[8] Aksoy, A. and Carlsson, L.A., *Interlaminar Shear Fracture of Interleaved Graphite Epoxy Composites.* Composites Science and Technology, 1992. **43**(1): pp. 55-69.

[9] Gao, F., Jiao, G.Q., Lu, Z.X., and Ning, R.C., *Mode II delamination and damage resistance of carbon/epoxy composite laminates interleaved with thermoplastic particles.* Journal of Composite Materials, 2007. **41**(1): pp. 111-123.
[10] Flannery, B.P., Deckman, H.W., Roberge, W.G., and Damico, K.L., *3-Dimensional X-Ray Microtomography.* Science, 1987. **237**(4821): pp. 1439-1444.
[11] Bagheri, R. and Pearson, R.A., *Role of particle cavitation in rubber-toughened epoxies: II. Inter-particle distance.* Polymer, 2000. **41**(1): pp. 269-276.
[12] Krug, K., Porra, L., Coan, P., Wallert, A., Dik, J., Coerdt, A., Bravin, A., Elyyan, M., Reischig, P., Helfen, L., and Baumbach, T., *Relics in medieval altarpieces? Combining X-ray tomographic, laminographic and phase-contrast imaging to visualize thin organic objects in paintings.* Journal of Synchrotron Radiation, 2008. **15**: pp. 55-61.
[13] Helfen, L., Baumbach, T., Cloetens, P., and Baruchel, J., *Phase-contrast and holographic computed laminography.* Applied Physics Letters, 2009. **94**(10).
[14] Shyr, T.W. and Pan, Y.H., *Impact resistance and damage characteristics of composite laminates.* Composite Structures, 2003. **62**(2): pp. 193-203.
[15] Xie, X.S., Tian, F., and Hong, Y.H., *Experimental Investigation into the Impact of Polypropylene Fibers and SRA on the Early Crack Resistance of Concrete.* Advanced Engineering Materials, Pts 1-3, 2011. **194-196**: pp. 858-864.
[16] Woods, D.W., Hine, P.J., Duckett, R.A., and Ward, I.M., *Effect of High Modulus Polyethylene Fibre Surface Treatment on Epoxy Resin Composite Impact Properties.* Adhesion Society Proceedings of the Sixteenth Annual Meeting and the International Symposium on the Interphase, 1993: pp. 69-72.
[17] Sampath, P.S., Murugesan, V., Sarojadevi, M., and Thanigaiyarasu, G., *Mode I and Mode II Delamination Resistance and Mechanical Properties of Woven Glass/Epoxy-PU IPN Composites.* Polymer Composites, 2008. **29**(11): pp. 1227-1234.
[18] Wright, P., Moffat, A., Sinclair, I., and Spearing, S.M., *High resolution tomographic imaging and modelling of notch tip damage in a laminated composite.* Composites Science and Technology, 2010. **70**(10): pp. 1444-1452.
[19] Khalili, S., Khalili, S.M.R., and Amidpour, M., *Numerical Analysis on Impact Behavior of Composite Sandwich Plates as Energy Harvesting Structures.* Mechanical and Aerospace Engineering, Pts 1-7, 2012. **110-116**: pp. 1296-1304.
[20] Qiu, L., Yuan, S.F., Zhang, X.Y., and Wang, Y., *A time reversal focusing based impact imaging method and its evaluation on complex composite structures.* Smart Materials & Structures, 2011. **20**(10).
[21] Britner, A., Ummenhofer, T., Elghazouli, A.Y., Bangert, F., and Durr, A., *Blast and impact - Experimental investigations on composite structures.* Stahlbau, 2010. **79**(8): pp. 580-589.
[22] Gregory, J.R. and Spearing, S.M., *Modeling inelastic matrix crack tip deformation in a double cantilever beam specimen.* Journal of Composite Materials, 2006. **40**(2): pp. 143-156.

[23] Moffat, A.J., Wright, P., Buffiere, J.Y., Sinclair, I., and Spearing, S.M., *Micromechanisms of damage in 0 degrees splits in a [90/0](s) composite material using synchrotron radiation computed tomography.* Scripta Materialia, 2008. **59**(10): pp. 1043-1046.

[24] Shan, Y. and Liao, K., *Environmental fatigue behavior and life prediction of unidirectional glass-carbon/epoxy hybrid composites.* International Journal of Fatigue, 2002. **24**(8): pp. 847-859.

[25] Gamstedt, E.K. and Talreja, R., *Fatigue damage mechanisms in unidirectional carbon-fibre-reinforced plastics.* Journal of Materials Science, 1999. **34**(11): pp. 2535-2546.

Chapter 7

The influence of toughening-particles in CFRPs on low velocity impact damage resistance performance

In this chapter, the role of particle-toughening for increasing impact damage resistance in carbon fibre reinforced polymer (CFRP) composites is investigated. Whilst chapter 6 highlights the key toughening micromechanisms, this chapter quantifies this behaviour across five material systems to establish the effectiveness of the various toughening mechanisms on damage resistance. These systems consisted of four particle-toughened matrices and one system containing no toughening particles that were subjected to low velocity impacts ranging from 25 J to 50 J. This was conducted so as to rank the impact damage resistance of each material system. Instrumented impact and ultrasonic C-scan were used to compare the damage resistant properties between the material systems. Synchrotron radiation computed tomography (SRCT) enabled a novel approach for damage assessment and quantification, including an accurate estimation of the damage area by mode and location. Toughening mechanisms were detected in the particle-toughened systems consisting of particle-resin debonding, crack-deflection and crack-bridging. Quantification of the bridging behaviour was undertaken as a function of distance from the crack tip, and in the wake of the crack the increase in crack path length and surface roughness was measured. Out of the three toughening mechanisms measured, particle systems exhibited a larger extent of bridging suggesting a significant contribution of this toughening mechanism compared to the system with no particles.

7.1 Introduction

In chapter 6, impact damage assessment was performed to gain a preliminary understanding of the influence of particle-toughening in controlling the impact damage resistance of laminated fibre composite material systems. It was revealed that particles had a considerable effect on suppressing delamination growth through various observable toughening mechanisms. The three key mechanisms observed were crack-tip shielding through bridging ligaments, crack deflection, and increasing the crack path length. This is in agreement with other studies where inclusion of particles in a matrix is reported to develop a variety of micromechanisms that may contribute to energy absorption and crack-tip shielding processes [1]. This includes: crack deflection, crack bridging, crack-tip blunting, particle-matrix interface debonding, and particle-induced localised yielding [1-7]. Whilst these micromechanisms are generally agreed to be present, there is much debate regarding which of these contributes significantly to toughness. There are many factors that may be anticipated to contribute to this such as particle size, particle geometry, volume fraction, particle/matrix interfacial adhesion and particle elastic properties, making comparisons difficult between published studies [1, 5, 8, 9]. A better understanding of the toughening micromechanisms which contribute most significantly to damage resistance is therefore required. This will enable the development of future toughened systems by focusing on improvements to the micromechanisms which work best.

The present work compares four particle-toughened systems and one system with no particles (untoughened) to gain a phenomenological appreciation of the roles that particles may play in impact damage resistance. To complement traditional methods of instrumented impact testing and ultrasonic C-scan inspection, synchrotron radiation computed tomography (SRCT) has been used for the assessment and quantification of damage micromechanisms. The use of SRCT in composite damage analysis has been reported previously [10-14]. To the authors knowledge this is the first time such high resolution CT has been used to assess the three-dimensional micromechanistic role of toughening particles after impact, with novel quantification of crack deflection and bridging processes being provided.

7.2 Materials and testing procedure

This chapter studied the five 4.5 mm thick material systems listed in section 3.1.2. Coupons were impacted at 25, 30, 40 and 50 J with three repeats for each energy level; this followed the procedure listed in section 3.2. After impact the projected damage area and dent depth were measured, see sections 3.5 and 3.6 respectively.

Material systems destined for SRCT scans were all impacted at 30 J. After a C-scan was performed to identify the projected damage area, a region of interest consisting of a ‘cube’ was cut at the edge of the damage area, see section 3.8.2. This was mounted on an SEM stub to make use of automated sample handling facilities at TOMCAT [15]. A voxel size of 1.5 µm was used at 19 kV with a sample to detector propagation distance of 39 mm to enable imaging in the edge detection regime.

In processing SRCT data, some quantification was performed to measure the extent of bridging, increase in crack path length, and roughness. This is described in section 3.9.3. In addition to this, some segmentation was performed to illustrate the 3D nature of damage; this process is described in section 3.9.2.

The T2 system was studied in greater detail using cross-sectional microscopy. The procedure can be found in section 3.7.

7.3 Results and discussion

7.3.1 Mechanical testing

The results of the mechanical testing are summarised in the graphs shown in Figure 7.1 to Figure 7.4. The projected damage area from ultrasonic C-scanning is plotted against impact energy in Figure 7.1 to give an overall representation of damage resistance for each of the materials. Damage areas were normalised against the largest measured damage area allowing trends between the material

systems to be compared. The variability of damage area between repeated tests was considered reasonable across all systems (on the order of ±10 % in terms of total range), with the exception of T3, with best fit lines being plotted. A linear fit is not shown for the toughened T3 system due to greater variability seen in damage areas in this system at the two highest impact energies (~40 and 50 J).

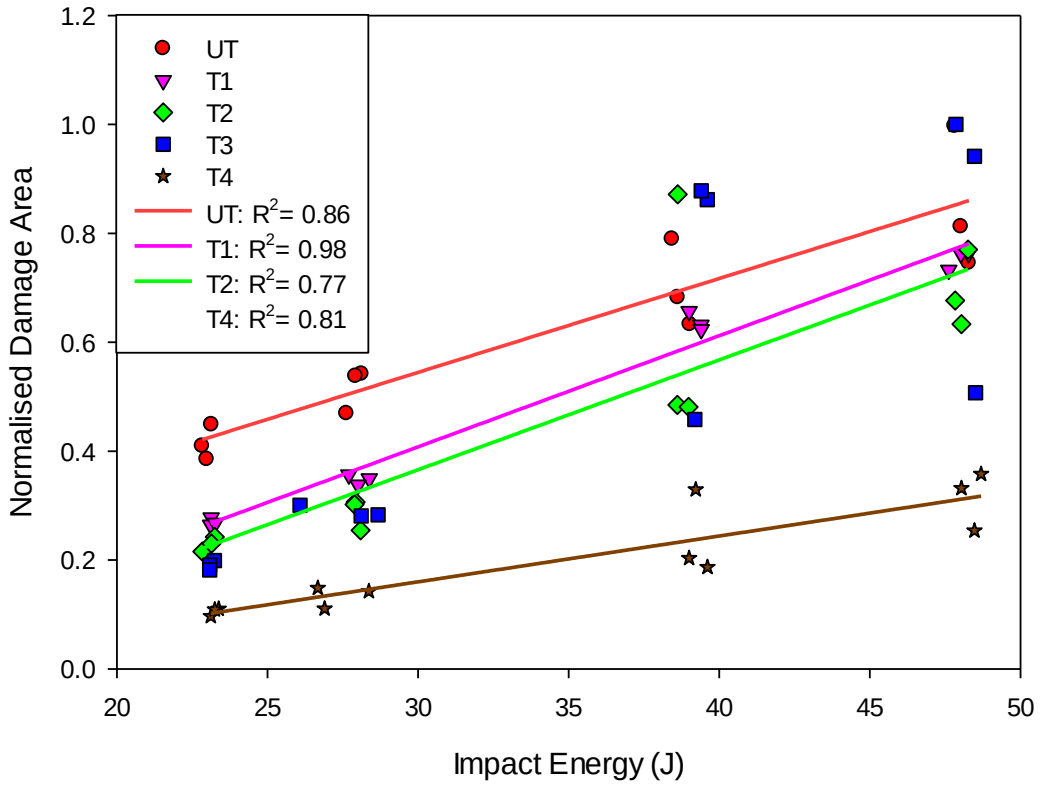

Figure 7.1: Plot of normalised projected damage area vs. impact energy.

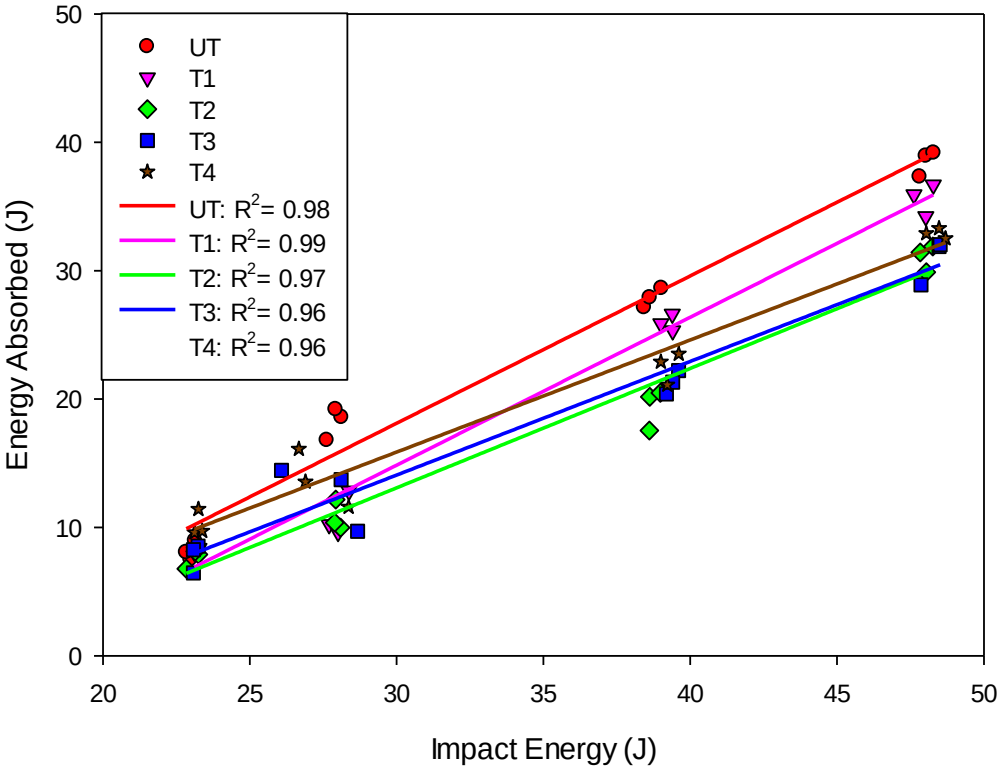

Figure 7.2: Plot of energy absorbed vs. impact energy.

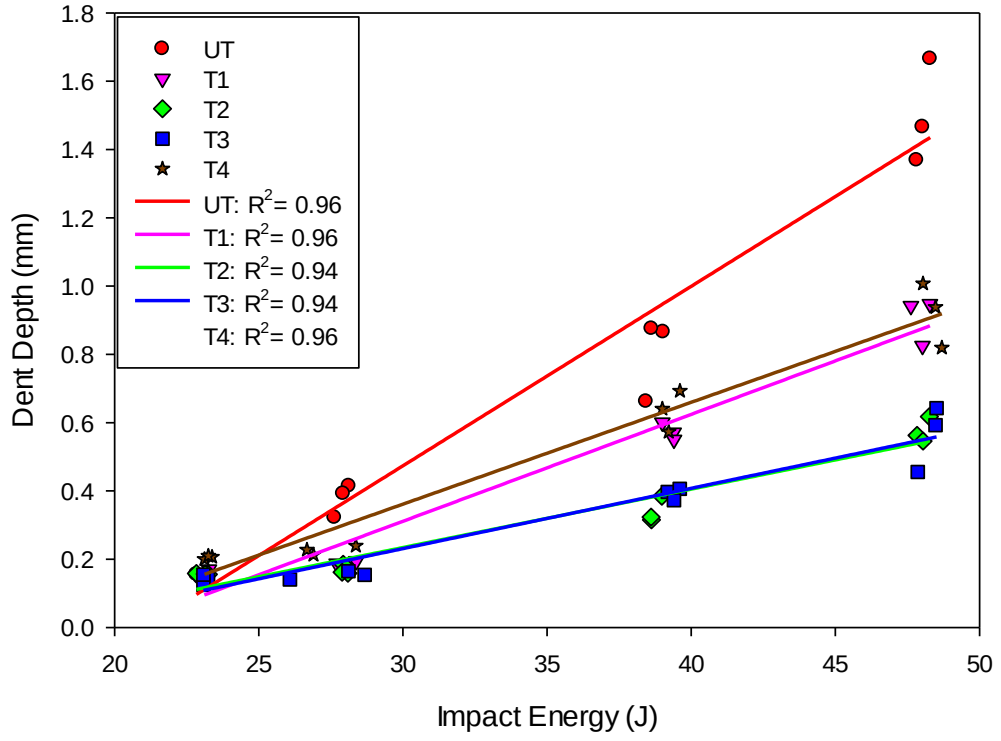

Figure 7.3: Plot of dent depth vs. impact energy.

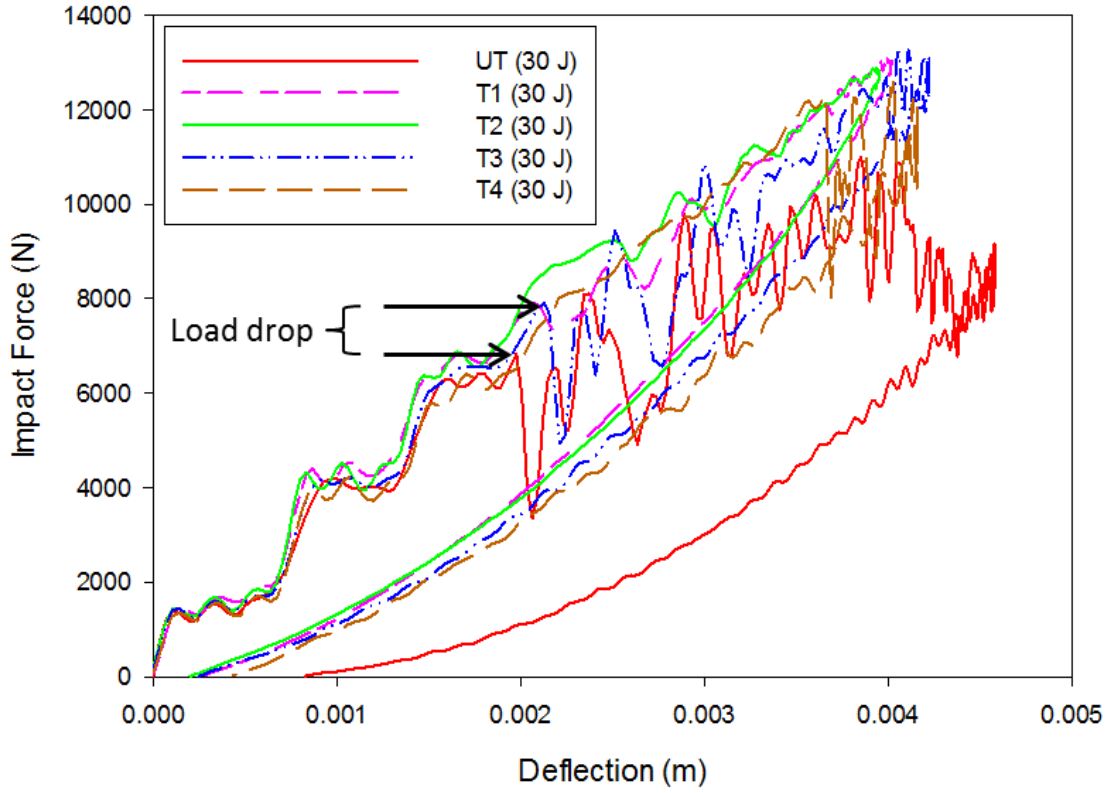

Figure 7.4: Plot of impact force vs. deflection - a load drop is observed on the UT and T3 system indicated by the arrows.

In general, a positive linear correlation between impact energy and projected damage area is observed. There is a clear distinction in impact damage resistance between the UT system and the T4 particle system for all impact energies tested. The T4 system is shown to suppress the extent of damage by approximately four times compared to the UT system, and outperforms the other three particle systems in terms of damage area for a given impact energy. T1 and T2 materials fall between the bounds proscribed by UT and T4, with T2 showing a small but consistent improvement over T1. The cause of the scatter in the T2 and T3 systems at the higher impact energies is unknown: careful cross-checking for anomalies in the instrumented impact data and sample micro-structures revealed no simple explanation of variations between otherwise identical tests. For the purpose of this chapter, impacts of 30 J are studied in greater detail from SRCT

scans; at these energies, variability between individual tests is modest (within -±10 % of the trend lines). A clear separation is seen between the untoughened and particle-toughened systems, and there is a consistent ranking of damage area resistance (low to high) UT < T1 < T2 ≈ T3 < T4.

Comparing the impact damage resistance against mode II fracture toughness, the T4 systems with the highest fracture toughness correlated to the highest impact damage resistance. Regarding the other particle-toughened systems there is little correlation between mode II fracture toughness and the corresponding impact damage resistance performance which suggests a possible strain-rate dependency for these material systems. For example the T2 and T1 systems had the lowest and second highest mode II fracture toughness values respectively yet still resulted in similar impact damage performance. This highlights the unreliability of fracture toughness values that are determined through quasi-static tests to inform the damage resistance under dynamic impact events, even when classed as low velocity. For this reason, it is important to relate the SRCT observations and measurements on impact data, as discussed later, directly to its effect on impact damage resistance.

The energy absorbed by each of the five materials is plotted against impact energy in Figure 7.2. For each system there is a distinct linear correlation (R^2 values in the order of ~0.97) of increasing absorbed energy with increasing impact energy. Variations between materials are generally modest, with the UT material exhibiting the highest absorbed impact energies, and T2 and T3 exhibiting the least.

Interestingly there is no simple mapping of the ranking of damage resistance (by C-scan measured areas) to the absorbed energies. One explanation is that C-scan typically only measures the projected delamination area however the energy absorbed can go to local deformation, matrix cracking, delaminations and fibre fracture [16]. This can be further complicated by the energy release rate [17] where more energy is required to propagate delamination and by the distribution of the delaminations.

Dent depth was plotted against impact energy in Figure 7.3. At the energies tested, dent depth increases approximately linearly with impact energy for all systems (R^2 values ~0.95). At 25 J, all systems exhibit roughly the same impact

dent depth of ~0.15 mm. At higher impact energies there is a clear divergence, with the UT system exhibiting the largest dent depths. However again, the damage resistance of the material does not correlate simply with the extent of the dent. In this case the T4 material with the best damage resistance properties resulted in the second largest dent depth for a given impact energy. The lowest dent depth was observed in the T2 and T3 systems. Impacts around 25 J for the untoughened composite, and 30 J for the toughened systems, fell within the typical BVID regime (~0.3 mm dent depth). Interestingly the ranking of absorbed energy correlates with dent depth. The T1 and T4 systems may exhibit greater local ductility hence the larger absorbed energy and dent depth compared to the T2 and T3 systems.

A plot of impact force against deflection is shown in Figure 7.4 representing impact from each of the five material systems subjected to a targeted 30 J of impact. The absorbed energy represented by the area contained in the hysteresis loop clearly shows the UT material has absorbed the greatest energy, consistent with Figure 7.2. It is also clear that the 30 J impact led to a higher deflection on the UT system compared to the toughened systems, approximately 4.5 mm and 4.0 mm respectively. The greater deflection in the UT system could explain why the T2 system resulted in a lower extent of impact damage despite having a lower mode II fracture toughness value. This is discussed in chapter 8 where low velocity impact and quasi-static indentation loading conditions are compared.

Beyond some mild oscillations in load seen in all cases, a distinct load drop was consistently seen in the UT and T3 tests as indicated by arrows. It has been reported previously [14, 18, 19] that the load drops arise from the effective brittleness of the material, indicating the onset of delamination and sudden loss in stiffness. Higher toughness systems generally tend not to exhibit a load drop, but exhibit non-linearity during the load increase during impact [7].

7.3.2 Damage micromechanisms

Cross-sectional SRCT slices showing delaminations near the crack tip of each of the material system are presented in Figure 7.5. A typical delamination crack is shown occurring in the interlaminar regions between two ply interfaces as

illustrated in (i). In contrast to UT, the delaminations in the T2 system (ii) are observed to propagate within the intralaminar region, typically several fibre diameters into the corresponding ply. This mechanism was confirmed via cross-sectional optical microscopy on another test coupon to check for conformity of this feature, see Figure 7.6.

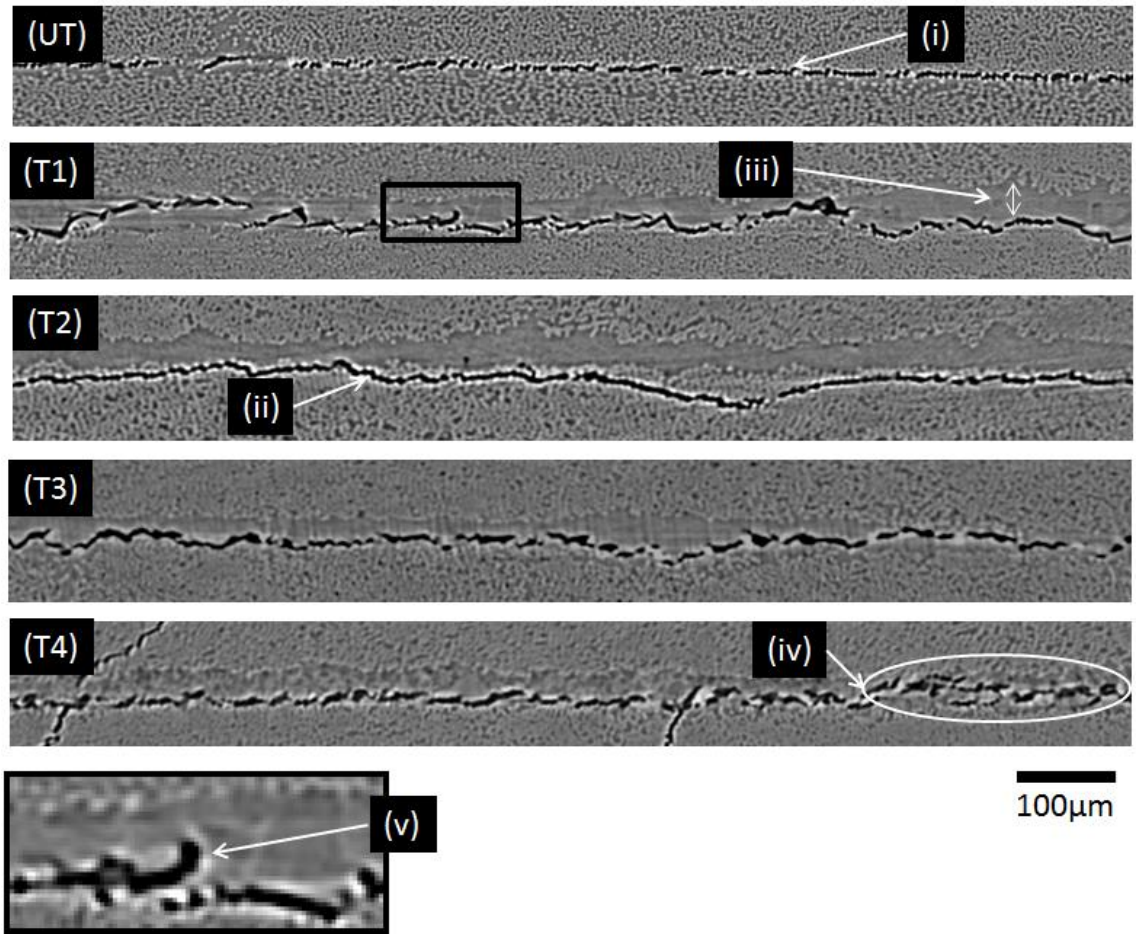

Figure 7.5: SRCT cross-section of delamination formation towards the edge of the damaged region for materials subjected to 30 J impact. (i) delamination within the interlaminar region, (ii) delamination/longitudinal ply split within the intralaminar region, (iii) resin-rich region, (iv) multiple crack formation, (v) close up of overlapping crack deflection in the T1 region indicated by the box.

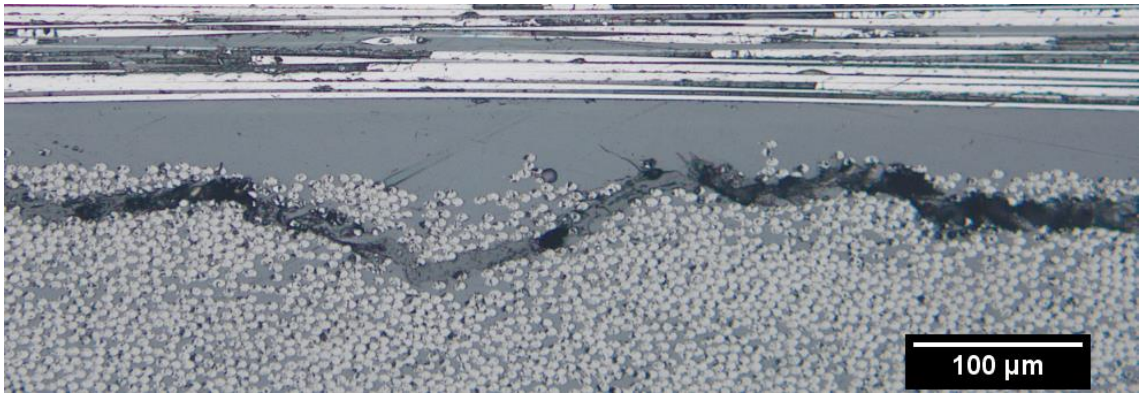

Figure 7.6: Optical cross-section showing delamination formation in the T2 system.

A key microstructural difference between the UT system and the four particle-toughened systems is clearly the presence of an approximately ~20 µm thick resin-rich region, as highlighted in Figure 7.5 (iii), attributable to toughening particles occupying space within this region [20]. The thickness of the resin-rich region is consistent across all four particle-toughened systems studied despite a difference in particle sizes used for the study. This is largely attributed to the consistent particle-resin concentration by weight between systems, i.e. smaller particle sizes enabled more particles to be used resulting in a similar volume of particles occupying the resin-rich region.

The resin-rich region appears to play a direct role in toughening in the T1, T3 and T4 systems, with failure occurring both within and at the interface of these regions. The echelon crack segments indicate that failure occurred predominantly locally in shear in agreement with the results presented in chapter 6 and a previous study [20]. Such behaviour supports the hypothesis that delamination propagation caused by low velocity impact occurs predominantly in mode II [19, 21-23].

In the case of the T1 and T4 systems where the particles can be directly observed in the SRCT images, deflections of cracks are observed around the particles (particle-resin debonding), this is shown in Figure 7.5 (v). Such deflection can be seen to increase the crack path length, and hence has the potential to increase energy absorption. Additionally, crack bridging is observed, creating traction sites between the upper and lower crack faces. Whilst toughening particles in the T3 material system could not be visualised directly, the crack morphology is

comparable to both the T1 and T4 systems, with the extent and frequency of crack deflection lying between these two systems.

In the T4 system, smaller particles enabled two to three particles to fill the thickness of the resin-rich region instead of single large particles as seen in the T1 system. In some instances this appears to have allowed crack bifurcation as highlighted in Figure 7.5 (iv) within the thickness of the interlaminar region, increasing the fracture surface area within a shorter crack length. However, the frequency of such multiple crack formation instances was low - accounting for less than 1 % of the total damage area investigated, and therefore may be considered a relatively minor micromechanical effect.

An in-plane cross-sectional slice of delamination micromechanisms in the T1 system is shown in Figure 7.7; the box in (a) highlights the location of the magnified image in (b) which is ahead of the main delamination crack tip. A 3D segmentation of this region in (c) shows the crack morphology within this region with cracks represented in red and particles in grey. Particle-resin debonding is highlighted at points (i) and (ii), with similar processes also being observed in the T4 system. Such particle-resin debonding may be seen as an energy absorption process itself, occurring well ahead of the main continuous crack in a process zone, although the energy absorption relative to that of neat resin failure is not strictly known. Such discontinuous failure also leads to bridging ligaments in the crack wake with particles bridging between the crack faces. Failure of these ligaments in the wake of the crack was observed to occur predominantly through complete debonding of the particle-resin interface causing a loss in traction across the ligament. From the SRCT data, fracture of particles was not detected in the T1 system, and was difficult to resolve in the T4 system.

It is very apparent from the 3D SRCT imaging that the distinction between such processes occurring ahead of, or in the wake of such ligamented and deflected cracks, is difficult to distinguish and may be best considered overall as a continuous semi-cohesive zone. Observations of delaminations at the fibre/matrix interface at points (iii) and (iv) show crack propagation parallel to the fibre directions at these boundaries, most likely consisting of fibre-resin debonding. This

effect accounted for approximately 4 % of the total delamination area in the T1 system, and is also observed in the wake of the crack circled in Figure 7.9 (i).

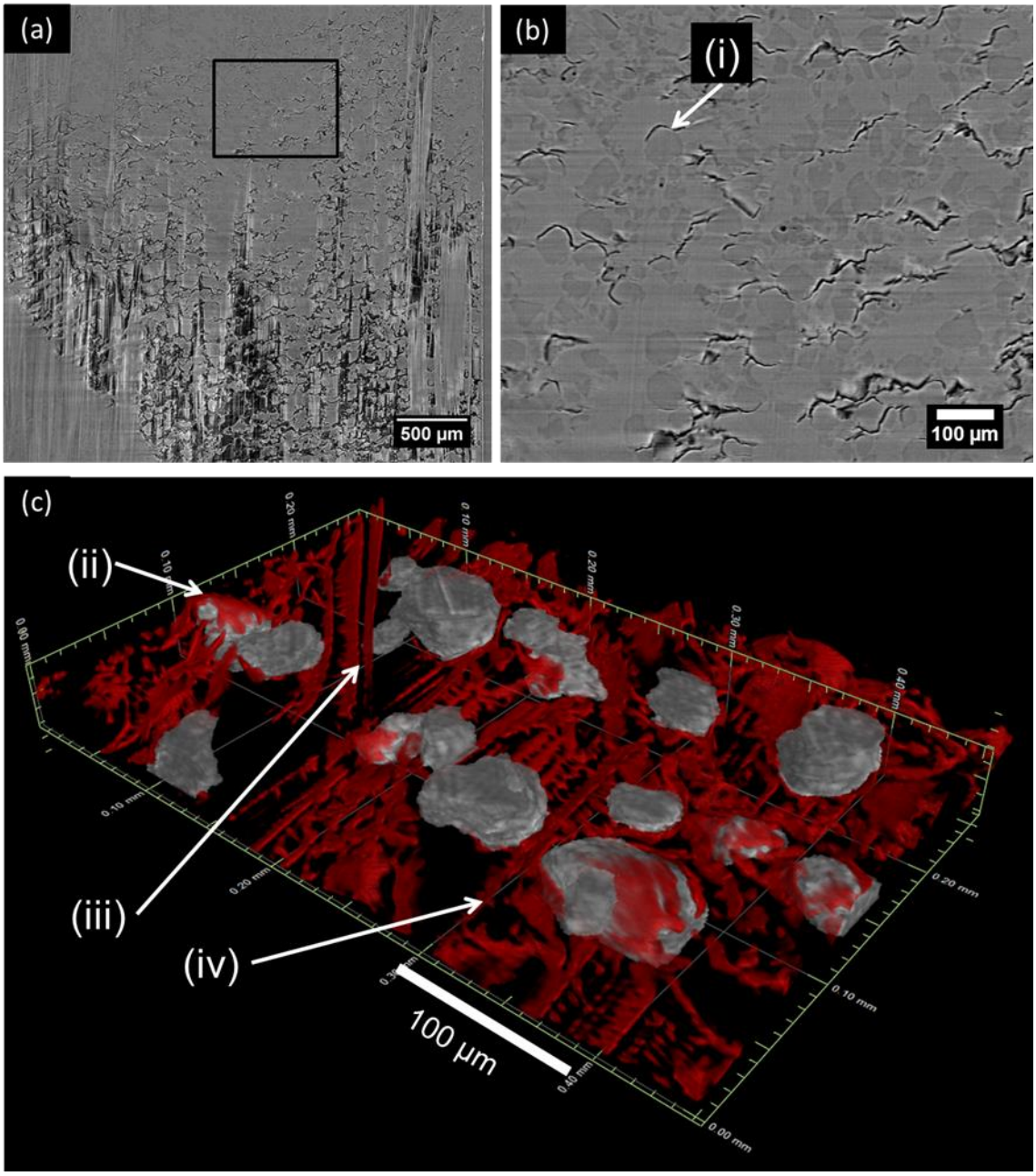

Figure 7.7: T1 SRCT volume showing (a) cross-sectional slice of delamination at the resin-rich region, the box indicates a close up location shown in (b) with (c) showing a 3D segmentation of cracks in red, and particles in grey at this representative region. (i) and (ii) indicates particle-matrix debonding, (iii) and (iv) highlight delamination cracks propagating along the fibre-resin interface .

In terms of the potential toughening mechanisms described above for particle-containing materials, the behaviour of the UT system reveals clear differences: in

Figure 7.5 the absence of particles and a thick resin-rich region evidently confines delamination cracking to a narrower interface layer; with little or no crack deflection and bridging. Whilst there is some ligamented behaviour in the crack wake, these ligaments have cross-sections of the order of a single fibre spacing, *i.e.* considerably smaller than those observed in the T1, T3 and T4 systems.

As shown in Figure 7.5 (ii), delamination in the T2 system takes a different path and has a different morphology compared to the other particle-toughened systems. Despite the presence of a similar resin-rich interface region, the great majority of delaminations observed in this material deflected out of the resin-rich region and propagated within the adjacent ply, parallel to the ply interface. It is possible that the local particle-resin interface toughness is high enough to prevent damage formation from occurring in the interlaminar region as evidenced by a lack of echelon cracking in this region, and this may also be linked to the stiffness mismatch between the particle and resin. For this reason, it may be the cause for the crack path to propagate into the intralaminar region following a path of lower resistance. The deflection of delaminations into the intralaminar region results in the potential reduction of energy absorption and crack tip shielding processes experienced in the interlaminar region as observed in the other particle-toughened systems. This potentially contributed towards the lowest mode II fracture toughness in comparison to the other systems and has a direct effect on its ability to suppress the extent of damage area as evidenced by a lower damage resistance compared to the T4 system.

A schematic shown in Figure 7.8 summarises the key toughening micromechanisms discussed in this section acting within the resin-rich region. In the process zone ahead of the crack tip there is abundance of particle-resin debonding sites and to a lesser extent fibre-resin debonding. In the wake of the crack, ligaments form consisting of both particles and resin enabling a load transfer bridging the crack faces. Failure of the ligaments occurred predominantly through debonding between the resin and particle interfaces and fracture of ligaments consisting of resin. It is possible that fracture across the particle may have also occurred. Higher resolution SRCT data are needed to determine the presence and extent of this behaviour. The ability for SRCT to detect geometrical information enables numerical quantification of the extent of bridging ligaments

near the crack tip and the extremity of crack deflection and increase in crack path length in the crack wake. One of the key questions is whether these toughening parameters correlate with an increase in impact damage resistance, and this is discussed in the next section.

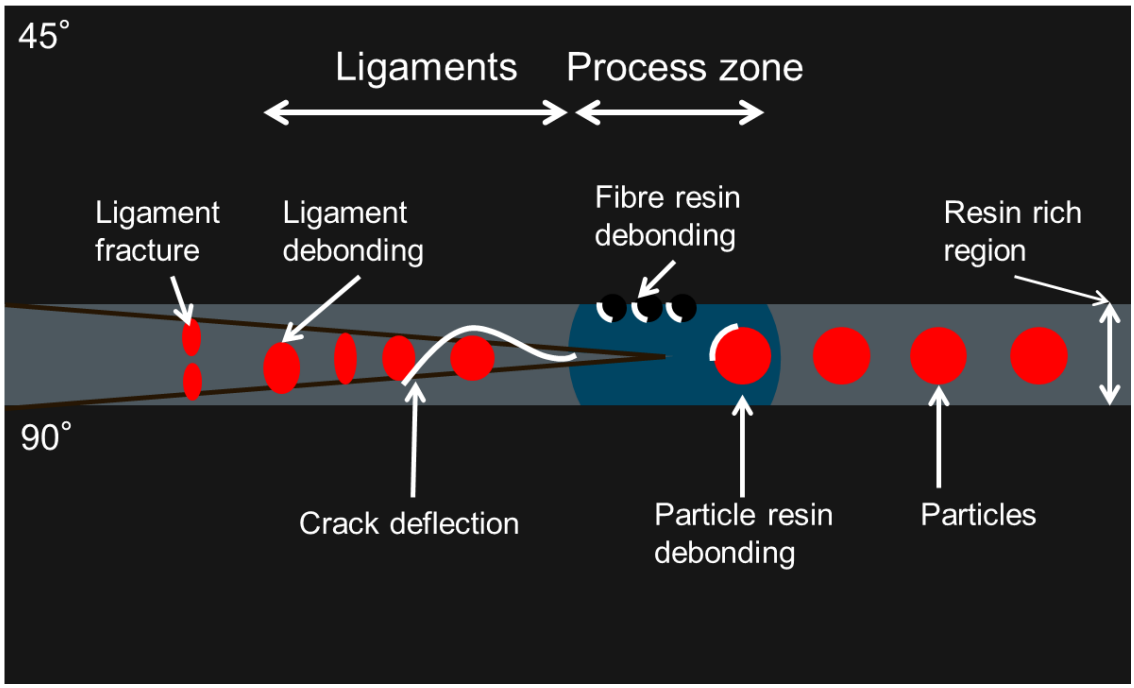

Figure 7.8: Schematic of toughening micromechanisms.

7.3.3 Quantification of crack path length, roughness and crack bridging

Several toughening parameters were measured from SRCT data: crack path extension, roughness, and bridging behaviour. Measurement of these parameters would indicate if there is any significant contribution from these toughening mechanisms and how they compare between material systems of varying impact damage resistance.

Measurements of crack path length and crack surface roughness were made in regions within the wake of the crack as presented in Figure 7.10. A plot of actual-to-projected crack length ratio for each of the material systems tested is shown in (a) and roughness in (b). The measurement of these two parameters is indicative of an increase in fracture surface area, and crack deflection. It is generally agreed

that an increase in crack path length would absorb more energy through increased fracture surface area *i.e.* more energy is required to propagate the crack [8]. Toughening through crack deflection is obtained by deflecting the crack so that its orientation is away from the path of maximum global strain energy release rate.

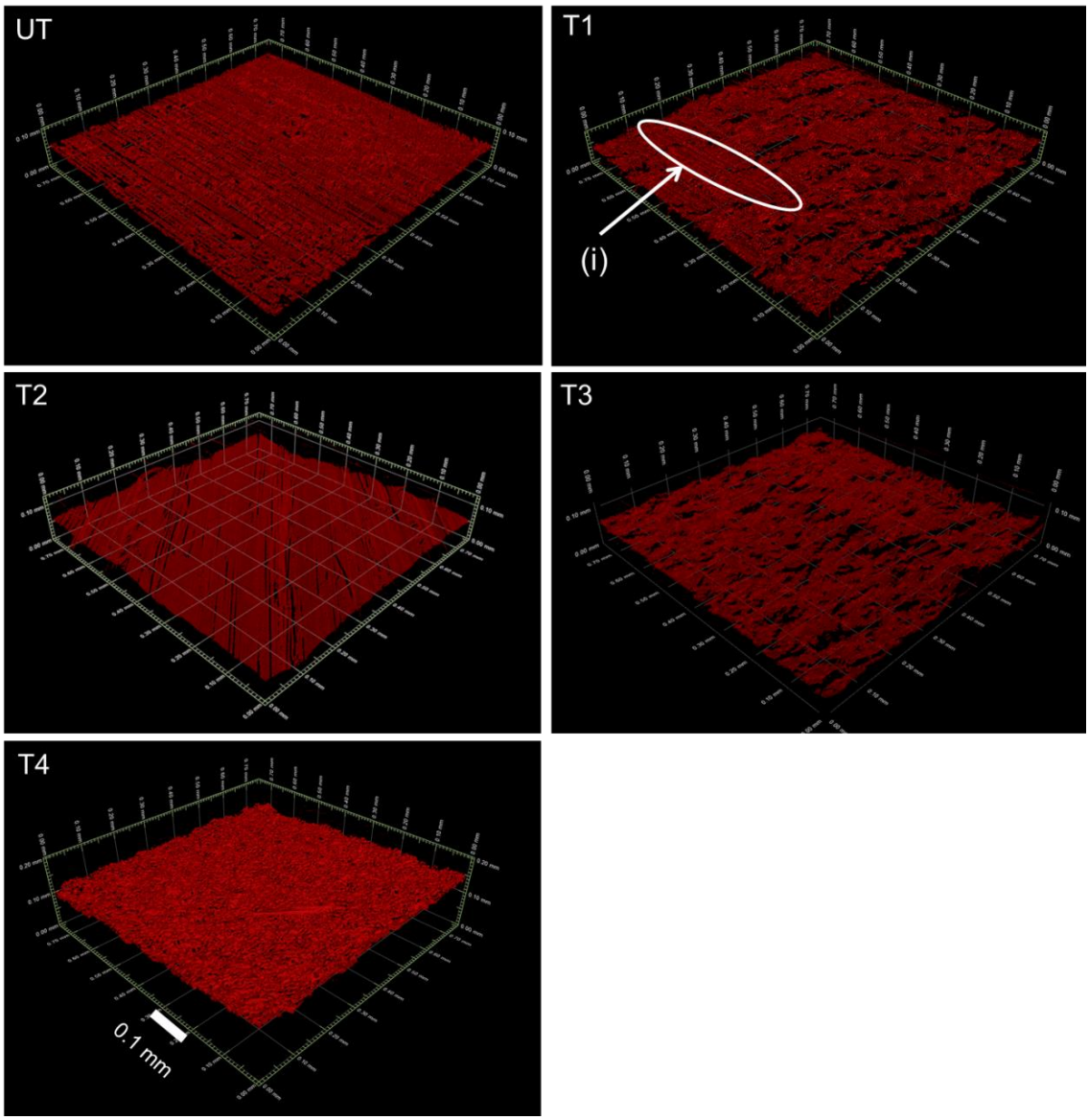

Figure 7.9: SRCT segmentation of delamination areas taken in the wake of the crack at the same ply interface position for the five material systems. (i) Delamination cracks propagating along the fibre-resin interface.

Across all the systems, there is an increase in crack path length due to some degree of crack deflection. The increase in crack path length was lowest in the UT and T2 systems, presumably due to the constraint imposed on the crack path by

the relatively thin interlaminar (UT) and intralaminar (T2) resin regions. In the T1, T3, and T4 systems, a greater extent of crack deflection is evidenced by a consistent but modest increase in the actual-to-projected crack path length ratio (from ~1.2 to 1.4). This has led to an increase in fracture surface area (~17 %) in the toughest T4 system, therefore increasing the energy absorption associated with generating the projected crack area. This is a small but important contribution to toughness, however, in this case the marginal increase in crack path length is unlikely to have a significant contribution to the overall impact damage resistance, which is in agreement with a previous study [8].

The measurements of crack wake roughness in terms of R_a are broadly consistent with the qualitative observations of crack deflection and crack length measurements: the particle-toughened systems show greater crack roughness in the crack wake compared to the untoughened and T2 systems, as shown in Figure 7.10 (b). Toughness does not scale simply with surface roughness however, with the T4 system exhibiting the greatest toughness but only an intermediate R_a value. The high surface roughness observed in the T1 system is due to the larger particles used in this system and these lead to large deflected crack segments, relative to the other systems. In comparison, the T4 system, in spite of approximately 30 % less roughness, an indicator of shorter crack deflections, showed approximately 120 % more deflected segments, resulting in a larger crack path extension. It is difficult to discern whether crack deflection contributed significantly to toughness by reorienting the crack to a plane of lower stress. It is also possible that a contribution to the toughness resulted from the deflection of the crack leading to bridging ligament formation, which is discussed subsequently.

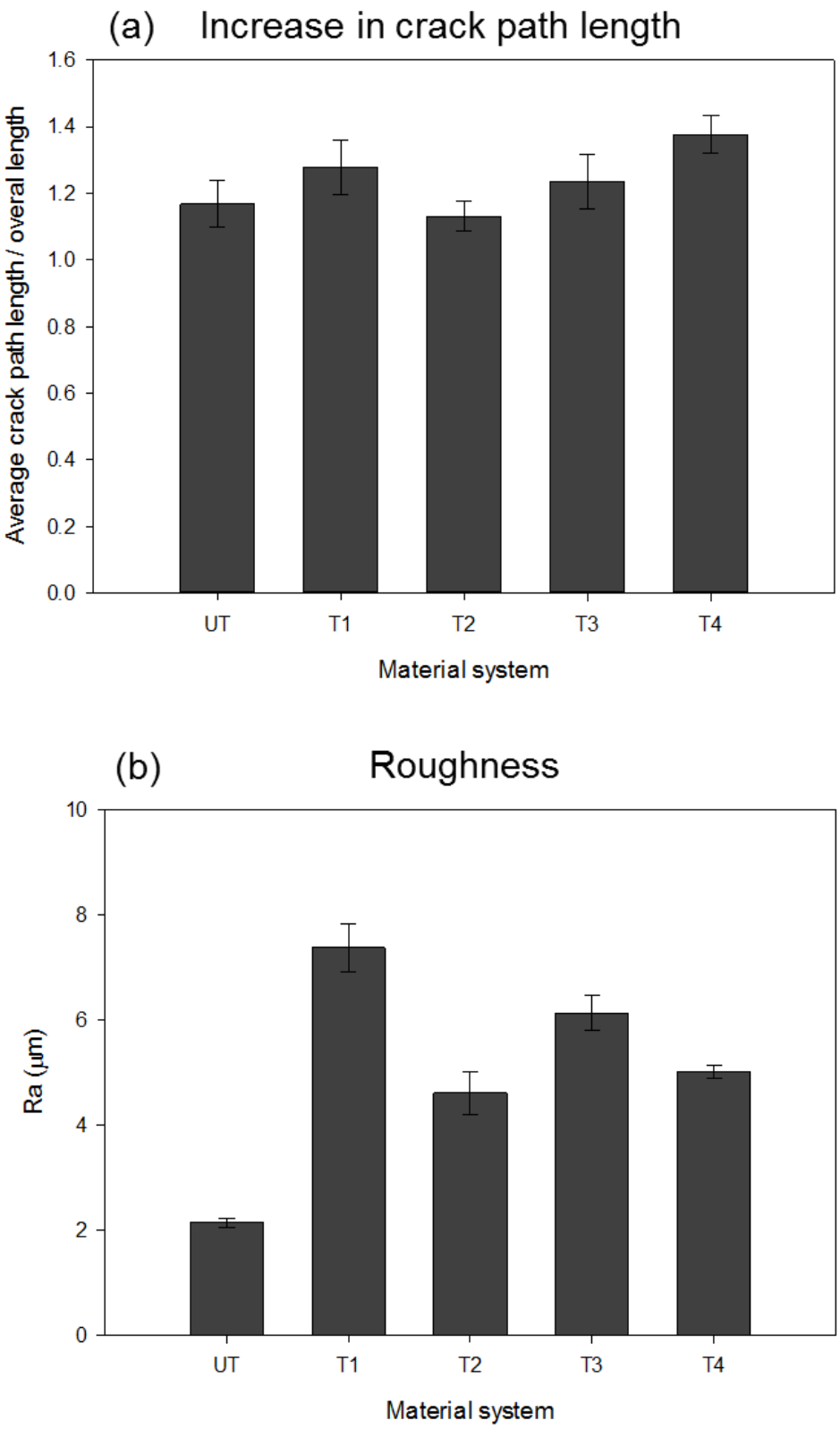

Figure 7.10: (a) Ratio of actual-to-projected crack length for each of the material systems tested. (b) Fracture surface roughness across the five material systems. Error bars indicate standard error in mean values based on 50 crack wake segments of ~750 µm length measured for each case.

Extents of crack wake bridging and the numbers of crack segments are plotted in Figure 7.11 and Figure 7.13 respectively. The extent of interconnectivity shown in Figure 7.11(a) is greater near the crack tip in the particle-containing systems; approximately 70-100 % more compared to the untoughened system. With the exception of the T2 system, it is evident that the extent of bridging drops as a function of distance from the crack tip. This decrease may be simply associated with increasing ligament strain, and hence the propensities for ligament failure; as crack-opening displacements grow larger with increasing distance from the crack tip. The T3 and T4 systems have a ~30 % smaller average ligament size near the crack tip compared to T1 and T2, see Figure 7.11(b), however there is approximately double the number of ligaments, as shown in Figure 7.13(a) and (b) - and this has led to a larger accumulated extent of bridging.

The scattered nature of bridging in the T2 system in the crack wake circled in Figure 7.11(b) is due to the crack deflecting from the intralaminar region into the resin-rich region, see (i) in Figure 7.12.

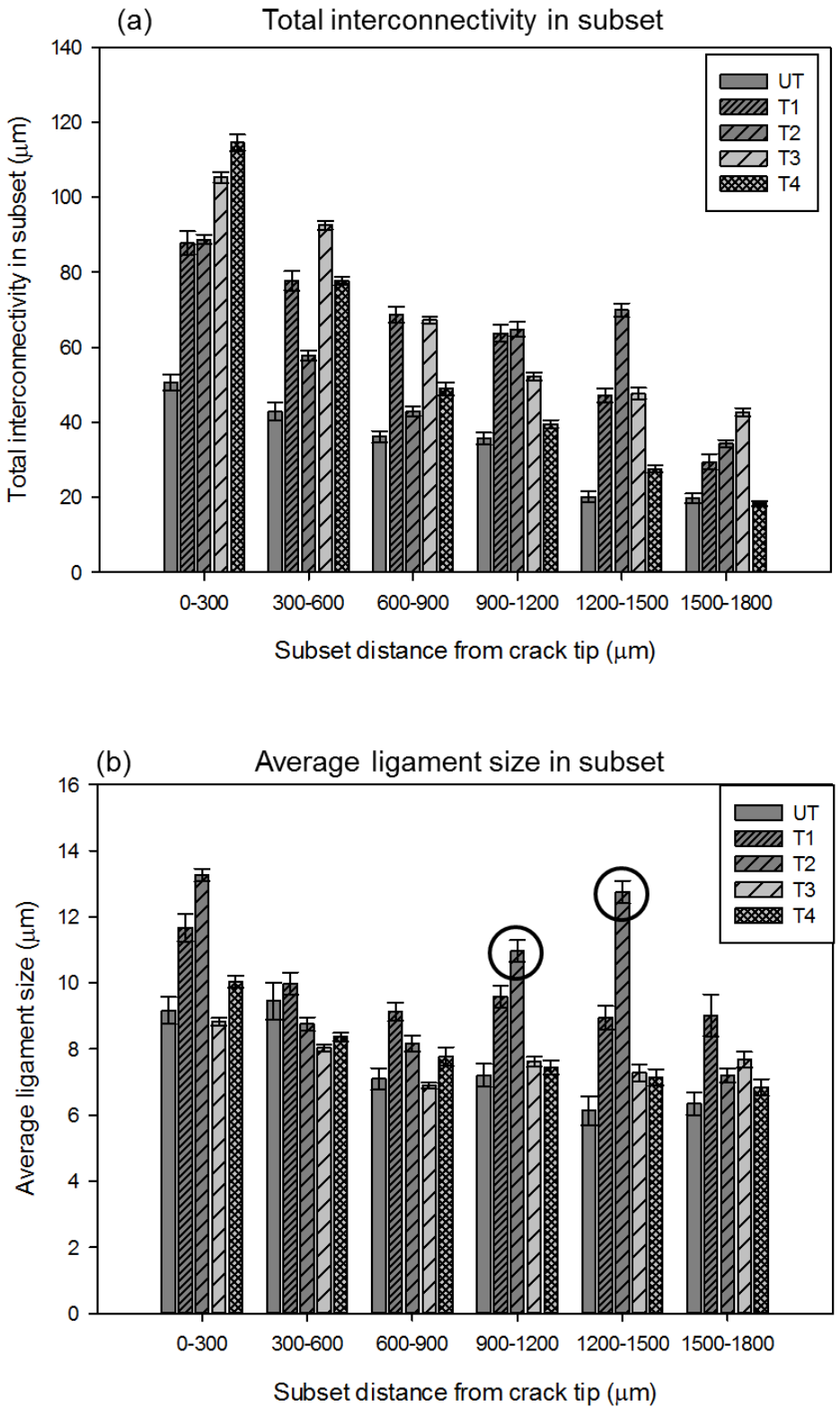

Figure 7.11: Plot of bridging behaviour as a function of sub-area distance from the crack tip. (a) The total interconnectivity in each sub-area, and (b) the average ligament size in each sub-area. The circled region in the T2 system represents the crack deflecting back into the resin-rich region.

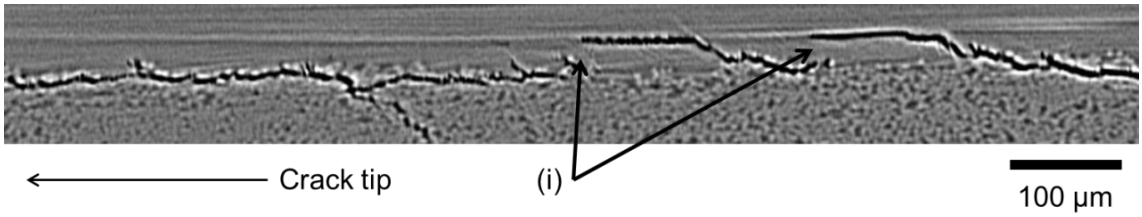

Figure 7.12: Cross-section of T2 system. (i) Crack deflected into resin-rich region at 900-1500 µm from crack tip.

Two categories of bridging sites as a function of sub-area distance from the crack tip are represented in Figure 7.13 consisting of: (a) oblique and (b) perpendicular cracks. The proportion of oblique ligaments is generally much lower than the perpendicular ligaments, with the exception of the large particle-containing T1 system, where a consistently greater proportion of oblique ligaments is seen. In relation to damage resistance, it is clear that the more resistant materials (T2-T4) are dominated by perpendicular ligament formation, particularly in the near-tip region.

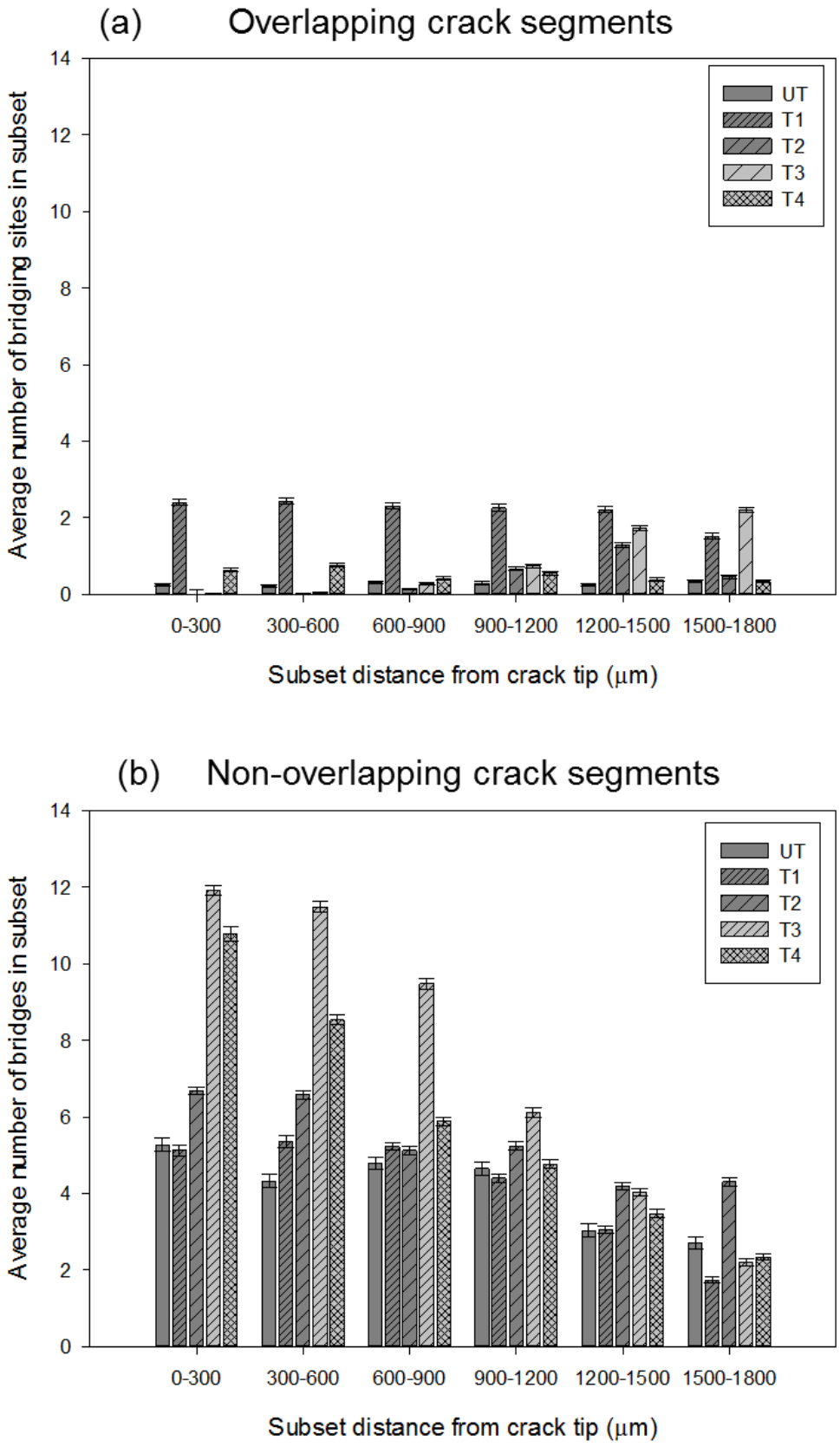

Figure 7.13: Plot showing average number of bridging sites in sub-area for (a) overlapping and (b) non-overlapping crack segments.

With the exception of T2, the average size of the ligaments decreases away from the crack tip. This is due to the growth of crack segments reducing the size of the bridging ligaments, Figure 7.11(b). The T3 and T4 systems have a larger number of non-overlapping crack segments, which decrease in number density with distance from the crack tip. This decrease in number is attributed to crack growth and fracture of the bridging ligaments. This characteristic is observed in the UT, T1 and T2 systems beyond 1.2 mm from the crack tip.

It is clear that bridging ligaments near the crack tip, as represented by the total interconnectivity in Figure 7.11(a), offers some indication to the corresponding impact damage resistance performance and can be ranked in terms of low (UT), intermediate (T1, T2 and T3) and high (T4). However, the relative improvements to the extent of interconnectivity between systems do not always correlate to the same magnitude of improvements in impact damage resistance, particularly between T3 and T4 systems. This suggests that whilst bridging ligaments may offer a significant contribution towards impact damage resistance, it is likely to be in conjunction with other parameters not measurable through SRCT, which can only capture geometrical information.

A key question is how the T4 system provides superior damage resistance, quantified as a 75 % reduction in damage area at a similar impact energy level compared to the untoughened system. Due to the difference in failure in the T2 system, the most direct micromechanistic comparisons may be drawn between the materials exhibiting true interlaminar failure, *i.e.* UT, T1, T3 and T4. From the quantification of the increases in crack path length, roughness, and bridging behaviour, both T3 and T4 systems show comparably similar results despite a 50 % lower projected damage area in the latter material system. This is interesting as one would expect to see a significant increase in the extent of one of these mechanisms. This suggests that whilst these toughening contributions are important characteristics to consider, there are additional factors that need to be understood which are not measurable from the SRCT data, therefore requiring other complementary techniques. These include, but are not limited to the inelastic deformation in the bridging ligaments, the resulting bridging traction-deflection

behaviour, interfacial strength between the particle and resin, energy absorbed by particle-resin interfacial debonding, and other factors such as fibre fracture.

7.4 Conclusions

As evident from mechanical testing and ultrasonic C-scans, particle-toughened systems show an improvement in low velocity impact damage resistance compared to an untoughened system. In this study, the T1, T2 and T3 systems improved damage resistance by a factor of two, and the T4 system by a factor of four when compared to the untoughened (UT) system at a 30 J impact. A poor correlation between mode II fracture toughness and corresponding impact damage resistance was observed across the material systems studied suggesting strain-rate dependency on some systems. For this reason, characterisation of toughness observations and measurements from SRCT impact data were compared directly to the impact damage resistance performance.

SRCT revealed that the toughening behaviour in the T1, T3 and T4 systems consisted of particle-resin debonding, crack bridging and crack deflection. In the T2 system, delaminations were driven into the intralaminar region with little damage existing in the interlaminar region. The lack of damage in this region points to a potentially high particle-resin interfacial strength causing failure to occur via the next competing fracture mechanism *i.e.* the intralaminar region, resulting in poor overall impact damage resistance.

Quantification of the increase in crack path length, roughness and bridging behaviour was undertaken via SRCT-derived images. A small ~17 % increase in crack path length was observed in the toughest system. It is considered the contribution of increase in crack path length as a toughening mechanism is small in comparison to the extent of bridging where a significant increase in this mechanism was observed in particle-toughened systems which correlated with gains in impact damage resistance. Whilst this study quantified these behaviours, it was unable to correlate this to the superior damage resistance in the T4 system, suggesting that other mechanisms need to be considered and further complementary work is required.

The measurements provided in this chapter indicate the potential of high resolution computed tomography to quantify the relative effects of toughening mechanisms in structural materials. The ability to quantify these mechanisms is an important element in the independent calibration of micro-mechanical models for fracture and failure processes. This represents an opportunity to pursue a strategy of data-rich mechanics, whereby limited numbers of *in situ* experiments can yield sufficient data to allow for the validation and calibration of sophisticated damage-based micromechanics models.

7.5 References

[1] Fu, S.Y., Feng, X.Q., Lauke, B., and Mai, Y.W., *Effects of particle size, particle/matrix interface adhesion and particle loading on mechanical properties of particulate-polymer composites.* Composites Part B-Engineering, 2008. **39**(6): pp. 933-961.

[2] Spanoudakis, J. and Young, R.J., *Crack-Propagation in a Glass Particle-Filled Epoxy-Resin .2. Effect of Particle Matrix Adhesion.* Journal of Materials Science, 1984. **19**(2): pp. 487-496.

[3] Hsueh, C.H., *Effects of Aspect Ratios of Ellipsoidal Inclusions on Elastic Stress Transfer of Ceramic Composites.* Journal of the American Ceramic Society, 1989. **72**(2): pp. 344-347.

[4] Groleau, M.R., Shi, Y.B., Yee, A.F., Bertram, J.L., Sue, H.J., and Yang, P.C., *Mode II fracture of composites interlayered with nylon particles.* Composites Science and Technology, 1996. **56**(11): pp. 1223-1240.

[5] Pearson, R.A., *Toughening Epoxies Using Rigid Thermoplastic Particles - a Review.* Advances in Chemistry Series, 1993(233): pp. 405-425.

[6] Spanoudakis, J. and Young, R.J., *Crack-Propagation in a Glass Particle-Filled Epoxy-Resin .1. Effect of Particle-Volume Fraction and Size.* Journal of Materials Science, 1984. **19**(2): pp. 473-486.

[7] Gao, F., Jiao, G.Q., Lu, Z.X., and Ning, R.C., *Mode II delamination and damage resistance of carbon/epoxy composite laminates interleaved with thermoplastic particles.* Journal of Composite Materials, 2007. **41**(1): pp. 111-123.

[8] Garg, A.C. and Mai, Y.W., *Failure Mechanisms in Toughened Epoxy-Resins - a Review.* Composites Science and Technology, 1988. **31**(3): pp. 179-223.

[9] Chai, G.B. and Zhu, S., *A review of low-velocity impact on sandwich structures.* Proceedings of the Institution of Mechanical Engineers Part L-Journal of Materials-Design and Applications, 2011. **225**(L4): pp. 207-230.

[10] Moffat, A.J., Wright, P., Buffiere, J.Y., Sinclair, I., and Spearing, S.M., *Micromechanisms of damage in 0 degrees splits in a [90/0](s) composite material using synchrotron radiation computed tomography.* Scripta Materialia, 2008. **59**(10): pp. 1043-1046.

[11] Aroush, D.R.B., Maire, E., Gauthier, C., Youssef, S., Cloetens, P., and Wagner, H.D., *A study of fracture of unidirectional composites using in situ*

high-resolution synchrotron X-ray microtomography. Composites Science and Technology, 2006. **66**(10): pp. 1348-1353.
[12] Scott, A.E., Mavrogordato, M., Wright, P., Sinclair, I., and Spearing, S.M., *In situ fibre fracture measurement in carbon-epoxy laminates using high resolution computed tomography.* Composites Science and Technology, 2011. **71**(12): pp. 1471-1477.
[13] Wright, P., Fu, X., Sinclair, I., and Spearing, S.M., *Ultra high resolution computed tomography of damage in notched carbon fiber-epoxy composites.* Journal of Composite Materials, 2008. **42**(19): pp. 1993-2002.
[14] Shyr, T.W. and Pan, Y.H., *Impact resistance and damage characteristics of composite laminates.* Composite Structures, 2003. **62**(2): pp. 193-203.
[15] Mader, K., Marone, F., Hintermuller, C., Mikuljan, G., Isenegger, A., and Stampanoni, M., *High-throughput full-automatic synchrotron-based tomographic microscopy.* Journal of Synchrotron Radiation, 2011. **18**: pp. 117-124.
[16] Morton, J. and Godwin, E.W., *Impact Response of Tough Carbon-Fiber Composites.* Composite Structures, 1989. **13**(1): pp. 1-19.
[17] Delfosse, D. and Poursartip, A., *Energy-based approach to impact damage in CFRP laminates.* Composites Part a-Applied Science and Manufacturing, 1997. **28**(7): pp. 647-655.
[18] Tang, Y.Y., Sun, B.Z., and Gu, B.H., *Impact Damage of 3D Cellular Woven Composite from Unit-cell Level Analysis.* International Journal of Damage Mechanics, 2011. **20**(3): pp. 323-346.
[19] Yang, F.J. and Cantwell, W.J., *Impact damage initiation in composite materials.* Composites Science and Technology, 2010. **70**(2): pp. 336-342.
[20] Wright, P., Moffat, A., Sinclair, I., and Spearing, S.M., *High resolution tomographic imaging and modelling of notch tip damage in a laminated composite.* Composites Science and Technology, 2010. **70**(10): pp. 1444-1452.
[21] Schoeppner, G.A. and Abrate, S., *Delamination threshold loads for low velocity impact on composite laminates.* Composites Part a-Applied Science and Manufacturing, 2000. **31**(9): pp. 903-915.
[22] Quaresimin, M., Ricotta, M., Martello, L., and Mian, S., *Energy absorption in composite laminates under impact loading.* Composites Part B: Engineering, 2013. **44**(1): pp. 133-140.
[23] Tan, K.T., Watanabe, N., and Iwahori, Y., *X-ray radiography and micro-computed tomography examination of damage characteristics in stitched composites subjected to impact loading.* Composites Part B-Engineering, 2011. **42**(4): pp. 874-884.

Chapter 8

An investigation of low velocity impact and quasi-static indentation loading on composite materials

This chapter investigates low velocity impact and quasi-static indentation (QSI) loading in four particle-toughened composite systems and one untoughened system. For impact tests, a range of energies were used between 25 to 50 J. For QSI, coupons were loaded and unloaded at increasing increments from 2 to 5 mm to allow for monitoring of damage initiation and propagation. In both the impact and QSI experiments, non-destructive inspection techniques were used, including ultrasonic C-scan and X-ray micro-focus computed tomography (μCT). These techniques are complemented with instrumentation to capture force-displacement data. Results show similarities between low velocity impact and QSI loading with regard to the projected damage area as a function of applied energy in all but two of the material systems which showed differences above 30 J. On these two systems, a lower damage area was recorded under QSI compared to impact at the highest energies with a corresponding increase in crack bridging behaviour. μCT enabled the evolution and distribution of delaminations to be quantified. Observations from QSI tests show that delaminations initiate and propagate below the mid-plane at the early stages of loading. At increasing out-of-plane displacements, the distribution of delaminations evens out across each of the ply interfaces throughout the thickness, with fibre fracture observed at the highest loads. The toughest system could accommodate more displacement prior to initiation of delaminations. Fibre fracture was observed at lower displacements in the toughened systems compared to the untoughened system.

8.1 Introduction

In addition to low velocity impact, composite structures may be susceptible to damage from non-transient out-of-plane point loads which can be represented using quasi-static indentation (QSI) experiments. It is reported by many studies that the two loading conditions yield similar damage characteristics in both experimental and analytical cases due to the analogous loading and boundary conditions that may arise [1, 2]. Controlled QSI loading may therefore present a valuable experimental strategy to imitate the chronology of processes occurring during impact. The non-destructive inspection capabilities of µCT [3] may then offer a powerful approach to monitor the evolution of damage, with the initiation and development of damage being measured with increasing displacement loads. Despite the similarities between QSI and impact, it is of course clear that QSI does not introduce the same dynamic and time-dependent components of impact events. It is debated within the literature as to the limits of utilising QSI to represent low velocity impact events, *e.g.* [1, 4].

In studies that compare QSI to impact loads, similarities have been reported in C-scan damage area and load displacement curves [5-11]. Whilst this provides an understanding of the general damage resistance response of such systems to loading, it neglects to identify if there are similarities in the interaction of different damage modes and if there are underpinning mechanistic similarities or indeed differences. Whilst previous studies have captured the micromechanisms of damage under increasing QSI loading, *e.g.* using cross-sectional microscopy, no time resolved 3D analysis has been reported. Such information may play a significant role in validating finite element models and guiding future toughening strategies, in which toughness may for example be targeted to certain ply interfaces [12].

This chapter aims to delineate and understand the micromechanical similarities and differences between QSI and impact damage in four particle-toughened and one untoughened composite system. Additionally, through use of interrupted QSI tests, this chapter aims to characterise the initiation and development of damage

with increasing out-of-plane displacements. µCT is used to provide novel, detailed comparisons of damage under low velocity impact and interrupted QSI conditions, complementing ultrasonic C-scan, dent depth and force-displacement data.

8.2 Materials and test procedure

The materials and testing procedures used in this chapter are described briefly here, with further details being found in chapter 3.

One untoughened (UT) and four particle-toughened (T1-T4) systems were studied using ~4.5 mm thick quasi-isotropic test coupons. Instrumented impact tests were conducted at 25, 30, 40 and 50 J and repeated three times for each material system. QSI was carried out at incremental applied displacements (2.0, 2.5, 3, 4 and 5 mm) on the same coupon on each material system and were repeated three times. After impact or application of QSI loading to the coupons, ultrasonic C-scans, µCT scans and dent depth measurements were carried out on intact uncut samples.

8.3 Results

8.3.1 Projected C-scan damage area

To assess damage resistance under quasi-static and impact loading conditions, normalised C-scan damage areas have been plotted against the applied energies in Figure 8.1 for both loading conditions. Data was normalised by dividing the measured projected damage area against the single largest damage area in the complete data set, *i.e.* comparisons can be made across all five materials. The applied energies for QSI data were calculated by integrating the area under force-deflection plots for the loading stages *e.g*. see Figure 8.2. Energies for each additional loading step were calculated by adding the energy applied beyond the previous displacement to the energy calculated from the previous loading stage to give the total energy applied. Applied energies for impacts were based on the measured impact energy.

The plots show a linear relationship between damage area and the applied energy for impact with the exception of the T3 system where scatter, on the order of a factor of two, was observed in the impact data at 40 and 50 J. The gradients of the trend lines are reasonably consistent for UT, T1, T2, and T3 systems with T4 showing a distinctly lower gradient trend line. For the UT system, the trend line approximately intersects the origin, and with the toughened systems the intersects with the axis occurred between 10-15 J indicating a translation to the data points and subsequently lower damage area for a given applied energy in comparison to the UT system.

It is interesting to note the correlation between QSI and impact loading conditions for each of the material systems. The UT, T2 and T4 systems represent good correlation on QSI data against the trend lines representing impact. However in two of the systems, T1 and T3 show a reasonably close correlation up to 30 J and a significantly lower damage area response (of the order of two to three times respectively) at the highest values of energy applied under QSI conditions compared to impact as circled in Figure 8.1. Furthermore, it should be noted that if the impact trend line in the T3 system were to follow the lower scattered data, then the QSI data would follow good correlation with the trend lines representing impact.

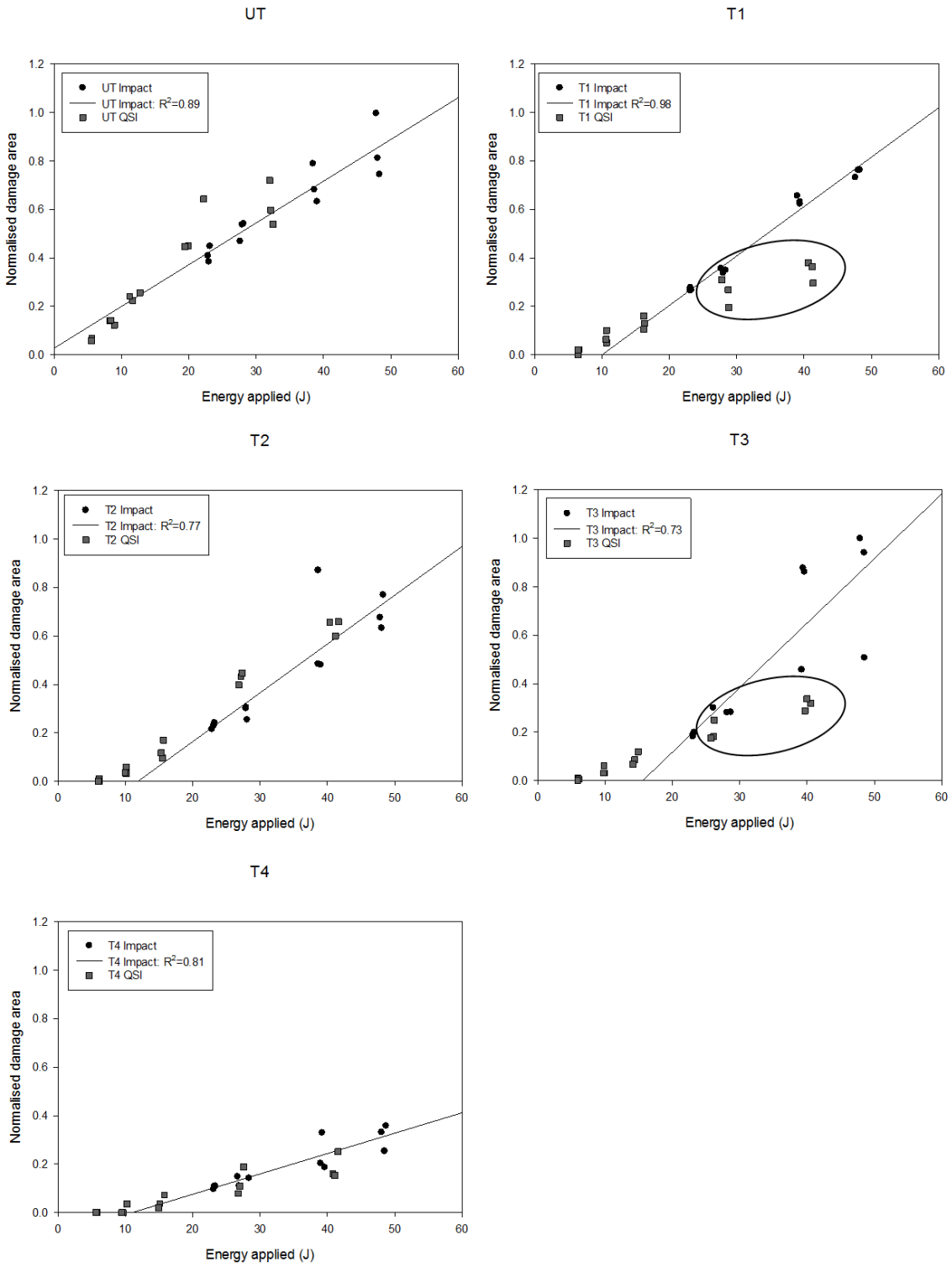

Figure 8.1: Graphs of normalised C-scan damage areas against the energy applied for impact and quasi-static loading conditions. Lines of best fit are shown for impact data. The T1 and T3 systems show different trends between QSI and impact loading which are circled.

A plot of QSI performance for all five material systems is shown in Figure 8.2 where the normalised damage area is compared against the applied energy. These are compared to impact performance rankings, see Figure 7.1 in chapter 7. Excellent linear correlations are shown (R^2>0.85) indicating the extent of the damage area is strongly linked to the applied energy. Studying the QSI performance rankings of each material system, the T1 systems shows a significant improvement compared to its impact performance, exceeding the T2 system and on par with the T3 performance. The T3 system also shows closer performance to the most damage resistant T4 system in comparison to how it performed under impact conditions.

The normalised damage area can be directly compared against the applied displacement, as shown in Figure 8.3. At a first inspection, the toughened systems seem to show similar corresponding behaviour, (*i.e.* the relative gradients are similar between both plots). However, a clear difference is observed for the UT system which has a trend line approaching that of the T2 system when damage area is compared against applied displacement in contrast to the impact energy applied.

The applied displacement of each load step was compared against the applied energy as plotted in Figure 8.4. All four particle-toughened systems display a similar response, *i.e.* for a given displacement, the applied energies are approximately the same. The UT system however shows a lower response and indicates that for a given displacement, there is a lower applied energy in comparison to toughened systems. This difference increases with applied displacement; at the highest displacement the UT system resulted in a ~20 % lower applied energy compared to the toughened systems.

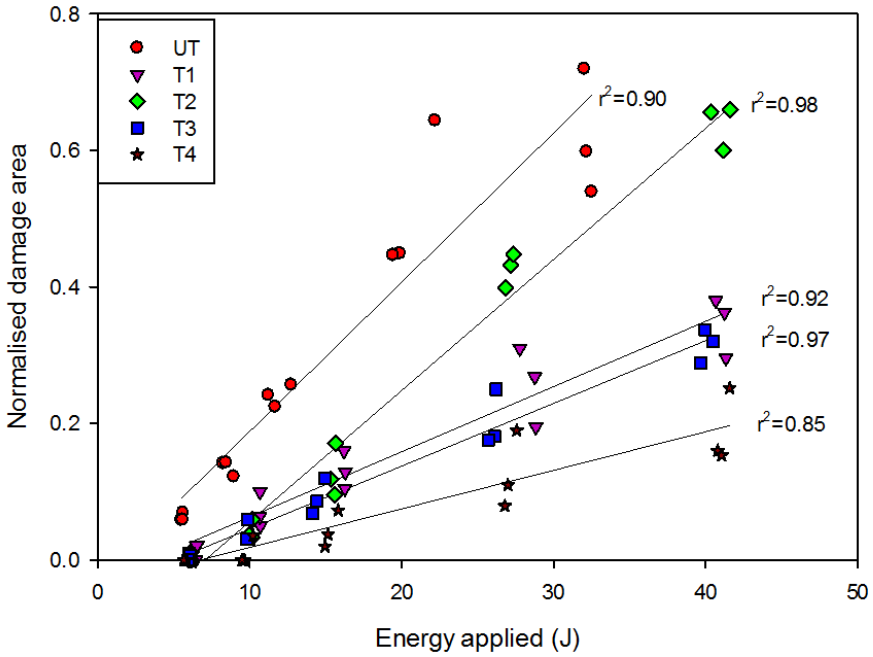

Figure 8.2: Plot of normalised damage area against energy applied for QSI tests on each of the five material systems.

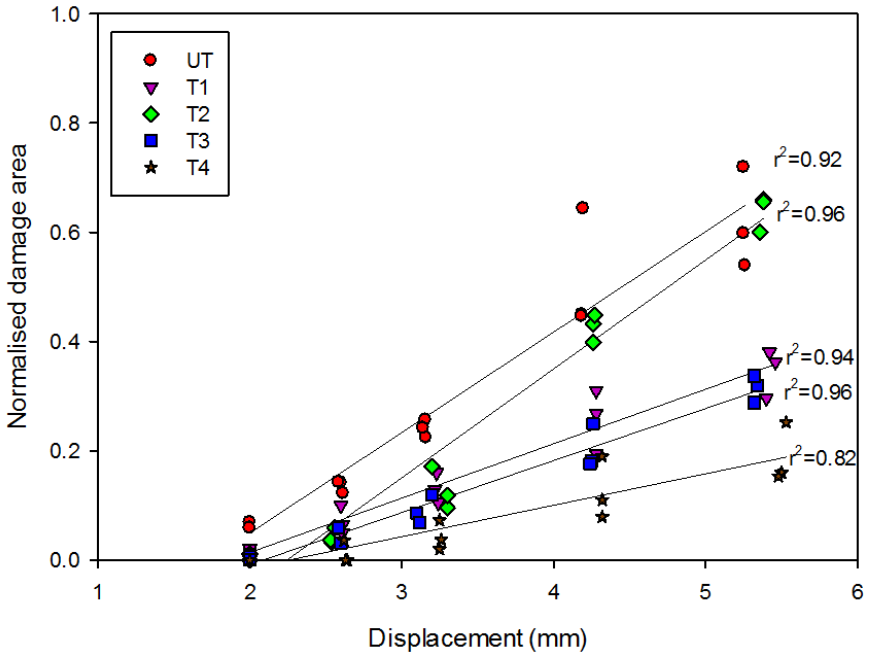

Figure 8.3: Plot of normalised damage area against displacement for QSI tests on each of the five material systems.

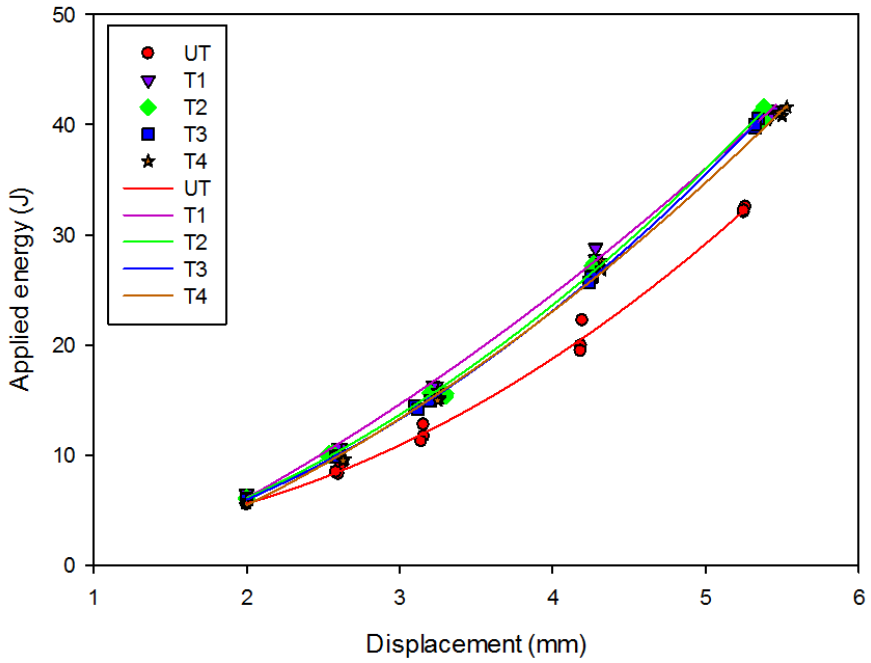

Figure 8.4: Plot of QSI applied energy against displacement for all five material systems.

8.3.2 Force-displacement comparisons

Force-displacement plots for quasi-static and impact loading conditions are shown in Figure 8.5. 40 J impact curves were plotted as a representative comparison with QSI due to similar resulting maximum displacement. Loading steps for each of the material systems are plotted together and show that the loading cycles on each incremental load are consistent as the load-displacement curves intersect or are in close proximity to the curves at the end of the previous load steps. The exception to this is on the T1 and T4 systems on the last loading stage where a difference in load at the previous displacement on the order of 1.5 kN was observed, ~15 % of the applied load at that point. Since the energies for each additional loading step was calculated by adding the energy applied beyond the previous displacement to the energy calculated from the previous loading stage, this may have ramifications for calculating the energy applied at the final load step which is likely to be underestimated.

A drop in load was observed in the UT system under both QSI and impact loading conditions at approximately ~1.8 mm displacement (see Figure 8.5 (i)). The drop in

load under impact conditions occurred at approximately the same displacement and force across the range of impact energies tested. Under QSI conditions, the load drop occurred at approximately the same displacement and force on the first loading stage of each of the three repeated UT samples.

It is likely that this drop in load is attributed to the brittle nature of this material system and corresponded to the onset of delamination which agrees with other studies [5, 7, 13]. The magnitude of this load drop was consistently higher at all impact energies, approximately 7 kN, compared to that consistently seen in the QSI tests, of approximately 5 kN. It is not known whether this difference in load drop is associated with the material response to the loading conditions or ringing/resonance of the instrumentation used in the impact apparatus.

Unlike the UT system which exhibited a load drop in the QSI test, the toughened systems did not exhibit a load drop, but rather increasingly non-linear load-displacement curves, as also observed in particle modified composites in [13]. A load drop was observed in the T3 system at the displacement indicated in Figure 8.5(ii) for impact but not QSI. Similar to the UT system, the drop in load was observed at approximately the same displacement and load across the impact energies tested. This load drop suggests a particular sensitivity to the dynamic nature of impact in this system.

At subsequent repeated loading cycles in the QSI test, there is an increase in non-linearity at the loading stages of the force-displacement plots, most noticeable at 4 and 5 mm displacements. This was observed across all material systems and is likely due to the loss in bending stiffness arising from delamination formation in the previous loading cycles, similar to results reported in [14].

At the highest displacement (4 or 5 mm), load drops were observed across all material systems indicated in Figure 8.5(iii) and (iv) for impact and QSI respectively. In the QSI test with the exception of T4, a smaller load drop (iv) preceded a significant load drop (v). This was consistent across all QSI tests when the load levels to cause this effect were reached. In the T4 system, the load drop indicated by (iv) was of a similar magnitude to the second load drop (v) in the other four material systems. The load drops in the impact instance occurred at

approximately the same load and displacement for 40 and 50 J cases across all the specimens tested.

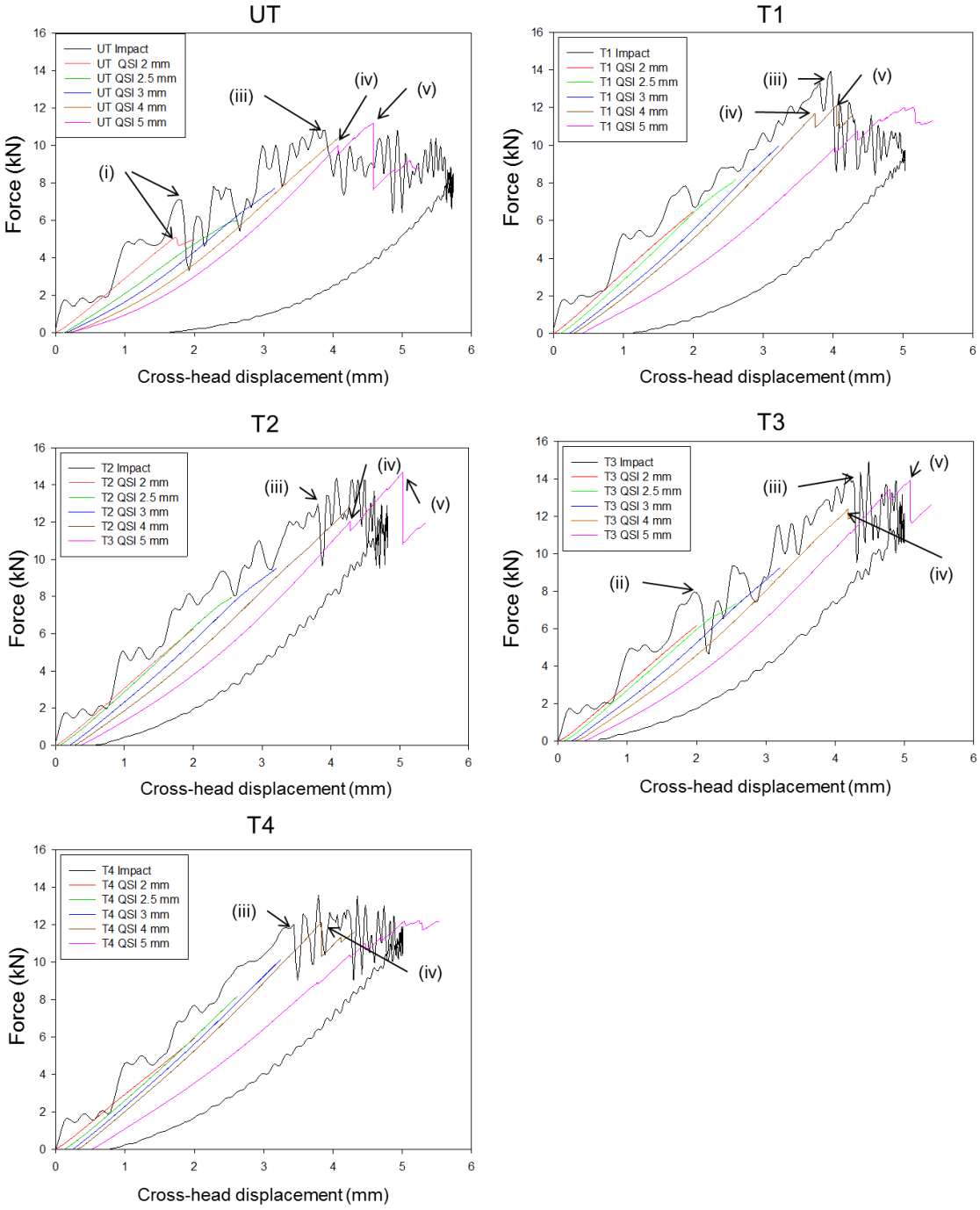

Figure 8.5: Force displacement curves for QSI and impact loading.

8.3.3 Comparison of QSI and impact from µCT scans

µCT cross-sections of damage from impact and QSI loading conditions are shown side by side in Figure 8.6. The T2 system was not scanned due to time constraints on the µCT scanner. For like-for-like comparison, the cross-sections shown are of similar out-of-plane displacements for both loading conditions, *i.e.* 25 J for UT and 30 J for T1, T3 and T4, led to a maximum out-of-plane displacement of approximately 4 mm. The peak force reached in the impact case was marginally greater but within 10 % of the QSI loading case. As noted above, both impact and QSI loading conditions show similarities in damage behaviour. This consisted typically of a cone of essentially undamaged material beneath the contact point of the tup. In the T4 system, fibre fractures are observed below the mid-plane in both loading conditions. Fibre fracture was distinguished against other damage modes by observing fracture across plies oriented with the fibres parallel to the page.

The presence of larger bridging ligaments (circled in Figure 8.6) was only observed in the T1 and T3 systems under QSI loads. This is shown more clearly on an enlarged view of the T1 system in Figure 8.7. The difference in bridging behaviour between the two loading conditions cannot be simply attributed to the displacements used in the QSI load case, as displacements and corresponding applied energies were in fact smaller in the impact case for these samples (~0.2 mm or ~1 J in both material cases).

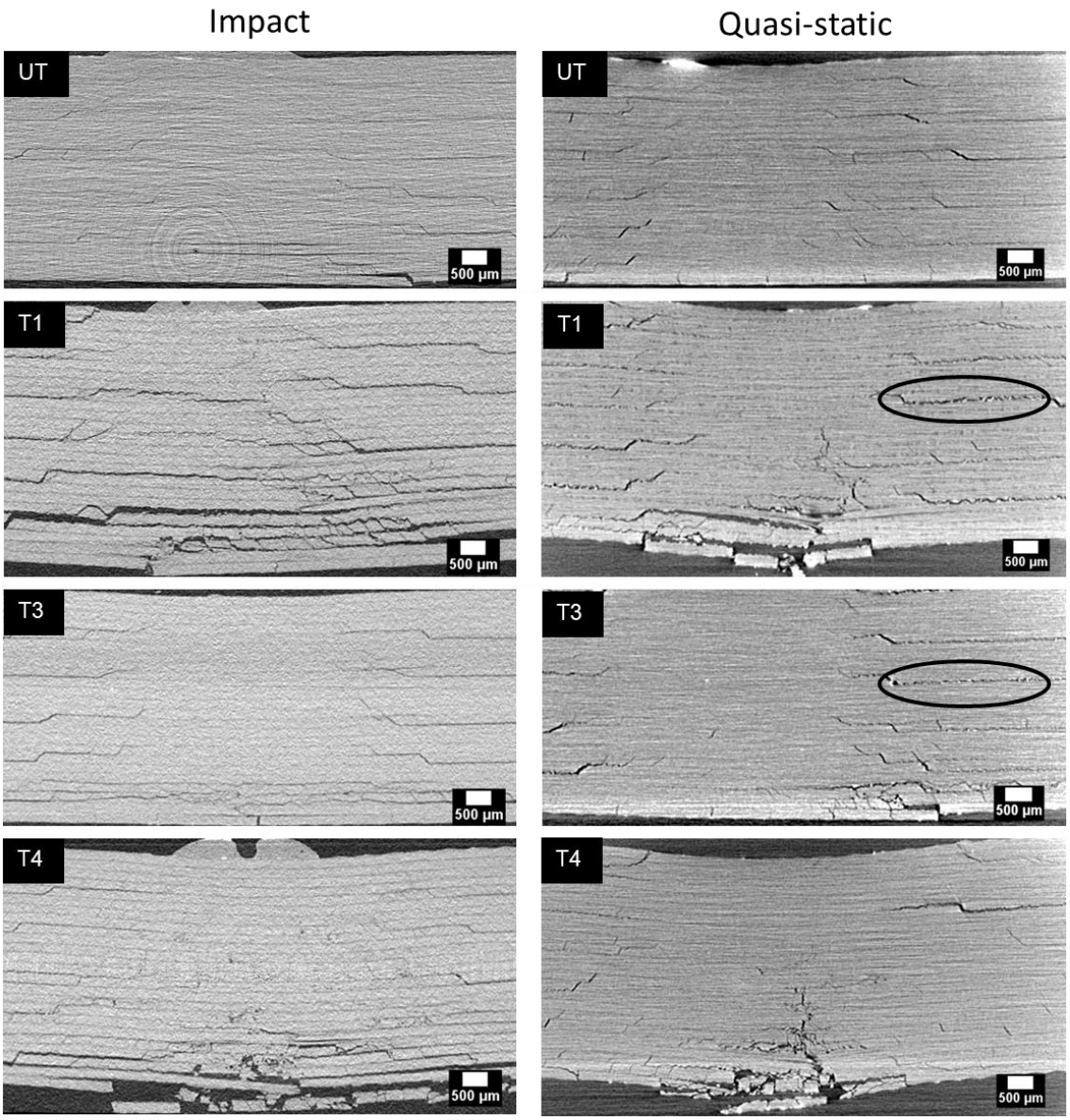

Figure 8.6: µCT cross-sections showing impact damage (left) and quasi-static indentation (right) at approximately the same maximum displacement. Observable bridging ligaments are circled.

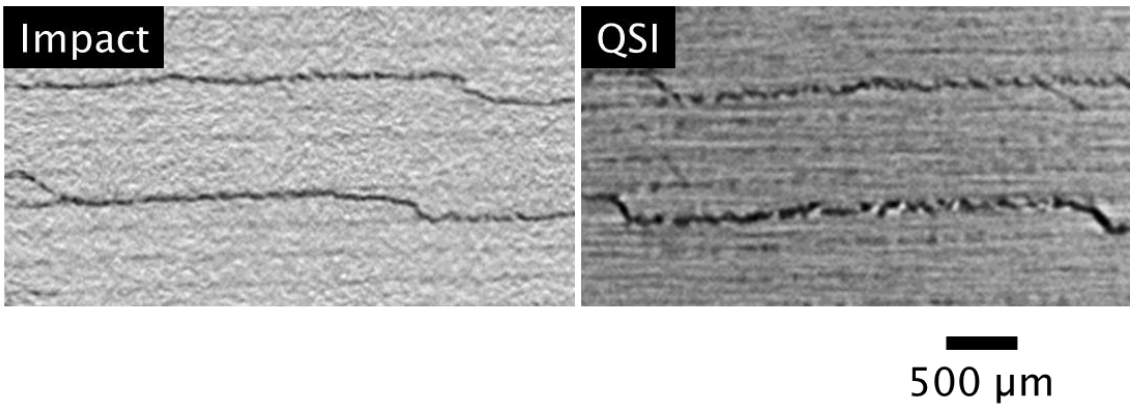

Figure 8.7: µCT cross-section comparing impact and QSI loading conditions of T1 system. More extensive bridging ligament behaviour is observed in the QSI loading condition.

8.3.4 Development of damage

The development of damage was captured from µCT scans in QSI tests as the applied displacement was increased. Cross-sections of the damage development are shown in Figure 8.8 to Figure 8.11 representing observations made on UT, T1, T3 and T4 systems respectively. The deflection and peak-force are indicated on each cross-section.

The T1 system (Figure 8.9) shows a reasonably clear sequence of damage initiation and propagation, as also observed in all the particle-toughened systems studied. It is revealed that matrix cracks initiate first (i) occurring predominantly below the sample mid-plane. In the toughened systems, matrix cracks are present at 2 mm applied displacements; conversely delaminations are shown to be suppressed unlike the UT system. With increasing displacements, delaminations are observed (ii) initiating at previously formed matrix cracks; in this case bridging ligaments are shown which are subsequently fractured at higher displacements (iii). At the highest displacement levels, fibre fractures occur (iv) which initiate below the mid-plane beneath the impact site due to tensile stresses and becomes more substantial (v) as the displacement is further increased. Fibre fracture was distinguished against other damage modes by observing fracture across plies oriented with the fibres parallel to the page.

Studying the µCT cross-sections (Figure 8.8 to Figure 8.11) fibre fracture was observed at 4 mm displacements in the toughened systems (T1, T3 and T4) under QSI loads and in the UT system this was only observed at 5 mm displacement. Initial fibre fracture was observed in the T1 and T3 systems at 4 mm and is indicated in region (iv). At 5 mm displacements, a substantial degree of fibre fracture was detected on the UT, T1 and T3 systems as indicated by (v), this was observed at 4 mm displacement for the T4 system.

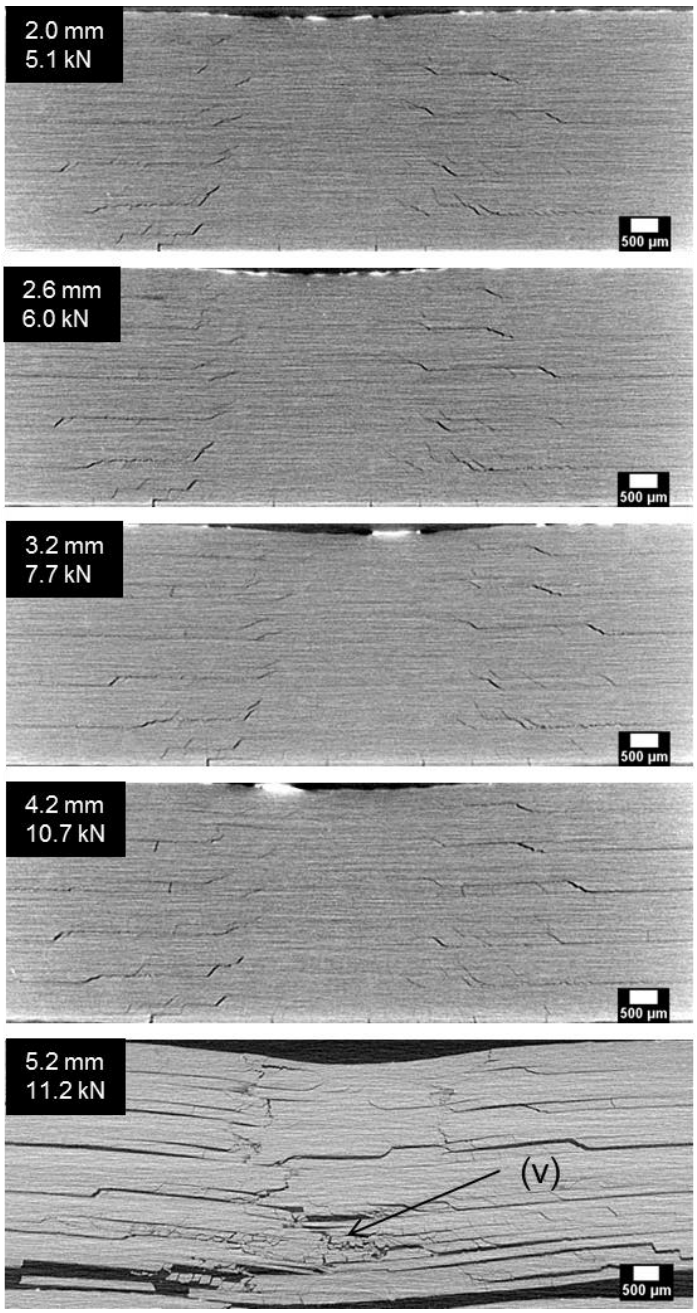

Figure 8.8: µCT cross-section of damage from the UT system at increasing QSI displacements. Peak displacement and peak forces are indicated. (v) shows substantial fibre failure.

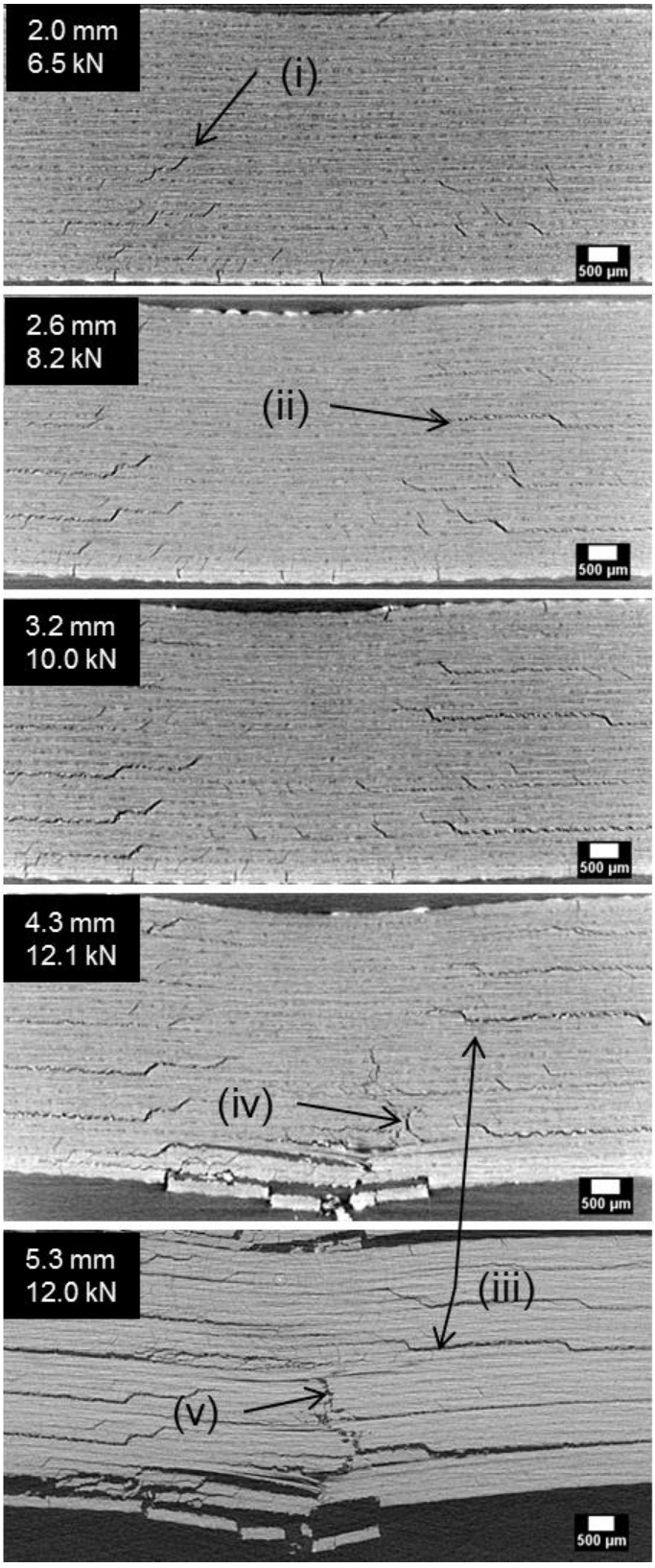

Figure 8.9: µCT cross-section of damage from the T1 system at increasing QSI displacements. Peak displacement and peak forces are indicated. Damage features are indicated consisting of (i) matrix crack, (ii) delamination with bridging ligaments, (iii) failure of bridging ligaments, (iv) fibre fracture and (v) substantial fibre fracture.

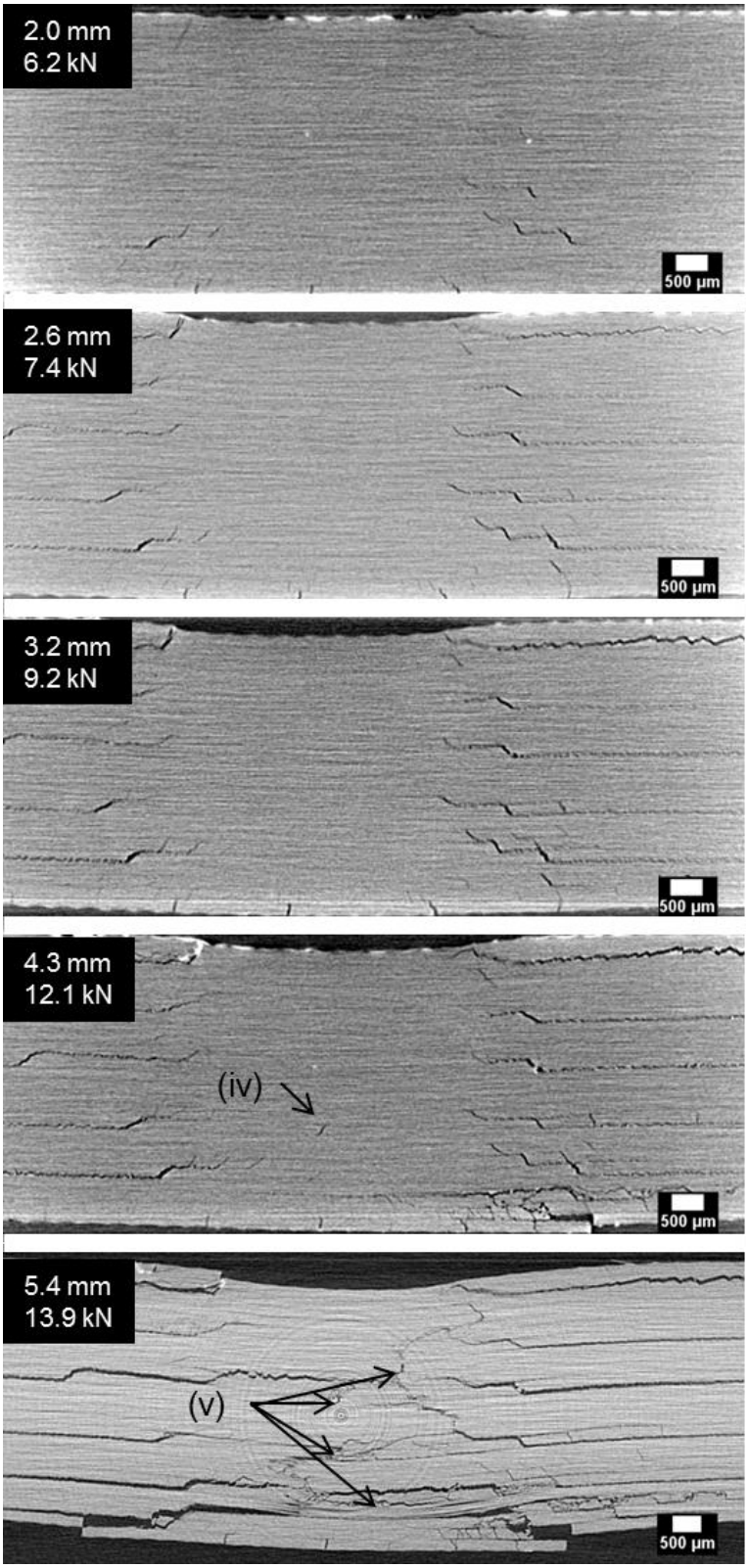

Figure 8.10: µCT cross-section of damage from T3 system at increasing QSI displacements. Peak displacement and peak forces are indicated. (iv) shows fibre fracture and (v) highlighting substantial fibre fracture.

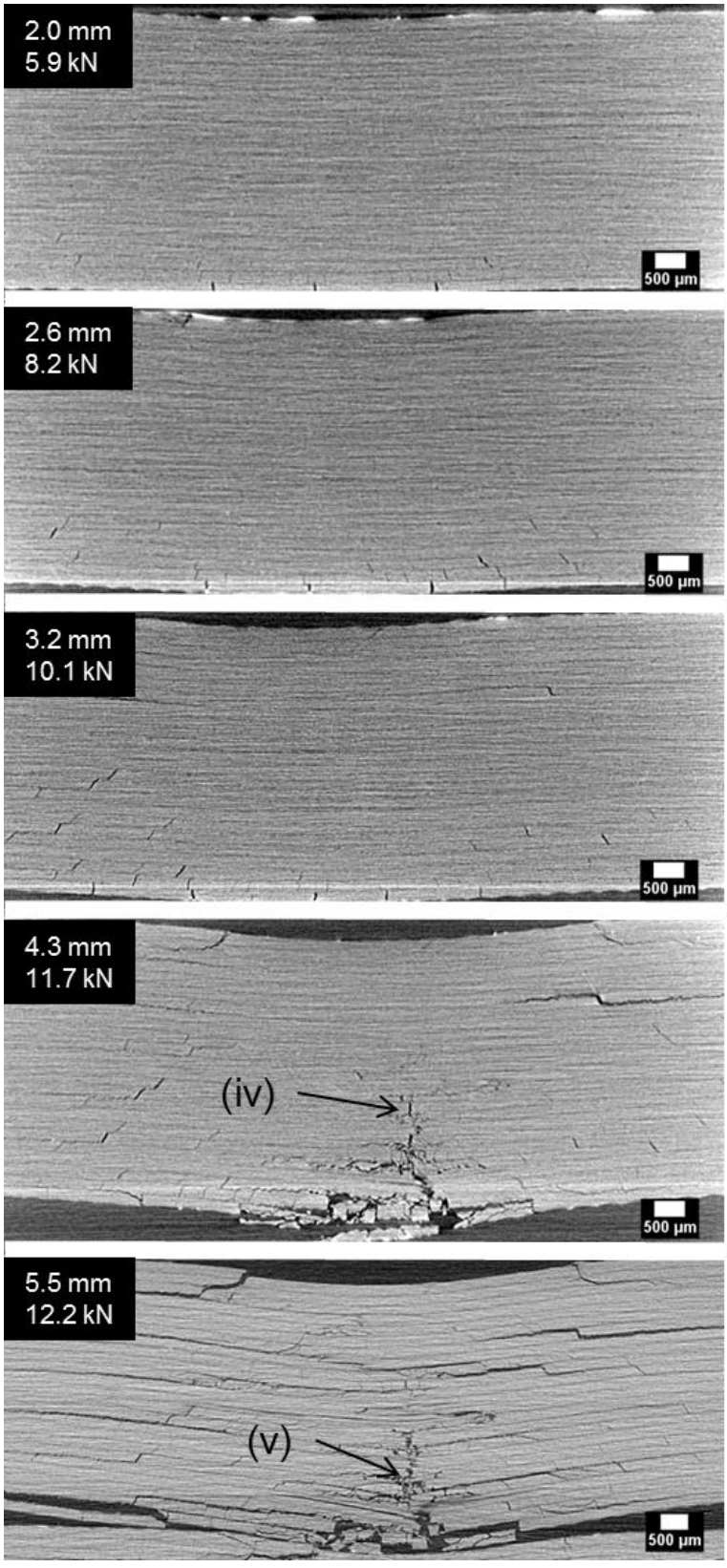

Figure 8.11: µCT cross-section of damage from T4 system at increasing QSI displacements. Peak displacement and peak forces are indicated. (iv) shows fibre facture and (v) highlighting substantial fibre failure.

The detectable extent of delaminations from QSI was measured from µCT scans at each ply interface and normalised to the largest delamination in that material system, see Figure 8.12. This allowed the through-thickness location and magnitude of the delamination to be plotted at increasing quasi-static displacements. The ply interface number on the plots represents the interface location where 1/2 indicates the first and second ply closest to the side in contact with the tup. In the UT, T1 and T2 systems, a significant proportion of detectable damage exceeded the field of view in the Benchtop µCT scan at 3 and 4 mm displacements and at 5 mm in the UT system with the HMX scan, therefore these were not plotted. No detectable delaminations were observed in the T4 system at 2 and 2.5 mm displacements.

It should be highlighted that the detectability of cracks is dependent on the voxel resolution used, in this case cracks with openings less than approximately 3 µm would not be expected to be detected (20 % of the voxel resolution) [15]. This limitation means that the extent of the actual length of the delamination is likely to be underestimated. However, it is anticipated that comparison/ranking is still possible between tests.

In all the toughened systems, delamination predominantly initiates and propagates below the mid-plane (Figure 8.12). As the load level increases, the distribution of delaminations evens out across the material system. The formation of damage initially below the mid-plane agrees with other studies which have considered the progressive nature of damage at increasing out-of-plane displacements [7, 14, 16].The largest delaminations occurred at the last ply interface (23/24) due to peeling stresses [17]. In this study, the delamination in the last ply exceeded the field of view of the µCT scan at the highest displacement levels. The reported delamination length is the measurable length within the field of view. In all tests, no delaminations were observed at the 12/13 ply interface, largely due to the same ply orientation ([90/90]) used at this interface [17, 18].

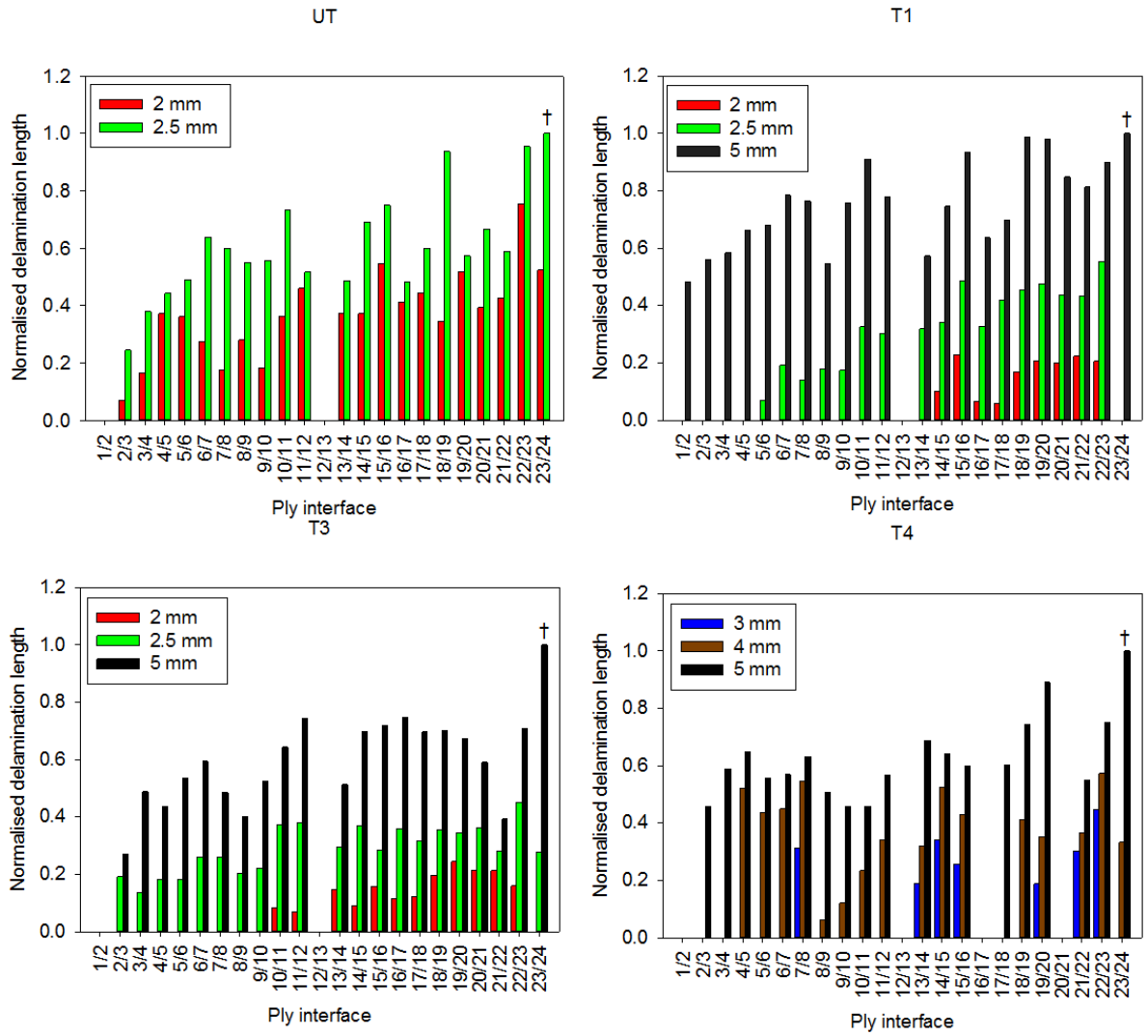

Figure 8.12: Graphs showing normalised delamination segment lengths on each respective ply after application of incremental quasi-static loads. † Note: on the 23/24 ply interface at 5 mm displacement, delaminations exceeded the field of view of the scan and would be expected to be greater than recorded. Data was normalised to the largest measured delamination within each material system.

8.4 Discussion

8.4.1 Loading rate sensitivity

The use of QSI to inform low velocity impact damage resistance performance has been shown to work reasonably well with close correlation between the extents of the damage area for a given applied energy under both loading correlations, see Figure 8.1. At energies in excess of 30 J, the T1 and T3 systems experience a

lower damage area under QSI conditions of the order of approximately two and three times respectively. This difference suggests an upper limit to this conformable behaviour, beyond which there are strain-rate dependencies on these systems. One of the definitions of “low velocity impact” (as discussed in section 2.2) is focused on there being a lack of strain-rate dependency. According to this definition, the T1 and T3 systems are no longer experiencing a low velocity impact event above 30 J. This transition away from a low velocity impact could explain the scatter in impact damage area observed at 40 and 50 J in the T3 system.

The strain-rate sensitivity is shown to affect the ligamented behaviour on both the T1 and T3 systems where larger bridging ligaments were present in the QSI case. This was shown on µCT cross-sections of the two material systems under impact and QSI at similar displacements in Figure 8.6 and Figure 8.7. From the understanding that bridging ligaments contribute significantly towards impact damage resistance as discussed in chapters 6 and 7, the presence of larger-scale bridging ligaments under QSI loads in T1 and T3 systems would appear to offer a straight-forward explanation of the load-rate sensitivity of these materials and why these systems maintained a lower extent of damage area under QSI loading conditions above 30 J.

To try and capture the strain-rate sensitivity, one suggestion for future work would be to test the feasibility of increasing the loading rates of mode II fracture toughness experiments and see if it offers comparable correlation to low velocity impact performance.

8.4.2 Damage characteristics

Comparisons of damage characteristics between QSI and impact show similar damage modes and interactions. In both loading cases, an undamaged cone formed beneath the contact point. This was preceded by delaminations which initiated from intralaminar cracks. Due to the same boundary and loading conditions, this is as expected. Where differences do arise, in the case of the T1 and T3 systems which showed a lower extent of damage area under QSI conditions, this was attributed to a larger extent of bridging ligaments. Therefore,

the differences in damage morphology between QSI and impact are likely to be attributed to the toughening micromechanisms associated with delamination formation. Higher resolution scans are however required to clarify as to how the micromechanisms between the two loading conditions differ.

The use of QSI has the benefit of enabling µCT time resolved studies to monitor delamination propagation across the through-thickness. From this study it is consistent across the three particle-toughened systems (T1, T3 and T4) that delaminations predominantly initiated and propagated below the mid-plane first. It is suggested that locally introducing additional toughening below the mid-plane could prevent the early stages of delamination formation. On the UT system, it is unknown whether this system exhibited a progressive or sudden damage growth as the first load step exceeded the load drop associated with the onset of damage. µCT scans prior to the load drop associated with the onset of damage in the UT system would be needed to confirm the behaviour.

The ability to measure the extent and distribution of delaminations as a function of displacement is useful for validating finite element models of QSI and impact events. A combination of µCT and ultrasonic C-scan data can provide a more accurate description of the delamination size and geometry. This information can be used to provide a much more realistic input of initial damage in finite element models, *e.g.* compression-after-impact modelling, in which these models are reported to be sensitive to delamination size, location and shape [24].

8.4.3 Load drops and fibre fracture

Combining the force-displacement plots with µCT scans, it is possible to associate the load drops that occur towards the highest displacements (4 and 5 mm) with fibre fracture, which was present on the back face below the tup. Some initial load drops were detected at 4 mm displacement and corresponded to some initial fibre fracture below the mid-plane beneath the contact point, and the latter load drop associated with significant fibre fracture. This is verified in Figure 8.9, where distributed, isolated fibre fracture was observed (iv) and localised fibre fracture

was detected (v) which corresponded to the load drops in Figure 8.5 (iv) and (v) respectively.

One interesting observation is the presence of significant fibre fracture which occurs at lower applied displacements in the T4 system, *i.e.* at 4 mm displacement in comparison to the other systems where it is present at 5 mm displacement. This behaviour appears to be independent of the peak-load reached, the T3 system which experienced a greater peak-load at 4 mm displacement showed no extensive fibre fracture. It is probable that the formation of a larger damage area observed on the other systems relieved the build-up of tensile stresses at the back-face of the material, delaying the fibre fracture process as explained by other studies [19, 20]. On systems that heavily suppress delamination formation, this presents a potential limitation. Considering that fibre fracture has been reported to have a detrimental effect on the residual tensile strength [21-23]; this may be of particular concern and may be a potential trade-off for toughened systems between suppressing delamination growth to maintain compression-after-impact strength at the expense of an earlier formation of fibre fracture which may reduce residual tensile strength.

8.4.4 Corresponding applied energy to out-of-plane displacement

There is a strong correlation between the applied energy and out-of-plane displacement for all four toughened systems, as shown in Figure 8.4. The UT system showed a lower applied energy for a given displacement compared to the toughened systems. This was reflected in the 40 J impact tests for which the toughened systems reached a peak displacement of ~5.0 mm and the UT system reached ~5.8 mm, see Figure 8.5. The cause of this behaviour is interesting, and can be explained by the QSI force-displacement loading curves. Across all five material systems, the gradients at the initial loading stage are consistent between systems (within 3 %). This corresponds to the very similar initial elastic properties between the systems. In the UT system, the load drop attributed at ~1.8 mm, reduced the stiffness and subsequently the energy applied needed for a given displacement.

The difference in displacement and corresponding energy curves highlights the need to make damage resistance comparisons across material systems against the applied energy. In the UT instance, this system shows poorer damage resistance to the toughened systems when using applied energy as a metric in contrast to displacement, see Figure 8.2 and Figure 8.3 respectively. Since applied energy was calculated by the integration of force-displacement plots, it takes into account load drops and different force-displacement loading response between material systems and makes straight forward comparisons with impact energy.

8.4.5 QSI: low cycle fatigue issues

The use of QSI as a method to allow the damage progression to be monitored through interrupting the experiment presents potential low cycle fatigue loading issues. In this study, the unloading and loading stages do not appear to influence the results significantly as evident by the damage areas being lower than the impact case in the T1 and T3 systems and correlating reasonably well with the other systems. If low cycle fatigue was to influence the data, one would expect to see a larger damage area with QSI than impact for all systems. Additionally, the incremental loading stages intersect or are in close proximity to the end of the previous loading stage on the force-displacement plots in Figure 8.5.

8.5 Conclusions

QSI and low velocity impact correlate reasonably well up to a limit with damage area corresponding closely with applied energy between both loading conditions. There was an upper limit to this correspondence observed in the T1 and T3 systems. Above 30 J, a lower damage area was recorded on these two systems under QSI conditions compared to impact. On these systems, more extensive bridging ligaments were detected under QSI loading compared to impact, based on µCT observations at similar applied energy levels. The extensive bridging and resulting lower damage area augments the evidence provided in chapter 7, in which the extent of interconnectivity (bridging ligaments) is shown to correlate with

a reduction in damage area. It is probable that the bridging ligaments in these systems are strain-rate sensitive such that a reduction in bridging leads to a significant increase in damage area. It can be inferred that a key to achieving higher impact damage resistance is to maintain bridging at higher strain-rates.

In the toughest system (T4), significant fibre fracture was observed at a lower displacement (4 mm) compared with the UT system (5 mm). It is suggested that the larger extent of delamination damage in the latter system relieved the tensile stresses leading to fibre fracture thereby delaying its onset. This suggests a potential trade-off in terms of performance and also a practical limit in terms of the maximum impact damage resistance that can be achieved.

Measurements of delamination length at increasing out-of-plane displacements showed that the earliest delaminations predominantly initiated and propagated below the mid-plane in all the particle-toughened systems tested. As the displacement increased, the distribution of damage became more uniform throughout the thickness of the coupon. This growth was gradual, starting with a very low extent of damage and is likely linked to the toughness of the particle systems. It is unknown whether the propagation of delamination in the UT system was gradual or sudden.

8.6 References

[1] Lagace, P.A., Williamson, J.E., Tsang, P.H.W., Wolf, E., and Thomas, S., *A Preliminary Proposition for a Test Method to Measure (Impact) Damage Resistance.* Journal of Reinforced Plastics and Composites, 1993. **12**(5): pp. 584-601.

[2] Wardle, B.L. and Lagace, P.A., *On the use of quasi-static testing to assess impact damage resistance of composite shell structures.* Mechanics of Composite Materials and Structures, 1998. **5**(1): pp. 103-121.

[3] Bull, D.J., Helfen, L., Sinclair, I., Spearing, S.M., and Baumbach, T., *A comparison of multi-scale 3D X-ray tomographic inspection techniques for assessing carbon fibre composite impact damage.* Composites Science and Technology, 2013. **75**: pp. 55-61.

[4] Swanson, S.R., *Limits of Quasi-Static Solutions in Impact of Composite Structures.* Composites Engineering, 1992. **2**(4): pp. 261-267.

[5] Kaczmarek, H. and Maison, S., *Comparative Ultrasonic Analysis of Damage in Cfrp under Static Indentation and Low-Velocity Impact.* Composites Science and Technology, 1994. **51**(1): pp. 11-26.

[6] Abdallah, E.A., Bouvet, C., Rivallant, S., Broll, B., and Barrau, J.J., *Experimental analysis of damage creation and permanent indentation on*

highly oriented plates. Composites Science and Technology, 2009. **69**(7-8): pp. 1238-1245.
[7] Aoki, Y., Suemasu, H., and Ishikawa, T., *Damage propagation in CFRP laminates subjected to low velocity impact and static indentation.* Advanced Composite Materials, 2007. **16**(1): pp. 45-61.
[8] Kwon, Y.S. and Sankar, B.V., *Indentation-Flexure and Low-Velocity Impact Damage in Graphite-Epoxy Laminates.* Journal of Composites Technology & Research, 1993. **15**(2): pp. 101-111.
[9] Lee, S.M. and Zahuta, P., *Instrumented Impact and Static Indentation of Composites.* Journal of Composite Materials, 1991. **25**(2): pp. 204-222.
[10] Symons, D.D., *Characterisation of indentation damage in 0/90 lay-up T300/914 CFRP.* Composites Science and Technology, 2000. **60**(3): pp. 391-401.
[11] Sjoblom, P.O., Hartness, J.T., and Cordell, T.M., *On Low-Velocity Impact Testing of Composite-Materials.* Journal of Composite Materials, 1988. **22**(1): pp. 30-52.
[12] Yasaee, M., Bond, I.P., Trask, R.S., and Greenhalgh, E.S., *Damage control using discrete thermoplastic film inserts.* Composites Part a-Applied Science and Manufacturing, 2012. **43**(6): pp. 978-989.
[13] Gao, F., Jiao, G.Q., Lu, Z.X., and Ning, R.C., *Mode II delamination and damage resistance of carbon/epoxy composite laminates interleaved with thermoplastic particles.* Journal of Composite Materials, 2007. **41**(1): pp. 111-123.
[14] Tan, K.T., Yoshimura, A., Watanabe, N., Iwahori, Y., and Ishikawa, T., *Effect of stitch density and stitch thread thickness on damage progression and failure characteristics of stitched composites under out-of-plane loading.* Composites Science and Technology, 2013. **74**: pp. 194-204.
[15] Schilling, P.J., Karedla, B.P.R., Tatiparthi, A.K., Verges, M.A., and Herrington, P.D., *X-ray computed microtomography of internal damage in fiber reinforced polymer matrix composites.* Composites Science and Technology, 2005. **65**(14): pp. 2071-2078.
[16] Yokozeki, T., Kuroda, A., Yoshimura, A., Ogasawara, T., and Aoki, T., *Damage characterization in thin-ply composite laminates under out-of-plane transverse loadings.* Composite Structures, 2010. **93**(1): pp. 49-57.
[17] Hull, D. and Shi, Y.B., *Damage Mechanism Characterization in Composite Damage Tolerance Investigations.* Composite Structures, 1993. **23**(2): pp. 99-120.
[18] McCombe, G.P., Rouse, J., Trask, R.S., Withers, P.J., and Bond, I.P., *X-ray damage characterisation in self-healing fibre reinforced polymers.* Composites Part a-Applied Science and Manufacturing, 2012. **43**(4): pp. 613-620.
[19] Wisnom, M., *The trade-off between damage and strength: why weaker may mean stronger.* Damage in Composites: Volume 5, ASC Series, 2012: pp. 211.
[20] Wisnom, M.R., *The role of delamination in failure of fibre-reinforced composites.* Philosophical Transactions of the Royal Society a-Mathematical Physical and Engineering Sciences, 2012. **370**(1965): pp. 1850-1870.

[21] Cantwell, W.J., Curtis, P.T., and Morton, J., *An Assessment of the Impact Performance of Cfrp Reinforced with High-Strain Carbon-Fibers.* Composites Science and Technology, 1986. **25**(2): pp. 133-148.
[22] Wang, S.X., Wu, L.Z., and Ma, L., *Low-velocity impact and residual tensile strength analysis to carbon fiber composite laminates.* Materials & Design, 2010. **31**(1): pp. 118-125.
[23] Richardson, M.O.W. and Wisheart, M.J., *Review of low-velocity impact properties of composite materials.* Composites Part a-Applied Science and Manufacturing, 1996. **27**(12): pp. 1123-1131.
[24] Craven, R., Iannucci, L., and Olsson, R., *Delamination buckling: A finite element study with realistic delamination shapes, multiple delaminations and fibre fracture cracks.* Composites Part a-Applied Science and Manufacturing, 2010. **41**(5): pp. 684-692.

Chapter 9

Observations of damage development from compression-after-impact experiments using *ex situ* micro-focus computed tomography

The development of damage mechanisms leading up to compression-after-impact (CAI) failure is studied in particle-toughened and untoughened systems. Micro-focus computed tomography (μCT) enabled non-destructive monitoring of the internal damage development in three-dimensions (3D) by taking scans after impact, after an application of near-failure compression loads and after coupon failure. In combination with μCT work, mechanical CAI testing and ultrasonic C-scans were conducted to determine the effect of the projected damage area on residual CAI strength and to complement the observations made from μCT scans. The important role of the undamaged "cone" of material immediately under the impact site for out-of-plane sublaminate stability is identified. The implication of delamination growth into this region is discussed. It was found that where particle-toughened systems suppressed delamination growth into this region, greater residual CAI strength was maintained on a like-for-like projected damage area.

9.1 Introduction

It is widely accepted that low velocity impact leads to damage in carbon fibre materials which has a direct effect on the residual compressive strength. It is reported that the loss in residual compressive strength scales with the size of the projected damage area (a representation of the extent of delaminations) [1-11].

This conclusion is based on conventional methods of measuring the damage area, typically using ultrasonic C-scans. Whilst this correlation based on projected damage area is widely accepted, the controlling mechanisms leading to catastrophic failure are still debated and not well understood. Such lack of understanding may be attributed to the complex and sudden nature of CAI failure making it difficult to identify the critical mechanisms contributing to the loss of compressive strength.

Whilst it is generally agreed that delaminations lead to a reduction in compression strength after impact, due to the formation of sublaminates with a reduced flexural stiffness which results in the earlier onset of buckling [6, 12], it is the sequence of events that is debated. Some studies report that sublaminate buckling leads to a sudden growth of damage extending laterally, leading to a sudden failure of the coupon [2, 13, 14]. Another reported mechanism is that the buckled sublaminates lead to a load redistribution resulting in compressive fibre fracture [4, 15]. One study using X-ray radiography to monitor damage growth at incremental compressive loads suggests that sublaminate buckling leads to a combination of bending and compressive loads in the remaining undelaminated regions. In this model the final failure is believed to occur when these stresses exceed the maximum compressive stress in the 0° plies [16].

To understand damage mechanisms that can develop and contribute towards critical failure, this study uses novel µCT experiments scanning coupons at various loading stages: after impact, after application of near failure in-plane compressive loads and after compressive failure. This technique allows for a non-destructive three-dimensional evaluation of the damage development within the same coupon [17] and is carried out in combination with conventional ultrasonic C-scan and compression-after-impact experiments. The aim of this study is to understand better the damage mechanisms leading up to compressive failure and any additional contribution towards damage tolerance in particle-toughened systems beyond the extent of the impact damage area. Such understanding will aid development of damage tolerant material systems and ensure finite element models for CAI tests are capturing the correct failure mechanisms in order to better predict critical failure loads.

9.2 Materials and test procedure

A brief outline of the materials used and testing procedures are described. Further details of the material systems and experiments are provided in chapter 3. Experimental procedures are divided into two parts consisting of conventional compression-after-impact testing and *ex situ* µCT studies on incrementally-loaded test coupons.

Compression-after-impact tests were performed on UT and T1-T4 material systems. Coupons were impacted at 25, 30, 40, and 50 J with three repeats per applied energy and material system. After impact, ultrasonic C-scan was performed to measure the damage area. Post-impacted coupons were placed in an anti-buckling rig and loaded in compression until failure to measure the failure stress.

To monitor damage progression at near-failure compressive loads, *ex situ* experiments were carried out. Coupons were impacted at 25 J for the UT system and 30 J for T1, T3 and T4. A lower incident impact energy was chosen for the UT system to enable the majority of damage to be within the field of view of the µCT scan. Two regions were locally scanned on each specimen, one directly in the vicinity of the impact site, and the other at the lateral edge of the damage area, as determined from C-scan. Due to time constraints, the T2 system was not scanned.

Coupons were µCT scanned after impact and following application of incremental load steps near the critical failure load, see Table 9.1. The first load was applied to two standard deviations below the mean failure load based on previous mechanical testing results. Subsequent loads were incremented at approximately 2 kN load steps or until audible damage was heard. The UT and T1 system reached loads higher than the eventual failure load at load step 5; this is likely attributed to sub-critical damage growth weakening the coupons at the load step prior to failure.

Table 9.1: Sequence of compressive load steps applied. Percentage loads are normalised to the measured failure load corresponding to the tested material system.

	Step 1	Step 2	Step 3	Step 4	Step 5	Step 6
UT	87.4 %	93.6 %	101.3 %	101.7 %	103.1 %	100 % (Failed)
T1	81.6 %	94.8 %	101.3 %	102.4 %	106.5 %	100 % (Failed)
T3	94.1 %	98.8 %	101.9 %	99.6 %	100 % (Failed)	
T4	94.0 %	98.3 %	96.6 %	98.7 %	100 % (Failed)	

9.3 Results and discussion

9.3.1 Mechanical testing

A plot of normalised failure stress against impact energy is shown in Figure 9.1. Normalisation of failure stress was calculated by dividing the failure stress against the largest failure stress in the data set. Across all systems tested, there is an approximately linear reduction of in-plane compressive failure stress as the impact energy increased. There are clear differences in damage tolerance of the four material systems tested, correlating with the impact damage resistance of each system. As expected, the UT system exhibits the least damage tolerant properties, T2 and T3 showed similar intermediate levels and the T4 system had the highest.

There was some scatter in the compressive failure stress across all the material systems at different impact energies. The effects of scatter made it difficult to predict the exact failure load during interrupted *ex situ* µCT tests which had the aim of achieving damage observations at loads near to failure. For this reason, the lower bound of failure to two standard deviations, as determined from these tests was used on the first loading cycle.

To show how the extent of the projected damage area correlates with a reduction in failure load, these data are plotted in Figure 9.2. The projected damage area based on ultrasonic C-scan measurements is representative of the scale of delaminations; detailed µCT measurements of impact-induced delaminations

shows the through-thickness delamination distribution to be fairly uniform across the though-thickness as presented in chapter 8. The projected damage area was normalised by dividing the particular damage area for a particular impacted specimen by the largest damage area in the set of data (all materials, all impact energies). Comparing the failure stress against the projected damage area, it is clear there is a correlation between the two parameters, allowing for the scatter in the data. Within the same systems, an increase in projected damage area clearly results in a loss in residual compressive strength. It is interesting to note, however, that there are variations in the gradients and overall values of the CAI strength-damage area relationships between material systems. As such it may be conjectured that several damage modes or toughening mechanisms may contribute to the damage tolerance. Compared to the UT system, the T2 and T3 systems share a similar gradient across the range studied. However, for a given damage area, the T2 and T3 systems showed a higher compressive failure stress, in the order of ~30 % more than the UT system. There was also a higher damage tolerance exhibited by the T1 system over the UT system, particularly at lower impact damage areas. In the most damage resistant, T4 system, the slope is significantly steeper than the other systems tested. Whilst T4 exhibits good CAI damage tolerance when considered in terms of impact energy, when plotting CAI load against damage area, failure loads are in fact quite similar to T1, T2 and T3 in the regime where they overlap with the T4 data. It is clear that the CAI failure stress decreases considerably more rapidly with damage area in the T4 system: extrapolating the T4 and UT results indicates that area-for-area, the T4 material may in fact be worse than the UT material at intermediate to high damage areas. As such, T4's CAI engineering performance may be identified as strongly impact damage resistance-driven, whilst T2 and T3 demonstrate greater damage tolerance for a given impact damage area. Overall it is clear that factors other than simple delamination area-controlled buckling contribute to residual CAI strength.

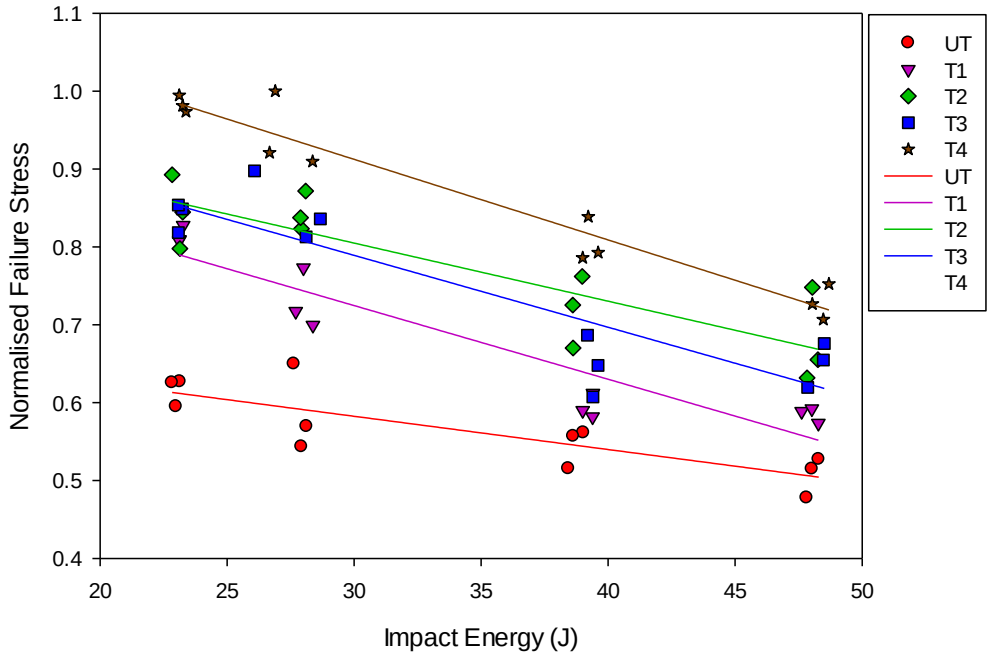

Figure 9.1: Graph showing normalised compression-after-impact failure stress vs. impact energy for the five systems tested.

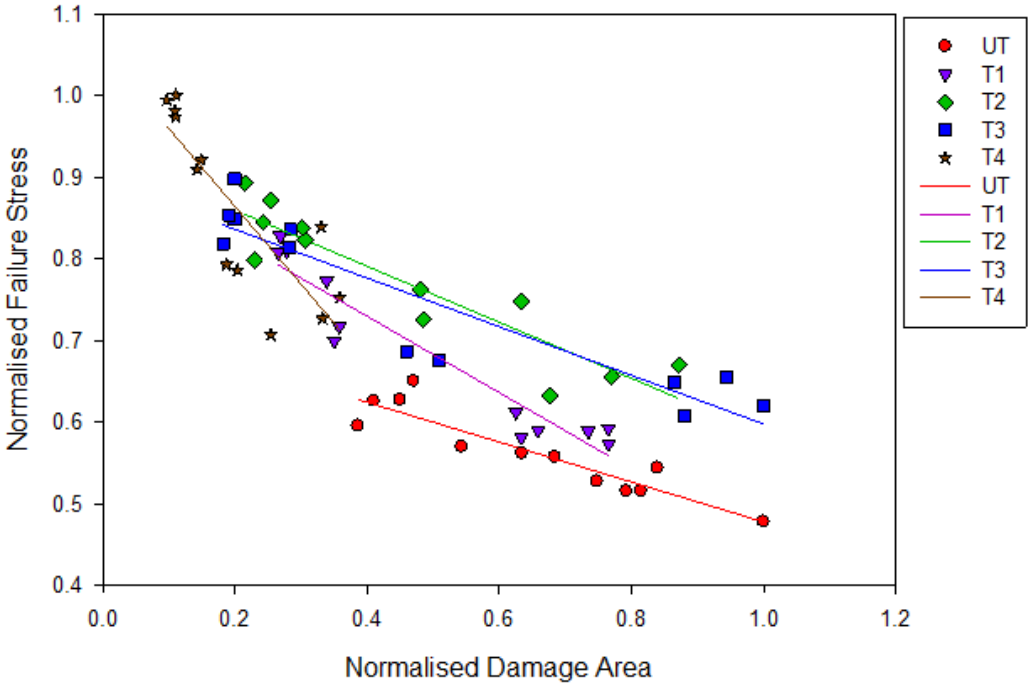

Figure 9.2: Graph showing normalised compression-after-impact failure stress vs. impact damage area for the five systems tested.

9.3.2 Compression-after-impact µCT damage development observations

9.3.2.1 Delamination development

Some early work prior to this experiment was carried out using ultrasonic C-scan to monitor damage growth, see Figure 9.3. As can be seen from the C-scan data, no significant increase in projected damage area occurred after application of a near failure load. After failure, damage was seen to grow laterally across the coupon.

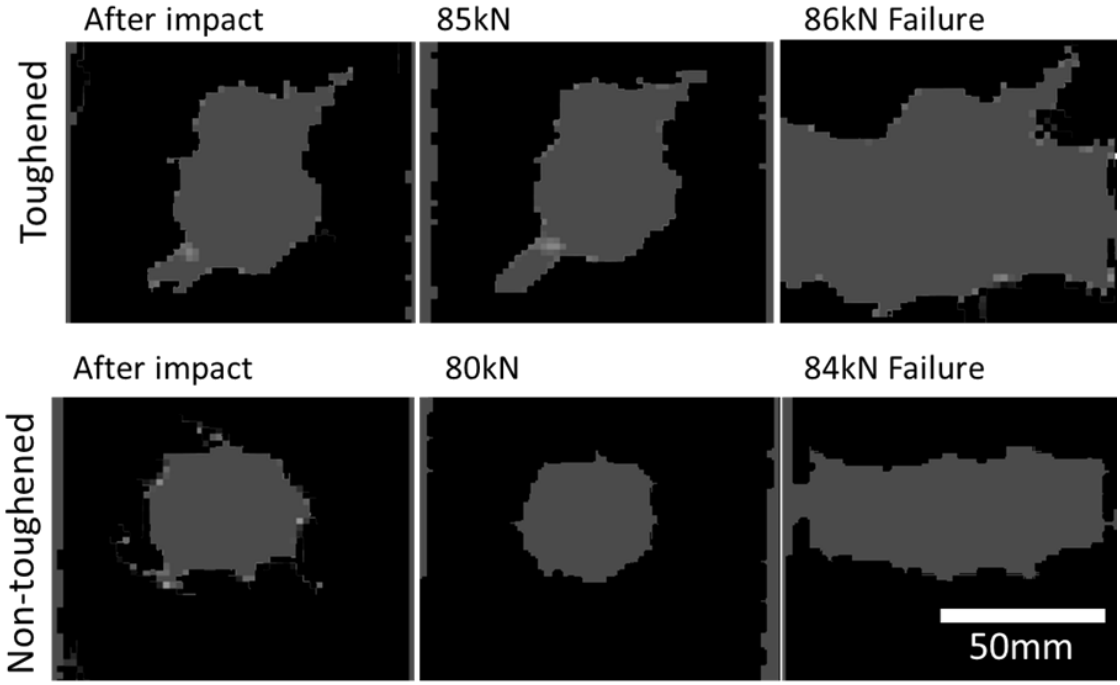

Figure 9.3: Interrupted CAI tests monitoring damage by C-scan undertaken on the T3 and UT material systems.

µCT cross-sections at the impact site after impact and after application of a near-failure compressive load are shown in Figure 9.4 for the T1 and T3 material systems. Common to the UT, T1 and T3 systems, an increase in residual crack-opening displacement two to four plies from the back face (*i.e*. opposite to the impact site) was observed as highlighted in (i). In combination with an increase in crack-opening, delamination growth was clearly detected, propagating into the undamaged cone beneath the impact site, *e.g.* (ii).

The sum of the residual crack-opening displacements above and below mid-plane was calculated at a particular cross-section using the partial volume correction algorithm presented in chapter 5. The measurements were taken 5 mm left of the impact site as to not include additional delamination propagating into the measured region; these are presented in Figure 9.5. It is clear that in all five material systems there is some increase in crack-opening after application of near-failure loads. Such observations of crack-opening may indicate sub-critical buckling of the sublaminates, this is discussed later.

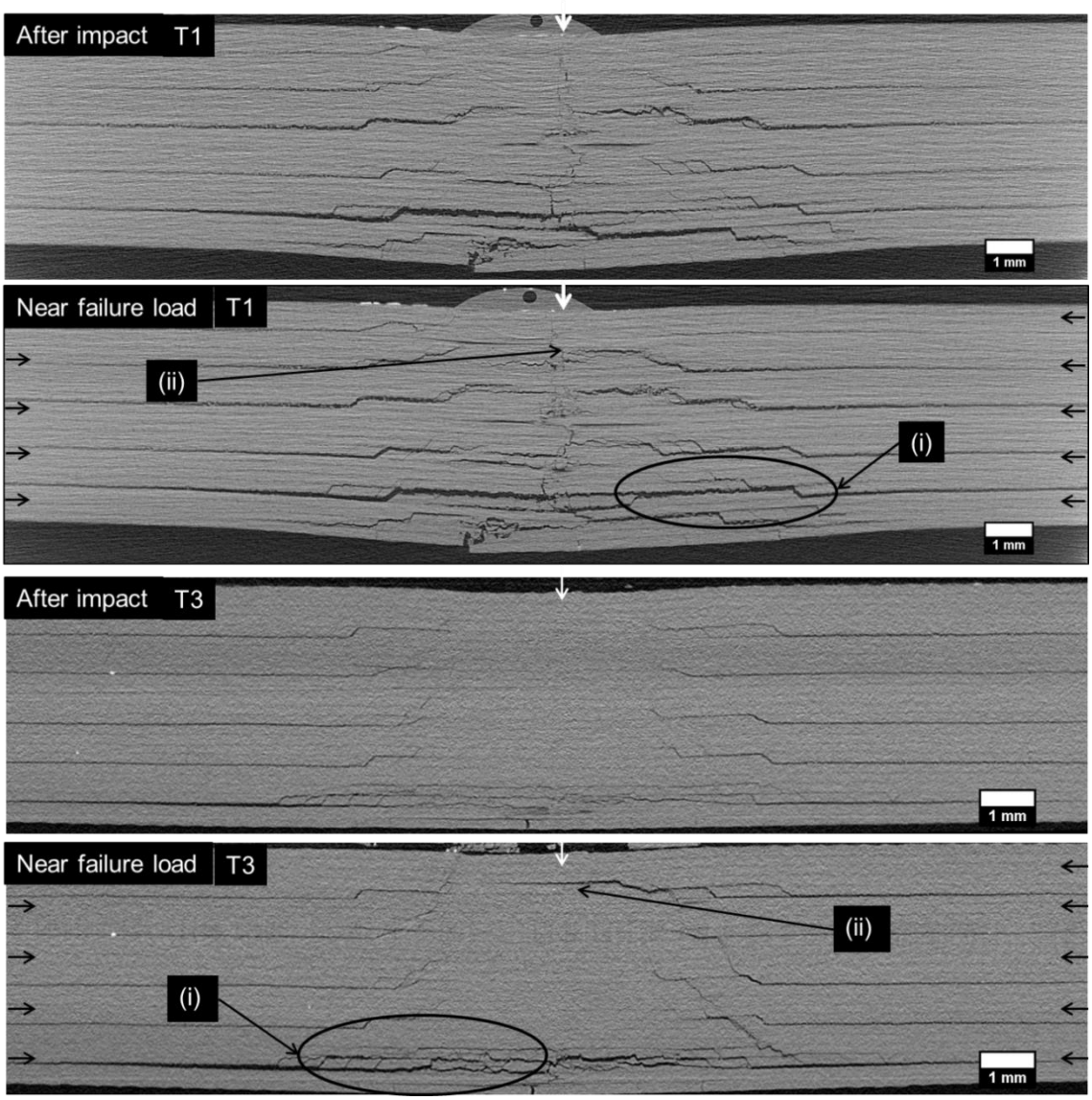

Figure 9.4: µCT cross-sections of T1 and T3 material systems showing: (i) increase in crack-opening and (ii) delamination growth into the undamaged cone after application of a near failure load. White arrow indicates location of impact and side arrows indicate loading direction.

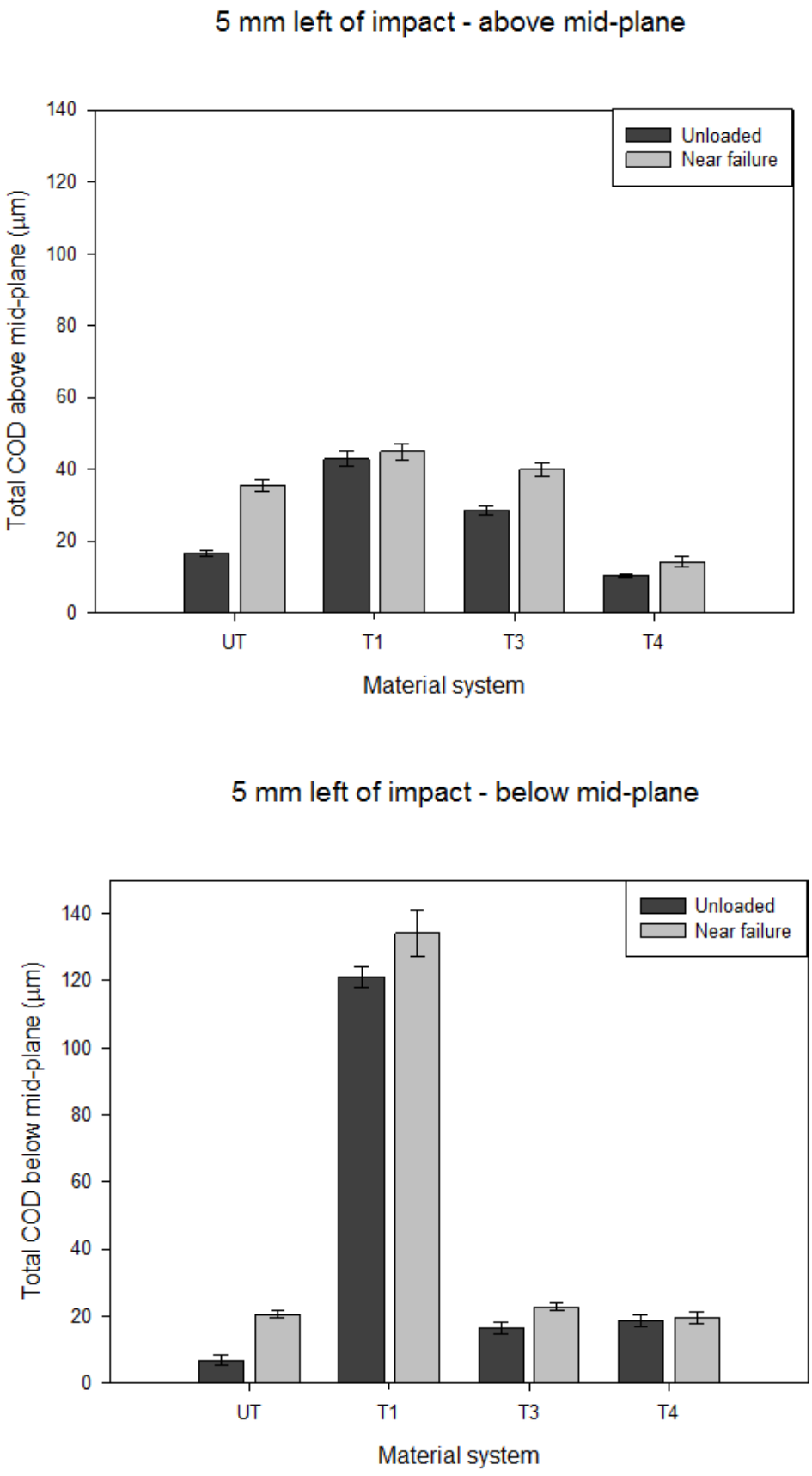

Figure 9.5: Measurement of the sum of the residual delamination crack-opening displacements above and below mid-plane as measured 5 mm to the left of the impact site.

Figure 9.6 shows a 3D segmentation of two modes of delaminations: (i) central where delaminations grow into the undamaged cone and (ii) 45° segments where delaminations grow away from the impact site, constrained at the interface between two matrix cracks 45° apart. The 45° delamination segments form a "spiral staircase" of delaminations through the thickness of the material; this is illustrated by the example shown in Figure 9.7 representing segmented delaminations at four ply interfaces with each colour representing a delamination at a particular ply interface. The combination of the 45° delamination segments forms a near circular pattern surrounding an undamaged "cone" of material immediately below the impact site. The projection of the near circular patterns represents the damage area typically obtained through ultrasonic C-scan methods. Across all systems studied, no detectable delamination growth was observed on the 45° delamination segments during loading up to the near failure loads. Delamination growth was only observed to occur within the undamaged cone region formed by the impact. The distribution of damage surrounding the undamaged cone is shown clearly in a 3D segmentation of the UT system in Figure 9.8.

To quantify this "inward" delamination growth, the total length across central delaminations was measured after impact and after application of near-failure loads. The arrows in Figure 9.6 (i) show how the total length of these central delaminations was measured. These measurements are plotted in Figure 9.9 representing the normalised central delamination length against the ply interface for impact and near failure loads. Delamination extents were normalised by dividing the measured length by the largest measured length for that material system. Ply interface numbers are labelled in order of distance from the impact side of the coupon with ply 1/2 representing the interface closest to the impact side. From the plot, it is clear central delamination growth is occurring into the undamaged cone in the UT, T1 and T3 systems at near failure loads. What is also interesting is the initiation of new central delamination sites that were captured at six interfaces in the UT system and two on the T1 system. These delaminations were observed initiating from pre-existing matrix cracks. The T1 system had central delaminations at nine ply interfaces after impact, this resulted in more

impact-induced damage growing into the undamaged cone in comparison to the other systems, see Figure 9.4.

Delamination growth can be explained by considering the out-of-plane buckling of the sublaminates created by compressive loading. Such out-of-plane buckling of the sublaminates provides a mode I driving force to propagate delaminations into the undamaged cone. The out-of-plane deflection during post-impact compression has also been observed in other studies through surface profilometry [2, 11, 12, 18].

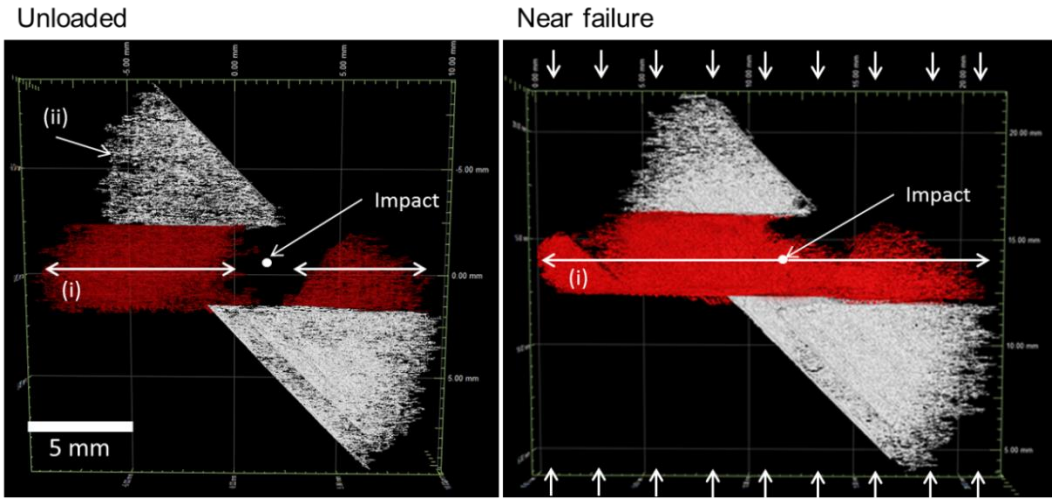

Figure 9.6: T3 material system showing (i) growth of ‘central’ delamination between the third and fourth ply interface into the undamaged cone. (ii) represents a 45° delamination segment, there was no detectable delamination growth of these delamination segments.

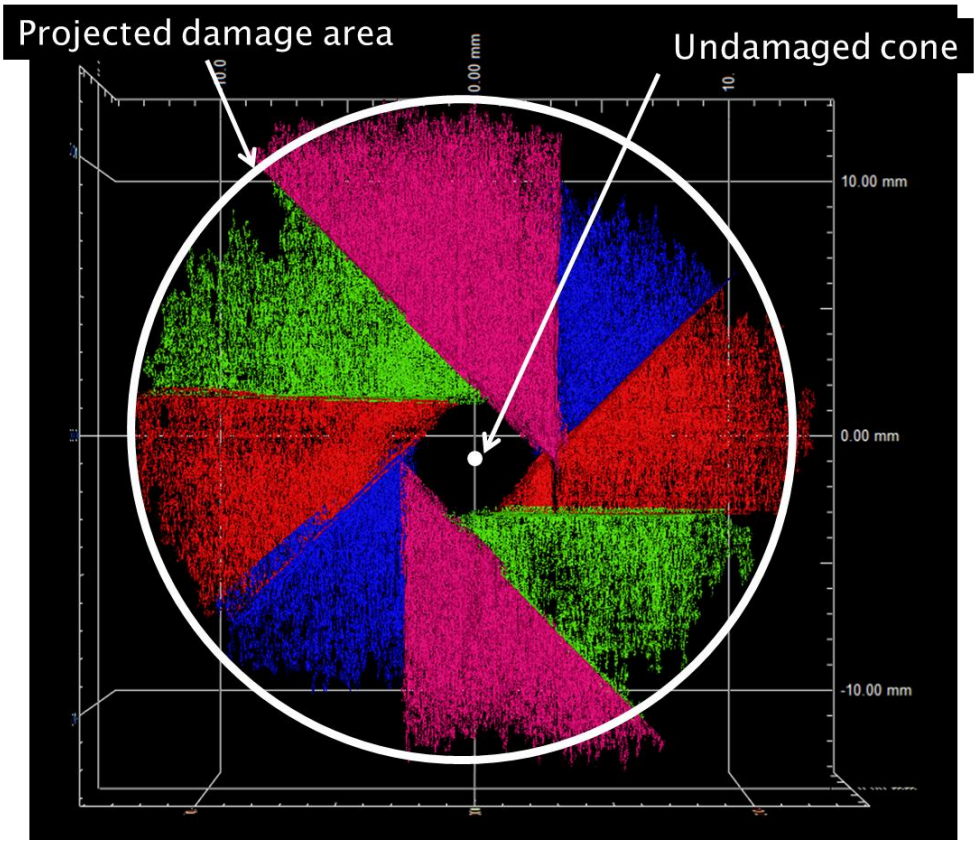

Figure 9.7: 45° delamination segments.

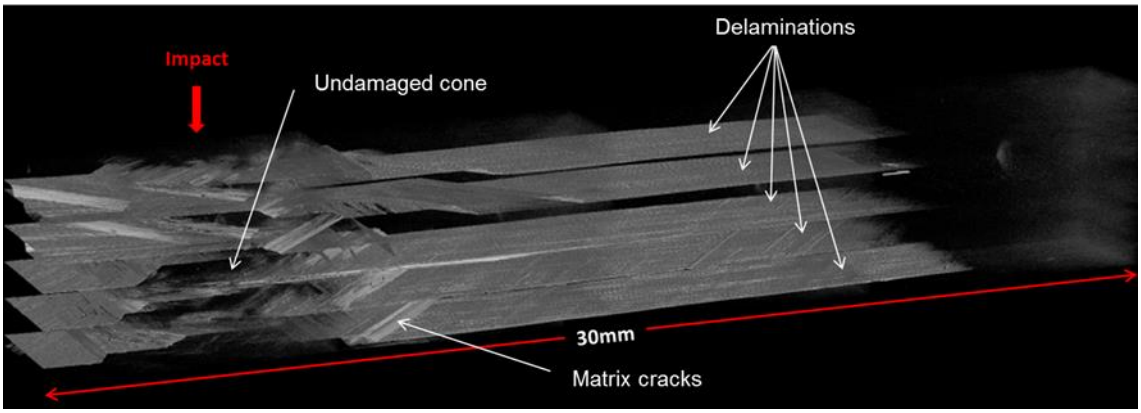

Figure 9.8: 3D segmentation of UT matchstick sample subjected to 25 J of impact. Note the undamaged cone forming beneath the impacted region.

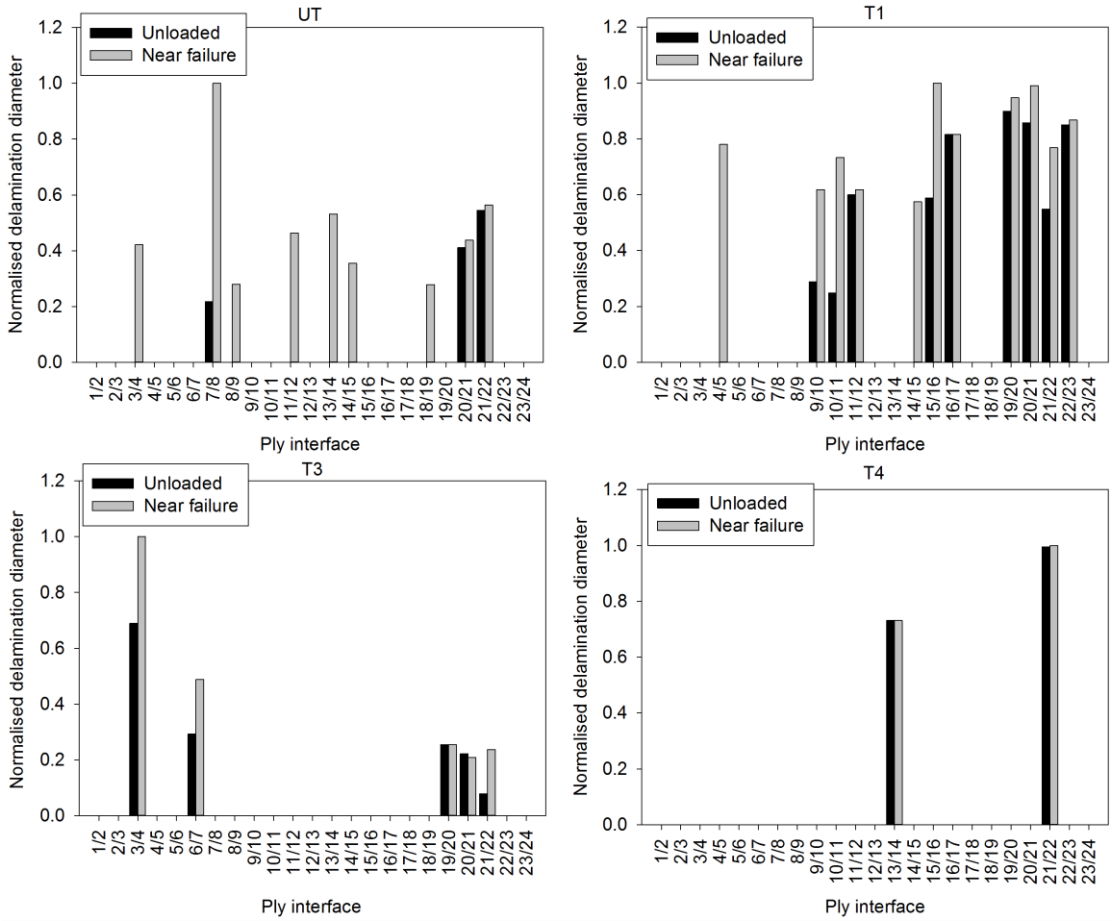

Figure 9.9: Measurements of the total 'central' delamination lengths within the undamaged cone region, measured at each ply interface after impact and after application of a near failure compressive load for each material system.

µCT cross-sections of the T4 system are shown in Figure 9.10. In the T4 system which has the greatest damage resistance, no delamination growth into the cone was observed at the near-failure load. However in the scan taken after CAI failure, delaminations were observed in this undamaged region indicated at (i). It is likely that the load step prior to CAI failure was not sufficiently high in this case to create delamination growth into this region. In comparison, the other systems were within 0.4 % or exceeded the failure load in the load step prior to failure, whilst the T4 load step prior to failure was 1.3 % below the failure load.

The other observation with the T4 system is the significant permanent out-of-plane deformation caused by the impact event highlighted in (ii) creating an indentation and locally bowed plies. An out-of-plane deformation of ~0.3 mm was measured at the mid-plane directly beneath the impact site. This was similar to the T1 system.

On the UT and T3 systems, the permanent out-of-plane deformation beneath the impact site at the mid-plane was approximately half, *i.e.* ~ 0.15 mm. The effective lateral extent of this out-of-plane deformation is ~15 mm for all systems tested.

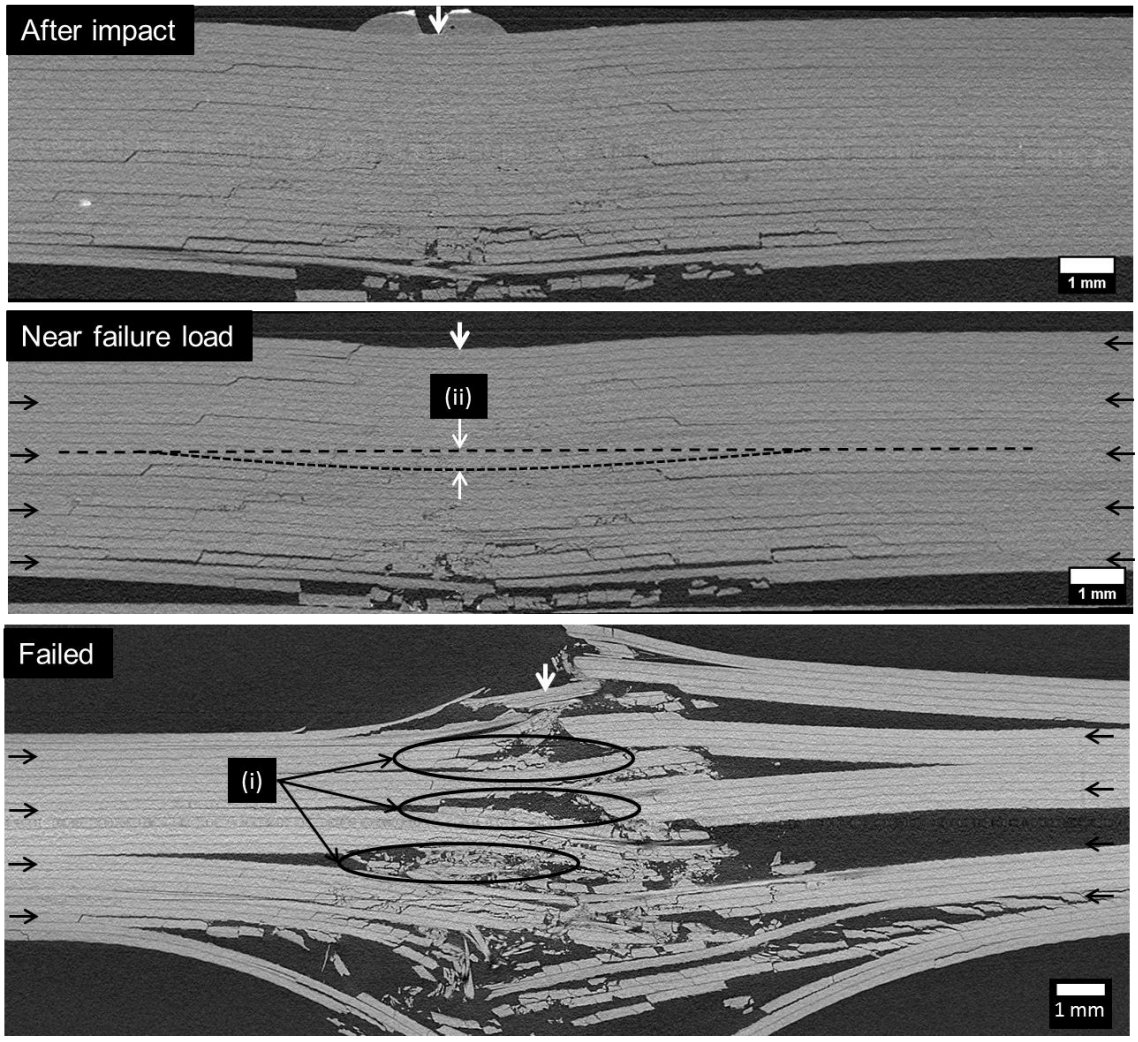

Figure 9.10: T4 material system, µCT cross-section at the impact region after impact, after application of near failure load and after failure. No significant observable damage was detected at the near failure stage. Black arrows on the side indicate loading direction. (i) represents delamination growth into the undamaged cone detected after failure and (ii) represents a ~0.3 mm out-of-plane deformation caused by the impact

9.3.2.2 Fibre fracture development

Pre-existing 0° fibre fracture in some of the particle-toughened systems was found to grow laterally across the ply at near-failure loads, as shown circled in Figure 9.11 (a). Similar observations have been made previously [19]. A 3D segmentation

of this fibre fracture (b) is shown in red, and can be seen to propagate across a load bearing 0° ply, which has delaminations at its interfaces with neighbouring ±45° plies, shown in blue and yellow. In systems where no 0° pre-existing fibre fracture was present after impact, there was no detectable fibre fracture at near failure loads. It is conceivable that pre-existing failed fibres led to a redistribution of load to the neighbouring 0° load bearing fibres, leading to a growth of fibre fracture laterally across the ply. Such fibre fracture in the load bearing 0° plies will inevitably contribute towards a reduction in compressive failure load. The current observations indicate this is most important for the T4 system which exhibited a greatly reduced projected impact damage area, but sustained significantly more fibre fracture during impact in comparison to the other systems. An interesting point to consider is the degree to which CAI load performance in these materials is a convolution of, or competition between, load bearing fibre fracture (and associated growth during loading) and loss of constraint from delamination. Independent of which case applies, the increased incidence of this additional damage mechanism appears to provide a simple explanation of greater CAI load sensitivity of the T4 system when compared on an equivalent delamination area basis in Figure 9.2.

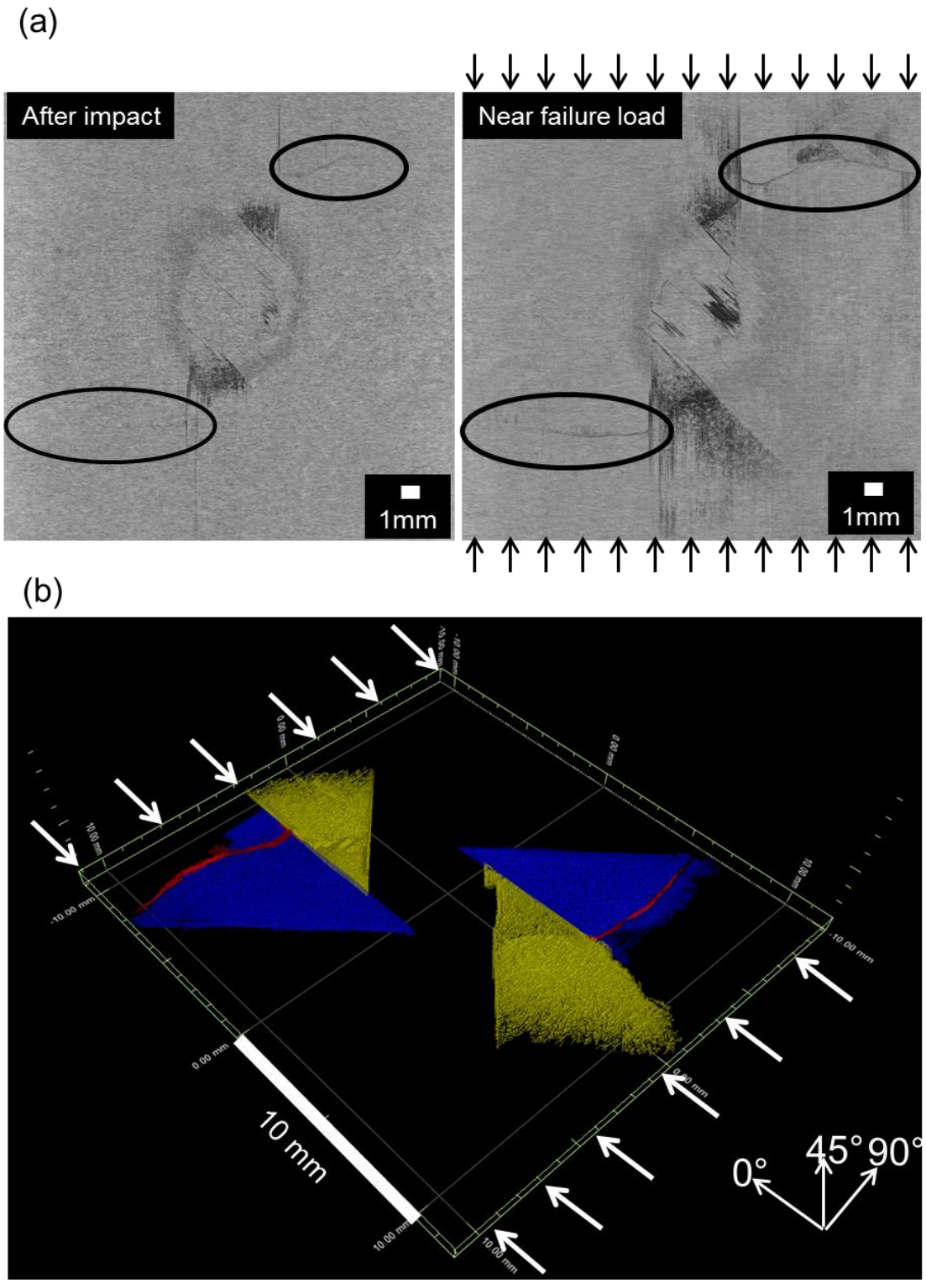

Figure 9.11: T1 material system, µCT cross-section (a) showing load bearing 0° fibre fracture growth propagating longitudinally off a pre-existing region of fibre fracture after application of near failure compression load. This occurred on the sixth ply from the impact side. 3D segmentation of this fibre fracture is shown in red in (b) with neighbouring delaminations occurring at the interfaces between the fifth and sixth (yellow), and sixth and seventh (blue) plies.

9.3.2.3 Sequence of events leading to compressive failure

In the UT, T1 and T3 material systems, central delamination growth was observed propagating into the undamaged “cone” beneath the impact site. The progress of delamination growth at the impact site is shown for a UT system in Figure 9.12 at three stages: after impact, after application of a near-failure compressive load and after the coupon failed. Key features contributing to critical buckling of the sublaminates in this region may be linked to: (i) representing the undamaged “cone”, (ii) showing delamination growth into this undamaged cone, and (iii) showing critical sublaminate buckling. In the load step prior to the near failure loading stage, delamination growth into the undamaged cone was only observed across the upper third and fourth ply interface. Substantial delamination growth into the undamaged cone occurred immediately prior to CAI failure resulting in a sudden loss of sublaminate stability.

The importance of the undamaged cone is simply illustrated schematically in Figure 9.13 where in (a) it offers support to the sublaminates at the centre resulting in a shorter unsupported length ‘L‘ of the sublaminates. As the compressive load is increased, out-of-plane deflection of the sublaminates occurs and is linked to delamination growth into the undamaged cone. When delamination growth within the cone allows the delaminations to extend, unbridged across the full near-circular impact damage region, it effectively more than doubles (in a one dimensional sense at least) the unsupported length ‘>2L’ of the sublaminates, (b). This sudden increase in unsupported length significantly reduces the load-carrying capability of the sublaminates resulting in local buckling.

The significance of the undamaged cone has been reported in finite element models by Craven et al. [20] which shows that the undamaged cone leads to two smaller local buckles compared to a single larger buckle in a system without an undamaged cone. As a result, the inclusion of an undamaged cone led to an increase in local buckling strain by a factor of approximately two, although the model did not include delamination growth into this region. Considering the occurrence of delamination growth into the undamaged cone, the local buckling strain is expected to be greater than a system modelled without an undamaged

cone but lower than the inclusion of an undamaged cone with no delamination growth.

The gain in buckling strain by the undamaged cone highlights a clear advantage for systems preventing delaminations propagating across the undamaged cone during loading in order to maximise the critical failure strain and load. Prevention of this delamination propagation is achievable by maximising the quasi-static fracture toughness. In particle-toughened systems, the increase in fracture toughness is achieved by providing traction sites between sublaminates, see Figure 9.14 (a). Whilst the presence of bridging ligaments was not easily observed from the μCT scans, used in the present study, their presence has been observed using higher resolution SRCT as shown in chapter 7, see (b). This process can be seen to suppress the onset of delamination growth into the undamaged cone. With the exception of the T2 system, particle-toughened systems resulted in bridging ligaments formed by the toughening particles bearing some of the load between the crack faces in the interlaminar region; this process acts to reduce the stress intensity at the crack tip. In the T2 system, delaminations occurred in the intralaminar regions where fibre bridging mechanisms were observed under mode I loading conditions in another study using the same material [21].

By suppressing delamination growth into the cone, sublaminates maintain a shorter unpinned length thereby increasing stability and load carrying capability. This is consistent with the observation that the T2 and T3 systems maintained ~30 % greater failure stress for a given projected damage area compared to the UT system. The more marginal improvement in the T1 system is consistent with initial delaminations within the undamaged cone reducing the extent of material available for delamination propagation. In addition to suppressing delamination growth, should the ligaments extend sufficiently far behind the crack tip they may also counter out-of-plane deflection of the sublaminates by ‘tying’ regions together in a similar way to Z-pinning strategies [7, 22]. Use of high resolution facilities, *e.g.* synchrotron radiation laminography [17] in future work would allow confirmation of the role of particles in restricting delamination and thus determining the CAI failure load.

The observation of delamination growth into the undamaged cone and the presence of bridging ligament formation highlights some of the limitations in simplified sublaminate buckling models such as those using a Rayleigh-Ritz solution of circular or elliptical delaminations [13, 20, 23]. Based on this solution, it is found that the buckling load and strain generally follows an inverse square dependency on delamination length as given by Equation (9-1):

$$\varepsilon_B, F_B \propto \frac{1}{L^2} \tag{9-1}$$

where ε_B is the buckling strain, F_B is the buckling load and L is the delamination length across the sublaminate in the loading direction. Based on this relationship, the buckling strain/load is governed by the size of the delamination length across the sublaminate. This is not so straightforward in this study, the ~30 % increase in failure stress for a given damage area in two of the particles systems compared to the untoughened system is attributed to the observed delamination growth through the undamaged cone, and bridging ligament formation creating traction sites between sublaminates. The complexity of the mechanisms observed in this study highlights features that are important to capture and include in models to accurately predict failure beyond a simplified critical delamination size.

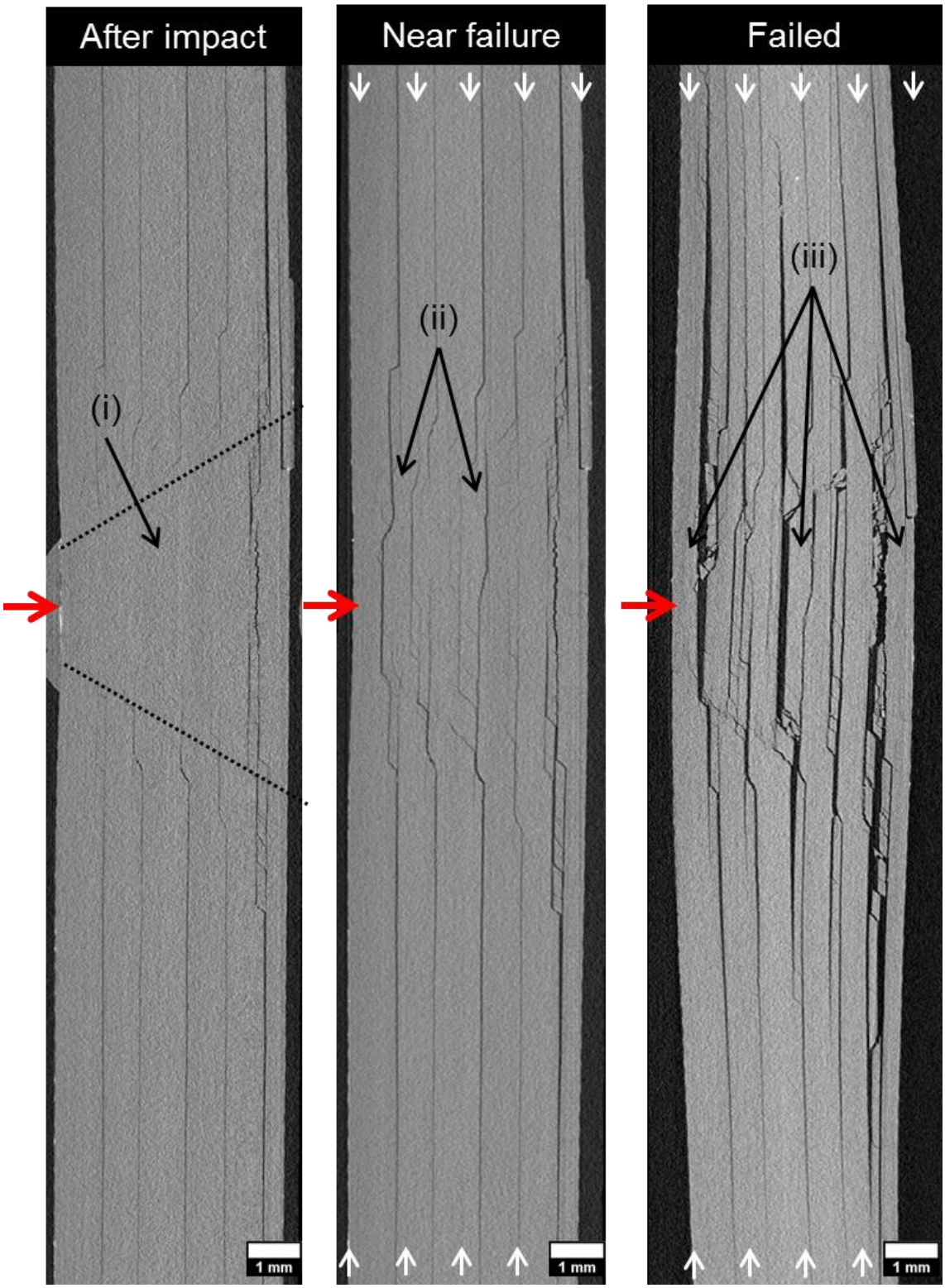

Figure 9.12: µCT cross-section at the impact site, red arrow indicating impact location, and white arrows indicating CAI loading direction. (i) undamaged cone, (ii) delamination growth into the undamaged cone and (iii) sublaminate buckling.

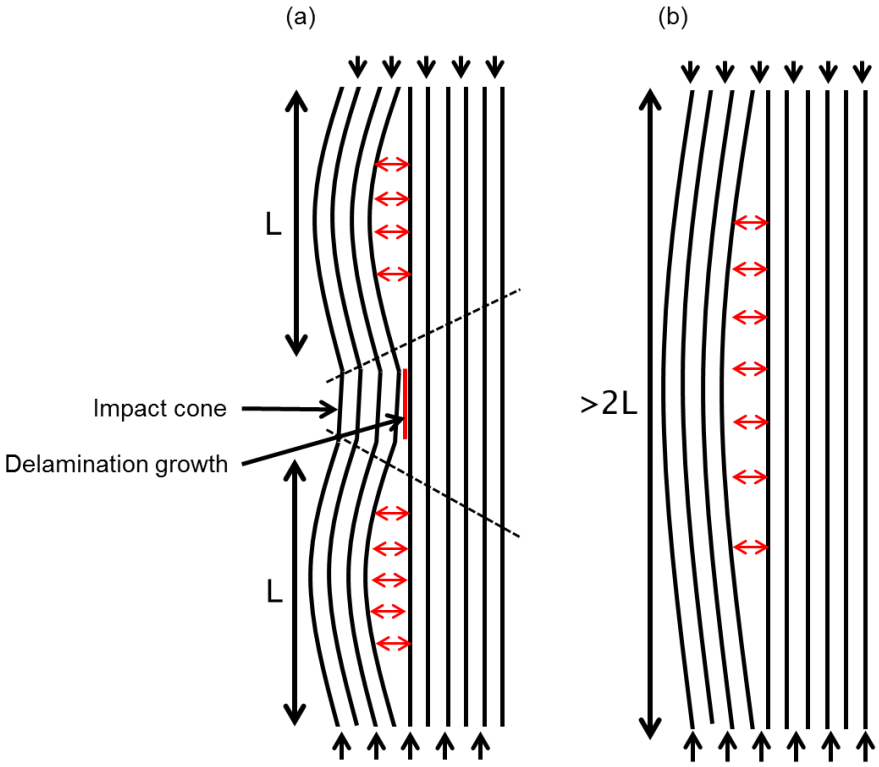

Figure 9.13:Schematic showing (a) the unsupported length of the sublaminate 'L' and delamination growth into the impact cone and (b) more than doubling of the unsupported length due to delamination growth.

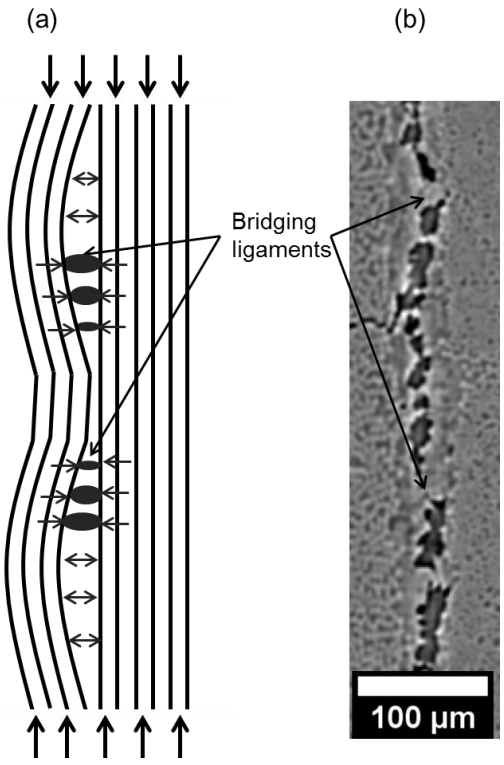

Figure 9.14: (a) schematic illustrating the effects of bridging ligaments on the sublaminates and (b) a high resolution SRCT image of the T4 system showing the presence of these ligaments within the delaminated region.

9.4 Conclusions

The CAI performance of four particle-toughened and one untoughened carbon fibre composite systems were examined. Consistent with previous work the CAI strength correlated strongly with the projected impact damage area.

In addition, for a given damage area, the CAI strength also correlated with the damage resistance: up to a certain point, tougher materials exhibited higher CAI strength. Compared to untoughened systems, particle toughened systems demonstrated up to 30 % improvement to failure stress for a given damage area highlighting that the link between failure stress and the size of the delamination area is not straightforward. Through use of µCT to study CAI damage growth, several observations were made regarding: delamination growth into the undamaged cone immediately under the impact site, driven by out-of-plane deflection of the sublaminates, growth of pre-existing 0° fibre fracture, and permanent out-of-plane deformation.

Regarding the T4 system, it is known from chapter 8 that despite being the toughest material system by suppressing delamination growth, it also led to more extensive fibre fracture. This behaviour provided a simple explanation of the greater CAI load-damage area sensitivity for this material system. It is therefore suggested that very tough material systems may be developed at the cost of being more prone to fibre fracture during impact, which may in turn also significantly contribute to a loss in CAI strength.

The importance of the undamaged cone of material under the impact site was observed to constrain the buckling deformation of the sublaminates. When delamination growth into this region occurs, it connects the surrounding delaminated regions, greatly increasing the unsupported length of the sublaminates and significantly reducing its residual load bearing capability. This mechanism apparently controls the buckling of the sublaminates and provides a mechanistic explanation for the role of toughness in determining the CAI strength for a given damage area. After application of near-failure compressive loads, no sub-critical delamination growth was observed beyond the envelope defined by the projected damage area caused by the impact event.

Whilst higher resolution would be required to increase confidence that these micromechanistic effects are indeed occurring, the findings in this work have pointed to a key topic for further study. If, as might be suspected, particle-bridging plays a key role determining the residual in CAI strength; this may be a vital area of improvement for the development of superior damage tolerant materials. It also raises questions regarding the transferability of CAI test data to the practical damage resistance and damage tolerance in composite structures. It is strongly indicated that CAI performance is strongly determined by quite subtle, local effects, such as rate dependences, formation (or not) of an undamaged cone, and the occurrence of fibre fracture. There is scope for work to be conducted to evaluate the robustness of CAI data in determining the *in situ* damage resistance and damage tolerance of more complicated built up structure subjected to typical in service damage events. This may be best achieved by modelling, with limited experimental verification.

9.5 References

[1] Cartie, D.D.R. and Irving, P.E., *Effect of resin and fibre properties on impact and compression after impact performance of CFRP.* Composites Part a-Applied Science and Manufacturing, 2002. **33**(4): pp. 483-493.

[2] Reis, L. and de Freitas, M., *Damage growth analysis of low velocity impacted composite panels.* Composite Structures, 1997. **38**(1-4): pp. 509-515.

[3] Garg, A.C., *Delamination - a Damage Mode in Composite Structures.* Engineering Fracture Mechanics, 1988. **29**(5): pp. 557-584.

[4] Wisnom, M.R., *The role of delamination in failure of fibre-reinforced composites.* Philosophical Transactions of the Royal Society a-Mathematical Physical and Engineering Sciences, 2012. **370**(1965): pp. 1850-1870.

[5] Davies, G.A.O., Hitchings, D., and Zhou, G., *Impact damage and residual strengths of woven fabric glass/polyester laminates.* Composites Part a-Applied Science and Manufacturing, 1996. **27**(12): pp. 1147-1156.

[6] Sanchez-Saez, S., Barbero, E., Zaera, R., and Navarro, C., *Compression after impact of thin composite laminates.* Composites Science and Technology, 2005. **65**(13): pp. 1911-1919.

[7] Zhang, X., Hounslow, L., and Grassi, M., *Improvement of low-velocity impact and compression-after-impact performance by z-fibre pinning.* Composites Science and Technology, 2006. **66**(15): pp. 2785-2794.

[8] Ishikawa, T., Hayashi, Y., and Matsushima, M., *Compression after Impact (Cai) Properties of Cf/Peek (Apc-2) and Conventional Cf-Epoxy Stiffened Panels.* Icas Proceedings 1992, Vols 1 and 2, 1992: pp. 1225-1234.

[9] Recker, H.G., Altstadt, V., Eberle, W., Folda, T., Gerth, D., Heckmann, W., Ittemann, P., Tesch, H., and Weber, T., *Toughened Thermosets for Damage Tolerant Carbon-Fiber Reinforced Composites.* Advanced Materials : The Big Payoff, 1989. **21**: pp. 283-293.
[10] Zhou, G. and Rivera, L.A., *Investigation on the reduction of in-plane compressive strength in thick preconditioned composite panels.* Journal of Composite Materials, 2007. **41**(16): pp. 1961-1994.
[11] de Freitas, M. and Reis, L., *Failure mechanisms on composite specimens subjected to compression after impact.* Composite Structures, 1998. **42**(4): pp. 365-373.
[12] Habib, F.A., *A new method for evaluating the residual compression strength of composites after impact.* Composite Structures, 2001. **53**(3): pp. 309-316.
[13] Chai, H., Knauss, W.G., and Babcock, C.D., *Observation of Damage Growth in Compressively Loaded Laminates.* Experimental Mechanics, 1983. **23**(3): pp. 329-337.
[14] Yan, H., Oskay, C., Krishnan, A., and Xu, L.R., *Compression-after-impact response of woven fiber-reinforced composites.* Composites Science and Technology, 2010. **70**(14): pp. 2128-2136.
[15] Soutis, C. and Curtis, P.T., *Prediction of the post-impact compressive strength of CFRP laminated composites.* Composites Science and Technology, 1996. **56**(6): pp. 677-684.
[16] Pavier, M.J. and Clarke, M.P., *Experimental-Techniques for the Investigation of the Effects of Impact Damage on Carbon-Fiber Composites.* Composites Science and Technology, 1995. **55**(2): pp. 157-169.
[17] Bull, D.J., Helfen, L., Sinclair, I., Spearing, S.M., and Baumbach, T., *A comparison of multi-scale 3D X-ray tomographic inspection techniques for assessing carbon fibre composite impact damage.* Composites Science and Technology, 2013. **75**: pp. 55-61.
[18] Ishikawa, T., Sugimoto, S., Matsushima, M., and Hayashi, Y., *Some experimental findings in compression-after-impact (CAI) tests of CF/PEEK (APC-2) and conventional CF/epoxy flat plates.* Composites Science and Technology, 1995. **55**(4): pp. 349-363.
[19] Aymerich, F. and Priolo, P., *Characterization of fracture modes in stitched and unstitched cross-ply laminates subjected to low-velocity impact and compression after impact loading.* International Journal of Impact Engineering, 2008. **35**(7): pp. 591-608.
[20] Craven, R., Iannucci, L., and Olsson, R., *Delamination buckling: A finite element study with realistic delamination shapes, multiple delaminations and fibre fracture cracks.* Composites Part A: Applied Science and Manufacturing, 2010. **41**(5): pp. 684-692.
[21] Borstnar, G., Bull, D.J., Mavrogordato, M., Sinclair, I., and Spearing, S.M. *Micromechanistic analysis of toughened carbon fibre composite laminate failure by computed tomography* in Proceedings of the 19th International Conference on Composite Materials, 2013. Montreal, Canada.
[22] Mouritz, A.P., *Review of z-pinned composite laminates.* Composites Part a-Applied Science and Manufacturing, 2007. **38**(12): pp. 2383-2397.
[23] Shivakumar, K.N. and Whitcomb, J.D., *Buckling of a sublaminate in a quasi-Isotropic composite laminate.* Journal of composite materials, 1985. **19**(1): pp. 2-18.

Chapter 10

Conclusions and future work

10.1 Conclusions

Lab-based µCT, synchrotron radiation computed tomography (SRCT) and synchrotron radiation computed laminography (SRCL) have been demonstrated as powerful tools for characterising the macroscopic and microscopic damage mechanisms in laminated CFRP material systems. Through use of both lab and synchrotron-based sources, a multi-scale failure analysis has been achieved. Due to trade-offs between voxel resolution and field of view, complementary use of SRCT, SRCL and µCT was employed to enable the overall extent of damage and corresponding toughening micromechanisms to be captured. The feasibility of locally scanning intact coupons was demonstrated via µCT scans using a fast acquisition time (~45 minutes) and at higher resolutions using synchrotron laminography. This enabled *ex situ* experiments to be performed allowing damage initiation and growth to be monitored on the same coupon. For laminography, the feasibility of locally scanning 4.5 mm thick coupons was shown to work well, this could enable *ex situ* experiments to be performed at micron and sub-micron level resolutions.

Crack-opening displacements were observed in this study down to approximately 30 % of the voxel resolution. To gain more accurate measurements of the crack-opening displacements through µCT scans, a partial volume correction algorithm was used and compared to the same cracks obtained through higher resolution synchrotron CT and laminography scans. In previous studies, this approach has been used before; however this correction technique has not been previously calibrated to higher resolution scan data. In general, partial volume correction measurements of detectable cracks were within 20 % of measurements obtained through SRCT. This correction method enabled more information to be extracted

from µCT scans and was useful for measuring changes to crack-opening displacements in *ex situ* compression-after-impact experiments.

The interaction between matrix cracks and delaminations in impact-damaged coupons was captured in 3D. It was indicated that matrix cracks initiated delaminations which propagated away from the impact site. This behaviour was also observed in the quasi-static indentation experiments. Regarding micromechanisms, toughening particles were most effective at suppressing the extent of delaminations whilst there was little effect on matrix cracks. Particles were seen to toughen the material through energy absorption and crack tip shielding processes. These consisted of particle-resin debonding, crack deflection, increase in crack path length, and bridging ligaments in agreement with observations made in previous studies on similar particle-toughened resin systems. One of the limitations in previous studies is that these toughening behaviours have not been quantified experimentally and in 3D, therefore the overall contributions to toughness are not well understood. Quantification of crack deflection, increase in crack path length, and bridging ligaments suggests bridging behaviour was the most significant mechanism. The extent of bridging near the crack tip was shown to be approximately 150 % greater in the toughest system compared to the untoughened system. Whilst this study has quantified these behaviours, the magnitude of the increase in bridging did not translate to a commensurate relative improvement to damage resistance. This suggests that other toughening mechanisms play important roles and that these are not measurable by SRCT. This will require use of other techniques to complement the SRCT analysis.

One material system (T2) exhibited delaminations occurring predominantly in the intralaminar region, unlike the other particle-toughened systems where delaminations were clearly seen to interact with particles in the interlaminar region. This material system exhibited the poorest mode II fracture toughness and a low impact damage resistance. In the other particle-toughened systems, the formation of particle-resin debonding ahead of the crack tip appeared to play a key role in confining the delamination within the interlaminar region, thereby maintaining the benefit of particle-toughening. It is suggested that there may be a maximum particle-resin interfacial strength beyond which other competing mechanisms of

fracture dominate, *e.g.* fibre-resin debonding and crack growth into the neighbouring ply.

Ex situ quasi-static indentation (QSI) experiments enabled the progress of damage initiation and growth to be monitored as a function of out-of-plane displacement and were compared with low velocity impact data. Whilst most of the literature including the ASTM D6264M standard suggests QSI and low velocity impact offer similar behaviour in terms of force-displacement relationships, sequence of damage and final damage state for an applied energy, this thesis showed similarities and differences between both loading conditions which varied between the material systems. Similarities were observed in the pattern of damage, *i.e.* a "spiral staircase" of delaminations surrounding an undamaged cone at the contact/impact point, and the reasonably close correlation with extent of the damage area vs. the applied energy up to a limit. Where differences were observed, two material systems exhibited a lower damage area under QSI compared to impact at applied energies above 30 J. This phenomenon correlated with a greater extent of microscopic bridging ligaments under QSI loading conditions on these two particle-toughened systems. This suggests that bridging ligaments (one of the key toughening mechanisms discussed in Chapter 7) are sensitive to the applied strain-rate. Maintaining similar levels of bridging under QSI and impact conditions could therefore potentially improve damage resistance to levels observed in the toughest system. Regarding the onset of fibre fracture, the toughest system exhibited a significant extent of fibre fracture at lower loading levels/displacements than the untoughened system. It is suggested that delamination formation in the untoughened system relieved the stresses leading to fibre fracture, thereby delaying its onset. In this instance there may be a possible trade-off between suppressing delamination which affects residual in-plane compression-after-impact strength, and fibre fracture which can also affect the compression-after-impact strength in addition to the residual tensile strength.

µCT scans of incrementally-loaded compression-after-impact tests enabled damage processes immediately prior to failure and post-failure to be observed. An increase in delamination crack-opening displacements was observed suggesting out-of-plane movement of the sublaminates caused by sub-critical buckling. It is apparent that this buckling behaviour provided the driving forces to propagate

delaminations into the undamaged cone of material immediately beneath the impact site. There was no observable delamination growth extending beyond the envelope of the projected damage area. The delamination growth into the undamaged cone resulted in surrounding delaminations linking up, more than doubling the maximum unsupported length of the sublaminates. This is anticipated to significantly reduce the load carrying capability of the sublaminates, which lead to critical buckling of the coupon. It is suggested that bridging ligaments in the toughened systems suppressed delamination growth into the undamaged cone and increased the out-of-plane stability within the sublaminates enabling a larger residual compressive strength for a given projected impact damage area in comparison to the untoughened system.

The study in this thesis highlights that whilst the size of the projected damage area controlled residual CAI strength as previously reported in the literature, delamination growth and interconnectivity through the undamaged cone is an important phenomenon that has not previously been considered and should be included in future models aiming to predict CAI failure. Furthermore, these observations call into question the relevance of the CAI test for screening materials and informing the selection of materials for structural applications. It is clear that relatively small features play a key role in the performance of materials in CAI. The presence of an undamaged cone of material after impact, the influence of rate effects and the onset of fibre failure can all significantly change the CAI response. It is not clear whether these sensitivities would be replicated in the operation of large scale structures. This merits further exploration.

10.2 Future work

The work conducted in this thesis has identified some interesting findings in addition to some unanswered research questions. The major questions lie as to how particles contributed to damage resistance. Whilst the key mechanism has been identified as the formation of bridging ligaments, the relative importance of other toughening mechanisms, not measurable through SRCT, requires further work. Consideration needs to be given to the many parameters associated with particle toughening and particularly bridging ligament formation *e.g.* particle constitutive behaviour (including rate effects), interface strength/toughness,

particle size, shape, concentration, residual stresses, *etc*. It is suggested that an approach involving microscale testing and observations in parallel with modelling is likely to be fruitful.

As an example, in one particle-toughened system (T2), delamination was observed propagating primarily in the intralaminar region; this translated to a poor mode II fracture toughness and low impact damage resistance. It is suggested that there is a critical particle-resin interfacial strength beyond which other mechanisms dominate. This could also be affected by residual stresses in the particle and a stiffness mismatch between the two constituents. The magnitudes of these effects are unknown but could be elucidated by modelling of the competing damage processes and to identify their sensitivity on material and processing parameters

Furthermore, the QSI and impact experiments showed that two material systems have a lower extent of damage area under QSI loading conditions compared to impact above 30 J. This transpired to a greater extent of bridging. Whilst this supports the notion that the bridging behaviour is key to achieving damage resistance, it also highlights the strain-rate dependency of this toughening micromechanism. This also ties in with the mode II fracture toughness values which correlated poorly with impact damage resistance, but did show improvements to the correlation under QSI loading. Considering mode II fracture toughness values are typically determined through quasi-static experiments, it is suggested that dynamic mode II fracture toughness experiments could be used to inform low velocity impact damage resistance. Further work into the effects of strain-rate on the micromechanisms is therefore required.

Fibre fracture was observed to occur at earlier stages in the overall failure of the toughest material systems. This observation highlights the potential trade-off between suppressing the extent of delaminations at the expense of earlier fibre fracture in very tough material systems. Since fibre fracture is known to affect residual tensile stresses, it would be interesting to explore experimentally the loss in tensile strength to understand if this outcome is truly significant.

Compression-after-impact experiments revealed the importance of delamination growth into the undamaged cone. The linking up of surrounding delaminations through the cone more than doubled the unsupported length of the sublaminates

leading to a significant loss in load carrying capability and subsequently critical failure. It is suggested that particle-toughened systems suppressed this growth into the cone which could explain why these systems maintained a greater failure load for a given damage area. Additionally, the traction provided by particle bridging may have also increased sublaminate buckling stability. These observations highlight the importance of including these mechanisms in models to better predict failure

10.2.1 Implementation of results into models

Based on the results found in this thesis, there is a need for multi-scale modelling at the micro-, meso-, and macroscopic levels. These models would have three distinct purposes: 1) to guide the development of more effective materials for damage resistance and damage tolerance, 2) to allow the influence of material choices on CAI performance to be predicted and 3) to predict how impact test and CAI performance might be translated to predict structural damage resistance and damage tolerance. These models need to be calibrated and validated with previous and future experimental work to increase confidence in the models. The models can then aid material development by enabling more informed constituent material selections.

10.2.1.1 Microscopic and mesoscopic models

A schematic shown in Figure 10.1 shows an idealization of a representative volume that might be translated into a micro-mechanical under mode I and mode II loading conditions. Parameters such as particle constitutive behaviour, density, residual stresses, interfacial strength, size, spacing, concentration, strain to failure and loading rates can be used to predict toughness and cohesive properties. While other approaches may be feasible, this problem is particularly amenable to exploration via parametric finite element analysis, most likely using extended or augmented finite element methods. In turn, at the mesocopic level, bridging ligaments forming in the wake of the crack should be modelled in 2D and/or 3D as

traction-separation responses, which could be implemented in cohesive-zone formulations.

It is envisioned that simplification/idealisation of the particle geometry and distribution will be needed to reduce the computational load and detail tied up with finding accurate constitutive equations for a relatively complicated microstructure. One important early study would be to compare the toughening response of an idealised geometry vs. an equivalent realistic geometry so as to understand what the critical elements are for effective idealisation/simplification. Validation of these models should be achieved through use of actual particle geometries obtained though SRCT data which are then meshed using Simpleware^{TM} software, as demonstrated in Figure 10.2. Finite element models should be then compared against SRCT data to check for similar behaviour and predictions of resulting fracture toughness could be made against mechanical tests. Following this, a model with simplified geometries should be compared with these data.

From the observations of the differences in bridging ligament formation between quasi-static indentation and impact loading, it is apparent that the effect of loading rate plays a key role. Therefore, one of the key parameters needed in the finite element models is the strain-rate sensitivity of the constituent properties, particularly of the toughening particles and possibly the interfaces. Being able to predict delamination fracture toughness at increasing strain-rates (in the order of 10 s^{-1} for low velocity impact [1]) may translate to better correlation to impact damage resistance performance.

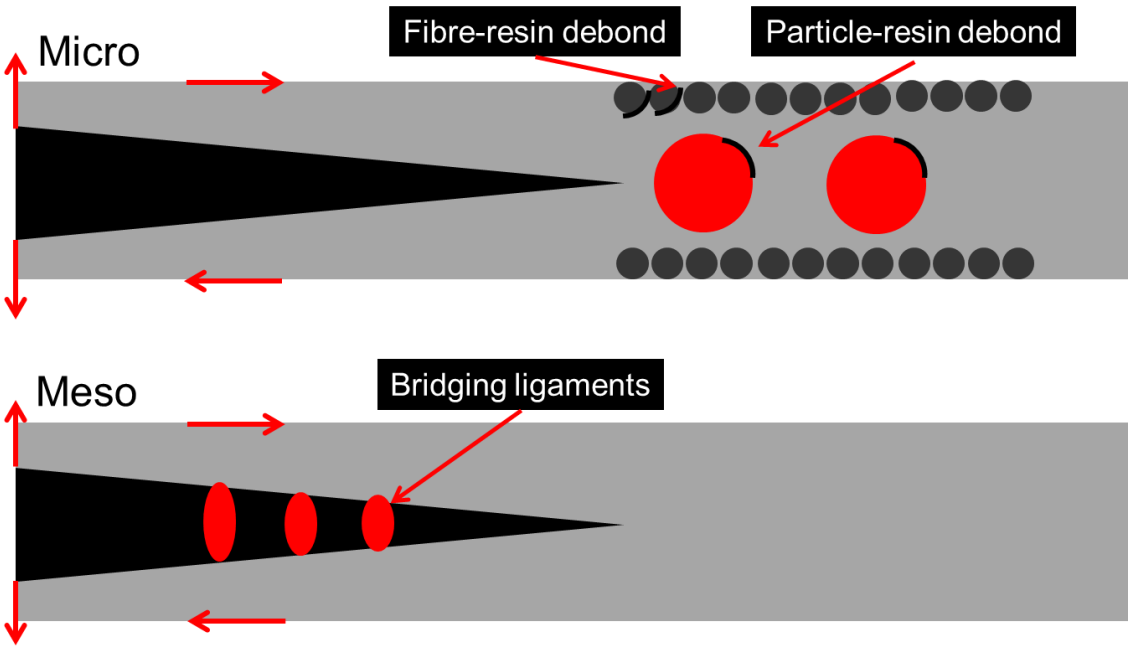

Figure 10.1: micro- and mesoscopic finite element models with mode I and mode II loading conditions. The effect of varying particle properties on toughness and cohesive behaviour can be predicted and used in macroscopic models.

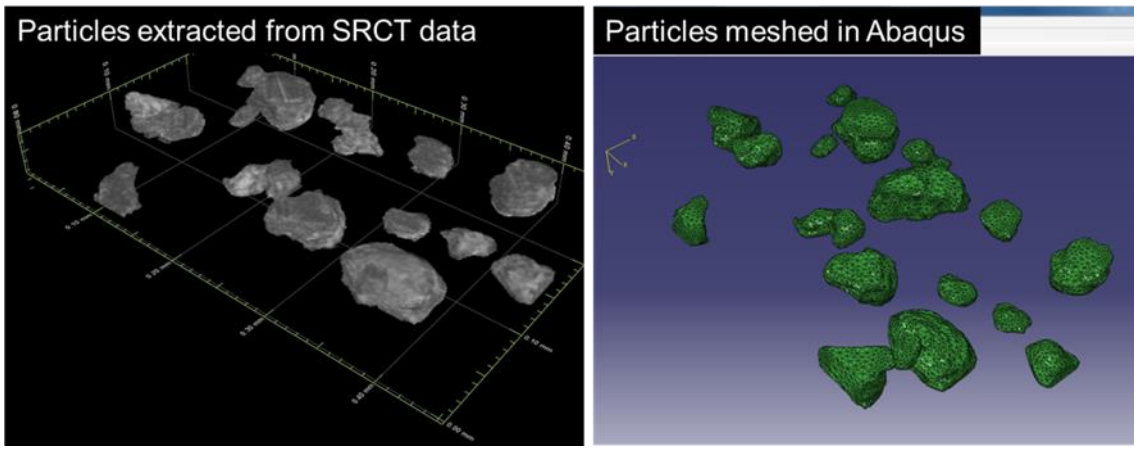

Figure 10.2: Particles extracted from SRCT data (T1 system) can be meshed using Simpleware ™ software. This enables micro- and mesoscopic models using actual particle geometries to be performed in finite element software.

10.2.1.2 Macroscopic models

The use of µCT has enabled a better understanding of the distribution, geometry and scale of the damage after impact and after application of near-failure compressive loads. This information may be used in finite element models to

predict more accurately the development of damage during impact and the compressive strength after a low velocity impact event. Again, XFEM or AFEM models appear to be suitable. These might include cohesive zone models derived from the micro/meso-scale models and/or meso-scale fracture tests, including the effects of strain rate. These models would be used to explore the effects of material parameters at the structural level, and also allow exploration of the similarity or otherwise of the response of representative structural geometries to those observed at the coupon level.

As an intermediate modelling step, the location, geometry and size of delaminations can be directly extracted from μCT data and implemented into finite element models. In a previous study it has been reported that the precise geometry and location of delaminations has a strong influence on the predicted failure load in finite element models [2]. This is in contrast to traditional models using circular idealised delaminations taken from C-scan information. What is now known, based on results in this thesis, is that the undamaged cone and delamination growth into this cone may play an integral role towards CAI strength.

Other factors that were observed from *ex situ* CAI work highlighted 0° fibre fracture growth along pre-existing fibre fracture, permanent out-of-plane deformation beneath the impact cone, and pre-existing delaminations on certain ply interfaces within the undamaged cone. These are all factors that are highly amenable to modelling. Parametrically testing the contribution of each of these factors towards the loss/retention of CAI strength will help identify their relative importance to damage tolerance and allow for informed decision-making in material development.

10.2.2 Image-processing

With such data rich imaging as described in this thesis, the process of feature extraction and obtaining quantitative data was laborious at times. Whilst some tools were developed to automate the measurement processes, preparation of regions of interest was only semi-automated and, therefore, still a manually-intensive procedure. ROI preparation involved extracting features from the scan,

and to achieve the level of detail and ensure the correct features were captured, considerable human intervention was required. Many hundreds of image slices were examined by eye; this highlights a need for further development. Automated identification and accurate extraction of key features such as matrix cracks, delaminations and crack segments would significantly speed up the processing of image data. In future this will enable many repeated tests, more scans to cover a larger region of interest and will provide scope for more material systems to be studied at this level of detail.

10.3 References

[1] Hsiao, H. and Daniel, I., *Strain rate behavior of composite materials.* Composites Part B: Engineering, 1998. **29**(5): pp. 521-533.

[2] Craven, R., Iannucci, L., and Olsson, R., *Delamination buckling: A finite element study with realistic delamination shapes, multiple delaminations and fibre fracture cracks.* Composites Part A: Applied Science and Manufacturing, 2010. **41**(5): pp. 684-692.